Title

Air Pollution Environmental Justice Analysis in California using Advanced Chemical Transport Modeling Systems

Author

Li, Yiting

Publication Date

2022

Peer reviewed|Thesis/dissertation

Air Pollution Environmental Justice Analysis in California using Advanced Chemical Transport Modeling Systems

By

YITING LI
DISSERTATION

Submitted in partial satisfaction of the requirements for the degree of

DOCTOR OF PHILOSOPHY

in

Atmospheric Science

in the

OFFICE OF GRADUATE STUDIES

of the

UNIVERSITY OF CALIFORNIA

DAVIS

Approved:

Michael J. Kleeman (Chair)

Ian C. Faloona

Shu-Hua Chen

Committee in Charge

2022

DEDICATION

To my dear mom and dad, and dearest meow friend Sissy, thanks for supporting throughout my education, thanks for making me see the adventure through to the end.

Table of Contents

Abstract

Air pollution exposure is associated with increased risk for multiple adverse health outcomes including neurological disorders, asthma, diabetes, ischemic heart disease, and death (Anderson et al., 2012; Brook et al., 2010; Dockery et al., 1993; Gauderman et al., 2004; Pope et al., 1995; Tagaris et al., 2009). Race/ethnicity and income are predictors for air pollution exposure across most cities in the United States due to past discriminatory housing practices such as redlining (Nardone et al., 2020; Zenou and Boccard, 2000). Future public policies must address this Environmental Justice issue so that all socio-economic groups have access to clean air.

Predicting air pollution exposure disparities under different future scenarios is a difficult task because non-linear chemistry governs the formation of many pollutants. Historical relationships between pollutant concentrations and land-use or even pollutant concentrations and emissions may therefore not be useful when predicting future conditions. Chemical Transport Models (CTMs) predict air pollution concentrations based on fundamental chemical and physical equations that can accurately transition to future conditions. The research in this thesis explores how to refine CTM inputs and configuring CTM spatial resolution to accurately quantify air pollution exposure disparities in the present day and in the future.

In Chapter 2, ten major spatial surrogates describing the detailed locations of air pollution emissions in California are created/updated for the base year 2010 and future years from 2015 to 2040. The updated spatial surrogates generally improve CTM predictions for PM mass and EC concentrations in the Sacramento area (~10% for PM, ~3% for EC), the Bay Area (~3% for PM, ~1.5% for EC), and the region surrounding Los Angeles (~5% for PM, ~4% for EC). The updated spatial surrogates also improve predicted NOx concentrations in the core region of Los Angeles (~6%).

Chapter 3 explores the relationship between domain size and spatial resolution that affects predicted air pollution disparities in present day and future simulations when data support from measurements is not available. Overall WRF/Chem CTM accuracy improves approximately 9% as spatial resolution increases from 4 km to 250 m in present-day simulations. Exposure disparity results are consistent with previous

findings: minorities experience higher exposure than White residents. Predicted exposure disparities are found to be a function of the model configuration. CTM configurations that use spatial resolution/domain size of 1 km / 10^3 km^2 and 4 km / 10^4 km^2 over Los Angeles can detect a 0.5 μg m^{-3} exposure difference with statistical power greater than 90%.

Chapter 4 conducts a comprehensive analysis of health co-benefits, racial disparities, and source / composition in air pollution exposure under six future energy scenarios and four future meteorology scenarios in California for future year 2050. Deeper reductions in the carbon intensity of energy sources progressively are found to reduce exposure to $PM_{2.5}$ mass and $PM_{0.1}$ mass for all California residents. The three energy scenarios that achieve an ~80% reduction in GHG emissions relative to 1990 levels simultaneously produce the greatest reduction in PM exposure for all California residents and the greatest reduction in the racial disparity of that exposure. The EJ assessment shows that adoption of low-carbon energy sources in the year 2050 reduces the race/ethnicity disparity in air pollution exposure in California by as much as 20% for $PM_{2.5}$ mass and by as much as 40% for $PM_{0.1}$ mass.

Future studies should apply the methods developed in this thesis to other locations across the United States in order to better understand how future policies such as a transition to low carbon energy can help to reduce air pollution exposure disparities by race/ethnicity.

Acknowledgments

I would like to express my deepest gratitude to my supervisor Prof. Michael Kleeman for his invaluable supervision, continuous support, and also patience during my PhD study. Thanks for giving me a chance to keep chasing on long long journey of PhD. Without those great opportunities and helps, I can't take to the end of this adventure. I'm also extremely grateful to Prof. Ian Faloona for bringing an amazing start of PhD life to me. I also could not have undertaken this journey without my defense committee, thank you, Prof. Shu-Hua Chen.

I would like to thank Prof. Cort Anastasio for his help on my qualify exam. I would like to thank Dr. Anikender Kumar, Dr. Caroline Rodier and Dr. Jeremy Lea for their technical support on my study. I would like to thank Dr. Melissa Venecek and Dr. Leonardo Ramirez at California Air Resources Board for their valuable advice on my research.

Special thanks to my colleague and also dear friend – Dr. Yin Li and Dr. Wei Xue. Glad having you two in my PhD journey and my everyday life.

Last, but not least, my warm and heartfelt thanks go to my family for their tremendous support, mom, dad, and kitty Sissy, you are always there, encouraging me, loving me, and strengthening me

Financial support:

Chapter 2 was supported by the California Air Resources Board under contract 15AQP009. Chapter 3 and Chapter 4 were funded by the United States Environmental Protection Agency under Grant No. R83587901.The statements and conclusions in these chapters are those of the authors and not necessarily those of the California Air Resources Board and the United States Environmental Protection Agency.

List of Figures

List of Tables

List of Abbreviations

ACS	American Community Survey
BAU	business-as-usual
BenMAP-CE	Environmental Benefits Mapping and Analysis Program – Community Edition
Caltrans	California Department of Transportation
CanESM	Canadian Earth Systems Model
CARB	California Air Resources Board
CCS	carbon capture and sequestration
CCSM	Community Climate System Model
CO	Carbon Monoxide
COGs	Council of Governments
CSTDM	Caltrans Statewide Travel Demand Model
CTM	Chemical Tranport Model
DUNS	Dun and Bradstreet Financial Database
EC	Elemental Carbon
EJ	Enviornmental Justice
EMINV	UCD emissions processing system
ENSO	El Nino Southern Oscillation
EPA	Environmental Protection Agency
ESAL	Equivalent Single Axle Loads
GAI	Geographic Area Index
GHG	Greenhouse Gases
GIS	Geographic Information System
LEHD	Longitudinal Employer-Household Dynamics
LES	Large Eddy Simulation
LUR	Land Use Regression
MFB	Mean Fractional Bias
MFE	Mean Fractional Error
MPOs	Metropolitan Planning Organizations
NAAQS	the National Ambient Air Quality Standards
NACIS	North American Industry Classification System
NEI	National Emission Inventory
NH3	Ammonia
NLCD	National Land Cover Database
NOx	Nitrogen Oxides
OC	Organic Carbon
PM	Paticulate matter
PWC	population weighted concentrations
RCP4.5	Representative Concentration Pathway 4.5
RCP8.5	Representative Concentration Pathway 8.5

SED	socio-economic data
SHOPP	State Highway Operation and Protection Program
SIC	Standard Industrial Classification
SMART	Stormwater Multiple Application and Report Tracking system
SMOKE	Sparse Matrix Operator Kernel Emissions
SOA	secondary organic aerosol
SoCAB	South Coast Air Basin
SOWC-HR	source-oriented WRF/Chem
SOx	Sulfur Oxides
TOG	Total Organic Gas
UCD/CIT	University of California Davis / California Institute of Technology
UCPRC	University of California Pavement Research Center
VOCs	Volatile Organic Compounds
VSL	value of a statistical life
WRF	Weather Research and Forecast

Chapter 1. Introduction

Exposure to atmospheric pollutants such as airborne particles with diameter less than 2.5 μm ($PM_{2.5}$) is estimated to cause 3.3 million premature deaths per year worldwide(Lelieveld et al., 2015a; World Health Organization, 2021). $PM_{2.5}$ exposure is also associated with increased risk for numerous adverse health effects including neurological disorders, asthma, diabetes, and ischemic heart disease (Anderson et al., 2012; Brook et al., 2010; Dockery et al., 1993; Gauderman et al., 2004; Pope et al., 1995; Tagaris et al., 2009). Each of these conditions results in lost schooldays, lost workdays, and reduced abilities to pursue personal and professional goals. Numerous Environmental Justice (EJ) studies have shown that race/ethnicity and income are predictors for air pollution exposure(Anderson et al., 2018b; Banzhaf et al., 2019; Brulle and Pellow, 2006; Harper et al., 2013a; Marshall et al., 2014; Miranda et al., 2011; Rowangould, 2013; Zhao et al., 2018) across the United States. Minority residents and lower-income residents usually experience higher levels of air pollution, which prevents them from reaching their full potential in society. Future policies based on sound science must address this Environmental Justice issue to provide access to clean air for all residents regardless of their socio-economic class.

Predicting air pollution exposure disparities under different future scenarios is a difficult task because non-linear chemistry governs the formation of many pollutants. Historical relationships between pollutant concentrations and landuse or even pollutant concentrations and emissions may therefore not be useful when predicting future conditions. Chemical Transport Models (CTMs) predict air pollution concentrations based on fundamental chemical and physical equations that can accurately transition to future conditions. CTMs are commonly used to predict present-day and future air pollutant concentrations over scales ranging from 10's of meters to 100's of kilometers. The accuracy of the emissions inputs and the spatial resolution of the calculations are two important factors that impact the accuracy of predicted pollutant concentrations.

These same factors will therefore affect the accuracy of EJ assessments, health co-benefit estimates, and environmental policy evaluations.

The research presented in this thesis explores how CTMs can be used to study air pollution exposure disparity under current and future conditions in California. Chapter 2 focuses on improvements to the location of low-level but ubiquitous area-source emissions. Area-source emissions totals are usually specified at the county level and then distributed into model grid cells using spatial surrogates. In Chapter 2, ten major spatial surrogates describing the detailed locations of air pollution emissions in regional air quality assessments for California were updated/created for the base year 2010 and future years from 2015 to 2040: (i) total population, (ii) total housing, (iii) single-family housing, (iv) total employment, (v) service & commercial employment, (vi) industrial employment, (vii) agricultural employment, (viii) industrial-related surrogate, (ix) off-road construction, and (x) on-road construction surrogates. The first seven surrogates were updated using the latest version of census-based datasets at finer resolution. New industrial-related, off/on-road construction surrogates were developed using realistic datasets to more accurately describe the location of construction projects and industrial facilities. All spatial surrogates were created for the years 2010, 2015 and extrapolated to the years 2020 through 2040. Updated emission spatial patterns were compared to previous emission spatial patterns and a regional air quality model was used to predict differences in ground-level pollutant concentrations resulting from adoption of the updated emissions. The findings from this study help to improve the spatial accuracy of emissions in California, which benefits the accuracy of CTM predictions.

Chapter 3 investigates the impacts of CTM spatial resolution and domain size on EJ assessments. Many studies have concluded that the errors introduced into CTMs by coarse spatial resolution could affect health impact assessments. However, the high computation burden of CTM calculations limits their ability to satisfy requirements for both high resolution and large domain size. Improvements in computational abilities continue to push these limits higher over time, but the tradeoff between resolution and domain size continues to act as a practical limit to the configuration of CTM studies now and in the near-term future. In

Chapter 3, we carried out year 2016 simulation using full CTM calculations over Los Angeles, California, to determine how the combination of domain size and spatial resolution affects predicted air pollution disparities. Spatial surrogates updated / developed in Chapter 2 were used to downscale 4km emissions to 1km / 250m spatial resolution. One set of simulations used the Weather Research and Forecasting (WRF) model coupled with Chemistry (WRF/Chem) with spatial resolution ranging from 250 m to 36 km, comparable to census tract sizes, over domains ranging in size from 320 km^2 to 10,000 km^2. A second set of simulations used the UCD/CIT CTM with spatial resolution ranging from 4km to 24 km over domains ranging in size from 98,000 km^2 to 1,000,000 km^2. Air pollutants disparities then were calculated for races/ethnicities categories and income categories for nine WRF/Chem and three UCD/CIT domain-resolution combinations. After a comprehensive comparison among 12 domain-resolution combinations, we identified a statistical power relationship between spatial resolution and domain size that can detect a 0.5 $\mu g/m^3$ maximum exposure disparity in California. These findings guide the configuration of CTM studies for EJ analysis conducted in Chapter 4.

Chapter 4 applied the framework established in Chapter 2 and Chapter 3 to future year 2050 and conducted a comprehensive analysis of health co-benefits, racial disparities, and source / composition in air pollution exposure under six future energy scenarios and four future meteorology scenarios. California is leading North America in the adoption of new sustainable energy sources to mitigate climate change. State law AB32 committed California to reduce GHG emissions to 1990 levels by 2020. California Governor's Executive Order S-3-05 commits California to an additional 80% reduction by 2050. This massive reduction in GHG emissions will require a transformation in the energy system that will involve choices about technological, fuel and energy resources. An ensemble of six different energy scenarios constructed using the energy-economic optimization model CA-TIMES were evaluated in future years, including (1) BAU – business as usual scenario; (2) GHGAi – a strict GHG reduction scenario that achieves 80% reduction of GHG emission by the year 2050; (3) 2030CAP – a loose GHG reduction scenario but only achieve 40% GHG reductio by the year 2030 without further reduction; (4) CCS – a scenario allows for more combustion to generate electricity by focusing on adoption of carbon capture and sequestration technology; (5) NGB –

a variation of GHGAi that allows for 20% more natural gas combustion for residential and commercial buildings; (6) NGT – another variation of GHGAi that allows for 20% more natural gas combustion for electricity generation. Criteria pollutant emissions were developed for each energy scenario using the CA-REMARQUE model using 4km spatial resolution over four major geographic areas in California: the greater San Francisco Bay Area including Sacramento (SFBA&SAC), the San Joaquin Valley (SJV), Los Angeles (LA), and San Diego (SD). The Weather Research & Forecasting (WRF) model was used to predict future meteorology fields by downscaling two different climate scenarios (RCP4.5 and RCP8.5) generated by two different GCMs (the Community Climate System Model and the Canadian Earth Systems Model). Simulations were performed over 32 weeks randomly selected during the 10-year window from the year 2046 to 2055 to build up a long-term average in the presence of ENSO variability. Health co-benefits were estimated for southern and northern California by races/ethnicities under six scenarios. Source apportionment analysis was done for four geographic areas by races/ethnicities under six scenarios. Air quality disparities were also estimated for $PM_{2.5}$ mass and $PM_{0.1}$ mass by regions and scenarios. These findings helps to identify whether the adoption of low-carbon energy can improve public health and reduce racial disparities through an improvement in air quality.

1.1. Published chapters

The work summarized in Chapters 2-4 has been published in peer reviewed journals. Future studies should cite those journal articles when referencing this work. Chapter 2 has been published as:

Li, Yiting, Rodier, C., Lea, J.D., Harvey, J. and Kleeman, M.J., 2021. Improving spatial surrogates for area source emissions inventories in California. *Atmospheric environment*, *247*, p.117665.

Chapter 3 has been submitted for publication to:

Li, Yiting, Kumar, A., Hamilton, S.D., Lea, J.D., Harvey, J. and Kleeman, M.J., 2022. Spatial resolution required to model air pollution environmental justice in Southern California. *Heliyon, accepted*.

Chapter 4 has been published as:

Li, Yiting, Kumar, A., Li, Y. and Kleeman, M.J., 2022. Adoption of low-carbon fuels reduces race/ethnicity disparities in air pollution exposure in California. *Science of The Total Environment*, *834*, p.155230.

Chapter 2. Improving Spatial Surrogates for Area Source Emissions Inventories in California

2.1. Introduction

Chemical Transport Models (CTMs) are used to predict air pollutant concentrations over scales ranging from 10's of meters to 100's of kilometers (Eastham et al., 2018; González et al., 2018; Hu et al., 2017; Joe et al., 2014; Kuik et al., 2016; Li et al., 2016; Schaap et al., 2015; Woody et al., 2016). One of the most important uses of CTMs is to assist in the design of emissions control programs that will achieve compliance with the National Ambient Air Quality Standards (NAAQS) (Herrera et al., 2010; Hogrefe and Rao, 2001; Kelly et al., 2019; Macpherson et al., 2017; Saylor et al., 1999; Zhang et al., 2011). Another important use of CTMs is to estimate population exposure to various air pollutants (Chen et al., 2014; Huang et al., 2018; Laurent et al., 2014, 2013; Ostro et al., 2015; Stieb et al., 2016; Van Donkelaar et al., 2015; Wang et al., 2016). Multiple studies have concluded that the errors introduced into CTMs by coarse spatial resolution could affect human health impact assessments (Fenech et al., 2018; Thompson and Selin, 2012) and so it is desirable to apply CTMs at the finest possible spatial resolution. Accurately describing the location of emission sources is often a critical factor that determines the fidelity of this overall process to protect public health across the United States (Cohan et al., 2006; Pan et al., 2017; Tan et al., 2015; Valari and Menut, 2008; Zheng et al., 2017).

A top-down approach is widely used to create spatial gridded emissions, and spatial surrogates play an important role in accurately mapping aggregated emissions to model grid cells (Bieser et al., 2011; Bun et al., 2010; Kuenen et al., 2014; US EPA, 2017). The effort needed to prepare spatially accurate emission inventories varies by source category that can be broadly summarized as (i) point sources, (ii) mobile

sources, or (iii) area-sources. Major air pollution point sources in the United States have exact latitude and longitude recorded with their emissions permits making it easy to specify their exact location in emissions inventories. Likewise, mobile sources emit pollutants along well-defined roadways that often have monitors to measure traffic volume (Fameli and Assimakopoulos, 2015; Fu et al., 2017; McDonald et al., 2014). In contrast, the location of area-sources (or non-point sources) are difficult to describe accurately in emissions inventories (Dai and Rocke, 2000; Gkatzoflias et al., 2013; Trombetti et al., 2018). Hundreds or thousands of different types of area sources exist in a typical urban region. As emissions from major point sources and mobile sources are reduced, these numerous area sources have emerged as a very important category for continued progress towards improved air quality (McDonald et al., 2018). Accurately describing the location of area source emissions is of paramount importance for the next generation of regulatory programs to address current and future conditions in the United States.

Area-source emission rates in the United States are often estimated using a formula such as

$$Total\ Emissions = Activity \times (Emissions/Activity)$$

where *"activity"* is a measure such as fuel consumed or production rate and *"(emissions/activity)"* describes the release of air pollutants for each unit of fuel consumed or product created. Emissions totals are calculated for broad spatial zones such as counties or Geographic Area Index (GAI) regions. For example, the California Air Resources Board (CARB) divides the state into 69 GAI regions based on the intersection of county, air basin, and air district political boundaries. The detailed location of area-source emissions within each GAI is then described using spatial surrogates that are assumed to be proportional to the target emission rates. Statistical activity data such as census data, industry registration, traffic information and fuel consumption are commonly used to disaggregate various county-level emissions, but the availability of these datasets varies by location. Population is the most common dataset used to create spatial surrogate (Bieser et al., 2011; Kuenen et al., 2014; Zasina and Zawadzki, 2017; Zhao et al., 2012; Zhou et al., 2017) but CARB currently uses over 100 additional spatial surrogates depending on the exact source-type as summarized in Appendix 1 Table S1-1.

The purpose of this paper is to update ten important spatial surrogates used to specify the location of area-source emissions in California: (i) total population, (ii) total housing, (iii) single-family housing, (iv) total employment, (v) service & commercial employment, (vi) industrial employment, (vii) agricultural employment, (viii) industrial-related surrogate, (ix) off-road construction, and (x) on-road construction surrogates. These ten spatial surrogates allocate emissions locations for sources ranging from lawn and garden equipment to construction and mining to residential/commercial/industrial natural gas combustion. The updated surrogates take advantage of publicly available datasets that can be extrapolated to future years. In the current study, new spatial surrogates were created for the years 2010, 2015 and extrapolated to the years 2020 through 2040. Updated emission spatial patterns were compared to previous emission spatial patterns and a regional air quality model was used to predict differences in ground-level pollutant concentrations resulting from adoption of the updated emissions. The findings from this study help to improve the spatial accuracy of emissions inventories in California, which can be used as a model for other locations in the United States.

2.2. Methods

The ten spatial surrogates updated in the current paper can be divided into three major categories based on their data source and emission source related to: socio-economic data (SED), industrial-related surrogates, and construction equipment surrogates. The construction equipment surrogate allocates 13.1% of particle matter and 8.46% of NOx within total area source emissions (Table 2-1). The industrial employment and industrial-related surrogates are used primarily to allocate gaseous emissions, including 13.9% of NOx, 12.4% of SOx, and 6.85% of TOG (Total Organic Gas). The industrial employment surrogate usually serves as a secondary surrogate for industrial emission that will be used when the primary surrogate is not available within the target geographical region. The SED surrogates accounts for a smaller fraction of the emissions across California compared to the construction equipment and industrial surrogates, but SED surrogates can still have non-negligible impacts on populated areas. Updates to each of the eight

spatial surrogates are described in the sections below. Two new SED surrogates – total employment and agricultural employment were created in Section 2.2.3.

Table 2-1 Fraction of total area source emissions allocated by each surrogate.

				Fraction of area source criteria emissions					
Original surrogate		**Updated surrogate**		**PM**	**TOG**	**NOx**	**CO**	**SOx**	**NH_3**
585	Construction equipment	586	Construction	13.1%	0.77%	8.46%	1.50%	0.15%	
		587	Off-road construction						
		588	On-road construction						
730	Industrial-related			0.26%	6.85%	13.9%	4.36%	12.4%	3.01%
300	Industrial employment								
250	Total housing				0.41%				
440	Total population			0.10%	5.69%	0.26%	0.33%	0.15%	17.8%
620	Service & commercial employment				0.21%	2.8%	0.25%	2.35%	
650	Single-family housing				1.20%	0.23%	2.56%		

2.2.1. Industrial-related surrogate

The industrial-related surrogate (730) is used to describe the location of manufacturing processes and industrial fuel combustion (including natural gas not associated with major point sources). The original industrial-source spatial surrogate was created from the 2016 Dun and Bradstreet Financial Database (DUNS database, http://www.dnb.com/). The DUNS database often lists the address for company headquarters rather than actual industrial facility locations where emissions are released. Moreover, DUNS employment types are classified by the Standard Industrial Classification (SIC) system, which groups industries based on demand or production of goods. As a result, DUNS employment totals include industrial occupations combined with office/managerial occupations that may not be correlated with emissions. Approximately 11% of organizations in the SIC-based DUNS database in California are actually not related to industrial process (Figure S1-1 in Appendix 1). In contrast, North American Industry Classification System (NAICS) groups are organized based on the likeness of the process used to generate goods or services. NAICS codes for industrial occupations used in the Longitudinal Employer-Household Dynamics (LEHD) "OnTheMap" dataset (United State Census Bureau, 2019) are distinct from NAICS codes for

office/managerial occupations yielding more accurate industrial employment totals. Furthermore, LEHD employment locations are specified at the actual industrial facility, which more accurately represents industrial activities than the headquarters location. Adoption of the LEHD manufacturing employment to replace the SIC manufacturing employment yields a spatial distribution with greater variability in Southern California (see Figure S1-2 in Appendix 1). LEHD manufacturing employment data is also consistent with major industrial activities permitted under the Stormwater Multiple Application and Report Tracking system (SMART) database maintained by the California Water Resources Board (see Figure S1-3 in Appendix 1). The agreement between these independent indicators of industrial activity builds confidence in the accuracy of the LEHD manufacturing distribution.

Future-year industrial-related surrogates were adopted from the future-year SED data related to industrial employment generated in Section 2.2.3. Figure S1-4 in Appendix 1 plots the industrial employment distribution alongside the location of industrial activities locations from the SMART database. The results indicate that the future-year industrial employment distribution also captures the spatial pattern of real industrial activities, building confidence in the approach to use future industrial employment as a spatial surrogate for future industrial emissions.

Figure 2-1 shows industrial employment surrogates for the years 2010 and spatial surrogate difference between 2040 and 2010. Total employment, industrial employment, and service & commercial employment are clustered in urban areas in both current and future years. Agricultural employment is significantly lower with most activity focused on the San Joaquin Valley in central California.

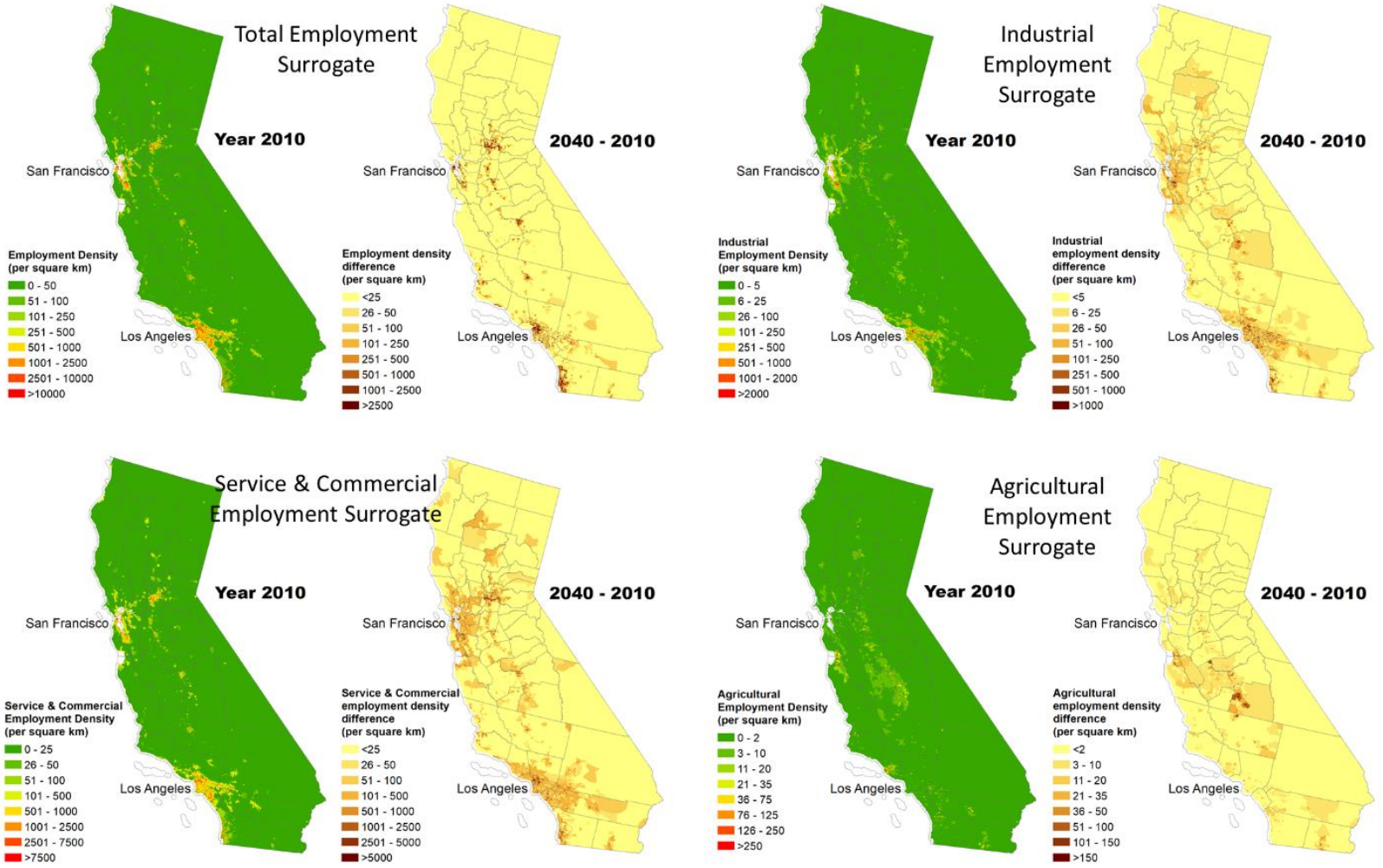

Figure 2-1: Total employment, industrial employment, service & commercial employment, and agricultural employment surrogates in the years 2010 and spatial surrogate difference between 2040 and 2010

2.2.2. Construction equipment surrogate

The construction equipment surrogate (585) is used to describe the spatial location of equipment burning gasoline and diesel fuel for the purpose of creating buildings and roads, and dust from construction activities. The current CARB construction equipment spatial surrogate blends information from two sources: (i) the change in "impervious surfaces (imperviousness)" between 2006 and 2011 from the National Land Cover Database (NLCD) and (ii) the California Department of Transportation (Caltrans) on-road Truck Network (482) surrogate. The combined construction surrogate weights the input impervious surface factor by 90% and the Truck Network factor by 10%. Impervious surfaces are mainly artificial structures or impenetrable materials such as pavements. Changes in imperviousness can be used to identify the pattern, nature and magnitude of the change in urban land cover. From an emissions perspective, an increase in impervious surfaces is almost always associated with construction equipment. However, some construction activities do not change impervious landscape, such as demolition and reconstruction activities for existing buildings. The NLCD impervious surface data is only available in 5-yr increments which does not identify the exact date of the construction activity. The Truck Network represents the location of commercial truck routes including terminal access to ports and national network routes. The construction surrogate assumes that all roads are subject to repair over their lifecycle, and so construction emissions are distributed uniformly on this network. This approach is reasonable over an averaging time of ~15 years but not realistic within in any given year. The surrogate created from the combination of NLCD imperviousness and truck network data only approximately represents construction activities and it is difficult to apply over all potential years of interest.

The construction equipment surrogate created in the current project was separated into three individual surrogates to better represent the different types of construction activity: (i) off-road construction surrogate (587) represents off-road construction recorded in the SMART database; (ii) on-road construction surrogate (588) represents projects from Caltrans highway records; and (iii) construction surrogate (586) is a

combination of 50% surrogate 587 and 50% surrogate 588 as recommended by staff at the California Air Resources Board based on their testing of a range of on-road and off-road weighting factors. Surrogate 586 is hereafter reserved as a backup or secondary surrogate if the primary surrogate is not available in certain areas.

Diesel engine exhaust is one of the major sources of NOx and PM emissions from construction activities (Millstein and Harley, 2009). Heavy diesel equipment including tractors, loaders, backhoes, and skid steer loaders account for 80% of all construction equipment and 78% of annual operating hours in California (California Air Resource Board, 2020, 2010). Tractors, loaders, backhoes, and skid steer loaders are estimated to contribute 67% of total NOx emissions and 70% of total PM emissions from statewide construction and mining activities (California Air Resource Board, 2020, 2010). Heavy diesel-powered equipment is used primarily in large-scale new construction projects or large-scale reconstruction/renovation projects as opposed to small scale construction projects. It is desirable for the off-road construction surrogate to represent these major construction/renovation projects as accurately as possible. Construction surrogates are also used to spatially allocate PM dust emissions during building/road construction. Construction dust comes from material, equipment and transportation (Sandanayake et al., 2016) which are also expected to be highest around large-scale construction sites.

Two updates were made to increase the accuracy of the current-year construction equipment spatial surrogate. First, the NLCD impervious surface surrogate was replaced with off-road construction project permits from the SMART database that describe the project location (lat/lon), construction type, imperviousness change, and distributed activity area. It should be noted that permits in SMART are only required for projects larger than 1 acre, meaning SMART data captures large-scale construction projects that account for the majority of the heavy-duty diesel equipment and dust construction emissions. As a second update, the generic Truck Network surrogate was replaced with the actual location of highway construction projects described in records publicly filed with Caltrans including highway number, the start and stop mile along that highway, and the number of active working days in the project. These actual off-

road and on-road construction locations were converted to the standard map projections used for CARB spatial surrogates, leading to increased accuracy in the location of construction emissions.

The off-road construction surrogate is mainly used to distribute building construction emissions. Most new buildings are associated with an increase in population (either residences or commercial services). A statistical analysis of the correlation between the county-level population growth between 2010 – 2015 and the number of new construction projects yields a high correlation ($R^2 = 0.89$), which builds confidence in the strength of the association between changes in population and changes in construction activity (see Figure S1-5 in Appendix 1). Therefore, future-year off-road construction surrogates are based on population increase calculated from the changes in population surrogates generated in Section 2.2.3. Figure *2-2* shows a current year and a future year off-road construction surrogate. Most of the current-year building construction activity occurs in urban areas (Figure 2-2(a)), which is consistent with the spatial pattern of population difference between years (Figure 2-2(b)).

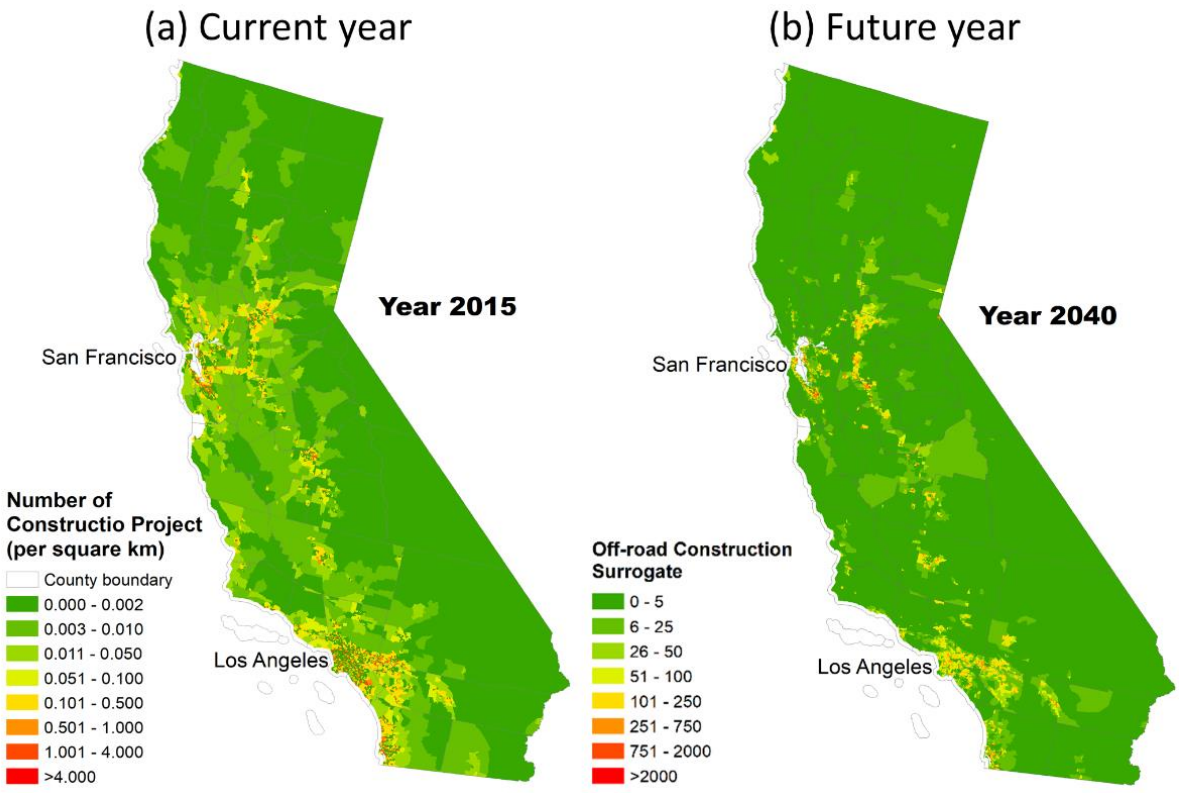

*Figure 2-2. Current and future off-road construction surrogate.*Figure (a) shows year 2015 off-road construction surrogate created from a dataset of construction permits. Figure (b) shows an example of future year off-road construction surrogate, which is the population growth in the preceding 5 year period.

The 10-year future on-road construction surrogate was created from the publicly available State Highway Operation and Protection Program (SHOPP) 10-year plan that lists all possible construction projects in the coming decade with accurate location and road treatment type. SHOPP is a product of information from the Caltrans pavement network analysis tool – PaveM system (Caltrans, 2015) and local Caltrans decisions made using that information. PaveM uses databases describing pavement type, pavement condition, project history, climate, and anticipated future load to predict future construction projects for each mile of pavement in California, and can be used to plan for the rehabilitation and reconstruction of all state highways. PaveM is directly integrated into the decision making and optimization tools used by Caltrans to allocate future funding. For on-road construction projects more than 10 years in the future, we

adapted the PaveM methodology to create a simplified projection of long-term future highway maintenance needs. A statistical forecast model was created to calculate the probability of replacing each mile of roadway in California based on pavement type, pavement condition, project history (age), climate zone, and anticipated future Equivalent Single Axle Loads (ESAL). Each segment of replaced roadway can select between different pavement types with probabilities determined by the same underlying factors that determine likelihood of replacement. A series of randomized "Monte Carlo" simulations were conducted to predict on-road construction projects by year in California through the year 2050. The average emissions from the Monte Carlo simulations were adopted as the future year on-road construction surrogate (see section S1.2.3 in Appendix 1 for additional details). The randomized "Monte Carlo" simulations to a certain degree were able to capture that the road rehabilitations will likely happen on highways where there are higher annual ESALs, such as Los Angeles, the Bay Area, and several main highway in California (I-80, I-5, US101, and State Route 99) , and more severe climate conditions (see Figure S1-8).

2.2.3. SED surrogates

SED-derived surrogates distribute emissions related to human activities. Total population surrogate 440 serves as a default surrogate if no other surrogate is assigned. Seven SED-derived surrogates were updated in the current study: total households (250), industrial employment (300), total population (440), service & commercial employment (620), single-family households (650), total employment (744, new), and agricultural employment (745, new). Three datasets served as the basis for the new surrogates: (i) data from Metropolitan Planning Organizations (MPOs)/local Council of Governments (COGs), (ii) data from the Caltrans Statewide Travel Demand Model (CSTDM), and (iii) the Longitudinal Employer-Household Dynamics (LEHD) "OnTheMap" data (United State Census Bureau, 2019). MPOs/COGs are agencies created by federal law to provide regional planning and implementation of federal transportation funds to urbanized areas with more than 50,000 people. Eighteen MPOs/COGs are designated in California (see Table S1-2 in Appendix 1), accounting for approximately 98% of the state's population (CALCOG, 2019). CSTDM is a tool used to forecast all personal travel made by every California resident, plus all commercial

vehicle travel (Cambridge Systematics Inc., 2014a, 2014b). CSTDM socioeconomic data includes population, housing, and employment within specific sectors. MPOs/COGs and CSTDM datasets have total population and housing data from the US census data. All three datasets have employment census data classified by the North American Industry Classification System (NAICS). NAICS is used by Federal statistical agencies to classify businesses for the purpose of collecting, analyzing, and publishing statistical data related to the U.S. business economy (https://www.census.gov/eos/www/naics/). LEHD provides annual employment statistics linking home and work locations (latitude/longitude) at the 2010 census block-level for individual NAICS categories, but the LEHD data is only available for historical years starting from 2002.

Updated SED surrogates were created for the base year 2010 and future years from 2015 to 2040, in 5-year increments. MPOs/COGs and CSTDM forecast future SED to multiple years up to 2050 (available years listed in Table S1-4 in Appendix 1) based on anticipated growth rate in each area in order to plan future infrastructure needs. Each of these local projections uses accepted practices for forecasting future trends. MPO/COG forecasts were interpolated in time as needed to produce uniform projections across California in target future years. Table S1-8 in Appendix 1 tests the accuracy of this time interpolation procedure for population and housing in the years 2010 and 2015 by comparing interpolated values to data from the United States Census for 2010 and 2015. Most of MPO/COG regions agree with the real census data within 5%. KERN, KINGS, SACOG, and SLOCOG had relatively minor errors (<10%), but the overall uncertainty introduced by time interpolation is still minor compared to the other uncertainty inherent in the surrogate projections.

The definitions of total population, total housing, single-family housing, and total employment for each MPO/COG and CSTDM are relatively consistent and so these spatial surrogates were derived directly from the variables provided by each new data source. Data from individual MPOs/COGs typically has better spatial resolution and has undergone more rigorous quality control than data from CSTDM. MPO/COG data was therefore used wherever possible, with CSTDM data filling in locations where MPO

data was not available (see Section S1.3.1 in Appendix 1 for additional details). The approach used in the current project retains the fine-grain detail of the original MPO data wherever possible to increase the accuracy of the final spatial surrogate fields. MPO/COG data greatly enhances spatial resolution for moderately urbanized areas, such as Sacramento and central CA, but has little impact in highly urbanized areas, such as the Bay Area and Southern California.

Spatial surrogates describing employment are more complicated than the SED categories discussed above. The definitions for each employment surrogate are shown in Table 2-2. Each MPO/COG creates its own specialized grouped employment categories and / or modifies the definition of the standard NAICS employment categories to suit their own needs. The LEHD dataset is used in the current study to unify these heterogeneous fields into a standard set of spatial surrogates for employment in subcategories of agriculture, industry and service & commercial within each county. The ratio of each individual LEHD sector to the LEHD lumped category total provides a profile that can be multiplied into the MPO/COG or CSTDM lumped categories to estimate employment which satisfy definitions in Table 2-2. An example given in Figure 2-3 shows how to calculate agricultural employment category (NAICS code 11) in MPOs/COGs area Southern California Association of Governments (SCAG). SCAG combined mining employment (NAICS code 21) and agricultural employment in a single native field, which is the optimal strategy (X_i') without invoking other datasets. Subscript i represents each geographic unit in MPOs/COGs or CSTDM, census block in MPOs/COGs and Traffic Area Zone in CSTDM. The ratio of agricultural employment (11) in SCAG data (r_i) can be estimated as LEHD agricultural sector (11) divided by LEHD lumped sector (11 + 21). Thus, the agricultural employment (11) in SCAG (X_i) can be calculated by multiplying the ratio of agricultural employment to the optimal strategy ($X_i = X_i' * r_i$). These NAICS employment totals are then recombined into the categories defined in Table 2-2 (see Section S1.3.2 in Appendix 1 for additional details).

Figure 2-1 and Figure 2-4 illustrates SED surrogates in the years 2010 and spatial surrogate difference between 2040 and 2010. All current and future year SED surrogates are concentrated in urban areas including the Bay Area, Sacramento, Los Angeles, Fresno, and Bakersfield along Highway 99. The spatial

patterns for socioeconomic surrogates (other than agricultural employment) expand outward from urban centers through year 2040.

Table 2-2 NAICS codes and LEHD fields name and definitions

Surrogate	NAICS code	LEHD field	Definitions
Agricultural Employment	11	cns01	Agricultural, forestry, fishing and hunting
Industrial Employment	21	cns02	Mining
	22	cns03	Utilities
	23	cns04	Construction
	31-33	cns05	Manufacturing
	42	cns06	Wholesale trade
	48-49	cns07	Transportation and warehousing
Service & Commercial Employment	44-45	cns08	Retail trade
	51	cns09	Information
	52	cns10	Finance and insurance
	53	cns11	Real estate rental and leasing
	54	cns12	Professional, scientific, and technical services
	55	cns13	Management of companies and enterprise
	56	cns14	Administrative and support and waste management and remediation services
	61	cns15	Educational service
	62	cns16	Health care and social assistance
	71	cns17	Arts, entertainment, and recreation
	72	cns18	Accommodation and food services
	81	cns19	Other services (except public administration)
	92	cns20	Public administration

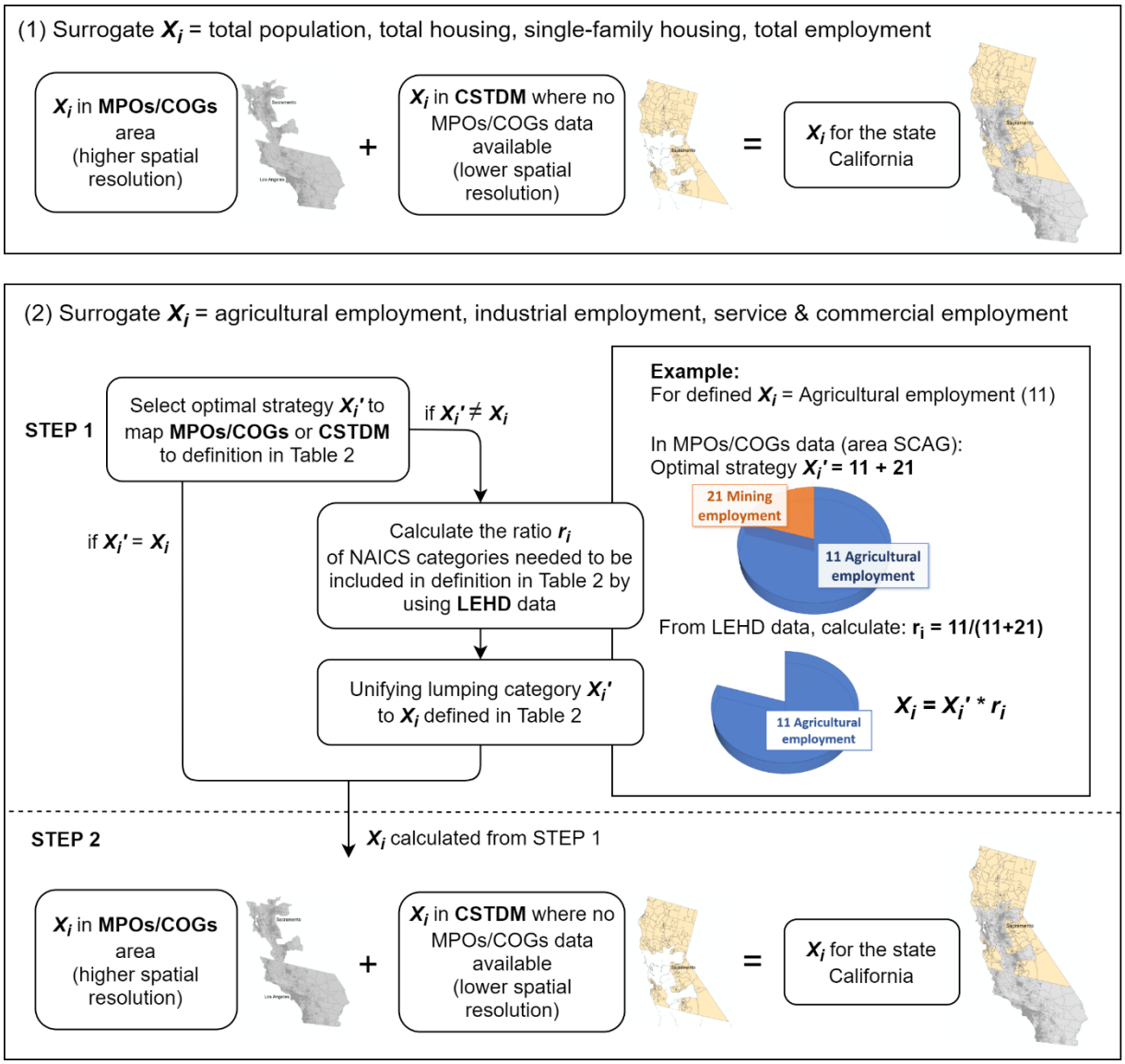

Figure 2-3. Flow chart of methodology for SED spatial surrogates including total population, total housing, single-family housing, total employment, agricultural employment, industrial employment and service & commercial employment. Subscript i is the geographic unit of SED dataset.

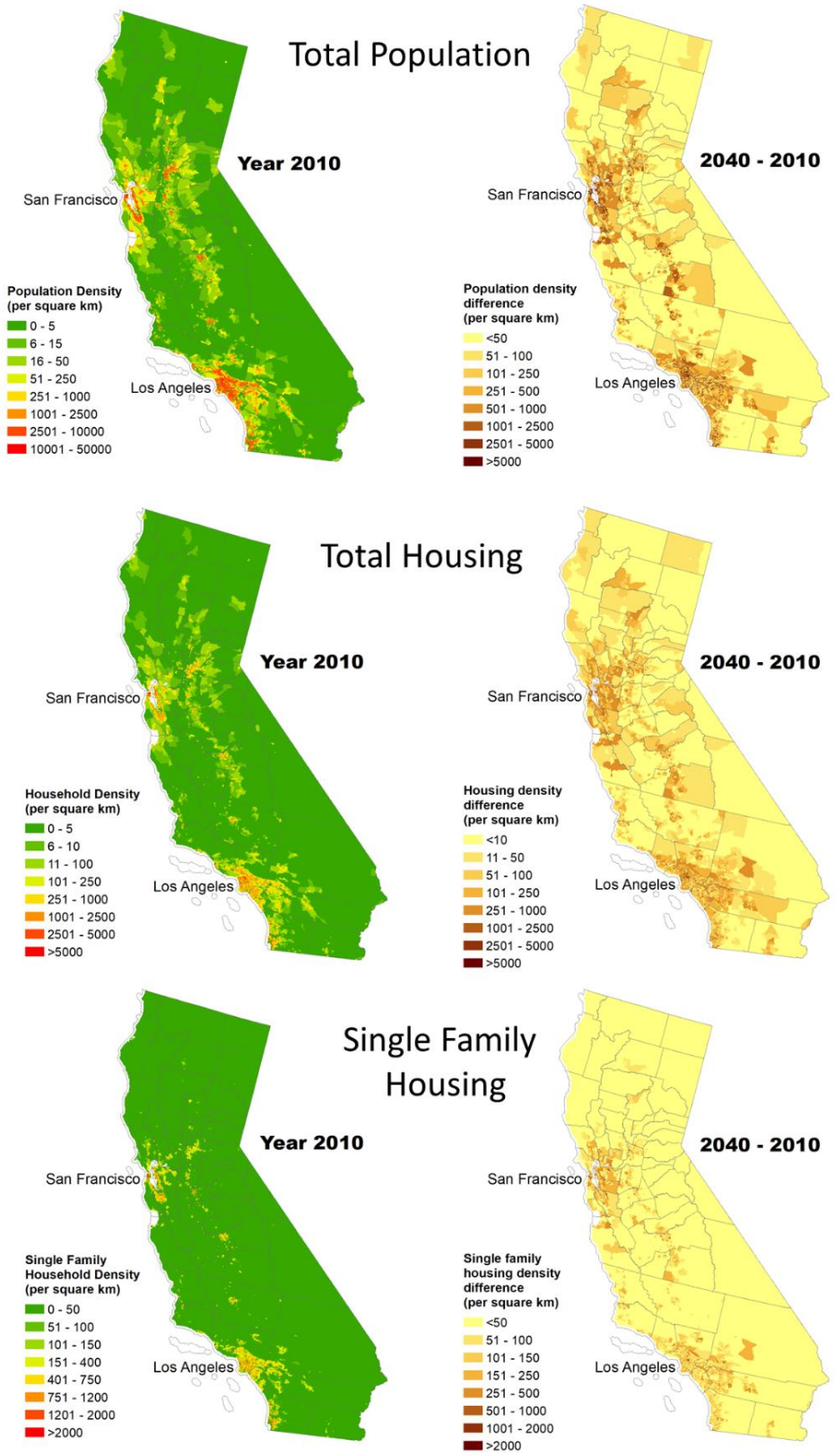

Figure 2-4: Total population, total housing, and single-family housing in the years 2010 and spatial surrogate difference between 2040 and 2010.

2.2.4. Surrogate Evaluation Methods

Gridded surrogates were generated using the spatial allocator tool from United States Environmental Protection Agency (EPA) (CMAS, 2019). The spatial allocator is a set of programs that allows users to generate data files related to emissions and air quality modeling without requiring the use of a commercial Geographic Information System (GIS) package. Given a map projection, domain boundaries, and weight shapefiles (developed in Section 2), the spatial allocator can generate gridded spatial surrogates that can be directly used in emission models, such as the Sparse Matrix Operator Kernel Emissions (SMOKE) (CMAS, 2016). In this project, the spatial allocator was applied with the Lambert Conformal map projection (-120.5 degree longitude, 37 degree latitude, standard parallels 30 degree and 60 degree) and 4km spatial resolution. Domain boundaries were specified based on the 69 Geographic Area Index (GAI) region shapefile (https://www.arb.ca.gov/ei/gislib/gislib.htm) which is consistent with previous statewide emissions inventories from ARB.

The raw spatial surrogates produced in the current project were combined with emissions inventories to analyze how the updates would influence the spatial distribution of actual emissions compared to the original CARB surrogates. These two cases are hereafter referred to as “updated” and “original”.

The new spatial surrogates for the year 2015 were processed using SMOKE along with the raw emissions for the year 2016 to generate gridded emissions for six pollutants: CO, NOx, TOG, NH3, SOx, and PM. These emissions were then processed with the UCD emissions processing system (EMINV) to create model-ready inputs including speciated VOCs and size- and composition-resolved PM. Emissions were segregated into nine source categories for easier interpretation of the results: (i) on-road gasoline, (ii) off-road gasoline, (iii) on-road diesel, (iv) off-road diesel, (v) woodsmoke, (vi) food cooking, (vii) aircraft emissions, (viii) natural gas, and (ix) miscellaneous, which are emissions not included in the categories listed above. Emissions were used by the UCD/CIT air quality model applied to the entire state of California.

2.3. Results

2.3.1. Relationships between surrogates and emissions

The relationship between the spatial pattern of surrogates and emissions was analyzed in two detailed case studies for Sacramento County and Los Angeles GAI 6059. Sacramento has the largest shift of predicted PM mass concentration in response to the adoption of updated spatial surrogates. Los Angeles is one of the most populated areas in California. Each emissions source within these two study regions is typically affected by a combination of spatial surrogates as described below.

Figure 2-5 illustrates how off-road diesel emissions are mainly affected by updated off-road construction equipment surrogates 585 and 587 (see Figure S1-9 and Figure S1-12 in Appendix 1). Since surrogates only allocate emissions within each GAI region, Figure 2-5(a) and (c) show the fractional change in each GAI total between original construction surrogate 585 and revised off-road construction surrogate 587. Figure 2-5(b) and (d) show the change in absolute $PM_{2.5}$ EC emissions. A strong spatial correlation is apparent between changes to off-road construction equipment surrogate 587 and changes to $PM_{2.5}$ EC emissions from off-road diesel vehicles. Figure 2-5(a) and Figure 2-5(b) both reflect a major increase in the area northeast of Sacramento between two major highways. Figure 2-5(c) and Figure 2-5 (d) also illustrate increasing emissions around major highways in the urban LA area, and major decrease northwest of LA. $PM_{2.5}$ EC from off-road diesel engines contributes strongly to total $PM_{2.5}$ EC concentrations. Changes to spatial surrogate 587 are therefore expected to significantly influence predicted overall $PM_{2.5}$ EC spatial patterns in cities.

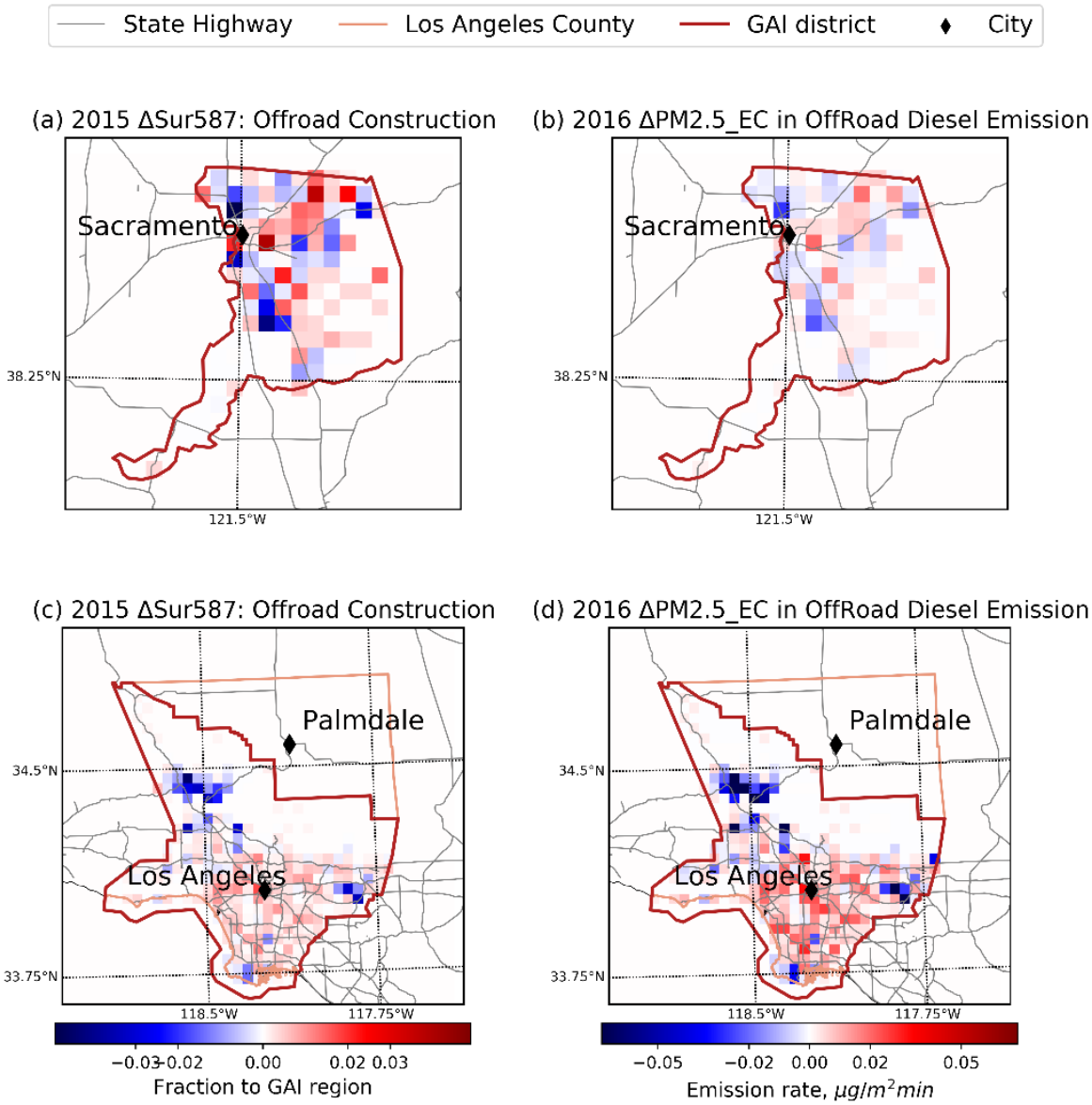

Figure 2-5. Relationship between off-road construction surrogate and PM2.5 EC in off-road diesel emission. Figure (a) and (c) are surrogate difference between original 585 and updated 587 at Sacramento County and Los Angeles GAI 6059. Figure (b) (d) are PM2.5 EC difference in off-road diesel emission at the same corresponding area.

California's emissions inventory treats a subset of the industrial and commercial natural gas combustion as area sources allocated using spatial surrogates 730 (industrial-related) and 620 (service & commercial employment), respectively. Figure 2-6 and Figure S1-15 in Appendix 1 illustrate how changes to updated surrogates 730 and 620 work together to change the pattern of natural gas combustion emissions

in Los Angeles and Sacramento. Figure 2-6(c) and Figure 2-6 (b)(d) show a strong spatial correlation between changes in surrogate 730 and natural gas combustion $PM_{2.5}$ OC and NOx emissions in Los Angeles. Note that increases in surrogate 730 are balanced by decreases in surrogate 620 in some locations (see Figure 2-6(a)(c)). Changes to surrogate 730 result in significant changes to $PM_{2.5}$ OC and NOx in natural gas combustion emissions in LA area, ~ 0.35 μg/m2/min for $PM_{2.5}$ OC and ~ 1 ppb/min·m for NOx. The updated surrogate 730 also alters the spatial pattern of natural gas combustion emission in the San Francisco Bay Area (see Figure S1-10 in Appendix 1). Updates to surrogate 620 modify the spatial pattern of natural gas combustion emissions in Sacramento (Figure S1-15 in Appendix 1), but changes are modest because past census data already produced accurate spatial patterns for surrogate 620 in the original inventory.

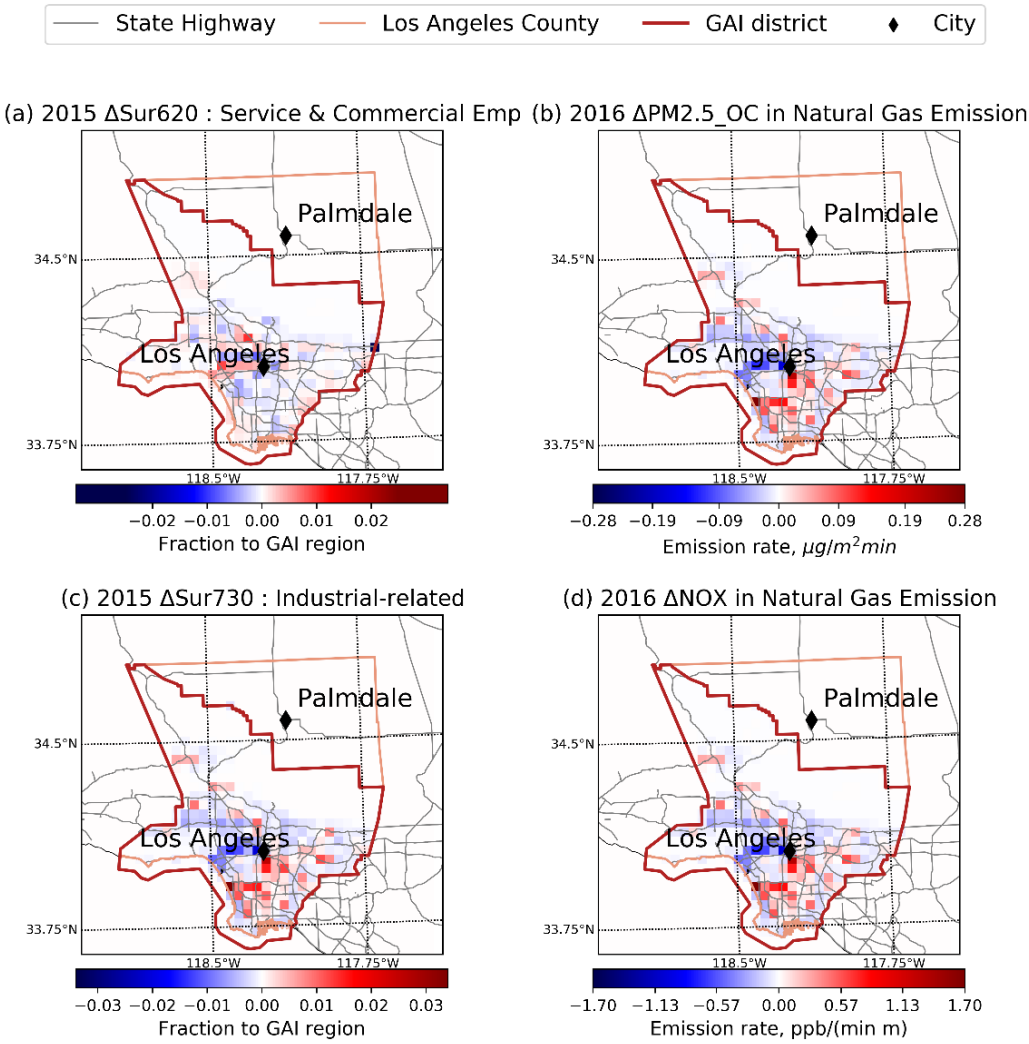

Figure 2-6. Relationship between service & commercial employment, industrial-related surrogates and $PM_{2.5}$ OC, NOx in natural gas emission. Figure (a) and (c) are surrogate difference between original and updated service & commercial/industrial-related surrogates at Los Angeles GAI 6059. Figure (b) (d) are $PM_{2.5}$ OC and NOx difference in natural gas emission at the same corresponding area.

Figure 2-7 illustrates how changes to surrogate 587 and 588 influence the spatial pattern of $PM_{2.5}$ total mass emissions from miscellaneous sources. In general, off-road/on-road construction equipment surrogates 587/588 work together on changes in $PM_{2.5}$ total mass, and off-road surrogate 587 has a relatively larger impact than on-road surrogate 588. In Sacramento County (see Figure 2-7(a) (b) and (c)), surrogates

587/588 have opposite change patterns northeast of Sacramento. The impact from changes to off-road surrogate 587 are weakened by changes to on-road surrogate 588. This causes a significant decrease for $PM_{2.5}$ total mass emissions in downtown Sacramento (~ 6 μg/m2/min). In Los Angeles (see Figure 2-7(d) (e) and (f)), off-road/on-road construction surrogates both increase PM mass emissions around the LA urban area, and decrease PM mass emissions to the northwest of downtown LA. The identical shift from surrogate 587/588 increased PM mass emissions in the LA urban area (~ 2.5 μg/m2/min), although surrogate 587/588 has less change compared to other regions across the state. $PM_{2.5}$ total mass emissions from construction contributes strongly to total $PM_{2.5}$ mass emissions. Changes to construction spatial surrogate 587/588 are therefore expected to significantly influence the spatial pattern of predicted overall $PM_{2.5}$ total mass concentrations.

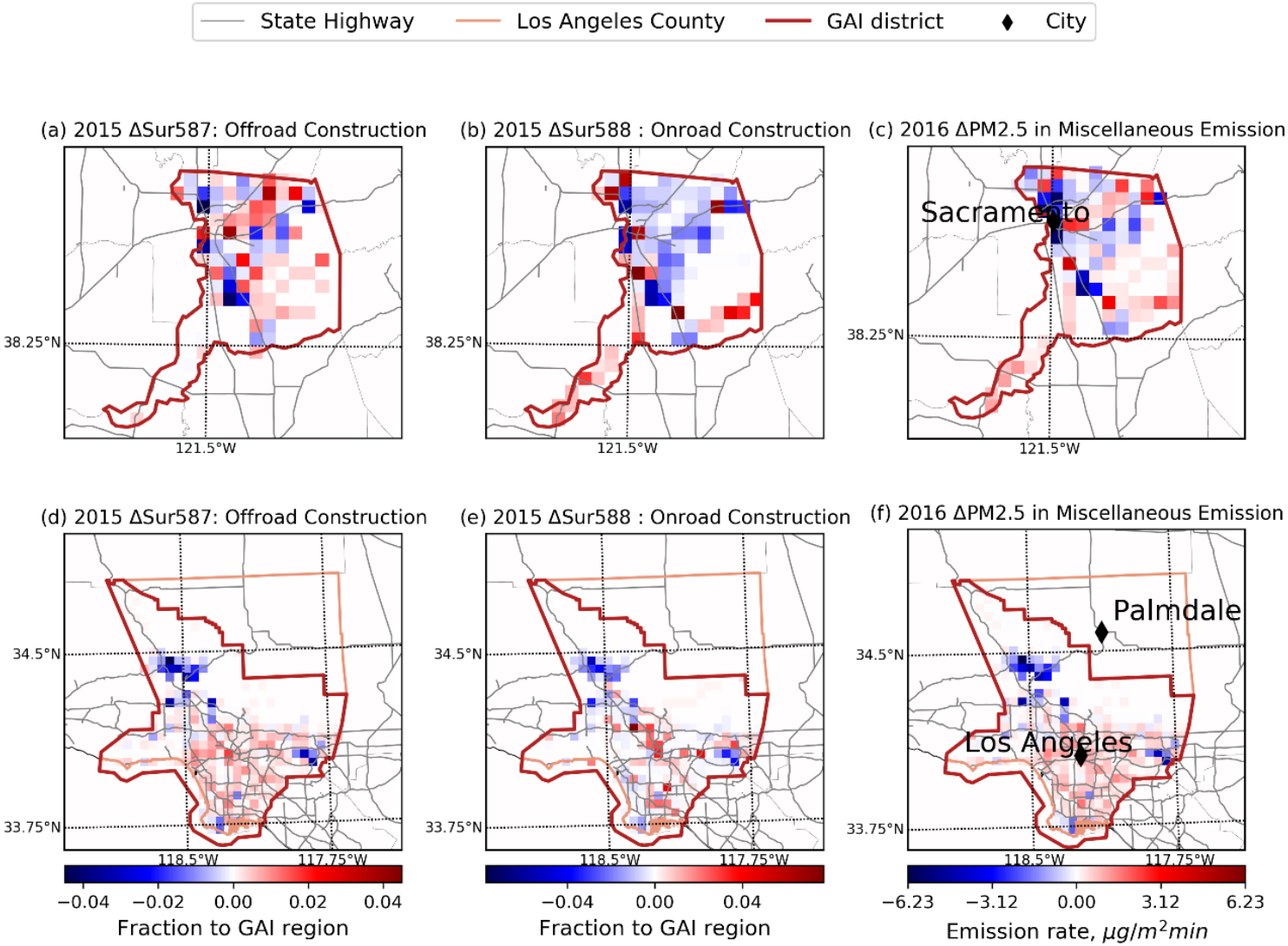

Figure 2-7. Relationship between off-road/on-road construction surrogates and PM2.5 total mass emissions from miscellaneous sources at Sacramento County and Los Angeles GAI 6059. Figure (a) (b) (d) and (e) are surrogate differences between original 585 and updated 587/588. Figure (c) (f) are differences in PM2.5 total mass emissions from miscellaneous sources as defined in Section 2.2.4

Figure 2-8 shows how changes to off-road construction surrogate 587 and industrial-related 730 affect NOx emissions from miscellaneous sources differently across the state. In Sacramento County, changes in NOx follow the pattern of surrogate 587. However, the absolute value of changes in NOx emissions is minor, because decreases in surrogate 587 are typically balanced by increases in surrogate 730 (see Figure 2-8(a) (b) and (c)). Changes to the spatial pattern of miscellaneous NOx emissions stem from a combination of changes in surrogate 730 and surrogate 587 in the region surrounding Los Angeles, with a maximum shift of ~ 1.5 ppb/min·m. These patterns add to the shifts in the spatial pattern of NOx emissions associated with natural gas combustion (Figure 2-6).

The specific trends illustrated in Figure 2-5 to Figure 2-8 are generally apparent throughout California. Changes for SED spatial surrogates are concentrated in cities or along highways where population is highest. In contrast, most of the changes in the spatial distribution of the industrial surrogates are found outside of the major urban areas. The off-road construction spatial surrogate 587 reflects the shift to project-based records as opposed to changes in impervious surfaces and is more concentrated within cities associated with urban renovation projects (see Figure S1-12 in Appendix 1). The on-road construction surrogate 588 also reflects the shift to describing emissions from individual road construction projects instead of evenly distributing road construction emissions along the entire Truck Network. The intensity of the construction spatial surrogate generally decreases slightly along major highways throughout California but increases in isolated locations along those highways (Figure S1-13 in Appendix 1). The updated industrial-related surrogate 730 generally concentrates industrial activity from a diffuse region into a concentrated source, perhaps associated with a central facility (see Figure S1-14 in Appendix 1). The updated surrogates mainly change the location of off-road diesel emissions, natural gas emissions, and miscellaneous emissions. In general, "miscellaneous emissions" of $PM_{2.5}$ total mass, and NOx have the strongest response to the adoption of updated spatial surrogates (Figure S1-11 in Appendix 1).

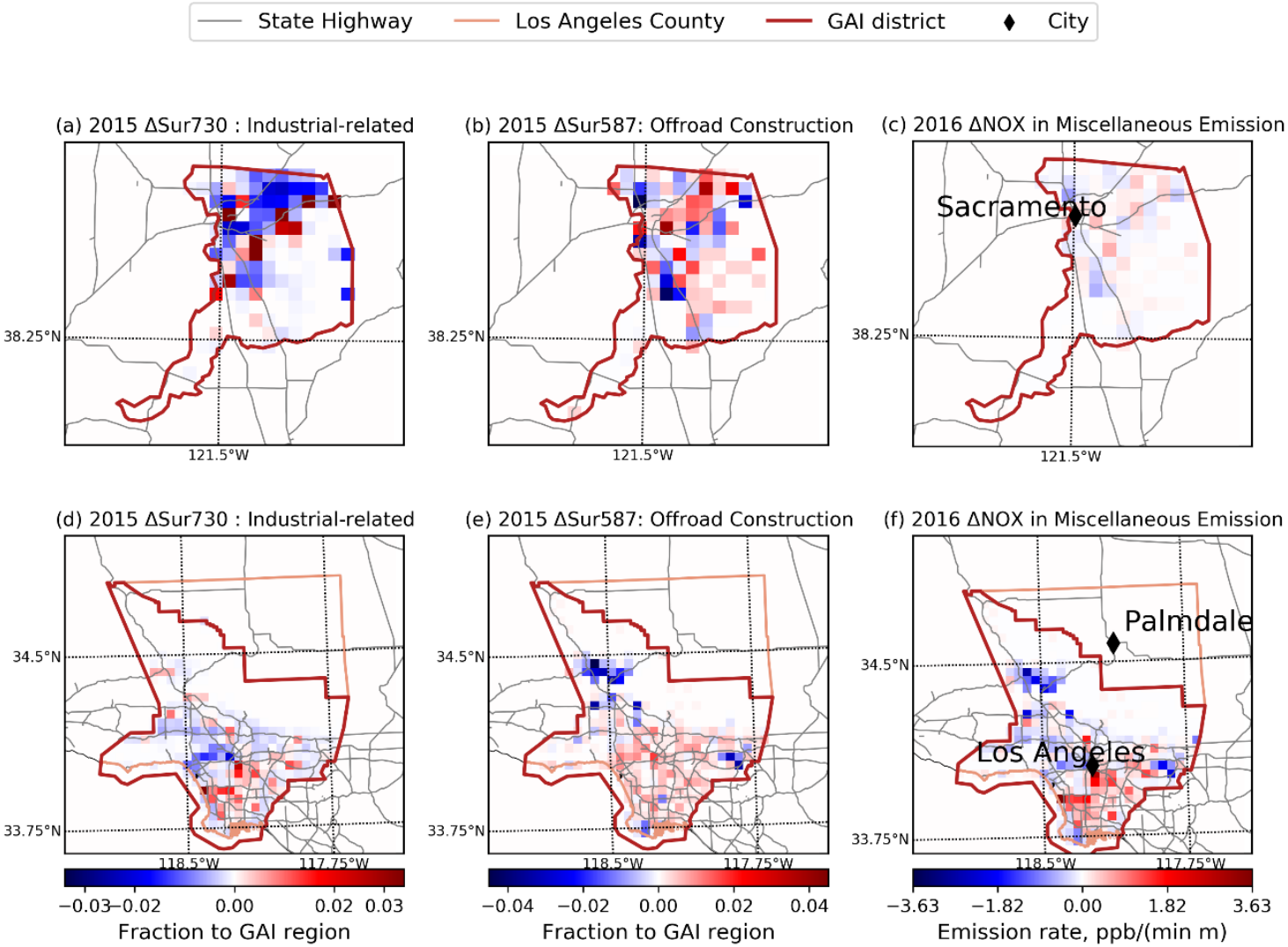

Figure 2-8. Relationship between off-road/on-road construction surrogates and NOx emissions from miscellaneous sources at Sacramento County and Los Angeles GAI 6059. Figure (a) (b) (d) and (e) are surrogate differences between original 585 and updated 587/588. Figure (c) (f) are differences in NOx emissions from miscellaneous sources as defined in Section 2.2.4..

2.3.2. Surrogates performance: air quality model predictions

The updated spatial surrogates created in the current study were tested using the source-oriented UCD-CIT air quality model (Kleeman and Cass, 2001a; Ying et al., 2008) for California during the year 2016. A single 24km domain covering the entire state and two nested 4km domains covering major population centers in northern California and southern California were selected for the analysis. Model simulations were carried out using both the original spatial surrogates and the updated spatial surrogates. Measurement data was downloaded from EPA website: https://aqs.epa.gov/aqsweb/airdata/download_files.html. There are 17 measurement sites in the southern California domain and 13 measurement sites in the northern California domain to evaluate $PM_{2.5}$ model performance; six sites across the state are available to evaluate $PM_{2.5}$ EC and OC predictions; 31 sites in southern California and 18 measurement sites in northern California are available to evaluate NOx predictions.

Figure 2-9 shows the time series of $PM_{2.5}$ mass, EC, OC and NOx daily average concentration at central Los Angeles and Sacramento during the year 2016 using the original spatial surrogates (orange line) and the updated spatial surrogates (green line). Observed values are illustrated as black dots. Predicted concentrations based on the original and updated spatial surrogates are similar. Both cases capture the routine $PM_{2.5}$ mass, EC, OC and NOx concentrations with reasonable accuracy but they fail to capture the peak $PM_{2.5}$ mass concentration events which mostly occur in wintertime. Total $PM_{2.5}$ mass has relatively greater differences between original and updated cases compared to species such as $PM_{2.5}$ EC. Changes to spatial surrogates have minor effect on predicted $PM_{2.5}$ OC and NOx concentrations at the 2 measurement sites.

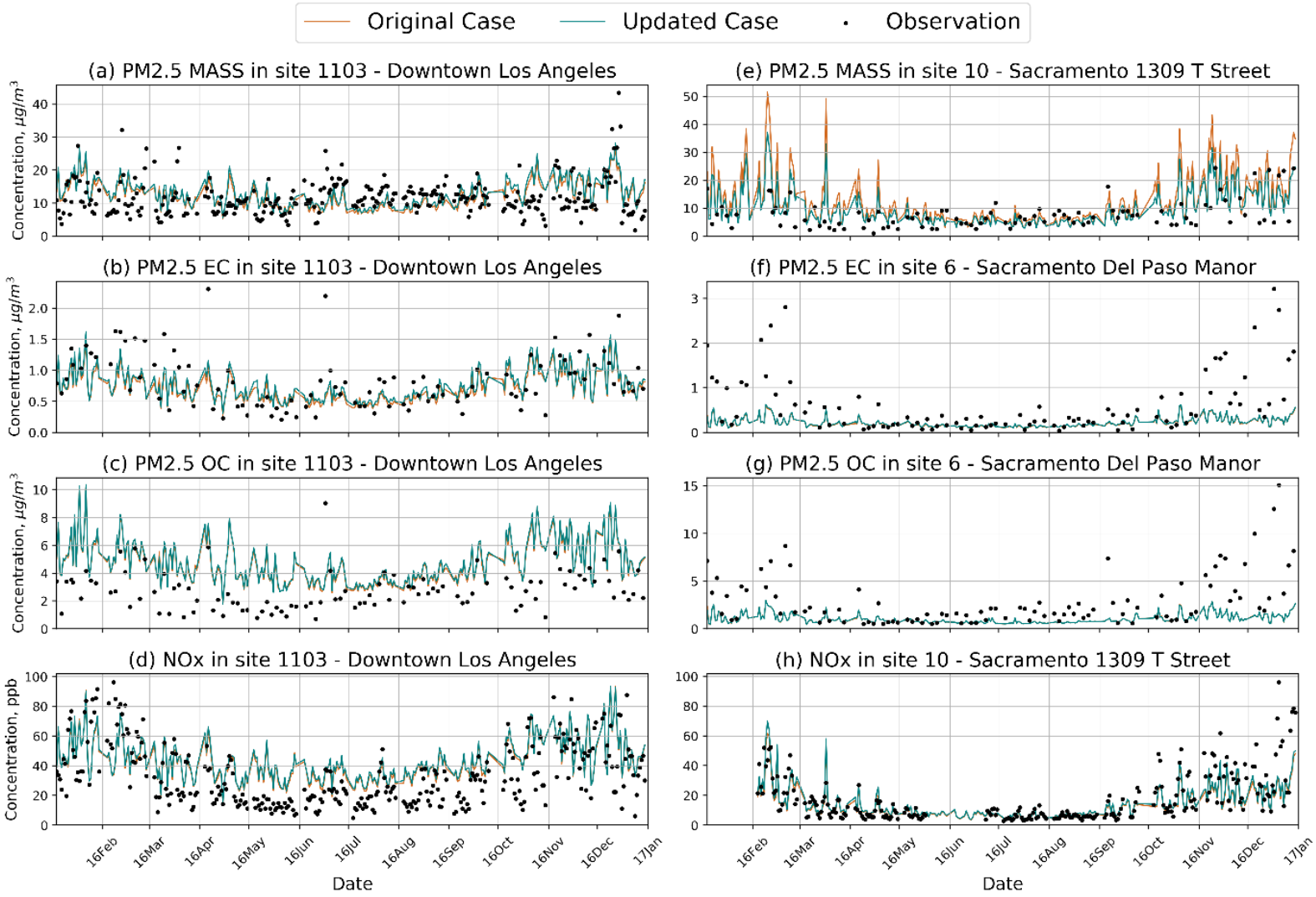

Figure 2-9. Time series for predicted (original case in green line and updated case in orange line) and observed (black dot) PM2.5 mass, PM2.5 EC, PM2.5 OC and NOx concentrations at Los Angeles (shown in figure (a) (b) (c) (d)), Sacramento (shown in figure (e) (f) (g) (h))) during year 2016

Statistical analysis was carried out for $PM_{2.5}$ mass, $PM_{2.5}$ EC, $PM_{2.5}$ OC, NOx, $PM_{2.5}$ nitrate, $PM_{2.5}$ sulfate, and two metals – Cu and Fe at all available measurement sites. $PM_{2.5}$ nitrate, sulfate, Fe and Cu do not respond strongly to the updated spatial surrogates and will not be discussed further in the present analysis. $PM_{2,5}$ mass Mean Fractional Bias (MFB) and Mean Fractional Error (MFE) are shown in Table 2-3 for southern California and

Table 2-4 for northern California. $PM_{2.5}$ EC and OC MFB/MFE for all available California sites are shown in Table 2-5. NOx MFB/MFE for measurement sites with changed model performance are listed in Table 2-6. In general, air quality simulations carried out over the entire year 2016 determined that the effects of the updated spatial surrogates on predicted PM and NOx concentrations at measurement sites across the state are positive in most populated area, including the South Coast Air Basin (SoCAB) (including Los Angeles, Orange and Riverside counties), the region surrounding Sacramento, and the region south of San Francisco. $PM_{2,5}$ total mass has ~ 5% of improvement at most locations sites in the SoCAB (see Table 2-3); ~ 10% of improvement at downtown Sacramento (see site 6067 0010 and 6067 4001 in

Table 2-4); and ~3% of improvement at San Jose (south of San Francisco). $PM_{2,5}$ EC improves by ~4% at two sites in southern CA, and ~2% at two sites in northern CA (see Table 2-5). NOx model performance improves (~6%) southeast of LA county, where industrial-related surrogate 730 has the largest changes (see Table 2-6). Updated spatial surrogates have minor impact on predicted concentrations of NOx in central and northern California. Likewise, updated spatial surrogates have minor impact on predicted concentrations of $PM_{2,5}$ mass, OC, and EC in central California (including Fresno and Bakersfield).

Table 2-3. Annual PM2.5 mass mean fractional bias (MFB) and mean fractional error (MFE) for South California Sites. ***Bold*** *Indicates improved performance.*

Site	Downtown LA[1]		Reseda[1]		Compton[1]		Pico Rivera[1]	
Site Number	6037 1103		6037 1201		**6037 1302**		**6037 1602**	
Statistics	MFB	MFE	MFB	MFE	MFB	MFE	MFB	MFE
Original Case	9.89%	39.70%	-34.81%	49.74%	-15.03%	42.35%	-27.58%	42.85%
Updated Case	16.40%	40.53%	-37.88%	51.84%	-8.05%	40.88%	-21.86%	39.78%
Site	Long Beach (South)[1]		Long Beach near Route 710[1]		Pasadena[1]		Long Beach[1]	
Site Number	6037 4004		**6037 4008**		**6037 2005**		**6037 4002**	
Statistics	MFB	MFE	MFB	MFE	MFB	MFE	MFB	MFE
Original Case	-0.50%	39.88%	-35.18%	45.70%	-10.46%	36.67%	-7.61%	42.73%
Updated Case	4.46%	40.35%	-29.56%	42.90%	-4.60%	35.87%	-2.06%	42.58%
Site	Anaheim[2]		Mission Viejo[2]		Rubidoux[3]		Mira Loma[3]	
Site Number	**6059 0007**		**6059 2022**		**6065 8001**		**6065 8005**	
Statistics	MFB	MFE	MFB	MFE	MFB	MFE	MFB	MFE
Original Case	-3.95%	39.11%	-8.53%	39.88%	-48.99%	59.19%	-56.07%	64.23%
Updated Case	0.45%	38.98%	-6.64%	39.42%	-47.66%	58.48%	-54.32%	62.87%
Site	Downtown San Diego[4]		San Diego military[4]		El Cajon[4]		Pala[4]	
Site Number	6073 1010		6073 1016		6073 1018		6073 1201	
Statistics	MFB	MFE	MFB	MFE	MFB	MFE	MFB	MFE
Original Case	10.69%	38.59%	14.00%	41.77%	0.65%	31.24%	-25.26%	47.06%
Updated Case	41.91%	53.92%	16.51%	41.88%	4.24%	31.77%	-25.08%	46.88%

[1] Los Angeles county

[2] Orange county

[3] Riverside county

[4] San Diego county

Table 2-4. Annual PM2.5 mass mean fractional bias (MFB) and mean fractional error (MFE) for North California Sites : Sacramento and Santa Clara counties. ***Bold*** *Indicates improved performance.*

Site	Sacramento - Del Paso Manor[1]		Sacramento - 1309 T Street[1]		Folsom[1]		Sacramento Health Department[1]	
Site Number	6067 0006		**6067 0010**		6067 0012		**6067 4001**	
Statistics	MFB	MFE	MFB	MFE	MFB	MFE	MFB	MFE
Original Case	-17.99%	43.23%	38.24%	57.34%	-0.74%	53.45%	22.48%	47.26%
Updated Case	-18.76%	43.41%	22.18%	50.49%	-1.08%	53.60%	15.03%	45.25%
Site	San Jose - Konx Avenue[2]		San Jose – Jackson[2]		Gilory[2]			
Site Number	**6085 0005**		**6085 0006**		6085 0002			
Statistics	MFB	MFE	MFB	MFE	MFB	MFE		
Original Case	-6.40%	38.52%	-20.66%	37.53%	15.70%	52.06%		
Updated Case	-3.56%	38.04%	-17.95%	36.68%	-16.55%	54.01%		

[1] Sacramento county

[2] Santa Clara county

Table 2-5. Annual PM2.5 elemental carbon (EC) and PM2.5 organic carbon (OC) mean fractional bias (MFB) and mean fractional error (MFE) for all available California sites. ***Bold*** *Indicates improved performance.*

Site	Downtown LA[1]				Lebec (rural)[1]			
Site Number	6037 1103				6037 9034			
Species	**PM2.5 EC**		PM2.5 OC		PM2.5 EC		PM2.5 OC	
Statistics	MFB	MFE	MFB	MFE	MFB	MFE	MFB	MFE
Original Case	-5.49%	33.38%	57.13%	59.55%	-46.88%	86.60%	-72.51%	96.25%
Updated Case	0.64%	32.09%	59.30%	61.41%	-48.32%	87.73%	-73.17%	96.84%
Site	El Cajon[2]				El Cajon 2[2]			
Site Number	6073 1018				60731022			
Species	**PM2.5 EC**		**PM2.5 OC**		PM2.5 EC		PM2.5 OC	
Statistics	MFB	MFE	MFB	MFE	MFB	MFE	MFB	MFE
Original Case	-67.75%	76.55%	-12.86%	45.51%	-82.37%	83.22%	-67.05%	68.24%
Updated Case	-62.56%	72.31%	-9.30%	44.42%	-80.92%	81.60%	-67.09%	68.27%
Site	Sacramento - Del Paso Manor[3]				San Jose - knox Avenue[4]			
Site Number	6067 0006				6085 0005			
Species	**PM2.5 EC**		PM2.5 OC		**PM2.5 EC**		PM2.5 OC	
Statistics	MFB	MFE	MFB	MFE	MFB	MFE	MFB	MFE
Original Case	-52.90%	70.77%	-64.07%	70.26%	-4.02%	44.73%	-12.31%	31.98%
Updated Case	-49.82%	68.97%	-63.84%	70.11%	-2.70%	44.48%	-13.23%	31.70%

[1] Los Angeles county

[2] San Diego county

[3] Sacramento county

[4] Santa Clara county

Table 2-6. Annual NOx mean fractional bias (MFB) and mean fractional error (MFE) for sites with changes in model performances. ***Bold*** *Indicates improved performance.*

Site	Compton[1]		Pico Rivera[1]		Long Beach (Hudson)[1]		Long Beach near Route 710[1]	
Site Number	6037 1302		**6037 1602**		**6037 4006**		**6037 4008**	
Statistics	MFB	MFE	MFB	MFE	MFB	MFE	MFB	MFE
Original Case	26.70%	56.27%	-13.89%	43.17%	-6.14%	44.45%	-34.31%	62.46%
Updated Case	32.50%	58.27%	-7.41%	42.64%	-1.55%	43.46%	-29.29%	59.71%
Site	Santa Clarita[1]		Lancaster - Division Street[1]		Glendora[1]		Anaheim[2]	
Site Number	6037 6012		6037 9033		**6037 0016**		6059 0007	
Statistics	MFB	MFE	MFB	MFE	MFB	MFE	MFB	MFE
Original Case	-21.61%	43.19%	-60.96%	93.20%	-24.34%	41.79%	21.87%	53.14%
Updated Case	-40.17%	55.89%	-65.05%	97.37%	-15.42%	37.41%	25.79%	54.41%
Site	Anaheim Near-road[2]		Mira Loma[3]		Rubidoux[3]		Lake Elsinore[3]	
Site Number	**6059 0008**		**6065 8005**		**6065 8001**		6065 9001	
Statistics	MFB	MFE	MFB	MFE	MFB	MFE	MFB	MFE
Original Case	-73.97%	74.89%	-19.64%	44.63%	-16.37%	56.38%	-31.59%	50.69%
Updated Case	-70.38%	71.39%	-17.97%	44.10%	-14.96%	56.04%	-36.32%	54.19%
Site	Alpine[4]		Donovan[4]		El Cajon[4]		Sacramento-Goldenland Ct.[5]	
Site Number	**6073 1006**		6073 1014		**6073 1018**		**6067 0014**	
Statistics	MFB	MFE	MFB	MFE	MFB	MFE	MFB	MFE
Original Case	-43.25%	60.27%	-5.02%	55.20%	-26.48%	47.06%	49.31%	57.73%
Updated Case	-40.65%	58.13%	-14.79%	56.22%	-20.86%	43.72%	45.14%	55.06%

[1] Los Angeles county

[2] Orange county

[3] Riverside county

[4] San Diego county

[5] Sacramento county

The spatial pattern of change caused by the adoption of the updated spatial surrogates can be understood more clearly by plotting the results over the entire region. Figure 2-10 shows the change in the predicted annual-average $PM_{2.5}$ mass, EC, OC and NOx concentrations in the northern California domain due to the adoption of the updated spatial surrogates. Red grid squares represent areas of increased concentrations while blue grid squares represent areas of decreased concentration. The measurement sites

in the model domain are represented as circles, with green coloring indicating improved performance and red coloring indicating degraded performance due to the adoption of the new surrogates. In Figure 2-10(a), $PM_{2.5}$ mass concentrations decrease by 1-2 μg m^{-3} in the region west of Sacramento in response to the updated surrogates, leading to a 8-14% improvement at two sites (60670010, 60674001) in Sacramento. $PM_{2.5}$ EC predictions in Sacramento also improve by ~3% (Figure 2-10(b)). Only one site (60670014) out of six in Sacramento has ~4% improvement for NOx (Figure 2-10(c)). $PM_{2.5}$ concentrations in San Jose are also influenced by the updated spatial surrogates, with generally higher $PM_{2.5}$ mass concentrations throughout the urban region. The two measurement sites in San Jose both have ~3% improvement. $PM_{2.5}$ EC in San Jose slightly increased and improved ~1.5% in response to the updated spatial surrogates.

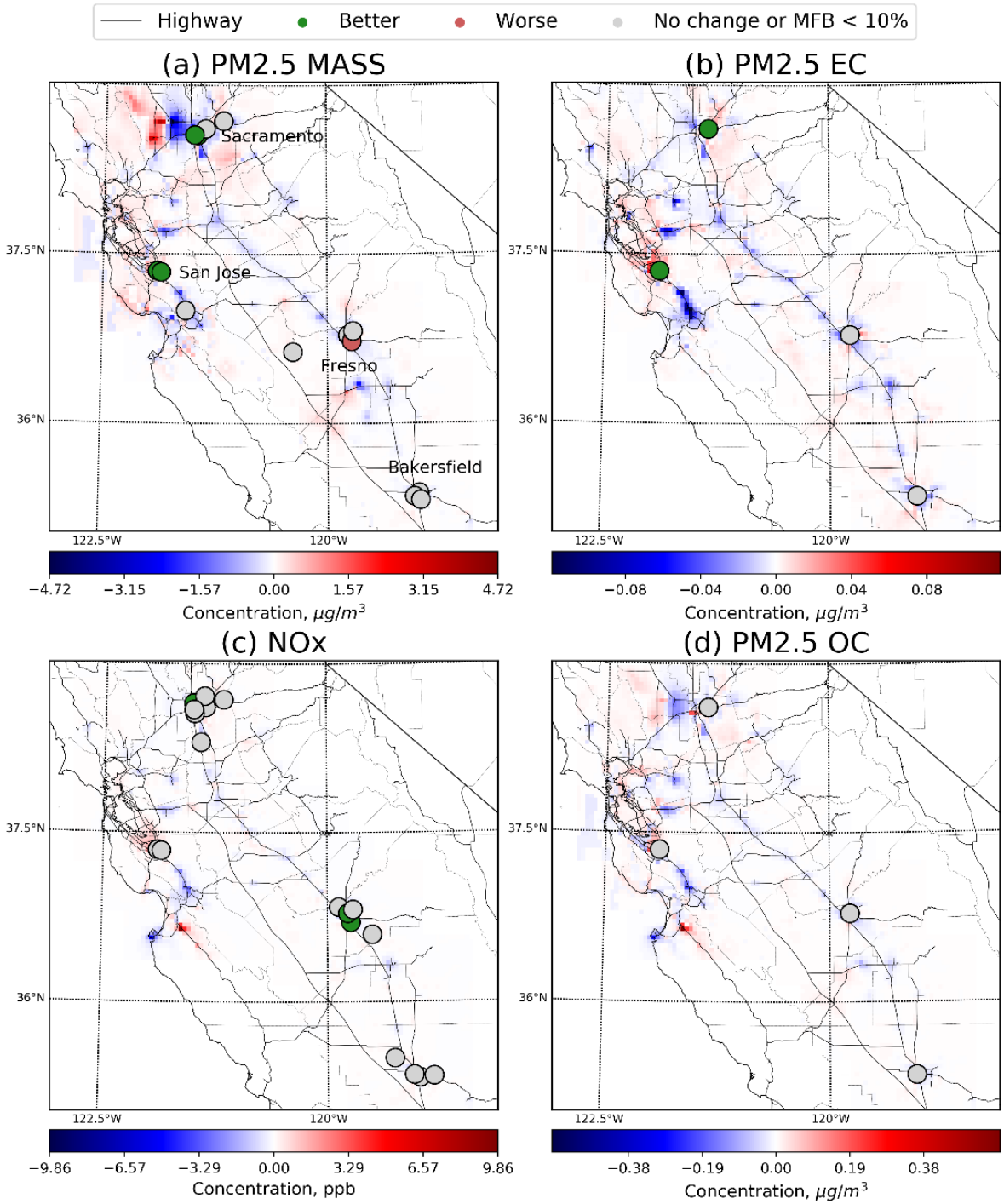

Figure 2-10. Change in predicted ground-level concentrations due to the adoption of new spatial surrogates in norther California. Blue indicates concentrations decrease while red indicates concentration increase as shown by the key below each panel. Circles quantify change in model performance when compared to measurements at monitoring locations. Green circles indicate improved performance, red circles indicate degraded performance relative to the original case.

Figure 2-11 displays the change in predicted annual-average $PM_{2.5}$ mass, EC and OC concentrations attributed to the updated spatial surrogates in southern California. Updated spatial surrogates have relatively larger impact in southern California compared to northern California. Figure 2-11(a) shows that $PM_{2.5}$ mass concentrations in the central region of Los Angeles increase by approximately 0.5 μg m^{-3} when the updated spatial surrogates are adopted, bringing the predictions into closer agreement with measured values at stations throughout this area. The overall spatial trends shown in Figure 2-11(b) and Figure 2-11(c) are similar to the trends shown in Figure 2-11(a), but the performance of $PM_{2.5}$ EC improves (or does not change) at all available measurement sites when the updated spatial surrogates are adopted. $PM_{2.5}$ OC has little response to updated surrogates. EC is a primary PM component and OC is dominated by primary emissions in the current simulations. Both primary emissions and secondary formation contribute to total $PM_{2.5}$ mass. This suggests that the complex pattern of increasing and decreasing performance illustrated in Figure 2-11(a) may be related to secondary PM formation rates and offsetting model errors. Figure 2-11(c) shows that NOx concentrations increase by approximately 2.5 ppb in Los Angeles area in updated case, bring the prediction into closer agreement with measured values in this area.

The PM total mass, EC, OC and gas-phase NOx concentration results summarized in Figure 2-10 and 2-11 are consistent with the changes in off-road diesel, natural gas combustion, and miscellaneous emissions discussed in Section 2.2. These patterns indicate that proximity to sources is a dominant factor that determines the impact of spatial surrogates on model performance. Off-road construction surrogate 587 and on-road construction surrogate 588 induce the largest change in predicted PM concentrations, followed by more modest changes associated with industrial-related surrogate 730, service & commercial employment surrogate 620 and single-family housing surrogate 650. Off-road construction surrogate 587 and industrial-related surrogate 730 induce the largest change in predicted NOx concentrations in southern California. Altered concentrations are associated with emissions from construction equipment, natural gas combustion, and industrial processes.

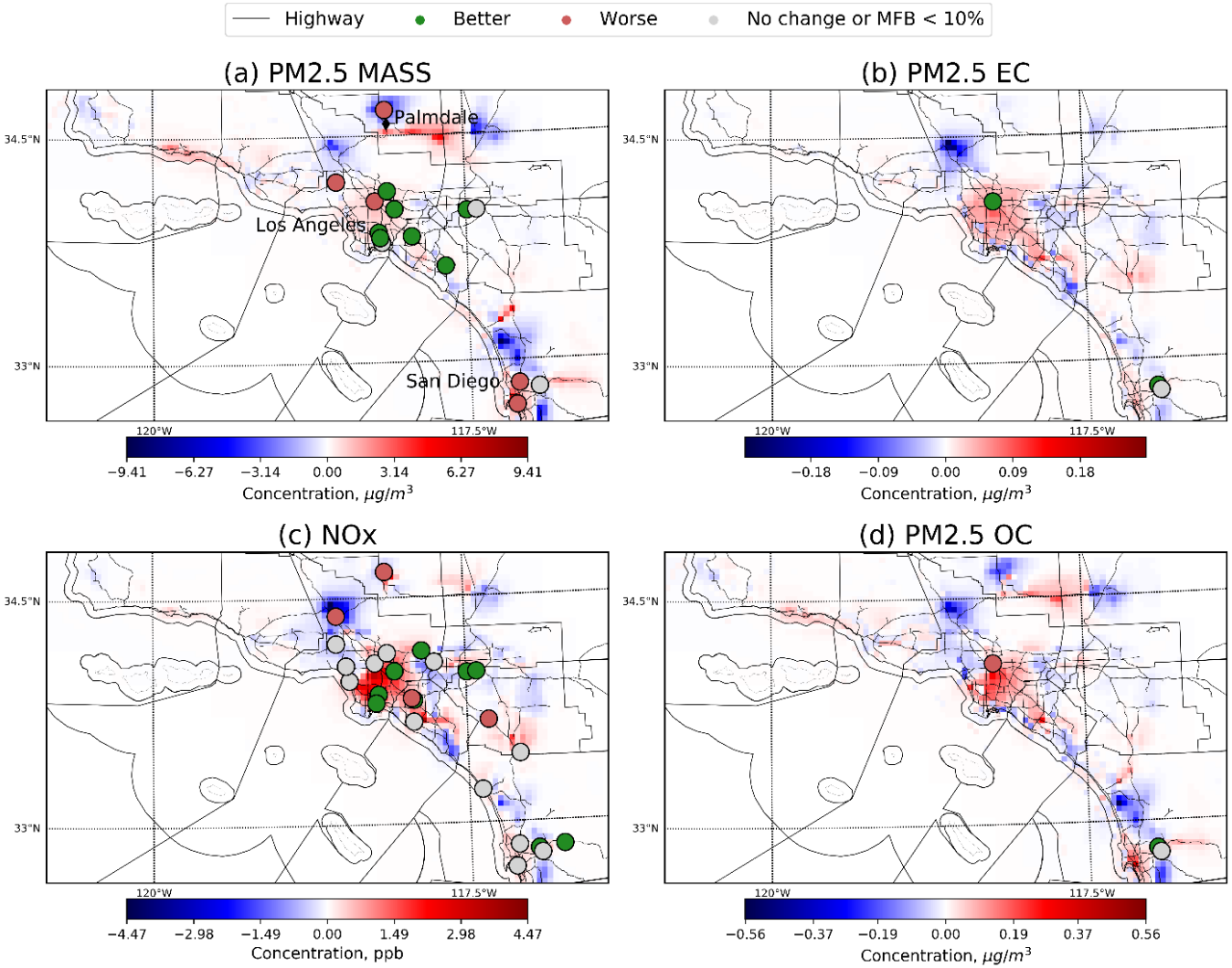

Figure 2-11. Change in predicted ground-level concentrations due to the adoption of new spatial surrogates in southern California. Blue indicates concentrations decrease while red indicates concentration increase as shown by the key below each panel. Circles quantify change in model performance when compared to measurements at monitoring locations. Green circles indicate improved performance, red circles indicate degraded performance relative to the original case.

2.4. Discussion

Spatial surrogates including total population, total housing, single family housing, total employment, service & commercial employment, industrial employment, agricultural employment, industrial-related, off-road construction, and on-road construction were updated for use with California emissions inventories. SED surrogates were updated using the latest version of census-based datasets at finer resolution. Off-road construction, on-road construction and industrial-related surrogates were developed using new methods to more accurately describe the location of construction projects and industrial facilities. All surrogates were created for the past years 2010 and 2015 and projected in 5- year increments to the year 2040.

The changes to the off-road construction spatial surrogate caused the largest shift in the distribution of PM emissions in the year 2015, followed by changes to the on-road construction spatial surrogate. These changes logically manifested as altered emissions patterns associated with construction sources. The changes to NOx emissions varied with location. In southern California, the changes to the industrial-related surrogate resulted in the largest shift in the distribution of NOx emissions in the year 2015. In northern California, changes to service & commercial employment, off-road construction equipment, and industrial-related surrogates are balanced leading to little impact on the spatial pattern of NOx emissions. The redistribution of industrial emissions based on a more exact description of industrial employment resulted in some isolated shifts in industrial emissions but no systematic pattern was observed. Changes in the spatial distribution of SED-derived surrogates, caused a slight reduction of emissions in the core of small cities and an increase in emissions in surrounding areas. SED changes were subtle and did not significantly influence emissions.

Air quality simulations carried out over the entire year 2016 determined that the updated spatial surrogates generally improve predicted PM mass and EC concentrations in Sacramento area (~10%), the Bay Area (~3%), and the region surrounding Los Angeles (~5%). Adoption of the updated spatial surrogates also improved predicted NOx concentrations in the core region of Los Angeles (~6%). These

improvements demonstrate that adoption of new methodologies to estimate the location of construction equipment related surrogates (separate to off-road and on-road) and industrial-related surrogates are feasible at 4km spatial resolution. Moreover, the updated construction-related and industrial-related surrogates may be suitable for even greater spatial resolution in future studies. The methods used to increase the accuracy of emissions locations in the current years may be extended to study emissions predictions and public health effects in future years.

It should be noted that spatial surrogates are an approximate approach for distributing area-source emissions. Even perfectly accurate spatial surrogates may not be perfectly correlated with emissions rates, and so this method has inherent uncertainty that varies depending on the exact emissions sources. Future applications of image recognition and GPS data may enable more accurate tracking of detailed activities that generate area-source emissions, but appropriate safeguards must be used to balance privacy vs. utility before widespread adoption of these techniques. Future studies should investigate these issues in order to improve the accuracy of area-source emissions inventories.

Chapter 3.
Spatial Resolution Required to Model Air Pollution Environmental Justice in Southern California

3.1. Introduction

Exposure to outdoor air pollutants such as airborne particles with aerodynamic diameter less than 2.5 μm ($PM_{2.5}$) is estimated to cause 3.3 million premature deaths per year worldwide (Lelieveld et al., 2015b). California is home to six out of the ten most polluted cities in the United States with respect to annual-average $PM_{2.5}$ concentrations (American Lung Association, 2019). This air pollution public health burden does not fall evenly across all socio-economic classes, leading to cases of air quality inequity (Anderson et al., 2018a). For example, exposure to $PM_{2.5}$ emitted from traffic and power generation is disproportionately higher for people of lower socio-economic status (Anderson et al., 2018a; Lelieveld et al., 2015b; Thakrar et al., 2020). Many studies have shown that food cooking is a major source of $PM_{2.5}$ (Bond et al., 2007; Butt et al., 2016; Lei et al., 2011; Ramanathan and Carmichael, 2008; Yu et al., 2019), and more recent studies also show that exposure to $PM_{2.5}$ emitted from urban restaurants may be even more skewed than traffic $PM_{2.5}$ (Shah et al., 2020). California is currently enacting climate policies that will lead to a once-in-a-generation improvement in air quality (Kleeman et al., 2013; Zapata et al., 2013, 2017). State law AB32 commits California to reduce GHG emissions to 1990 levels by 2020 (California Air Resource Board, 2006); California Governor's Executive Order S-3-05 commits California to an additional 80% reduction below 1990 levels by 2050 (Schfwarzenegger, 2005). The latest AB617 is focusing on developing and implementing new strategies to reduce exposure in communities most impacted by air pollution(California

Air Resource Board, 2017). It is urgent that an EJ assessment be carried out to ensure that these future benefits are distributed equitably across all members of society. New frameworks are needed to evaluate air quality and Environmental Justice (EJ) in future emissions scenarios.

Understanding the spatial distribution of air pollution fields is a critical first step in any air quality EJ assessment. Exposure fields used in EJ assessment can be obtained from Land Use Regression (LUR) models (Ouyang et al., 2018; Su et al., 2012), dispersion models (Houston et al., 2014), reduced complexity models (Tessum et al., 2019), chemical transport models (CTM) (Izquierdo et al., 2020; Marshall et al., 2014), and data fusion methods that incorporate information from air quality monitoring networks and/or satellites (Di et al., 2016; Donkelaar et al., 2019; Hernandez et al., 2021; Kloog et al., 2014; Van Donkelaar et al., 2016). All of these methods can predict historical exposure fields with very high spatial resolution, but only CTMs work as well in future episodes as they do in historical episodes because they are not reliant on data support from historical monitoring data. Reliable future exposure fields are needed to support the increasing demand for future air quality health impact / EJ assessment (Dimanchev et al., 2019; Yiting Li et al., 2022; Wang et al., 2020; Zapata et al., 2017).

Measurements show that approximately 60-80% of $PM_{2.5}$ in California is composed of material formed by secondary aerosol formation in the atmosphere (Heo et al., 2013; US EPA, 1999). The non-linear nature of atmospheric chemical reactions makes the relationships between precursor gas-phase emissions and final ambient particle-phase concentrations complex. Increasing precursor emissions may either increase or decrease the final ambient concentration depending on the chemical regime. CTMs are based on fundamental equations describing atmospheric physics and chemistry, and so they can be used to predict exposure fields in situations where the underlying emissions inventory changes, including scenarios where the atmospheric chemical regime changes from NOx-rich to NOx-limited (Seinfeld and Pandis, 2016). Full CTMs therefore provide the most accurate method to predict future health impacts or EJ analyses in a changing world.

CTMs properly account for complex atmospheric chemistry, but their high computation burden limits their spatial resolution and/or domain size (the size of study area), which can introduce errors into health impact assessments (Fenech et al., 2018; Jiang and Yoo, 2018; Thompson et al., 2014; Thompson and Selin, 2012) and EJ assessment (Paolella et al., 2018). Previous EJ studies in the US have shown that populations with lower socio-economic status are more likely to live near pollution emissions sources and therefore in zones with sharp pollution spatial gradients (Sheppard et al., 1999). Analyzing air pollution exposure in these regions requires high-resolution emissions inventories (Cohan et al., 2006; Markakis et al., 2015; Pan et al., 2017; Tan et al., 2015; Zheng et al., 2017) but even with these inventories in place, the analysis may be limited by the tradeoffs between spatial resolution and domain size. Many studies show that gradients in pollutant concentrations and socio-economic status over intermediate and large spatial scales can be key factors in the analysis of environmental inequity, making the choice of domain size (city-, county-, state-, or national-wide) an important consideration in the EJ assessment (Baden et al., 2007; Chakraborty et al., 2011; Walker, 2009). CTMs applied for EJ assessment therefore need to use a sufficiently large domain size combined with an appropriately fine spatial resolution to capture sharp spatial gradients to bring the critical EJ issues into focus. The goal of this study is to find an appropriate balance between these competing requirements.

CTM computational time and energy consumption generally increase in proportion to the number of active model grid cells (=spatial domain size / grid cell size) in the calculation. The computational burden of CTMs limits their reasonable application to some maximum number of active grid cells. If the resolution of the CTM grid cells increases (smaller cells) then the spatial domain size must decrease to maintain the target number of active cells. Improvements in computational abilities continue to push these limits higher over time, but this factor continues to act as a practical limit to the configuration of CTM studies now and in the near-term future. It is necessary to find a balance between the target domain size and spatial resolution before starting an EJ assessment so that the results are sufficiently reliable and the calculations are computationally efficient. Here we explore how various combinations of (grid resolution x spatial domain size) influence CTM air pollution EJ studies over Southern California. Spatial resolutions ranging from

100's of meters (comparable to census tract levels) up to 36 km are investigated, with associated domain sizes ranging from 320 km^2 to 10,000 km^2. In the current study, the number of active model grid cells for 4 km, 1 km, and 250 m domains were 27×27, 40×40, and 80×64, respectively. Domains with higher spatial resolution are nested inside of coarse parent domains, and so the time and energy requirements are cumulative for the 4 km, 1 km, and 250 m domains. The computational burden normalized to the 4 km domain is 3.2 times higher for the 1 km domain and 10.2 times higher for the 250 m domain. In this study, the ability of each CTM configuration to bring EJ issues into focus is analyzed, and the relationship between spatial resolution, domain size, and statistical power is identified. The results guide the design for future CTM studies to support EJ assessment in California, and the methods provide a roadmap for the design of similar CTM - EJ studies in other regions.

3.2. Materials and Methods

Emissions inventories with spatial resolutions of 36 km, 12 km, and 4 km were first processed with the Sparse Matrix Operator Kernel Emissions (SMOKE) model. Major point sources were specified at their exact latitude and longitude so that these sources can easily be incorporated into fine-scale emissions inventories (1 km/250 m). The locations of area source (non-point source) and mobile emissions inventories were then specified at finer scales using spatial surrogates that were correlated with the true emissions activity. The base year 2016 California Air Resource Board (CARB) emissions inventory (California Air Resources Board, 2019) that served as the starting point for these downscaling calculations used spatial surrogates with a default resolution of 4 km. Emissions are described for six criteria pollutants: PM, NOx, SOx, TOG, CO and ammonia. The emissions within each 1 km/250 m subset of the parent 4 km cell were assigned in proportion to a refined spatial surrogate developed in previous work (Li et al., 2020) as summarized in Appendix 2 (Table S2-1). This methodology is consistent with the standard approach used to downscale county-level emissions to 4 km resolution in the National Emission Inventory (NEI) and CARB emissions inventories. The accuracy of the technique ultimately depends on the accuracy and suitability of the spatial surrogates used to represent the emissions. Further details are provided in the

sections below. CARB raw inventories are described at the hourly level using monthly, weekly, and diurnal time profiles for each emission source.

3.2.1. High resolution area emissions

Spatial surrogates based on seven source categories and fourteen in total with 1 km/250 m resolution were used in the current study: (1) service and commercial employment and single-family housing (emissions from off-road gasoline engines); (2) off-road construction equipment, farm road vehicle miles travel (VMT), industrial-related/industrial employment (emissions from off-road diesel engines); (3) residential wood burning (emissions from biomass combustion); (4) restaurant sale volume (emissions from food cooking); (5) residential heating gas, industrial-related/industrial employment, service and commercial employment (emissions from natural gas combustion); (6) primary road, secondary road, unpaved road (emissions from road dust); (7) off-road/on-road construction equipment, industrial-related, farm road VMT, total population (emissions from miscellaneous sources). Surrogate data sources and algorithms are listed in Table S1.

3.2.2. High resolution mobile emissions

Mobile emissions include both tailpipe emissions and tire/brake wear emissions. Tailpipe emissions can be further divided into gasoline mobile (light-duty vehicles) and diesel mobile (medium- and heavy-duty trucks) by engine type. Surrogates for each of these three subcategories are discussed below.

3.2.2.1 Gasoline and diesel tailpipe emissions

Explicit traffic counts collected by the U.S. Highway Performance Monitoring System (HPMS) were used to distribute the majority of the tailpipe emissions to highways and other principal arterial roads. McDonald et al. (McDonald et al., 2014) showed that approximately 70% of gasoline and approximately 80% of diesel vehicle fuel consumption in California occurs on roads with traffic count information. Emissions on these roads can be represented by VMT (i.e., traffic count x road length). The remaining approximately 30% of gasoline and approximately 20% of diesel vehicle activity can use road length as a

spatial surrogate. This approximate treatment for the residual portion of the tailpipe emissions should be done separately for urban and rural areas to ensure rural emissions are not overestimated (Brondfield et al., 2012). In California, the approximately 30% of the residual gasoline activity occurs mostly in urban areas (90%) with the balance in rural areas. Data sources can be found in SI Section 1.1. The final mobile gasoline and diesel surrogates were calculated using the equations (1) and (2):

$$Surr\ (Gasoline) = 70\% \times (AADT \times Len)_{normalized} + 30\% \times (Len')_{normalized} \quad (1)$$

$$Surr\ (Diesel) = 80\% \times (\ AADT' \times Len)_{normalized} + 20\% \times (Len'')_{normalized} \quad (2)$$

$$Len'' = 90\%\ \times Len\_urban + 10\%\ \times Len\_rural \quad (3)$$

where $Surr\ (Gasoline)$ is the Gasoline mobile surrogate; $Surr\ (Diesel)$ is the Diesel mobile surrogate; AADT is the Annual Average Daily Traffic; AADT' is the Truck Annual Average Daily Traffic; Len is the Road length with AADT; Len' is the Road length without traffic accounts; Len'' is the Truck road length without traffic accounts; Len_urban is the Urban road length; and Len_rural is the rural road length.

3.2.2.2 Tire & brake wear emissions

Tire and brake wear emissions were estimated as a fixed fraction of tailpipe emissions for all engine types. The CARB SIP 2016 emissions inventories (California Air Resource Board, 2016.) specify that gasoline / diesel emissions account for 86% / 14% of total mobile emissions. Thus, the tire and brake wear spatial surrogate was calculated using the equation (4):

$$Surr\ (Tire\ and\ Brake\ wear) =$$
$$86\% \times Surr(Gasoline)_{normalized} + 14\% \times Surr(Diesel)_{normalized} \quad (4)$$

where $Surr\ (Tire\ and\ Brake\ wear)$ is the Tire and Brake wear surrogate.

3.2.3. Exposure field – CTM configuration

Annual-average exposure fields over Southern California for the year 2016 were generated using the source-oriented WRF/Chem (SOWC-HR) CTM (Joe et al., 2014; Zhang et al., 2014) coupled with high-resolution emissions inventories summarized above. This version of SOWC used Large Eddy Simulation (LES) to simulate domains with spatial resolution as fine as 250m. LES predicts turbulent mixing at fine

scales where traditional first order closure models are not valid. Thompson graupel scheme was used for microphysics option (mp_physics = 8). ACSM2 was used for boundary-layer option (bl_pbl_physcis = 7). Kain-Fritsch scheme was used for cumulus option (cu_physics = 1). SPRAC11 chemical mechanism was used in this simulation. Multiple domain settings were used (Figure S1) to explore the effects of domain size and spatial resolution. The largest domain with 36 km resolution (D01) covered the entire state of California. A slightly smaller domain with 12 km resolution (D02) covered the South Coast Air Basin (SoCAB). More highly resolved domains with 4 km (D03), 1 km (D04), and 250 m (D05) spatial resolution (employing LES) were nested over Los Angeles. The domain with the highest resolution D05 (250 m) was centered on the community of East Los Angeles, Boyle Heights, West Commerce that has been identified for special study under California's Assembly Bill 617 (AB617). WRF/Chem was configured with two-way nesting between 36km-12km-4km domains and one-way nesting between 4km-1km-250m domains.

A second set of exposure fields was also developed using the University of California Davis / California Institute of Technology (UCD/CIT) CTM (Kleeman and Cass, 2001b). The UCD/CIT model was configured with one parent 24 km statewide domain and one nested 4 km domain covering the SoCAB (Figure S1). One-way nesting was used between the domains. UCD/CIT model simulations employed a different set of emissions inventories. Primary dust emissions used by the WRF/Chem model are higher than the dust emissions used by the UCD/CIT model. Comparison of the concentration fields predicted by both models suggests that different dust emissions can account for a change in predicted $PM_{2.5}$ mass concentrations of approximately 1.5 μg m^{-3}. The UCD/CIT model used standard 4km CARB mobile emissions developed using travel demand models combined with the EMFAC model. The WRF/Chem model used mobile emissions with 1km spatial resolution developed using the methods summarized in Section 3.2. In addition to having different spatial resolutions, the different approaches used to develop these inventories yield slightly different spatial patterns for the mobile emissions. Results from WRF/Chem and the UCD/CIT model will be compared to identify common trends.

3.2.4.Socio-economic data

Socio-economic data were obtained from the American Community Survey (ACS) 2012-2016 (United State Census Bureau, 2020). The dataset describes four race/ethnicity groups that were analyzed in detail in the current study: Black (Black & African American alone), Hispanic (Hispanic or Latino, regardless of race), Asian (Asian alone), and non-Hispanic White (White, not Hispanic or Latino). Population maps for these race/ethnicity groups are shown in Figure S2-2 to S2-3 in Appendix 2 with a summary for each model domain presented in Table S2-2 in Appendix 2. The Hispanic fraction of the population increases as the model domains becomes more focused on central Los Angeles, rising from 38% in D01 to 67% in D05. Conversely, the Non-Hispanic White fraction of the population decreases steadily from 38% in D01 to 10% in D05. Asian (13-16%) and Black and African American (6-10%) population fractions are more constant across the model domains D01 through D05. The ACS dataset also includes seven income categories spanning the range from less than 50% of the poverty level to greater than twice the poverty level. Income distributions across the model domains D04 and D05 are summarized in Table S2-3 in Appendix 2. Intermediate income levels are similar across domains, but 28% of the population in D05 is below the poverty level compared to 20% in D04, and only 42% of the population is more than 2x above the poverty level in D05 compared to 57% in D04. These statistics illustrate that the inner D05 modeling domain employed in the current study contains a larger fraction of the poorest population. D05 is a subset of D01-D04, but the larger regions contain areas with cleaner air and a higher proportion of white residents. Thus, analysis carried out over D01-D04 dilutes the disparities experienced by the poorest residents.

Socio-economic data with census tract resolution was used for the analysis. Within the primary study region (Los Angeles D02), 51% of census tracts are below 1 km resolution and 72% of census tracts are below 1.2 km resolution. A histogram of census tract size is shown in Figure S4. The resolution of the socio-economic data is well matched with the resolution of the model domains in the current study. Population data used in EJ assessment were regirded into spatial resolutions that was comparable to the CTM exposure fields.

Population weighted concentration were calculated for four race/ethnicity groups and two poverty level categories. Both absolute disparity and relative disparity were calculated and analyzed. Relative disparity results are expressed as relative percentage difference relative to the total population average ($(PWC_{race/income} - \overline{PWC}) / \overline{PWC} * 100\%$).

3.2.5. Statistical power

EJ assessments were performed using several combinations of domain size and spatial resolution in the current study. Statistical power was used as a metric to evaluate the capability of each combination to detect a given disparity value and therefore to determine whether the combination of domain size and spatial resolution was suitable for future studies. Statistical power is calculated using standard statistical procedures involving Type II error during a test of the means in two samples. Type II error occurs when the null hypotheses is not rejected even though it is false. A lower probability of a Type II error (β) generates a higher statistical power (1-β) and a more sensitive test. Statistical power and Type II error for tests of the means are related to four parameters: mean of two samples (two races/ethnicities or two income groups); standard deviation of two samples; sample size, and Alpha level (α), which were provided in Appendix 2 Section S2.2.3. We chose α = 0.01 in this study. The statistical power results are presented in Section 3.3.4.

3.3.Results and discussion

3.3.1.CTM exposure fields and model performance

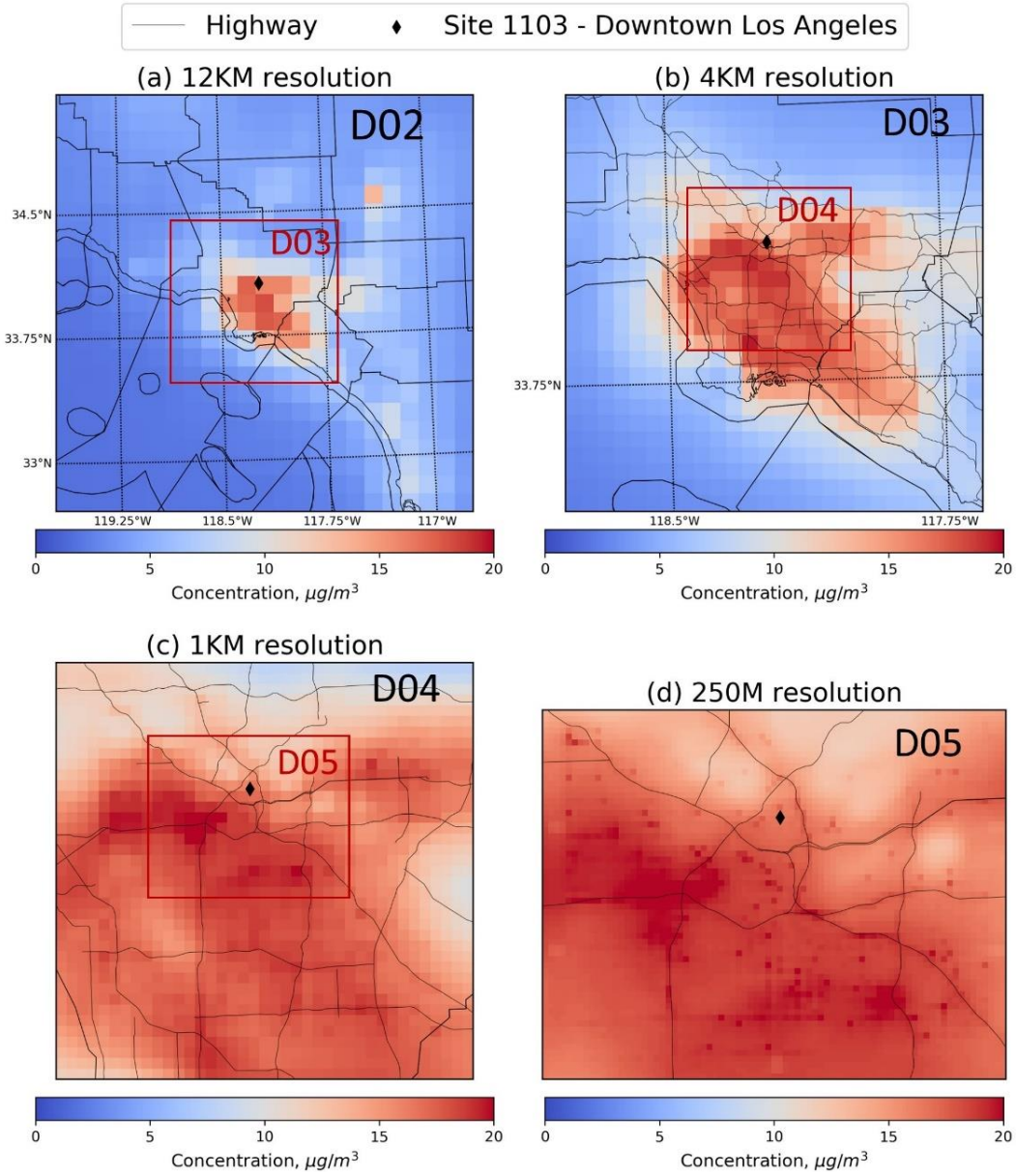

Figure 3-1. Year 2016 predicted annual average $PM_{2.5}$ mass concentration *($\mu g/m^3$) at 12 km (a), 4 km (b), 1 km (c), 250 m (d) spatial resolution.*

Figure 3-1 shows the annual average $PM_{2.5}$ mass concentration predicted by WRF/Chem in the year 2016 at spatial resolutions of 12 km (D02, Figure 3-1a), 4 km (D03, Figure 3-1b), 1 km (D04, Figure 3-1c) and 250 m (D05, Figure 3-1d). Annual average concentrations of $PM_{2.5}$ Elemental Carbon (EC), Organic

Carbon (OC), primary and secondary aerosol mass are shown in Figures S2-5 to S2-8 in Appendix 2. Thin gray lines in Figure 3-1 panels b,c,d represent state highways, black lines in panels a, b, c represent California GAI boundaries, which combine county boundaries and air basin boundaries. Pollutants with shorter atmospheric lifetimes (such as primary particles) have concentrations that rapidly decay downwind of emissions locations (Karner et al., 2010). Higher spatial resolution therefore reveals sharper concentration spatial gradients around major traffic corridors and large stationary emissions sources. Maximum concentrations and the number of "hotspots" both increase with finer spatial resolution in Figure 3-1, yielding a more complex exposure field that captures the influence of both local sources as well as regional background concentrations.

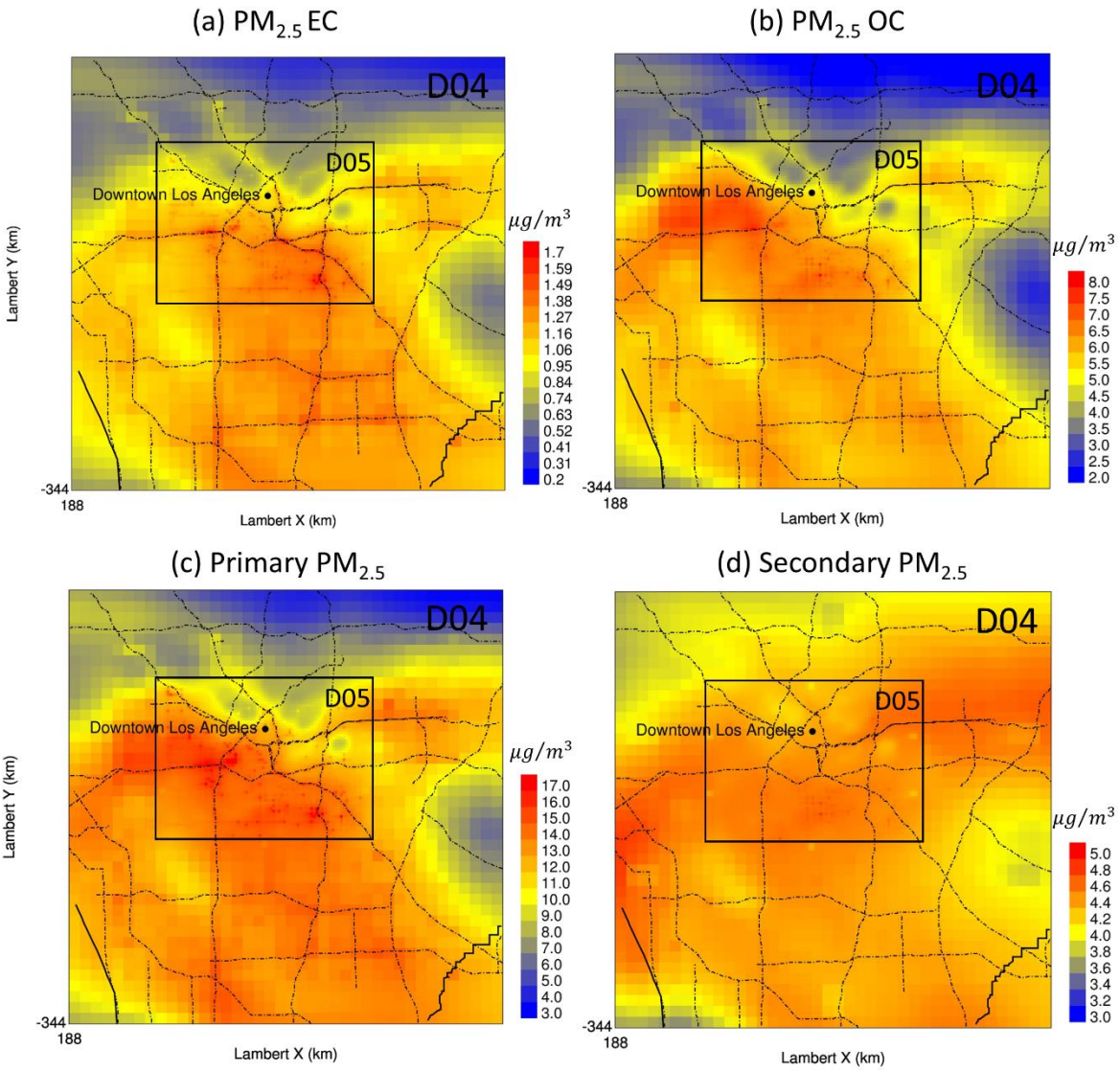

Figure 3-2. Year 2016 annual $PM_{2.5}$ EC, OC, primary, and secondary aerosol mass concentration *($\mu g/m^3$) at 1 km (domain D04) and 250 m (domain D05) spatial resolution. Dashed line is state highway.*

Figure 3-2 illustrates annual-average concentrations of $PM_{2.5}$ EC, OC, primary mass, and secondary mass predicted at 1 km (D04) and 250 m (D05) spatial resolution. Figure 3-2 shows that $PM_{2.5}$ EC concentrations are elevated around major transportation corridors, with sharper spatial gradients coming into focus at finer spatial resolution (Figure 3-2a, D04 vs. D05). Increased $PM_{2.5}$ EC concentrations can also be observed around major surface streets at 250 m resolution (Figure 3-2a, D05). Predictions at 12 km and 4 km spatial resolution are too coarse to detect elevated $PM_{2.5}$ EC concentrations adjacent to highways or major roadways, but these coarser predictions do still capture the general increase over the urban area

(Figure S2-5 in Appendix 2). $PM_{2.5}$ OC concentration fields are smoother than $PM_{2.5}$ EC concentration fields at all spatial resolutions (Figure 3-2b vs. Figure Figure 3-2a and Figure S2-6 vs. Figure S2-5 in Appendix 2). Primary $PM_{2.5}$ OC (Figure 3-2b) is emitted by a larger number of sources (food cooking, traffic, biomass combustion) than $PM_{2.5}$ EC (primarily traffic) in the current simulations. Secondary reactions in the atmosphere also produce $PM_{2.5}$ OC over periods of hours to days, which smooths the resulting concentration fields. Primary $PM_{2.5}$ mass (Figure 3-2c) consisting of EC, primary OC, metals, and other crustal elements responds to spatial resolution similarly to EC, with sharper spatial gradients revealed at higher resolution. In contrast, secondary $PM_{2.5}$ mass (Figure 3-2d and Figure S2-8 in Appendix 2) has relatively smooth spatial gradients that do not change significantly as spatial resolution is increased. The overall results illustrated in Figure 3-2 show that finer spatial resolution captures the sharp gradients associated with primary pollutants such as EC but reveals few additional features for secondary aerosol.

Predicted concentrations of $PM_{2.5}$ mass, EC, and OC were compared to all available measurements during the study period (Figure S2-12 to S2-13 in Appendix 2). Daily $PM_{2.5}$ mass, Mean Fractional Bias (MFB) and Mean Fractional Error (MFE) of the CTM predictions at 12km, 4km, 1km and 250m are calculated at ten available sites. Daily $PM_{2.5}$ EC, OC MFB and MFE are calculated at one site (downtown Los Angeles). Monthly average / daily predicted and measured $PM_{2.5}$ mass, EC, OC at Downtown Los Angeles site are shown in Appendix 2 (Figure S2-10 and Figure S2-11). In general, simulations at all spatial resolutions capture time trends in $PM_{2.5}$ mass, EC, and OC concentrations. $PM_{2.5}$ mass, EC, OC have been slightly overestimated in summer months, which was caused by underestimation of wind speed of summer months. All MFB are $\leq 60\%$ and MFE values are $\leq 75\%$, meeting typical CTM performance criteria(Boylan and Russell, 2006). Three out of four sites that used 1 km spatial resolution met typical CTM performance goals(Boylan and Russell, 2006) (MFB $\leq 30\%$ and MFE $\leq 50\%$). Model performance (both MFB and MFE) improved by 5% when the spatial resolution was increased from 4 km to 1 km; model performance improved an additional 4% when the spatial resolution was increased from 1 km to 250 m. It is noteworthy that model performance degrades slightly as spatial resolution increases from 12 km to 4 km, and then improves as spatial resolution increases from 4 km to 1 km to 250 m at the available measurement sites.

UCD/CIT Model performance is summarized in Figure S9. UCD/CIT model results meet typical CTM performance goals (Boylan and Russell, 2006) (MFB $\leqslant$ 30% and MFE $\leqslant$ 50%) for all available measurement sites.

Model performance as a function of location was analyzed by comparing annual-average predicted concentration to measurements across the study domain as recommended by Paolella et al. (Paolella et al., 2018) The reasonably high correlation coefficient calculated in this analysis (R^2 = 0.61 in Figure S2-14) shows that predicted concentration fields have a spatial pattern that is consistent with measured concentrations.

While the CTM error analysis builds confidence in the accuracy of the overall modeling system, it does not address the key issue of the appropriate combination of domain size and spatial resolution to capture a sufficiently large population with enough concentration contrast to best support epidemiological studies.

3.3.2. EJ analyses at different CTM domain size and spatial resolution

The following sections analyze air quality EJ as a function of the CTM domain size and spatial resolution. Nine combinations of domain size and spatial resolution were chosen for analysis, including D01 - 36KM, D02 – 12KM, D03 – 12KM, D03 – 4KM, D04 – 4KM, D04 – 1KM, D05 – 4KM, D05 - 1KM and D05 – 250M. The domain size-resolution combinations selected for analysis were constrained by the computational burden at fine spatial resolution and sufficiently large sample size at coarse resolution. Fine-scale domains with more than 10,000 grid cells were not used in order to maintain reasonable computational burden. Coarse-scale domains with fewer than 20 grid cells were not used to maintain sufficiently large sample size. This experimental design reflects the trade-off between spatial resolution and domain size at the core of the present analysis.

Results are stratified by the population socio-economic class information available in the public ACS datasets. One EJ assessment is based on combined race/ethnicity (Black and African American, Hispanic,

Asian, and non-Hispanic White) and two income categories (below the poverty level and above the poverty level). A second EJ assessment is based on income alone using seven categories (the highest of which is 2x more than the poverty level). Annual-average population-weighted concentrations (PWC) of $PM_{2.5}$ mass, EC, OC, primary mass, and secondary mass are calculated to represent exposures for each socio-economic group across all CTM domains and spatial resolutions (Figure S2-15 for race-income D04, 05, Figure S2-16 for race-income D01,02,03, Figure S2-17 for income alone D04-D05 in Appendix 2).

Absolute and relative disparities of $PM_{2.5}$ mass and its components were calculated across all WRF/Chem CTM domains and for their intersection with UCD/CIT CTM domains, including statewide 24km, 4km on D03 (UCD/CIT, D03-4KM), and 4km on D04 (UCD/CIT, D04-4KM). UCD/CIT results were developed independently from WRF/Chem results and so they serve as a comparison group to identify trends common across model platforms.

In general, Los Angeles residents in lower socio-economic groups are predicted to experience higher exposure to air pollutants, especially primary pollutants, regardless of CTM domain size and spatial resolution. This finding is consistent with the results from previous studies over Los Angeles (Cushing et al., n.d.; Paolella et al., 2018; Tessum et al., 2019). However, the current study predicts that exposure to secondary $PM_{2.5}$ mass was similar across all races and income categories. Below we discuss further details of the combined effects of CTM domain size and spatial resolution on the EJ results and the statistical power of the analysis.

3.3.2.1Absolute disparity

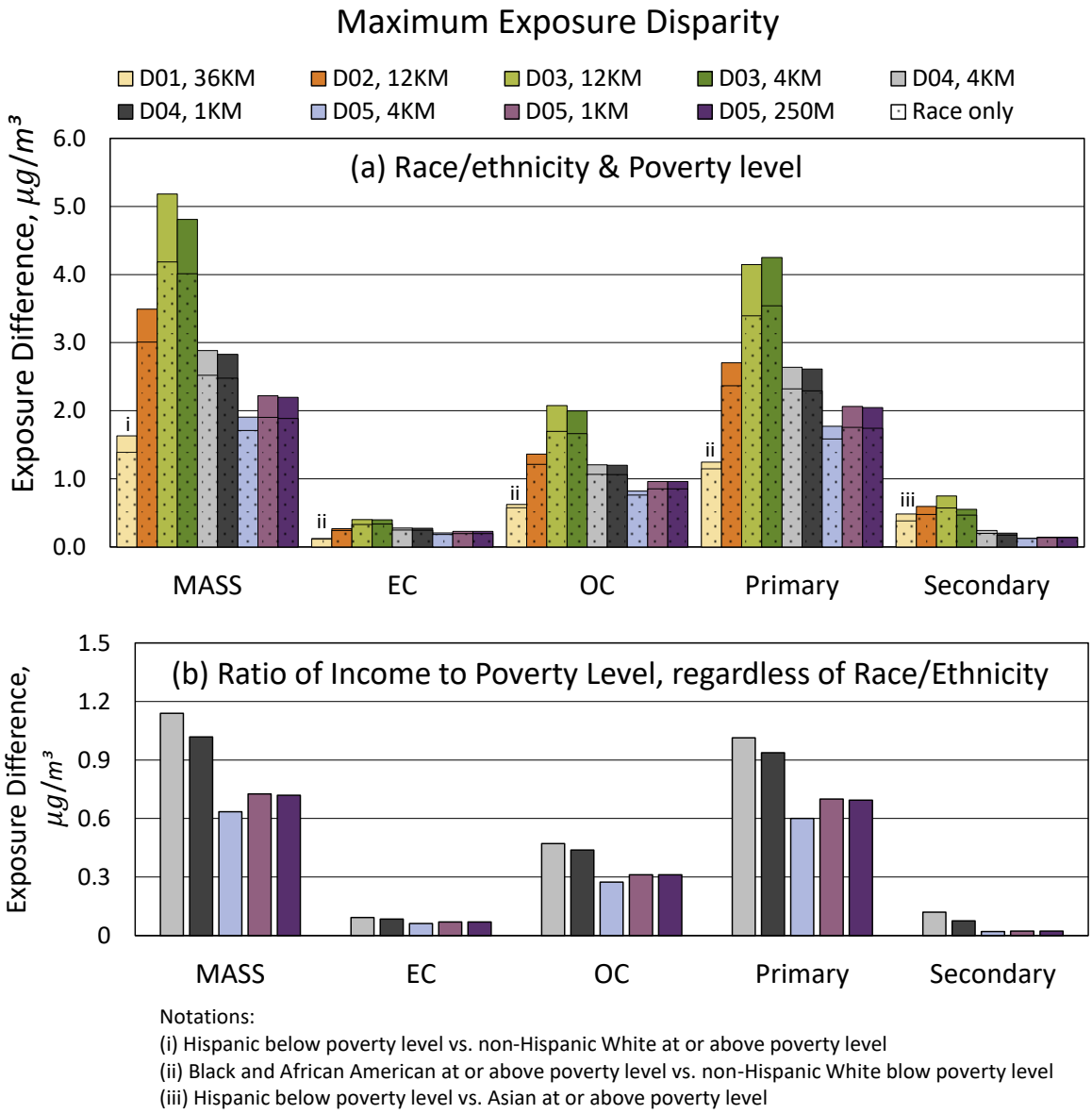

Figure 3-3. Pollutant exposure difference between the maximum disparity groups. *Comparison groups in (a) are Black and African American below poverty level vs. non-Hispanic White above poverty level except for D01, 36KM result. Comparison groups in panel (b) are people who are less than 0.5x the poverty level vs. people who are more than 2x the poverty level. CTM domains are shown in Figure S2-1.*

Figure *3-3* summarizes the exposure difference between the largest disparity groups across all combinations of CTM domain size and resolution as a function of race-income (Figure *3-3* (a)) and income

alone (Figure *3-3* (b)). The largest absolute disparity in the current study was observed between low-income Black and African American and high-income non-Hispanic White groups, except at the statewide domain level D01, 36 km (see caption in Figure *3-3* (a)). Observed race-income related maximum exposure disparities were 1.63 to 5.18 $\mu g/m^3$ for $PM_{2.5}$ mass; 0.12 to 0.4 $\mu g/m^3$ for $PM_{2.5}$ EC; 0.63 to 2.0 $\mu g/m^3$ for $PM_{2.5}$ OC; 1.25 to 4.25 $\mu g/m^3$ for primary mass; 0.12 to 0.75 $\mu g/m^3$ for $PM_{2.5}$ secondary. The choice of model domain size at a constant resolution changed calculated absolute disparity values by 12%-28%. The choice of model spatial resolution at a constant domain size changed calculated absolute disparity values by 1%-6%. Changing of domain size has relatively larger effect on absolute disparity. Note that income level did not have a statistically significant effect on air pollution exposure over the largest domain (D01) that employed the coarsest spatial resolution. When exposures were analyzed without regard to income level, the maximum disparity between race groups decreased approximately 8% (D01) to 18% (D04) (shaded area in Figure *3-3* (a)).

Absolute exposure disparities between different racial groups calculated by WRF/Chem and the UCD/CIT model are compared across statewide, D03-4KM, and D04-4KM domains in in Figure S2-19 in Appendix 2. The trends in exposure disparity as a function of domain size and domain resolution are consistent between the two CTM predictions. Absolute values of exposure disparities calculated with the models are in better agreement when over-predictions in dust emissions in the WRF/Chem model were subtracted from the predicted concentration fields. The agreement between results produced by these independent models builds confidence in the exposure disparities identified in the current study.

Hypothesis tests were conducted for population-weighted $PM_{2.5}$ mass exposures across race and poverty levels to further investigate poverty-related disparity. The population-weighted exposures are calculated with a finite number of grid cells with a total count that is far smaller than the number of people in the study region. The calculated population exposure can therefore be viewed as a sub-sample of the individualized population exposure (that is impractical to calculate). Test statistics were calculated using the weighted mean and the weighted standard deviation for each population exposure across all available

model grid cells (summarized in Tables S2-4 to S2-8 in Appendix 2). Further details of the calculation approach are provided in Appendix 2 and Tables S2-9 to S2-10. P-values were calculated to test the hypothesis that each paired comparison group had the same exposure. Three stratifications were considered: (i) combined race and poverty level; (ii) race only; and (iii) poverty level only. Statistically significant maximum exposure disparities (p-values < 1%) were identified in most CTM configurations when considering race and poverty level together or race alone, except for the comparison between low-income Asian and high-income White groups. The dependence on CTM domain size and spatial resolution became more apparent when testing the smaller effects of poverty alone. Statistically significant differences by poverty level were only detected at higher resolution regional/community-level domain (4km at D03, 1km at D04 and 250m at D05) that had sufficient combined size and resolution. All of the subsequent tests involving income levels will focus on regional/community-level domains in order to maintain statistical power at a meaningful level.

The largest air pollution exposure disparities based on income occur between the highest and the lowest income categories, but the maximum income exposure disparities (Figure *3-3* (c)) were approximately 50% smaller than maximum race exposure disparities (shaded bar in Figure *3-3* (a)) over the income categories tested. The effect of income was further analyzed by comparing exposure disparities between households with income greater than $200,000/yr and households with income below $10,000/yr in D03, D04, and D05 (see Table S2-11 in Appendix 2). Exposure disparity for $PM_{2.5}$ mass is 1.5-4 times higher when comparing these more divergent income categories, with similar increases for the exposure disparities in the components of $PM_{2.5}$ mass. These results suggest that income is an important factor in air pollution exposure disparity, but it must be recognized that income and race are often highly correlated (see (Paolella et al., 2018) for discussion on this topic). More than 80% of the households with income greater than $200,000/yr in the current study are non-Hispanic White, making it is difficult to separate income vs. race contributions to exposure disparity.

Figure *3-3* illustrates how maximum exposure disparity for primary and secondary PM responds to CTM domain size and spatial resolution. The largest statewide domain (D01) has the lowest maximum exposure disparity for primary PM due to the corresponding coarse spatial resolution. In contrast, exposure disparities for secondary PM increase with domain size regardless of spatial resolution since spatial gradients for secondary pollutants occur over larger distances. Maximum exposure disparity for all $PM_{2.5}$ mass and components increased from source-oriented WRF/Chem statewide D01 to region-level D03, then decreased from D03 to D05.

Two trends are apparent when comparing results with different spatial resolutions but the same domain size (D03, 04, and D05) in Figure *3-3*. Within the community-level domain (D05), the exposure disparity increased with spatial resolution (4 km-1 km-250 m). The opposite trend is observed in the regional domain (D03 and D04), where the exposure disparity slightly decreased with spatial resolution (12 km-4 km-1 km). D03 and D04 include more coastal areas that inherently have lower exposures because they have fewer upwind sources. Thus, analysis conducted in D03 and D04 captures the increased disparity between those who live closer to the coast (non-Hispanic White or wealthy people) and those who live in inland (other non-White categories). In this case, the effects of the larger domain size overwhelm the effects of the higher spatial resolution.

3.3.2.2Relative disparity

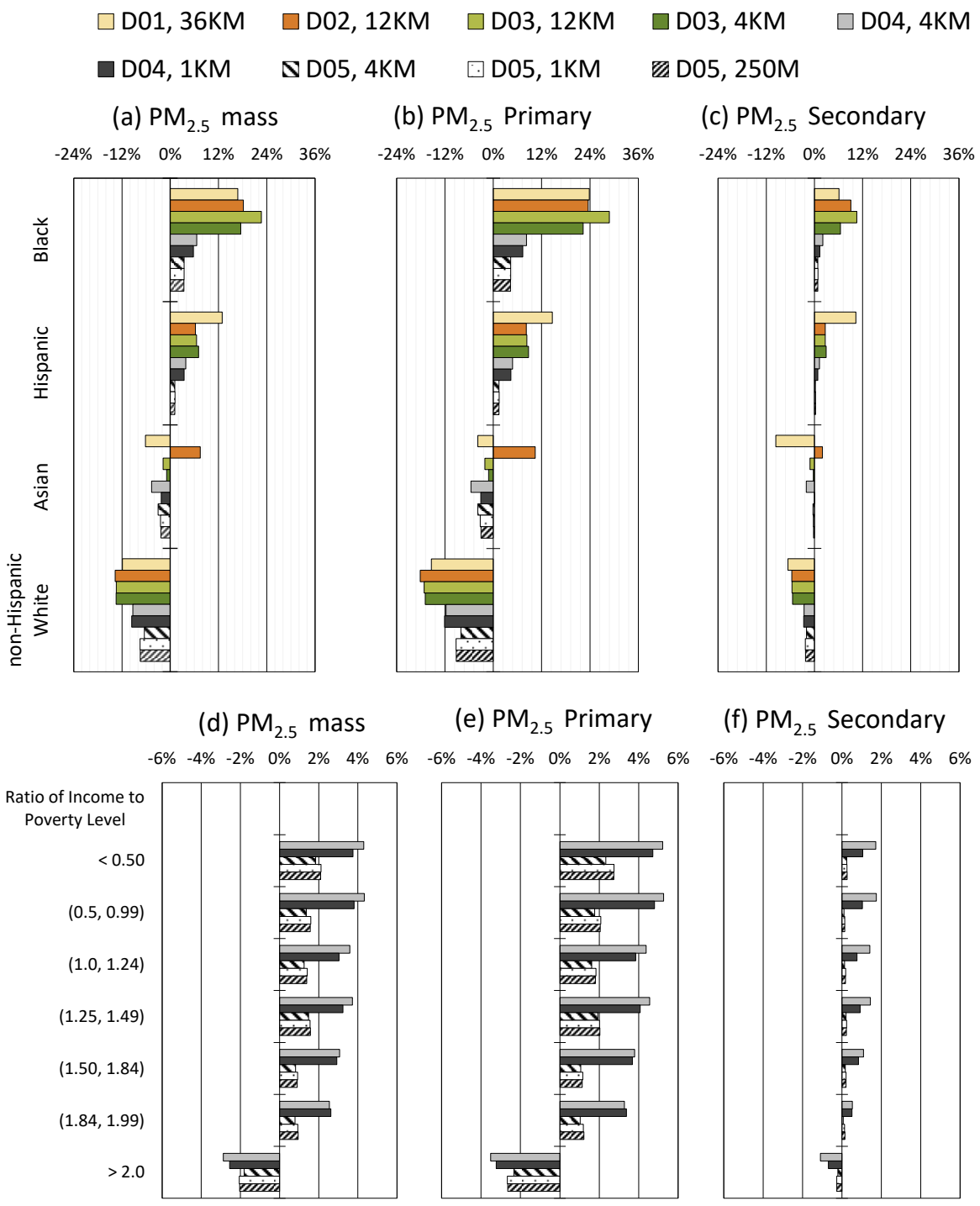

Figure 3-4. Exposure difference relative to population average *for (a,d) $PM_{2.5}$ total mass, (b,e) primary $PM_{2.5}$ mass, and (c,f) secondary $PM_{2.5}$ mass as a function of domain size and resolution. Upper panels analyze race/ethnicity and lower panels analyze income.*

Figure 3-4 illustrates deviations from the total population average concentrations estimated for each socio-economic group for $PM_{2.5}$ total mass, primary mass, and secondary mass (similar results for $PM_{2.5}$ EC and OC are presented in Figure S2-18 in Appendix 2). Overall, Black and African American and Hispanic residents experience higher than average exposure to $PM_{2.5}$ total mass (2% - 23%) and to $PM_{2.5}$ secondary aerosol (1% - 10%); Non-Hispanic White and Asian residents experience lower than average exposure to $PM_{2.5}$ total mass (4% - 13%) and to $PM_{2.5}$ secondary aerosol (1% - 6%). People with income lower than twice the poverty level generally experience similarly higher air pollution exposures, whereas people with income more than twice the poverty level experience lower air pollution exposure. Further refinement of income categories at higher levels would likely reveal even greater levels of exposure disparity.

Relative exposure disparities between different racial groups calculated by WRF/Chem and the UCD/CIT model are compared across statewide, D03-4KM, and D04-4KM domains with results provided in Figure S2-20 in Appendix 2. Trends in exposure disparities across different racial groups are in strong agreement between the two model predictions. Black and African American and Hispanic residents consistently have higher than average exposure to total $PM_{2.5}$, while non-Hispanic White residents consistently have lower than average exposure. Asian residents have exposure levels that are very close to average. The biological significance of the PM2.5 exposure disparities can be quantified using the methods that are used to estimate the public health burden of air pollution exposure. The mortality risk ratio (RR) associated with air pollution exposure is often represented using the equation

$$RR = e^{\beta(C_{exposure} - C_{background})} \qquad (5)$$

where C_exposure is the exposure concentration and C_background is the background concentration for the pollutant of interest. (Krewski et al., 2009) performed a follow-up analysis of the American Cancer Society (ACS) cohort and derived a β value of 1.036 for exposure to $PM_{2.5}$ mass. Applying eq (5) to the population-weighted-concentrations experienced by each racial group in domain D04-4KM yields a risk

ratio for Black and African American residents that is approximately 30% higher than the risk ratio for the Non-Hispanic White group. It should be noted that the risk ratio calculation is non-linear and so a more exact treatment would apply eq (5) separately for residents in different exposure bands and then combine the results. The current analysis provides a rough estimate of health impacts, with a more exact treatment described in other work (see for example (Li et al., 2022).

CTM domain size and spatial resolution combine to influence the exposure disparities illustrated in Figure 3-3 and Figure 3-4. Maximum exposure disparities generally come into clearest focus when intermediate combinations of domain size and spatial resolution are used since this balanced configuration captures exposure gradients for both primary and secondary PM. The exception to this finding in the current study is that Hispanic exposure disparities were highest in the largest domain (D01) that covered the entire state of California. Results for exposure disparity based on income shown in the lower panels of Figure 3-4 do not include the largest spatial domain because these findings were not statistically significant (see Tables S2-9 to S2-10 in Appendix 2 and associated discussion section 3.3), but the intermediate combinations of domain size and spatial resolution once again bring the largest exposure disparities into clearest focus.

The asymmetry of the exposure disparities in Figure 3-4 are noteworthy. Within larger domains (D01-D03), the maximum exposure disparities based on race were +23% for the highest exposure group and -13% for the lowest exposure group. Within smaller domains (D04-405), the asymmetry pattern reversed, with +6% for the highest exposure group and -10% for the lowest exposure group based on race. Similar asymmetry patterns were observed for maximum exposure disparities based on income: +4% for the highest exposure group and -3% for the lowest exposure group within the larger domain D04. Smaller but similar deviations (+2%/-2%) were observed for the highest and lowest exposure groups within the smaller domain D05. This asymmetry was largely driven by exposure to primary PM, with substantially lower exposure disparities associated with secondary PM. Smaller domains have higher average concentrations that can reduce the maximum exposure disparities. The combined trends illustrated in Figure 3-3 and Figure 3-4

emphasize the need for a balanced selection of domain size and spatial resolution when quantifying exposure disparities, with slightly higher priority given to selection of a sufficiently large domain to represent the large-scale exposure features. Increasing the spatial resolution beyond approximately 1 km appears to produce diminishing returns in the current study.

3.3.3. Exposure distribution

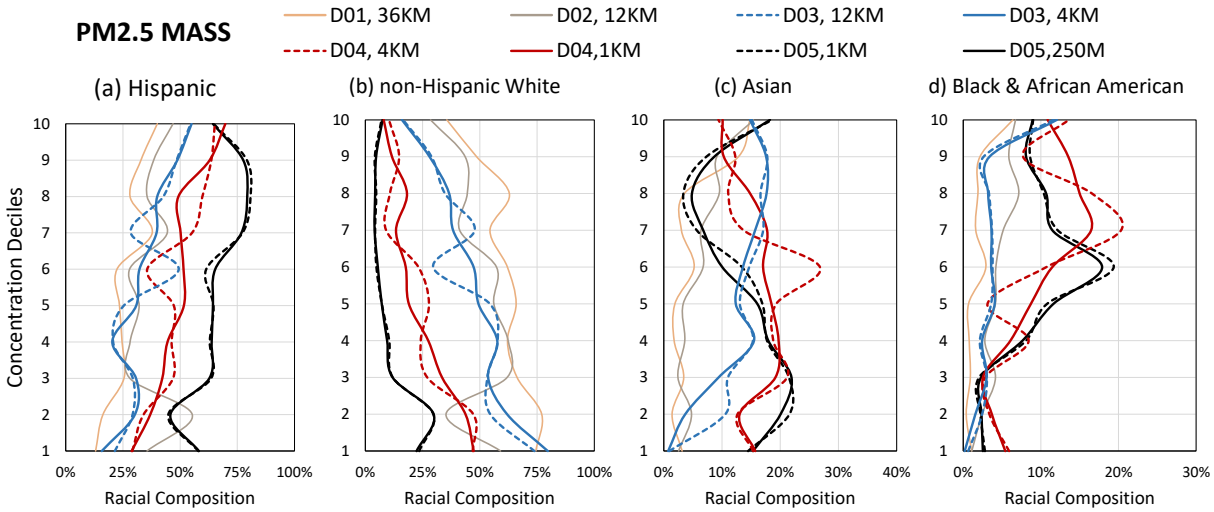

Figure 3-5. $PM_{2.5}$ mass exposure distribution across racial-ethnic population. *(a), (b), (c), (d) focus on spatial resolution and domain scope changes on racial-ethnic population exposure distribution. Population profile at a given concentration level can be found by following a horizontal line across each sub-panel and comparing results from lines with the same color across panels.*

Figure 3-5 illustrates the distribution of $PM_{2.5}$ mass exposure disparities across different race/ethnicity groups as a function of the CTM domain and spatial resolution. Calculations using different CTM domain size and spatial resolution are shown as different colors within each panel of Figure 3-5. Exposure distributions are divided into concentration deciles and exposures for each race/ethnicity group are expressed on a relative scale within each decile. Similar exposure distributions for $PM_{2.5}$ EC, OC, primary mass and secondary mass are presented in the Appendix 2 (Figure S2-21). The results in Figure 3-5 and Figure S2-21 illustrate which race/ethnicity groups experience the highest and lowest PM exposures in California. For reference, the $PM_{2.5}$ mass racial/ethnicity compositions of absolute concentration deciles for

each domain-resolution combination are shown in Figure S2-22. It should be noted that each race/ethnicity group comprises a different fraction of domain total population, and so it is not expected that exposure distributions would be equal when comparing between race/ethnicity groups. Rather, the most equitable distribution of exposures in Figure 3-5 would be for each race/ethnicity group to have relatively uniform exposure across all concentration deciles (straight vertical line).

The sloped exposure distributions illustrated in Figure 3-5 reflect the disparities discussed in the previous sections. Results vary slightly with domain size, but Hispanic and Black and African American racial groups experience increased exposure to the highest deciles of PM concentration while the non-Hispanic White group experiences lower exposure to the highest concentration. Balanced combinations of domain size and domain resolution once again bring the disparities (slope of each line) into sharpest focus. Domain size generally does not change the slope of the exposure distribution lines for Hispanic and non-Hispanic White groups because their populations are distributed more uniformly across California (De La Cruz-Viesca et al., 2016). Domain size has a larger influence on the shape and slope of the exposure distribution lines for Asian and Black and African American groups because these populations are more concentrated in urban areas.

Figure 3-5 shows that lower spatial resolution, especially 4 km, 12 km and 36 km, generates larger fluctuations across the exposure distribution because the coarse resolutions cannot adequately resolve the combined population and concentration spatial gradients. A larger grid cell incorporates a larger fraction of the population into one decile. Breaking large grid cells into small grid cells divides the same population among multiple concentration deciles resulting in a smoother (and more realistic) exposure distribution. This same issue will influence the calculated average exposure for each socio-economic group shown in Figure 3-3 and Figure 3-4, emphasizing the need for a sufficiently fine spatial resolution to resolve EJ issues.

3.3.4.Statistical Power

The analysis presented in the previous sections shows that CTM calculations for EJ assessment that balance both domain size and spatial resolution in the context of race and income patterns can obtain

meaningful results with reduced computational burden. This finding is illustrated with an example in Figure 3-6 showing the statistical power of different CTM configurations over Southern California to correctly identify $PM_{2.5}$ mass exposure disparities between groups in cases where the true disparity is 0.5 $\mu g/m^3$. The horizontal axis of Figure 3-6 represents increasing spatial resolution to the right, while the vertical axis represents increasing active domain area (CTM grid cells with non-zero population) towards the top. Statistical power to detect the indicated concentration difference between maximum disparity groups is shown as color, with statistical power above 90% shown in red. Figure 3-6 shows that EJ statistical power can be increased by either increasing the domain size or increasing the spatial resolution. Achieving statistical power above 90% in our target area requires 4 km spatial resolution with a domain size greater than 10^4 km^2, 1 km spatial resolution with domains size greater than 10^3 km^2, or 250 m spatial resolution with domain size greater than 10^2 km^2.

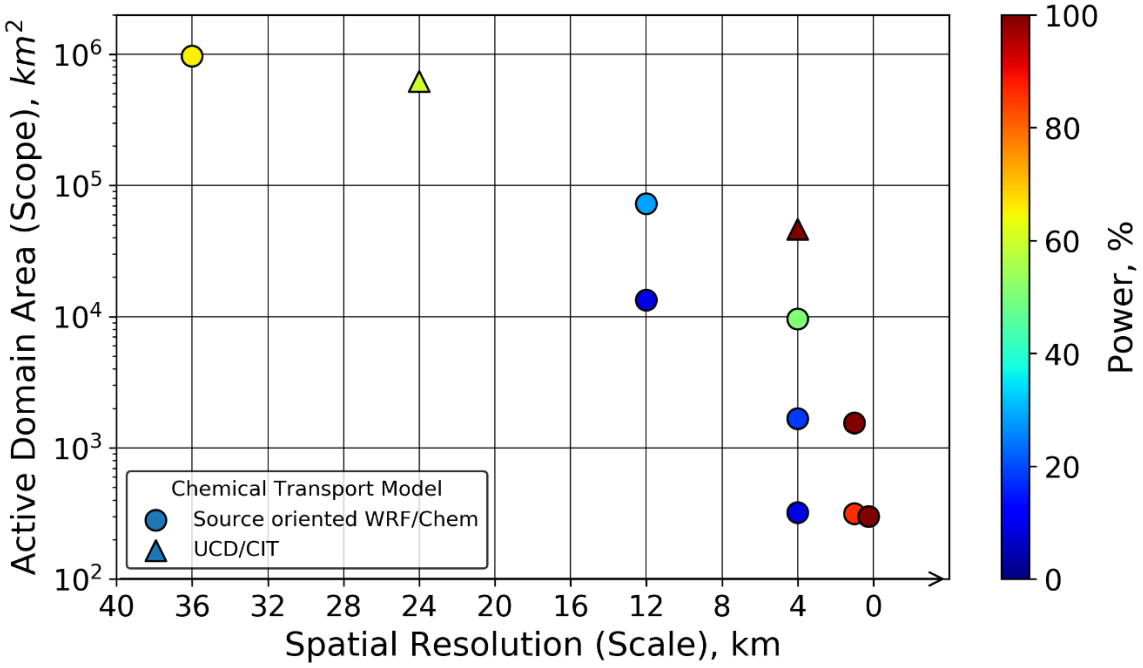

Figure 3-6. Power of detecting a 0.5 $\mu g/m^3$ maximum exposure disparity between groups for each combination of spatial resolution and domain scope, *including both source oriented WRF/Chem (dot) and UCD/CIT (triangle) CTM results. A power of 90% indicates that there is a 90% probability of correctly concluding that exposures are different between the groups.*

3.4.Discussion

Increasing the spatial resolution of CTM calculations should increase the accuracy of the predicted concentration fields. In the current study, simulations with higher spatial resolution were able to better resolve sharp spatial gradients downwind of major transportation corridors and large point sources. Model performance improved by approximately 5% when the spatial resolution was increased from 4 km to 1 km; model performance improved an additional approximately 4% when the spatial resolution was increased from 1 km to 250 m. This overall approximately 9% increase in model performance must be weighed against the need to reduce the spatial domain size from approximately 10,000 km^2 (4 km resolution) to approximately 320 km^2 (250 m resolution) in order to keep the computation burden manageable. The limited coverage of the 250 m simulations reduces the population in the study region and it prevents an analysis of the concentration gradients that occur over lengths of 100's of km.

Envrionmental disparities by race/ethnicity groups and poverty groups were done at nine resolution-domain combinations. A regional analysis with 4 km or 1 km spatial resolution appears to bring EJ issues into focus across the different scales in Southern California. In the current study, 4 km spatial resolution with a domain size greater than 10^4 km^2 or 1 km spatial resolution with domains size greater than 10^3 km^2 identify $PM_{2.5}$ exposure disparities as large as 17.5% that translates into a 30% increase in the mortality risk ratio. The air pollution domains balance the accuracy of model predictions vs. measurements, they include populations in all important subregions, and they maximize the accuracy of the exposure distributions across all socio-economic groups.

The statistical power for each domain-resolution combination calcualted in the current study is determined by the spatial distribution of pollution and the demographics of regional housing patterns within each doman. The shape of the relationship between statistical power vs. domain-resolution identified in the current study is expected to be typical for other regions, but the exact thresholds for achieving a target level of statistical power at a relevant level of exposure disparity will need to be recalculated for each new study domain. The current study provides a single data point that fine-scale spatial resolution below 1km

may not be needed (or even optimal if it requires diminished domain size). Similar studies should be carried out in other geographic regions in order to determine the appropriate CTM domain size and spatial resolution for EJ assessment in the context of their spatial distributions for race and income.

Chapter 4.
Adoption of Low-Carbon Fuels Reduces Race/Ethnicity Disparities in Air Pollution Exposure in California

4.1. Introduction

Exposure to atmospheric pollutants such as airborne particles with diameter less than 2.5 μm ($PM_{2.5}$) is estimated to cause 3.3 million premature deaths per year worldwide (Lelieveld et al., 2015b). The majority of this excess mortality occurs in heavily populated regions of Asia, but even cleaner regions in North America and Europe experience a public health burden associated with air pollution (Organization, 2021; Strak et al., 2021). Numerous environmental justice (EJ) studies have shown that lower socio-economic classes in the United States experience higher levels of air pollution, which subjects them to a lifetime of health risk (Anderson et al., 2018b; Bravo et al., 2016; Colmer et al., 2020; Cushing et al., 2015; Liu et al., 2021; Miranda et al., 2011; Tessum et al., 2021; Thakrar et al., 2020). This exposure disparity can come from many different sources of air pollution, including transportation (Gunier et al., 2003; Houston et al., 2014; Rowangould, 2013), food cooking (Shah et al., 2020), residential combustion (Tessum et al., 2019), electricity (Thind et al., 2019) and industrial facilities (Perlin et al., 2002). Exposure to poor air quality at any stage of life is associated with a variety of health problems that burden our collective health care system and reduces our economic output. A sustainable future in an increasingly globalized and competitive world requires that we minimize costs for avoidable illness to help all people reach their full potential regardless of their socio-economic class.

Energy consumption across the economy is inherently associated with air pollution, linking the issues of climate change and air quality. A recent study suggests that global air pollution mortality could double by the year 2050 under a business-as-usual (BAU) energy scenario (Lelieveld et al., 2015b). Many previous studies have estimated health co-benefits of various GHG reduction pathways, including adopting carbon capture and sequestration (CCS) technology, limiting bioenergy, using renewable energy in electricity generation, and reducing fossil fuels in power plants (Dimanchev et al., 2019; Markandya et al., 2018; Ramaswami et al., 2017; Sampedro et al., 2020; Wang et al., 2020; West et al., 2017; Zapata et al., 2018a). Global reductions in GHG emissions have been estimated to reduce premature mortality by 17%-23%. The health co-benefits in many scenarios exceed the mitigation costs. India and China obtain greater co-benefits than other countries (Markandya et al., 2018; Sampedro et al., 2020), but impressive life-saving and health co-benefits were also demonstrated in the US by adopting the United States (US) Clean Power Plan (Driscoll et al., 2015; Levy et al., 2016), sub-national renewable energy policies (Dimanchev et al., 2019) and multi-sector GHG mitigation pathway (Zhang et al., 2017, 2016). However, these same studies also concluded that air quality improvements and health co-benefits varied significantly by region, suggesting that location-specific analyses may be warranted.

California is the most populous state / province in North America, has the largest sub-national economy in the world, and is home to six out of the ten most polluted cities in the US based on annual-average $PM_{2.5}$ concentrations (American Lung Association, 2019). California is leading North America in the adoption of new sustainable energy sources to mitigate climate change. State law AB32 commits California to reduce GHG emissions to 1990 levels by 2020 (California Air Resource Board, 2006); California Governor's Executive Order S-3-05 commits California to an additional 80% reduction by 2050 (Gov Arnold Schwarzenegger, 2005). This massive reduction in GHG emissions will require a transformation in the energy system that will involve choices about technological, fuel and energy resources. All of these choices will fundamentally change the patterns of air pollution exposure in California. Multiple previous studies have evaluated the health co-benefits that can be achieved under various GHG mitigation pathways (Kleeman et al., 2013; Wang et al., 2020; Zapata et al., 2018a; Zhao et al., 2019), but very few

studies have explicitly explored the intersection of GHG emissions reductions, air pollution exposures, and racial disparities in exposure.

Here we conduct a comprehensive analysis of health co-benefits, racial disparities, and source / composition in air pollution exposure under six future energy scenarios and four future meteorology scenarios in California. Air pollution exposure is calculated for four racial groups defined by the American Community Survey (ACS): Black, Hispanic, Asian, and White (United State Census Bureau, 2020). Public health benefits associated with reduced air pollution in different energy scenarios are calculated using standard epidemiological relationships (US EPA, 2021). Energy scenarios are identified that reduce the racial disparity in air pollution exposure and total population exposure. The most promising strategies / emissions sources to reduce future racial disparities / total population exposure to air pollution are then discussed.

4.2. Methodology

4.2.1. Energy Scenarios

Future energy scenarios for California are described in detail by Li et al.(Yin Li et al., 2022) and so only a brief summary is presented in here. All energy scenarios were created using the CA-TIMES energy economic model (McCollum et al., 2012; Yang et al., 2015) that predicts the statewide least-cost technology mix across all energy sectors in California to achieve target GHG reductions subject to external policy constraints. Three energy scenarios achieved the objective of an 80% reduction in GHG emissions relative to 1990 levels, while the remaining scenarios achieved lower reductions. Table *4-1* summarizes the major features of each energy scenario.

Table 4-1. Energy scenarios descriptions

Scenario Name	Description
BAU	A business-as-usual scenario that includes current regulations and future growth projections.
GHGAi	A strict GHG reduction scenario that achieves 80% reduction of GHG emission (relative to 1990 levels) by the year 2050. More than 60% of California's primary energy supplied by renewables including biomass, wind, and solar.
2030CAP	A loose GHG reduction scenario that meets current policy references but only achieves a 40% GHG reduction by the year 2030 with no further reductions thereafter.
CCS	A scenario that allows for more combustion to generate electricity by focusing on adoption of carbon capture and sequestration technology. Meets the 80% GHG reduction target by counting "negative emissions" from carbon capture technology.
NGB	A variation of the GHGAi scenario that allows for 20% more natural gas combustion for residential and commercial buildings.
NGT	A variation of the GHGAi scenario that allows for 20% more natural gas combustion for electricity generation

Criteria pollutant emissions with 4km spatial resolution associated with each energy scenario were calculated with the CA-REMARQUE model (Yin Li et al., 2022). CA-REMARQUE applies tailored procedures for each energy sector in California to estimate how the adoption of low-carbon fuels will modify criteria pollutant emissions. Emissions from the production and combustion of bio-fuels incorporate the latest measurement data available in the literature.

4.2.2. Meteorological Scenarios

Meteorological scenarios were produced using the Weather Research and Forecast (WRF) model v3.4 (NACR, 2012) based on initial and boundary conditions predicted by the Community Climate System Model (CCSM) (Gent et al., 2011) and the Canadian Earth Systems Model (CanESM) (Swart et al., 2019). The global climate scenarios associated with Representative Concentration Pathway 4.5 (RCP4.5) and RCP8.5 were selected for both CCSM and CanESM, yielding four different meteorological scenarios. Thirty vertical layers were used up to a top height of approximately 15 km. The maximum spatial resolution

of the results used in the present analysis was 4km. Thirty-two weeks were randomly selected for study across the ten-year window from 2046 to 2055. Sensitivity analysis indicates that the average air pollution concentrations predicted over this thirty-two week sample captures the long-term average concentrations with a standard error of 0.23 $\mu g\ m^{-3}$ in the presence of the El Nino Southern Oscillation (ENSO).

4.2.3. Air Quality Simulations

Air quality simulations were performed using the UCD/CIT chemical transport model (Kleeman and Cass, 2001a; Ying et al., 2007). Three nested domains were used to cover all of California at 24 km resolution, Southern California at 4 km resolution, and Central / Northern California with 4 km resolution. Fifteen telescoping vertical levels were used up to a total height of 5 km with the first ten levels in the lowest 1 km of the atmosphere. Numerous previous studies have demonstrated the suitability of this model configuration when simulating historical pollution events in California (Hu et al., 2017, 2015, 2014; Laurent et al., 2014; Li et al., 2020; Mahmud et al., 2012; Ostro et al., 2015).

All simulations used the SAPRC11 chemical mechanism to predict oxidant concentrations and the formation of photochemical products including ozone (O_3), acids such as nitric acid (HNO_3), and semi-volatile organic species. The condensation of inorganic salts such as ammonium nitrate (NH_4NO_3) was predicted using the ISSOROPIA thermodynamic routine (Fountoukis and Nenes, 2007) coupled with the APCD gas-particle partitioning scheme (Jacobson, 2010). The formation of secondary organic aerosol (SOA) was simulated using an n-product model tuned to account for vapor wall losses during smog chamber experiments (Cappa et al., 2016). The ability of the modeling system to accurately predict $PM_{2.5}$, $PM_{0.1}$, and particle number concentrations at locations across California is described in detail by Yu et al. (Yu et al., 2019).

4.2.4. Socio-economic data

Socio-economic data from the American Community Survey (ACS) 2012-2016 (United State Census Bureau, 2020) was used to calculate air pollution exposure for different race/ethnicity groups in California.

The ACS dataset includes race/ethnicity information for Black (Black & African American alone), Hispanic (Hispanic or Latino, regardless of race), Asian (Asian alone), and non-Hispanic White (White, not Hispanic or Latino) at the census tract level. The future EJ analysis focuses on four geographic regions across California: (i) Los Angeles (LA), (ii) San Diego (SD), (iii) San Joaquin Valley (SJV), and (iv) the San Francisco Bay Area & Sacramento (SFBA & SAC). The population densities of each race within each of these geographic regions are shown in Figure S1-S10. These four regions include more than 90% of California's population, making the EJ analysis in current study representative of the entire state.

Table *4-2* shows the race/ethnicity composition of the population in each geographic region analyzed in the current study. Black & African American residents account for 4-6% of the total population in each region, Asian residents account for 6-20% of the total population, White residents account for 30-48% of the total population, and Hispanic residents account for 26-54% of the total population. Figures S3-1 to S3-10 in Appendix 3 show that some race/ethnicity groups are clustered in sub-regions of each domain. Specifically, Black & African American residents are clustered into neighborhoods south of central Los Angeles, and Asian residents are clustered into neighborhoods in Oakland. These clustering effects have a significant impact on the air pollution exposure for race/ethnicity groups.

Table 4-2. Socio-economic data summary

	Population				Percentage			
Region	LA[a]	SFBA & SAC[b]	SJV[c]	SD[d]	LA	SFBA & SAC	SJV	SD
All	14,384,814	11,299,258	2,526,861	2,967,636				
Black[1]	920,808	674,400	99,250	146,401	6.40%	5.97%	3.93%	4.93%
Hispanic[2]	6,690,133	2,921,051	1,364,228	934,465	46.51%	25.85%	53.99%	31.49%
Asian[3]	2,141,542	2,287,506	159,652	357,288	14.89%	20.24%	6.32%	12.04%
White[4]	4,270,607	4,901,766	853,299	1,420,956	29.69%	43.38%	33.77%	47.88%

[1] Black and African American; [2] Hispanic or Latino, regardless of races; [3] Asian Alone; [4] non-Hispanic White

[a] Los Angeles; [b] San Francisco Bay Area & Sacramento; [c] San Joaquin Valley; [d] San Diego

4.2.5. Population exposure, environmental justice, and health co-benefits calculations

$PM_{2.5}$ and $PM_{0.1}$ population weighted concentrations (PWC) were calculated for total population and each race/ethnicity group under an ensemble of six energy scenarios and four meteorological scenarios in four sub-regions in California. Absolute/relative exposure and absolute disparity by race/ethnicity were analyzed to show the ability of each scenario i) to reduce air pollutants exposure for all residents; and ii) to mitigate the exposure disparity between races/ethnicities. Results are shown in Section 4.3.1 and 4.3.2.

The health co-benefits of $PM_{2.5}$ and $PM_{0.1}$ within each member of the ensemble was calculated using the Environmental Benefits Mapping and Analysis Program – Community Edition (BenMap-CE) v1.4.8 developed by US EPA (US EPA, 2021). The BAU scenario was used as a baseline and the GHGAi, 2030CAP, CCS, NGB and NGT were used as controls in the BenMap analysis. Four health impact functions were analyzed, including Krewski et al., 2009, Laden et al., 2006, Lepeule et al., 2012 and Pope et al., 2002 (Krewski et al., 2009; Laden et al., 2006; Lepeule et al., 2012; Pope et al., 2002). Economic benefits were then calculated with the value of a statistical life (VSL) of $7.6M. Results are shown in Section 4.3.3.

Emissions source contributions to $PM_{2.5}$ / $PM_{0.1}$ exposure were analyzed for each scenario, race/ethnicity, and region. Nine emissions source sectors were used in this study, including i) tire & brake wear; ii) on-road mobile tailpipe; iii) off-road equipment; iv) aircraft & marine vessels; v) residential & food cooking; vi) electricity generation; vii) fuel supply that depends on the energy scenario; viii) fuel supply that doesn't change with scenarios; and ix) biomass burning & construction dust (wildfires are excluded due to inherent uncertainty about location and timing). Further details of the emissions patterns associated with each sector under each scenario are discussed by Li et al. (Yin Li et al., 2022). Results are shown in Section 4.3.4. The further investigation of impacts of each source contribution to total PWC and EJ are presented in Section 4.3.5.

4.3. Results

4.3.1. Absolute exposure

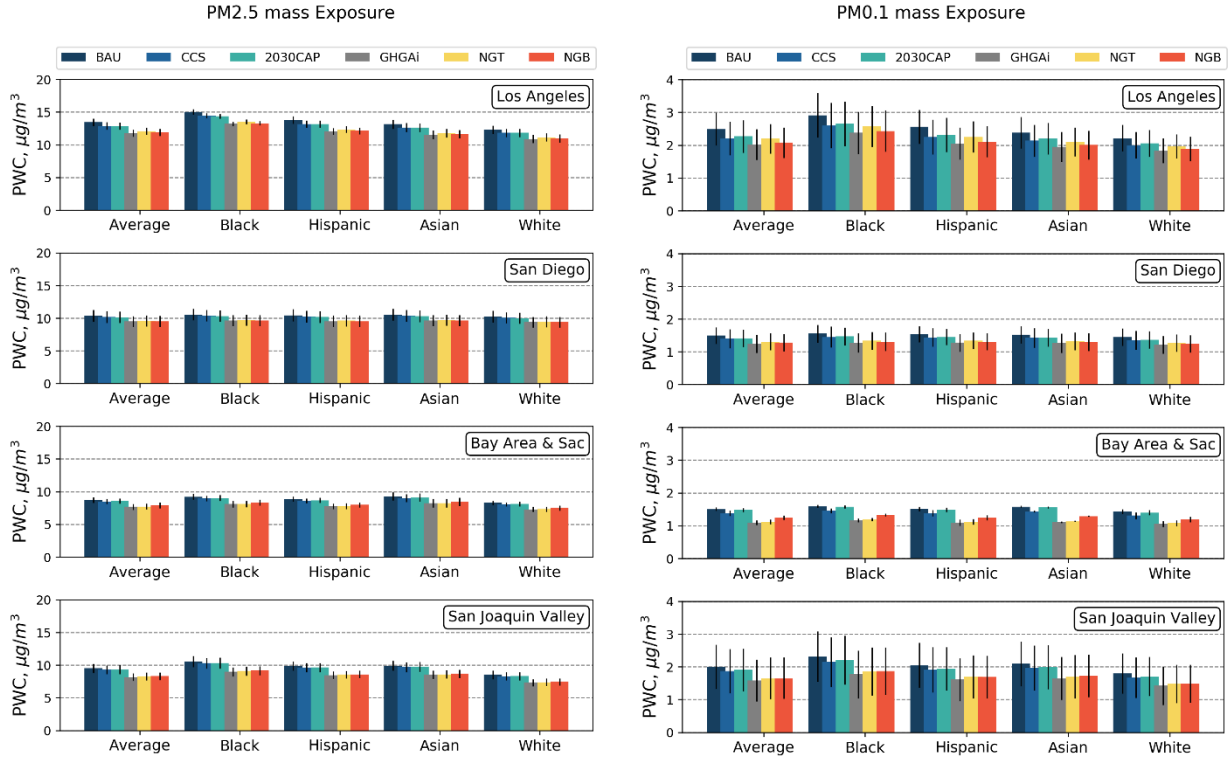

Figure 4-1. Future year (2050) PM2.5 (left) and PM0.1 (right) Population Weighted Concentrations (PWC) by energy scenario and race/ethnicity across four regions in California. *Each bar and associated uncertainty range represents the average and standard deviation across four meteorological scenarios (CCSM8.5, CCSM4.5, CAN8.5, CAN4.5).*

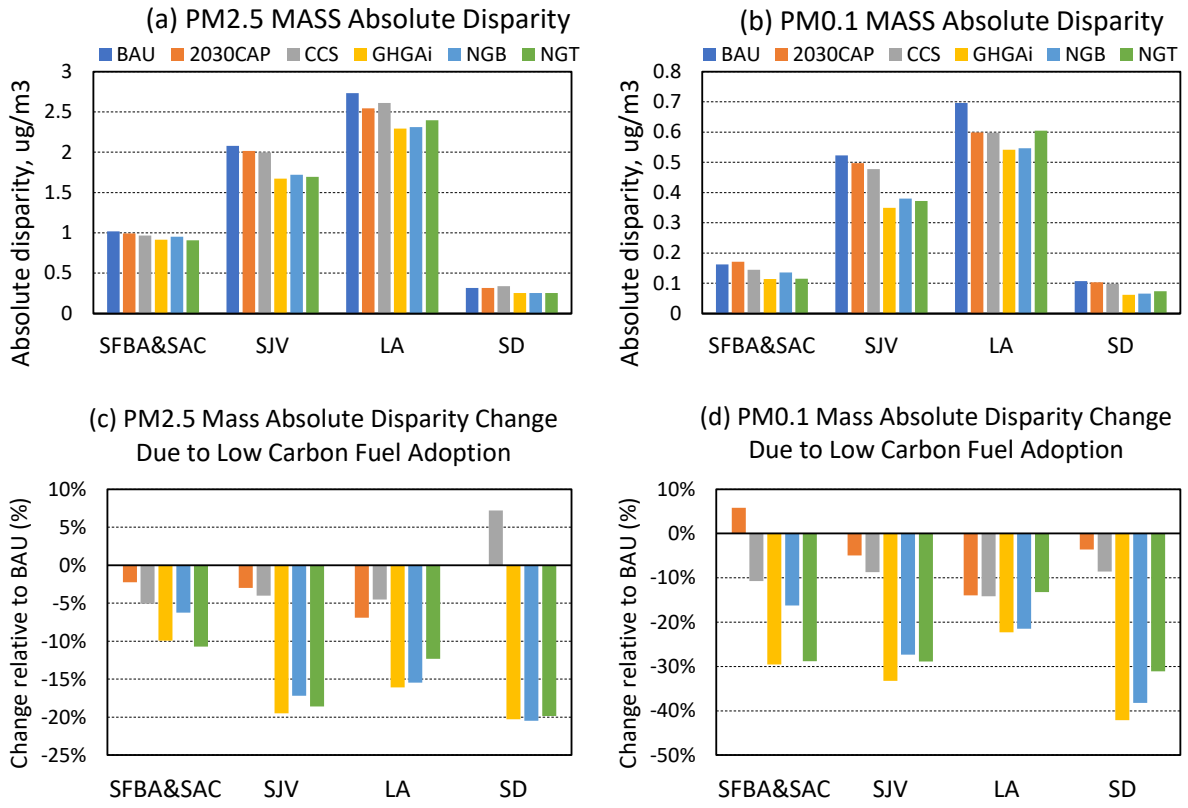

Figure 4-2. Change in $PM_{2.5}$ mass and $PM_{0.1}$ mass absolute exposure disparities under different future energy scenarios. *Absolute exposure disparities between race/ethnicity groups were calculated as the difference between the group with the highest exposure concentration and the group with the lowest exposure concentrations. Top panels show absolute values of population-weighted concentrations, while bottom panels show changes relative to the BAU scenario.*

Figure *4-1* shows population-weighted concentrations (PWC) for $PM_{0.1}$ and $PM_{2.5}$ mass in four different California regions: Los Angeles, San Diego, the Bay Area & Sacramento, and the San Joaquin Valley. Results for individual race/ethnicity groups and for the average across all groups are shown for each energy scenario. All exposure concentrations were averaged across the four meteorology scenarios, with uncertainty bars shown to represent one standard deviation between the meteorological scenarios. Meteorological variability influences $PM_{0.1}$ and $PM_{2.5}$ mass concentrations but does not significantly affect comparisons between different energy scenarios. The absolute exposure concentrations for individual meteorological scenarios are provided in Appendix 3 Figure S3-11 to S3-18.

Both $PM_{2.5}$ and $PM_{0.1}$ absolute exposure concentrations vary across regions. The highest $PM_{2.5}$ and $PM_{0.1}$ concentrations are predicted to occur in Los Angeles, followed by the San Joaquin Valley, with lower absolute exposure concentrations predicted in San Diego and the Bay Area & Sacramento. Averaged across all energy scenarios, $PM_{2.5}$ absolute exposure ranges from 8.2 $\mu g/m^3$ to 12.5 $\mu g/m^3$, $PM_{0.1}$ absolute exposure ranges from 1.3 $\mu g/m^3$ to 2.2 $\mu g/m^3$.

The choice of future energy scenario influences the absolute PWC for $PM_{2.5}$ and $PM_{0.1}$. Absolute PWCs of both $PM_{2.5}$ and $PM_{0.1}$ are highest in the BAU scenario and lowest in the GHGAi scenario for all regions. The $PM_{2.5}$ exposure concentrations in the CCS and 2030CAP scenarios are only slightly lower than the concentrations in the BAU scenario. The $PM_{2.5}$ exposure concentrations in the NGT and NGB scenarios are slightly higher than the concentrations in the GHGAi scenario.

$PM_{0.1}$ exposure concentrations are more variable than $PM_{2.5}$ exposure concentrations on a relative scale across energy scenarios and geographical regions. For example, NGT produces 8.2% / 5.5% higher $PM_{0.1}$ exposure than GHGAi / NGB in Los Angeles, but the corresponding relative increase in $PM_{2.5}$ concentrations is only 2.3% / 1.6%. In the San Francisco Bay Area and Sacramento, NGB increases $PM_{0.1}$ exposure by 12% / 10% compared to GHGAi / NGT, but corresponding increases to $PM_{2.5}$ exposure are only 2.7% / 2.5%. Thus, relative changes to $PM_{0.1}$ concentrations across energy scenarios can be as much as four times greater than relative changes to $PM_{2.5}$ concentrations. These results once again reflect the greater variability of $PM_{0.1}$ emissions than $PM_{2.5}$ emissions across different energy scenarios (Yin Li et al., 2022; Zapata et al., 2018b).

Absolute exposure disparities are commonly used to quantify the severity of an environmental justice problem (Clark et al., 2017; Harper et al., 2013b; Liu et al., 2021; Paolella et al., 2018). Absolute exposure disparities between race/ethnicity groups were calculated as the difference between the group with the highest exposure concentration (minority) and the group with the lowest exposure concentrations. The lowest exposure group was consistently White residents in this study. Exposure disparities for PM2.5 concentrations exist in all geographical regions within California, with the maximum value predicted in

Los Angeles and the minimum value predicted in San Diego (see Figure 4-2). Locations with high exposure disparity have neighborhoods dominated by one race/ethnicity group with air pollution concentrations that are significantly different from regional average concentrations.

Trends in absolute exposure disparities across energy scenarios are similar to the trends in the underlying $PM_{2.5}$ and $PM_{0.1}$ absolute exposure concentrations. None of the clean fuel energy scenarios can eliminate environmental disparity in the future year 2050, but adoption of low-carbon energy sources in the year 2050 reduces the race/ethnicity disparity in air pollution exposure in California by as much as 20% for $PM_{2.5}$ mass and by as much as 40% for $PM_{0.1}$ mass (see Figure 4-2). Deeper reductions in the carbon intensity of energy sources progressively reduced exposure to $PM_{2.5}$ mass and $PM_{0.1}$ mass for all California residents. The greater adoption of low-carbon fuels also reduced the race/ethnicity disparity in the PM exposure. The three energy scenarios that achieved an ~80% reduction in GHG emissions relative to 1990 levels (GHGAi, NGB, NGT) simultaneously produced the greatest reduction in PM exposure for all California residents and the greatest reduction in the race/ethnicity disparity of that exposure. The energy scenarios that allow continued use of combustion to generate a substantial fraction of California's energy demand (2030CAP, CCS) typically produce less than half of the reduction in absolute exposure disparities.

4.3.2. Relative exposure

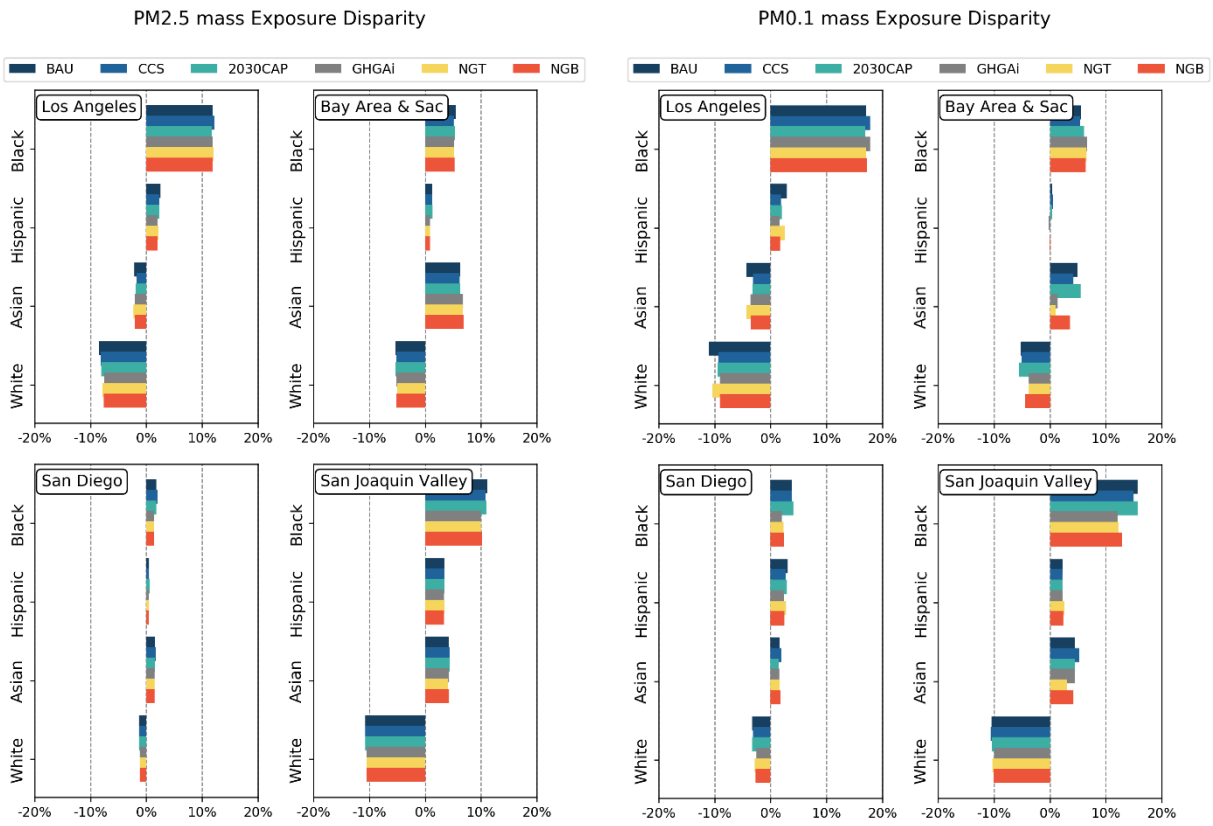

Figure 4-3. Future year (2050) PM2.5 mass (left) and PM0.1 mass (right) exposure disparity (relative to total population) by scenario and race/ethnicity across four regions in California. *Each bar represents the average across four meteorological scenarios (CCSM8.5, CCSM4.5, CAN8.5, CAN4.5).*

Figure *4-3* shows the $PM_{2.5}$ and $PM_{0.1}$ exposure disparity (relative to average exposure) for Black & African American, Hispanic, Asian, and non-Hispanic White residents in different geographic regions within California. Results are averaged across all meteorological scenarios but shown individually for all energy scenarios. Details of each meteorology scenario are shown in Figure S3-19 to S3-26 in Appendix 3. Relative exposure disparities greater than zero indicate that the race/ethnicity group has greater-than-average exposure, while relative exposure disparities less than zero indicate that the race/ethnicity group has less-than-average exposure. Black & African American residents experienced higher-than-average exposure to $PM_{2.5}$ and $PM_{0.1}$ in all future energy scenarios in all study regions (Los Angeles, San Francisco, Sacramento, San Diego, and the San Joaquin Valley). Asian residents in San Francisco experienced higher-than-average exposure to air pollution in all future energy scenarios. Peak exposure disparities reached ~10%

for $PM_{2.5}$ and ~20% for $PM_{0.1}$. White residents experience lower-than-average exposures in all regions, with peak disparity values of approximately -10% for both $PM_{2.5}$ and $PM_{0.1}$. Hispanic residents generally experience exposure concentrations that are close to average. Asian residents experience lower-than-average $PM_{2.5}$ exposure concentrations in Los Angeles but higher-than-average exposure concentrations in the San Francisco Bay Area and Sacramento.

The results summarized in Figure *4-3* reflect the spatial distribution of each race/ethnicity group within each geographic region. Black & African American residents in California are clustered into neighborhoods near the center of urban cores or near major transportation corridors where air pollution emissions are higher. The historical policies that have produced these housing patterns are beyond the scope of the current study, but interested readers are referred to studies on the effects of "redlining" (see for example (Nardone et al., 2020; Zenou and Boccard, 2000)). Due to their proximity to higher emissions, Black & African American residents often experience higher-than-average exposure concentrations. White residents are more dispersed in suburban neighborhoods that are further away from urban cores. This housing pattern leads to lower-than-average exposure for White residents. Asian residents are clustered near urban cores in Northern California (such as downtown San Francisco, San Jose, etc.) leading to higher-than-average exposure concentrations. Asian residents are dispersed in suburban neighborhoods in Southern California, leading to lower-than-average exposure concentrations in this sub-region. The contrast between exposure concentrations for Asian residents living in Northern California vs. Southern California emphasizes the importance of the distance between the home address and the urban core when calculating exposure concentrations.

4.3.3. Health Co-benefits

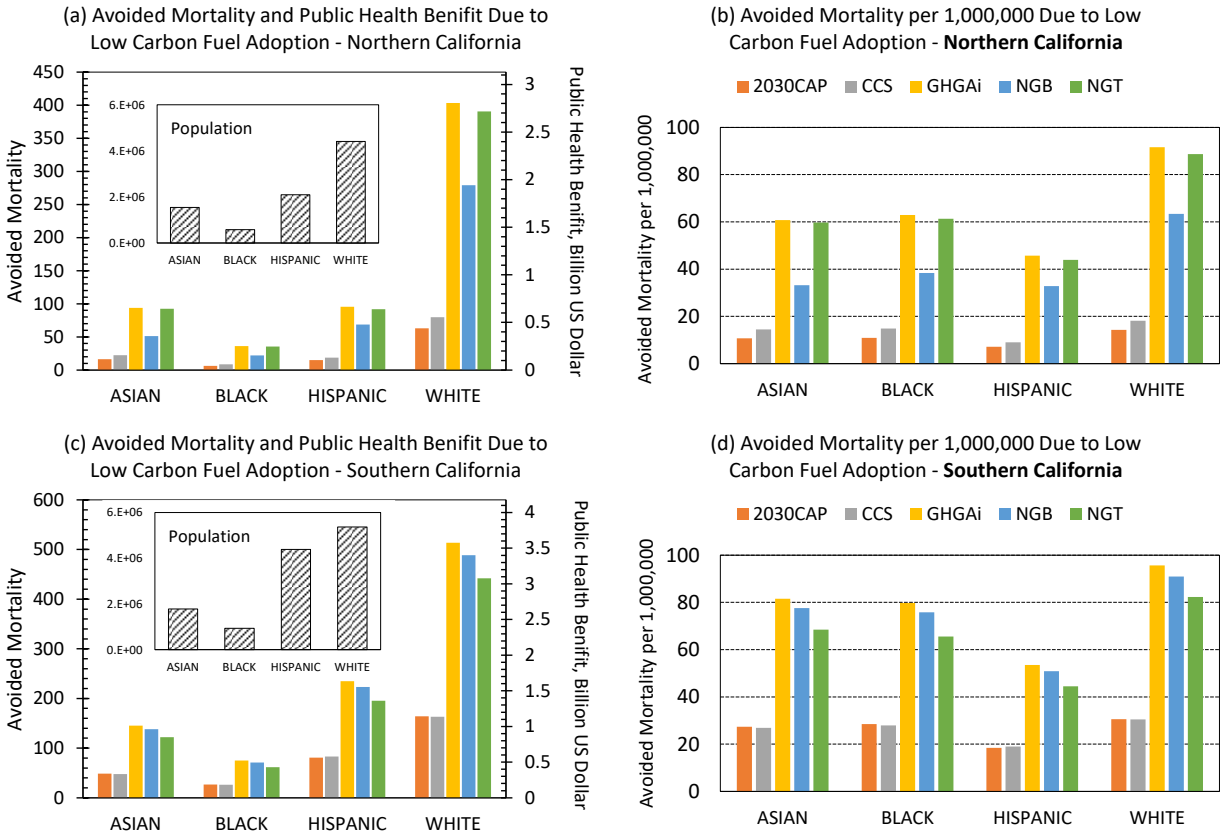

Figure 4-4. Avoided mortality and public health benefits associated with low-carbon energy scenarios (relative to the BAU scenario) in Northern California (SFBA&SAC, SJV) and Southern California (LA, SD). Public health benefits calculated using Value of a Statistical Life (VSL) estimated to be $7.6M in the year 2050.

Figure 4-4 quantifies the avoided mortality and public health benefits associated with each energy scenario. Health benefits per 1M residents are similar for Asian and Black & African American residents, slightly lower for Hispanic residents, and slightly higher for White residents (see right panel Figure 4-4). These patterns reflect the spatial distribution of the population comprising each racial group relative to the average air pollution exposure fields. Total health benefits for each racial category expressed as avoided mortality and public health savings (billions of USD) are calculated by multiplying average health benefits by total population (see left panel of Figure 4-4). Energy scenarios with deeper cuts to GHG emissions produce greater public health benefits for all racial categories.

4.3.4. Source contributions

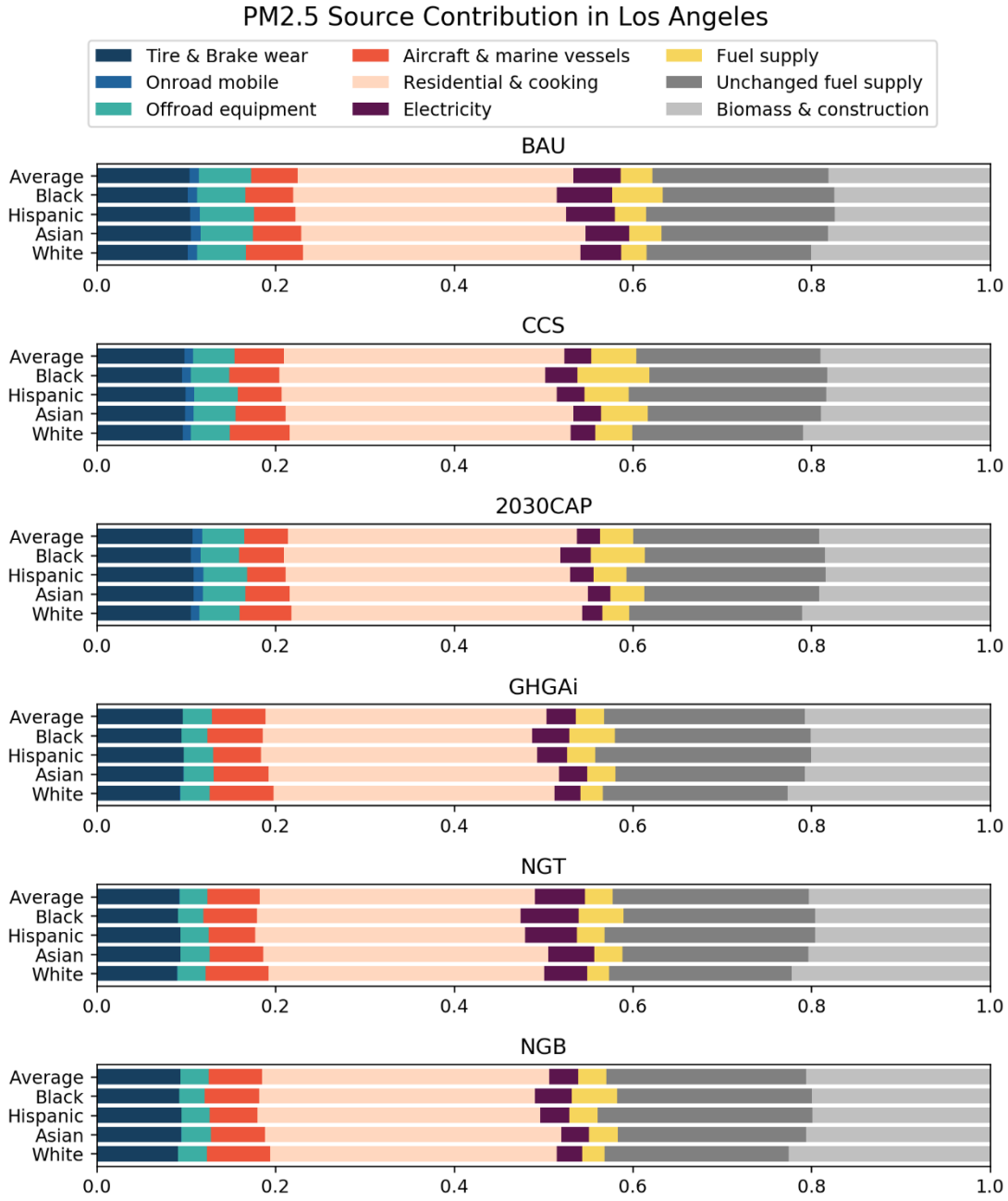

Figure 4-5. *PM2.5 source contributions in Los Angeles area by energy scenarios and race/ethnicity. Each value represents the average across four meteorological scenarios.*

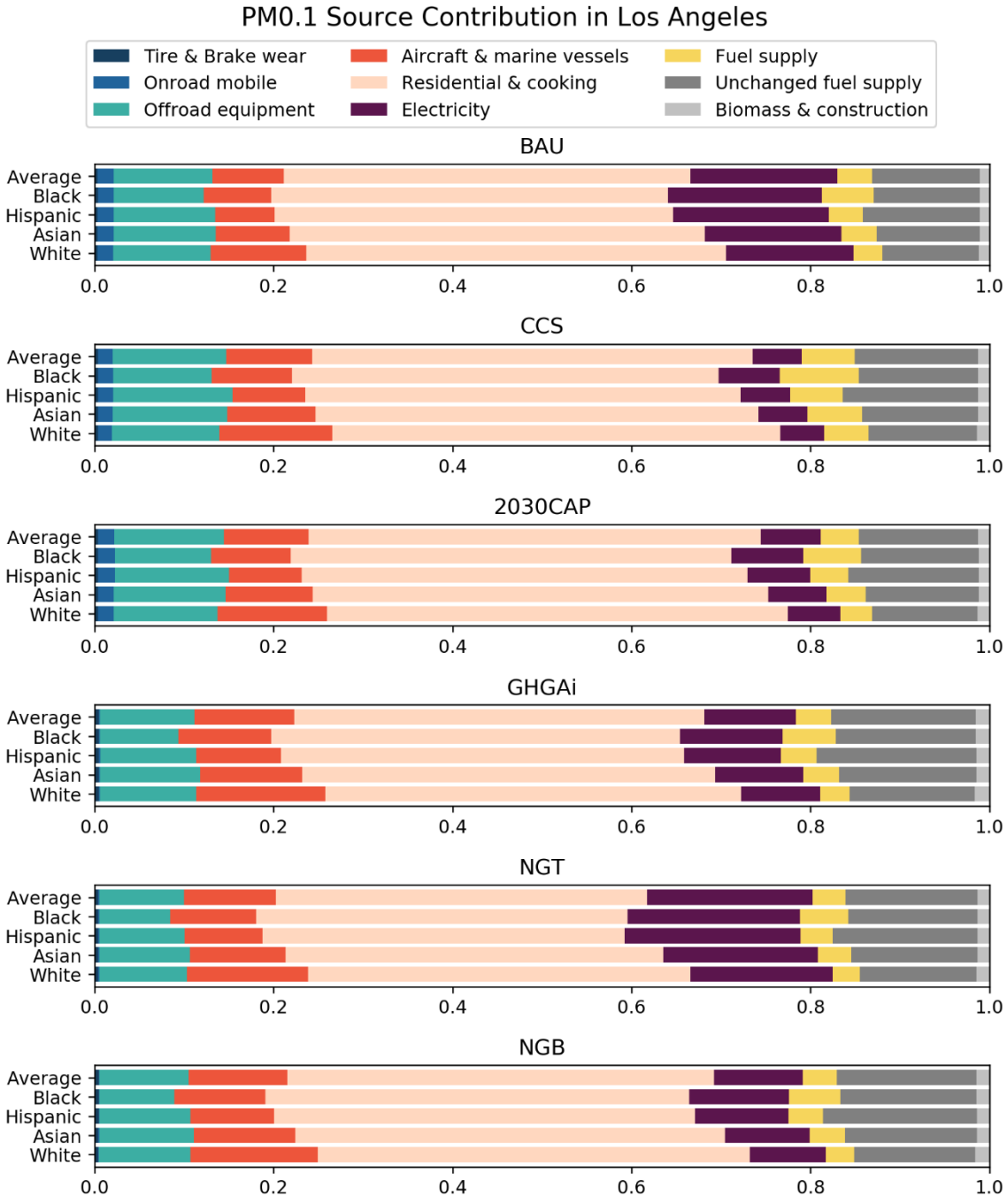

Figure 4-6. PM0.1 source contributions in Los Angeles area by energy scenarios and race/ethnicity. Each value represents the average across four meteorological scenarios.

Figure *4-5* and Figure 4-6 show predicted exposure to primary sources of $PM_{2.5}$ and $PM_{0.1}$ for different race/ethnicity groups in Los Angeles under the six different energy scenarios. The X-axis in Figure *4-5* and 4-6 represents the primary contribution from each source to the total PM exposure. Similar plots for

other geographic regions are shown in Figure S3-27 to S3-32 in Appendix 3. All results are based on the average of the four meteorological scenarios since trends within each meteorological scenario were consistent.

Different sources dominate exposure to $PM_{2.5}$ vs. $PM_{0.1}$. Tire & brake wear, residential & cooking, unchanged fuel supply, and construction dust are the major sources for $PM_{2.5}$. Emissions from these sources generally do not change significantly between energy scenarios, and so the predicted $PM_{2.5}$ source contributions are relatively constant across Figure *4-5*. Off-road equipment, residential & cooking, electricity generation, and unchanged fuel supply are the major sources of $PM_{0.1}$ exposure. The fuels used for off-road equipment and electricity generation change significantly between energy scenarios, and so there is significant variability in $PM_{0.1}$ source contributions illustrated in Figure 4-6. $PM_{0.1}$ concentrations are dominated by primary emissions (Hu et al., 2014) leading to sharper spatial gradients (Karner et al., 2010). $PM_{0.1}$ concentrations are therefore influenced by local emissions to a larger degree than $PM_{2.5}$ concentrations, making the spatial distribution of each race/ethnicity group more important when determining exposure concentrations.

It is noteworthy that residential & cooking emissions are a dominant source for both $PM_{2.5}$ and $PM_{0.1}$. These emissions are related to human activities, and they are located close to residences, leading to higher intake fractions (Evans et al., 2002; Marshall et al., 2005, 2003). Targeted reductions for residential & cooking sources could be used to reduce future PM concentrations.

4.3.5. Potential for Further Improvements

The GHGAi scenario improves public health, but it does not completely eliminate race/ethnicity disparity in exposure to air pollution in California. The detailed source apportionment information embedded in the UCD/CIT model can be analyzed to identify additional measures to further reduce disparity. This analysis will use the GHGAi scenario as the most promising starting point for further improvements.

4.3.5.1 Improvements for Total Population Exposure

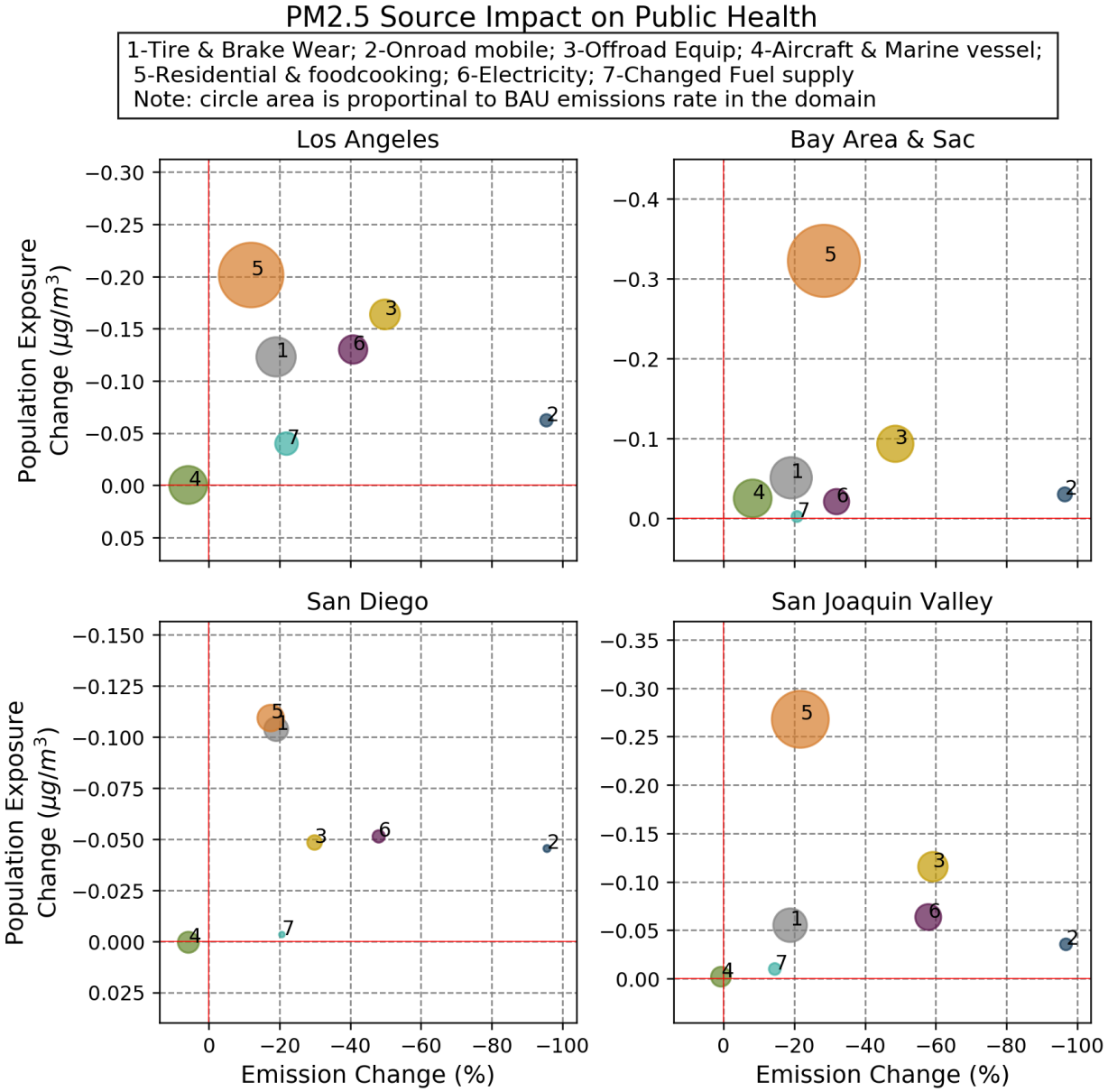

Figure 4-7. PM2.5 source impact on public health (regardless of race) for GHGAi energy scenario. X-axis indicates emissions (source) changes between BAU and GHGAi scenario. Y-axis indicates PWC changes between BAU and GHGAi scenario for specific source. All results averaged across four meteorological scenarios.

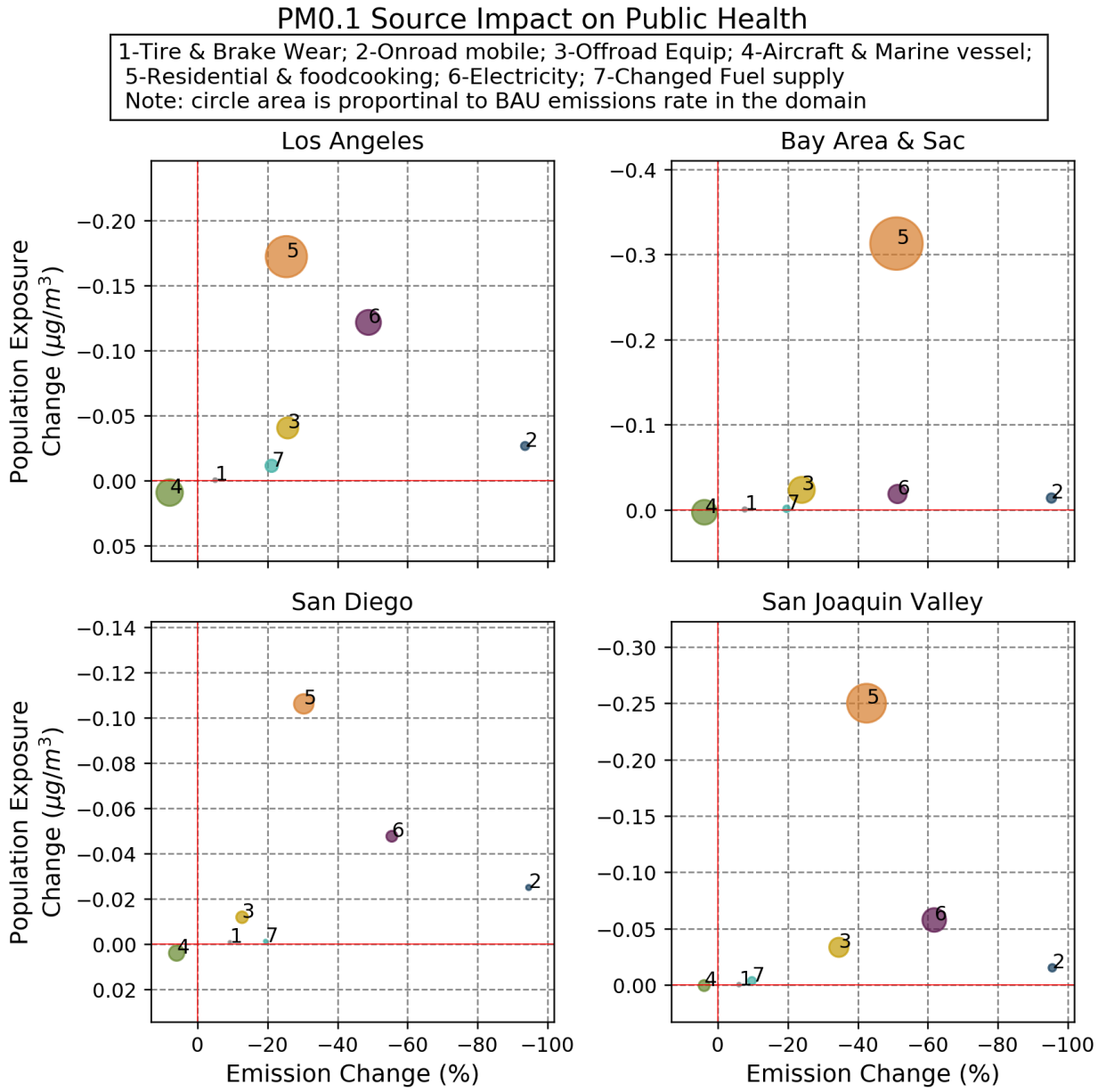

Figure 4-8. PM0.1 source impact on public health (regardless of race) for GHGAi energy scenario. X-axis indicates emissions (source) changes between BAU and GHGAi scenario. Y-axis indicates PWC changes between BAU and GHGAi scenario for specific source. All results averaged across four meteorological scenarios.

Figure 4-7 illustrates the efficiency of $PM_{2.5}$ emissions reductions in the GHGAi scenario quantified as the change in total exposure concentrations (without regard for race/ethnicity). Similar plots for other energy scenarios shown in Figure S3-33 to S3-36 in Appendix 3. The horizontal axis of each subpanel in Figure 4-7 indicates the amount of emissions reductions in the GHGAi scenario relative to the BAU scenario for each of the indicated source categories. The vertical axis of each subpanel indicates the

corresponding change in population-weighted concentration. The position of each symbol in Figure 4-7 reflects the intake fraction of the source emissions determined by the emissions location relative to the population. The size of the symbol in Figure 4-7 is proportional to the amount of $PM_{2.5}$ emissions associated with the indicated source category. Emissions from residential and food cooking sources are large, have high intake fraction, and they have been reduced by only a modest amount in the GHGAi scenario. Further reductions in emissions from residential and food cooking sources could significantly reduce $PM_{2.5}$ exposure in the future years.

$PM_{2.5}$ tailpipe emissions from on-road mobile sources undergo the greatest relative reduction in the GHGAi scenario, but the corresponding absolute reduction in population-weighted concentration is modest because tailpipe emissions from motor vehicles were already quite low in the BAU scenario due to the adoption of advanced emissions control technology. The near-total elimination of tailpipe emissions from motor vehicles achieved by converting the majority of the light-duty vehicle fleet to non-combustion power therefore has modest benefits for public health in the GHGAi scenario. It is noteworthy that tire and brake-wear emissions from mobile sources are significantly greater than tailpipe emissions in the GHGAi scenario. Further reductions from mobile sources should focus on reduced dust from braking systems (Cai et al., 2019; Gramstat, 2018) and development of new tire compounds (Dalmau et al., 2020; Fonseca et al., 2020; Panko et al., 2018) in order to further reduced $PM_{2.5}$ exposure.

Figure 4-8 illustrates the efficiency of $PM_{0.1}$ emissions reductions using the same format as Figure 4-7. Results for other energy scenarios are shown in Figure S3-37 to S3-40 in Appendix 3. Large residential and cooking emissions are once again identified as a category that has high $PM_{0.1}$ intake fraction and that has undergone only partial emissions controls in the GHGAi energy scenario. Electricity generation is the next most promising source of $PM_{0.1}$ emissions reduction, but the GHGAi scenario already controls these emissions by >50% and the intake fraction is relatively low because most electricity generation stations are located far from major population centers.

Based on Figure 4-7 and Figure 4-8, aircraft emissions have the lowest relative reduction in both $PM_{2.5}$ and $PM_{0.1}$ emissions in the GHGAi scenario, suggesting that this category could be targeted for further reductions. Such measures would reduce primary $PM_{2.5}$ / $PM_{0.1}$ (shown in Figure 4-7 + 4-8) and nucleated ultrafine particles (not shown) (Yu et al., 2019).

4.3.5.2 Improvements to Reduce Disparity across Race/Ethnicity

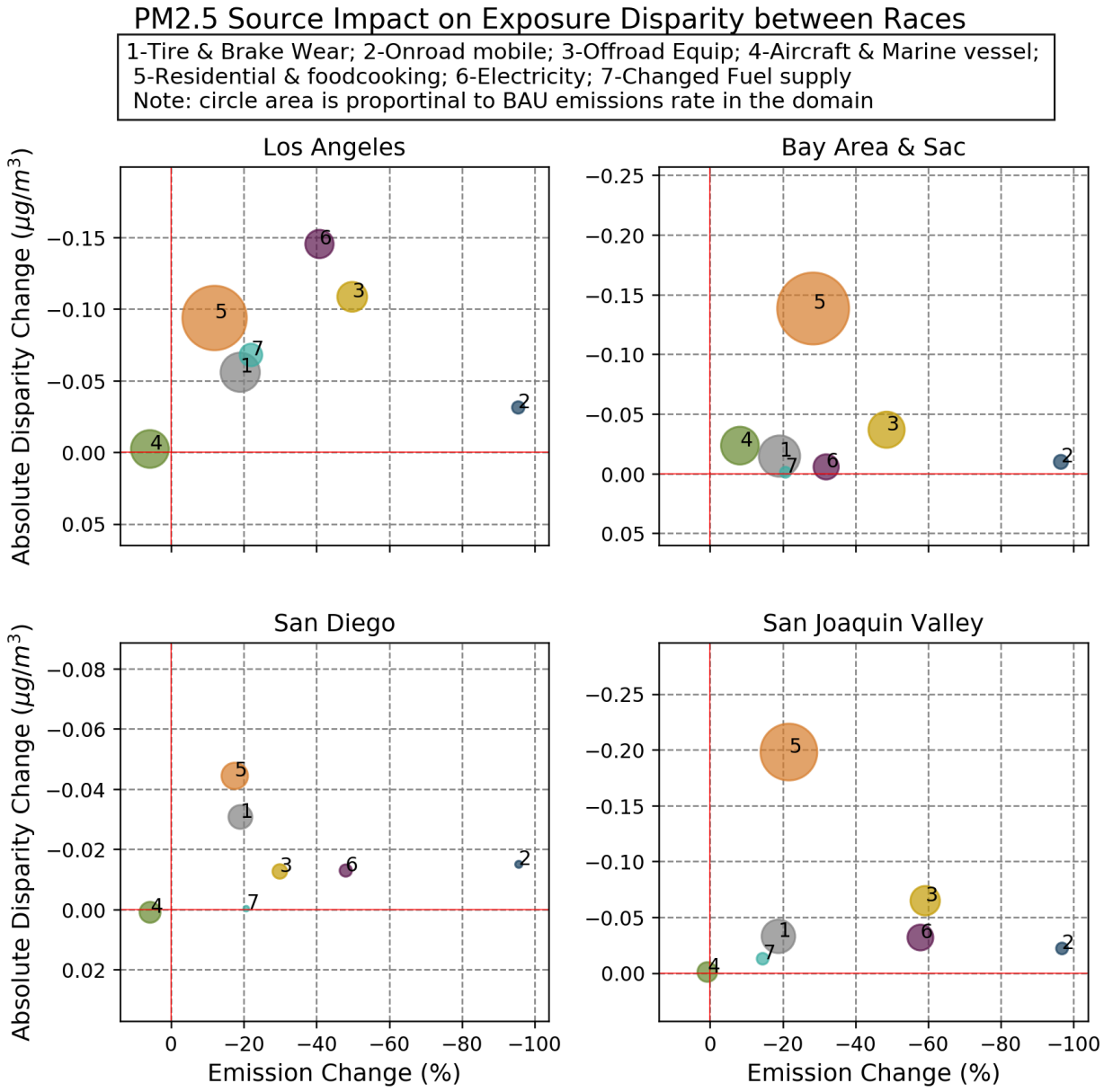

Figure 4-9. PM2.5 source impact on exposure disparity between races for GHGAi energy scenario. X-axis indicates emissions (source) changes between BAU and GHGAi scenario. Y-axis indicates emission

absolute disparity changes between BAU and GHGAi scenario for specific source. All results averaged across four meteorological scenarios.

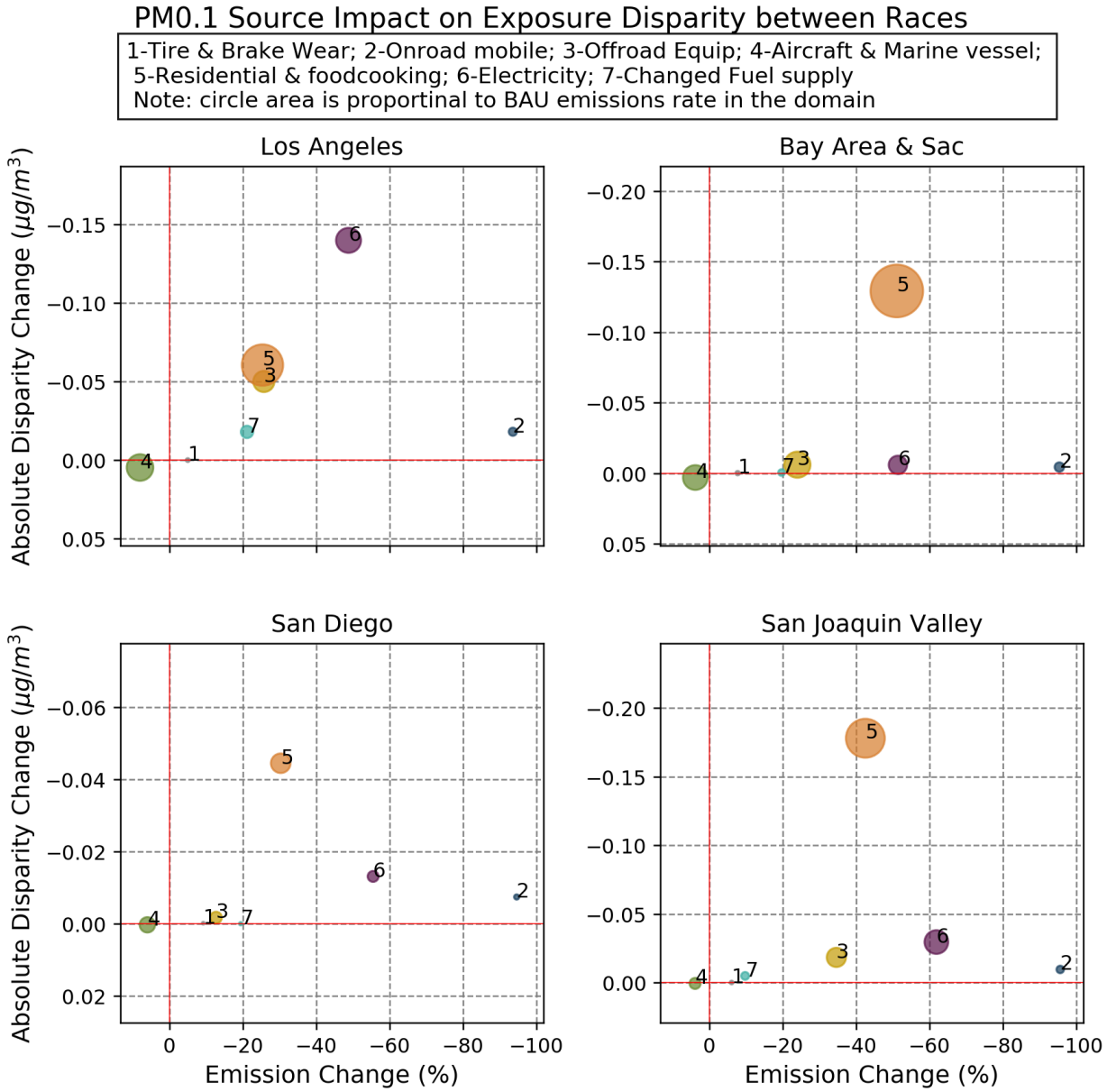

Figure 4-10. PM0.1 source impact on exposure disparity between races for GHGAi energy scenario. X-axis indicates emissions (source) changes between BAU and GHGAi scenario. Y-axis indicates emission absolute disparity changes between BAU and GHGAi scenario for specific source. All results averaged across four meteorological scenarios.

Reducing $PM_{2.5}$ exposure disparities across race/ethnicity requires that emissions reductions be prioritized for source categories that disproportionately affect groups with the highest exposure concentrations. Figure 4-9 illustrates the emissions reduction for each source category in the GHGAi

scenario relative to the BAU scenario along with the corresponding reduction in absolute disparity. Plots for other energy scenarios are shown in Figure S3-41 to S3-48 in Appendix 3. Ideal emissions sectors for further reductions are represented as large circles in the upper left quadrant of each plot. Large residential and food cooking emissions are a promising sector for further emissions reductions across all regions since each unit of emissions reduction produces a significant reduction in disparity. Further reductions in electricity generation emissions would reduce disparity in LA, but would have lower impact in other regions. Figure 4-10 identifies candidate emissions sectors that could be targeted to reduce $PM_{0.1}$ exposure disparities. Large emissions from residential and food cooking and electricity generation contribute strongly to $PM_{0.1}$ exposure disparities across all regions. These sources could be targeted in future efforts to reduce $PM_{0.1}$ exposure disparities.

4.3.5.3 Balancing Benefits for Total Population and Reduced Disparity

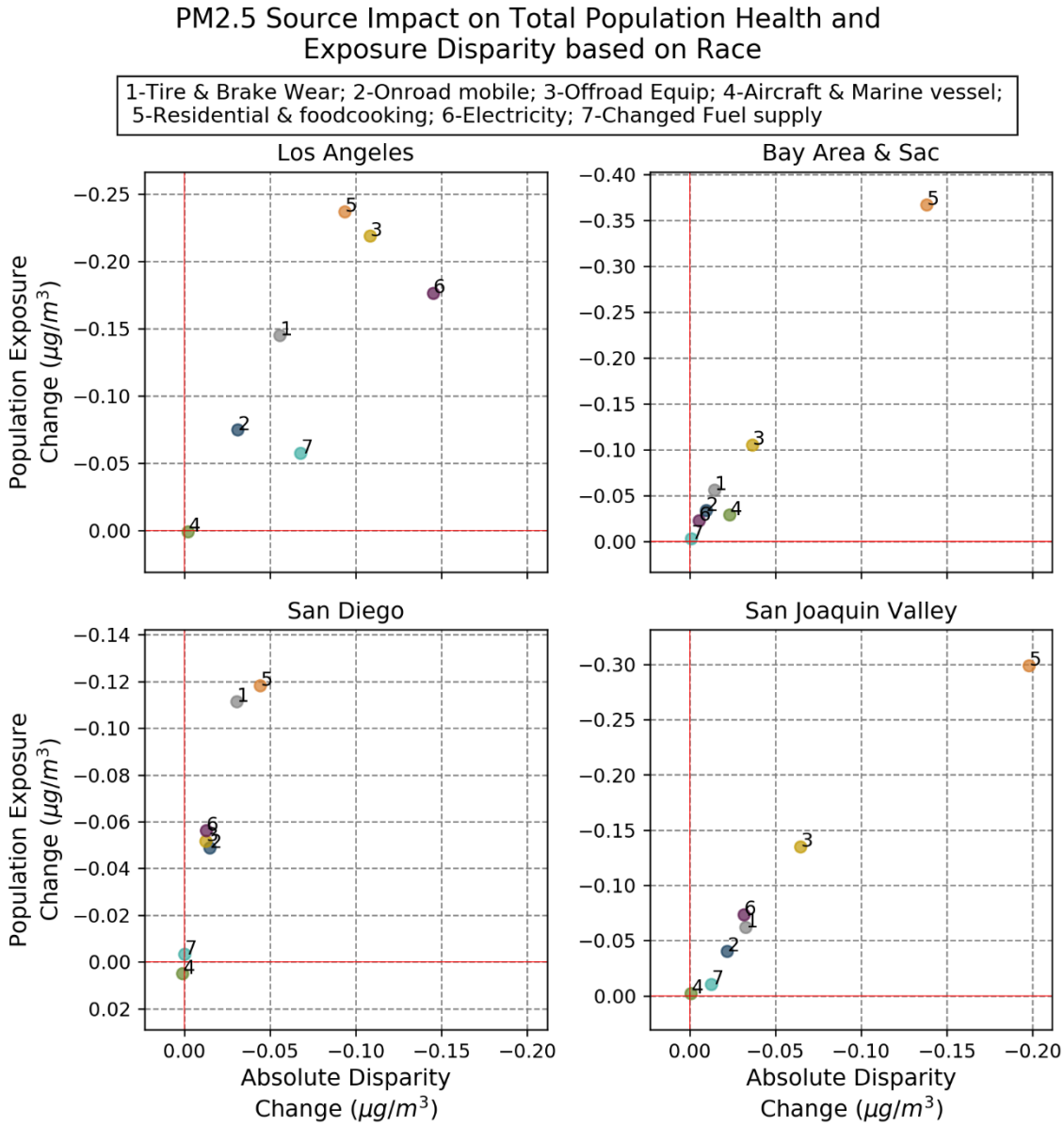

Figure 4-11. PM2.5 source impact on total population exposure and exposure disparity based on race for GHGAi energy scenario. X-axis indicates largest disparity changes between BAU and GHGAi scenario for each specific source. Y-axis indicates PWC changes between BAU and GHGAi scenario for each specific source. All results averaged across four meteorological scenarios.

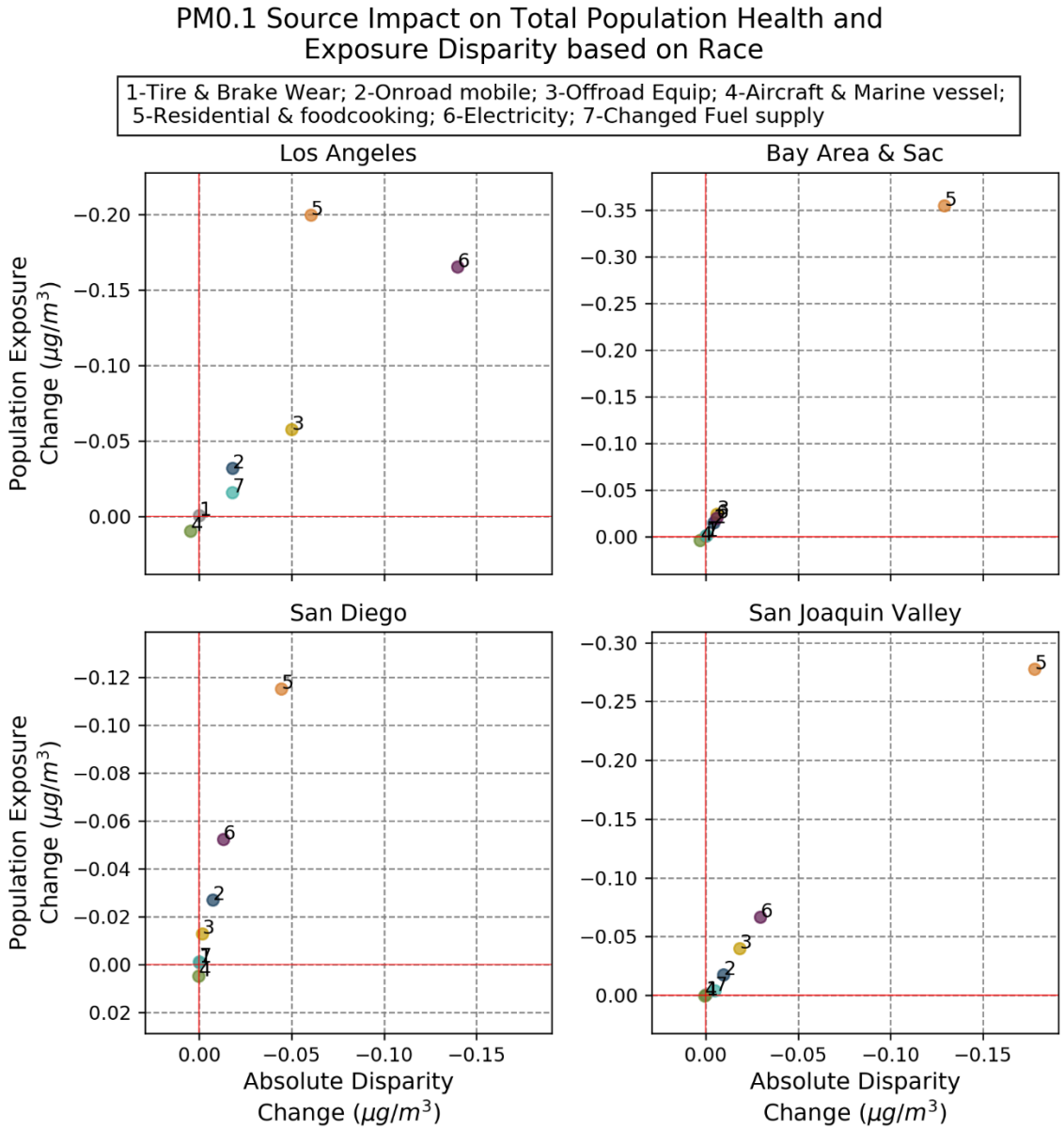

Figure 4-12. PM0.1 source impact on total population exposure and exposure disparity based on race for GHGAi energy scenario. X-axis indicates largest disparity changes between BAU and GHGAi scenario for each specific source. Y-axis indicates PWC changes between BAU and GHGAi scenario for each specific source. All results averaged over four meteorological scenarios.

The ideal future energy scenario will reduce exposure for the total population while simultaneously reducing exposure disparity between race/ethnicity groups. Figure 4-11 illustrates how changes in the GHGAi scenario relative to the BAU scenario affected total population exposure to $PM_{2.5}$ and the absolute exposure disparity. Figure 4-12 illustrates the same plot for $PM_{0.1}$ concentrations. Results for other scenarios are shown in Figure S3-49 to S3-56 in Appendix 3. All points in the upper right quadrant of each

sub-panel indicate beneficial reductions in both disparity and total population exposure. Points below the 1:1 line (45^{o} angle) reduce disparity by a larger amount than they reduce total population exposure. All points in Figure 4-11 and Figure 4-12 generally fall above the 1:1 line, indicating that statewide adoption of low carbon energy sources reduces total population exposure by an amount that is greater than or equal to the corresponding reduction in exposure disparities between racial groups. This finding suggests that statewide energy policies are not the ideal tool to reduce exposure disparities across race/ethnicity categories. Additional emissions controls may need to be applied in targeted neighborhoods to eliminate exposure disparity.

4.4. Discussion

Total population exposure to $PM_{2.5}$ and $PM_{0.1}$ in California decreased when GHG mitigation strategies using low-carbon fuels or carbon-capture and sequestration were adopted compared to a Business as Usual (BAU) scenario in the year 2050. The relative pattern of air pollution exposure for different GHG mitigation strategies scenarios was consistent across the four meteorology scenarios considered in the present analysis. The greatest exposure reduction occurred under the deepest GHG reduction scenario (GHGAi), closely followed by two scenarios with slightly higher exposure due to increased natural gas utilization (NGB and NGT). Population-weighted $PM_{2.5}$ exposure averaged across all energy scenarios ranged from 8.2 $\mu g/m^3$ to 12.5 $\mu g/m^3$ depending on the region (LA, SD, SFBA & SAC, SJV), while $PM_{0.1}$ exposure ranged from 1.3 $\mu g/m^3$ to 2.2 $\mu g/m^3$. Within the same region, relative reductions in $PM_{0.1}$ concentrations due to the adoption of low-carbon energy were up to four times larger than relative reductions in $PM_{2.5}$ concentrations (10-12% reduction for $PM_{0.1}$ vs. 2.5-2.7% reduction for $PM_{2.5}$).

Trends in $PM_{2.5}$ and $PM_{0.1}$ absolute exposure disparity between race/ethnicity groups under different energy scenarios were similar to trends in total population exposure. Deep GHG reduction scenarios, including GHGAi, NGT, and NGB, produced the greatest reduction in absolute exposure disparity for $PM_{2.5}$ and $PM_{-0.1}$. None of the clean energy scenarios completely eliminated air pollution exposure disparity in

the future, but adoption of low-carbon-energy sources did reduce the race/ethnicity disparity in California by as much as 20% for $PM_{2.5}$ mass and by as much as 40% for $PM_{0.1}$ mass.

Black & African American residents experienced higher-than-average exposure to $PM_{2.5}$ and $PM_{0.1}$ in all future energy scenarios in all study regions (LA, SD, SFBA & SAC, SJV). Asian residents in San Francisco experienced higher-than-average exposure to air pollution in all future energy scenarios. Peak exposure disparities reached ~10% above the average for $PM_{2.5}$ and ~20% above the average for $PM_{0.1}$. White residents in all regions experienced lower-than-average exposures in all energy scenarios, with peak disparity values of approximately -10% below the average for both $PM_{2.5}$ and $PM_{0.1}$. Health co-benefits calculations predict that adoption lower carbon energy scenarios (GHGAi, NGT, NGB) produce greater public health saving for all races/ethnicities. Health benefits per 1M residents are similar for Asian and Black & African American residents, slightly lower for Hispanic residents, and slightly higher for White residents.

The pattern of exposure disparities identified in the current study reflects the geographical distribution of each race/ethnicity group relative to the urban cores of each study city. Black & African American residents in California are more likely to live in urban cores or near major transportation corridors / industrial facilities where air pollution emissions are higher. In contrast, White residents are more dispersed in suburban areas that are further away from concentrated emissions sources. Additional emissions controls at the regional or local level will be needed to address these location-based disparities. Future demographic changes associated with population aging and population migration could either reduce or increase the need for additional emissions controls depending on how those changes affect the clustering of race/ethnicity groups towards urban cores.

Three source categories were identified for potential additional controls to further reduce $PM_{2.5}$/$PM_{0.1}$ exposure disparities: i) residential heating & food cooking, ii) tire and brake wear emissions, and iii) electricity generation. Local or regional emissions controls that target these categories could include the adoption electric heating to replace biomass combustion and natural gas combustion, modification of

commercial cooking methods to reduce smoke emissions, increased use of regenerative braking to reduce brake emissions, development of new tire compounds to reduce tire wear emissions, and selective upgrading of electrical generating equipment to solar/wind/geothermal/hydro sources with battery backup. Future studies should consider the cost-effectiveness of each additional measure to create an optimized strategy to reduce $PM_{2.5}$/$PM_{0.1}$ exposure disparities in California.

Chapter 5. Conclusions

A framework was established to improve the emissions inventories and to evaluate relationship between CTM configurations and health impact assessments (including health co-benefit and EJ assessments). This framework was then applied to the year 2050 in California to quantify levels of air pollution exposure disparity and health co-benefit under six energy scenarios that reduce GHG emission by 80% (relative to 1990 levels).

In the first phase of research, ten spatial surrogates including total population, total housing, single family housing, total employment, service & commercial employment, industrial employment, agricultural employment, industrial-related, off-road construction, and on-road construction were updated for the base year 2010 and future years from 2015 to 2040 in 5- year increments. Socio-economic data (SED) surrogates were updated using the latest version of census-based datasets at finer resolution. Off-road construction, on-road construction and industrial-related surrogates were developed using new methods to more accurately describe the location of construction projects and industrial facilities. Adoption of the new spatial surrogates caused changes to the spatial distribution of air pollution emissions in air quality calculations. The changes to the off-road construction surrogate resulted in the largest shift in PM emissions distribution for year 2015, followed by changes to the on-road construction surrogate. Industrial-related, service & commercial employment, and off-road construction surrogates all contributed to changes in NOx emissions. The changes to SED-derived surrogates were subtle and did not significantly influence emissions. Air quality simulations were carried out over the entire year 2016 to examine the impact of the new surrogate methodologies on simulated concentration fields. Changes to predicted pollutant concentrations followed the same pattern as changes in emissions, which indicates that proximity to sources is a dominant factor to determine the impact of spatial surrogates on model performance. The updated spatial surrogates generally improved predicted PM mass and EC concentrations in the Sacramento area (~10% for PM, ~3%

for EC), the Bay Area (~3% for PM, ~1.5% for EC), and the region surrounding Los Angeles (~5% for PM, ~4% for EC). The updated spatial surrogates also improved predicted NOx concentrations in the core region of Los Angeles (~6%). These improvements indicate that development and adoption of new methodologies for emissions spatial surrogates can improve the accuracy of regional chemical transport models for criteria air pollutants.

In the second phase of research, the effects of CTM spatial resolution and domain size on EJ assessments were studied based on present-day conditions in California. Emissions inventories were downscaled from 4km to 1km / 250m by fourteen spatial surrogates including ten updated / developed spatial surrogates obtained in phase one. A full set of WRF/Chem simulation was conducted with spatial resolution ranging from 250 m to 36 km, comparable to census tract sizes, over domains ranging in size from 320 km^2 to 10,000 km^2. Simulations with higher spatial resolution were able to better resolve sharp spatial gradients downwind of major transportation corridors and large point sources. Model performance improved by ~5% when the spatial resolution was increased from 4 km to 1 km; model performance improved an additional ~4% when the spatial resolution was increased from 1 km to 250 m. Overall 9% improvement of WRF/Chem model accuracy was detected as spatial resolution increased from 4 km to 250 m, with similar results expected for future simulations. Exposure disparity results are consistent with previous findings: the average Non-Hispanic White person in the study domain experiences $PM_{2.5}$ mass concentrations 6-14% lower than the average resident, while the average Black and African American person experiences $PM_{2.5}$ mass concentrations that are 3-22% higher than the average resident. Predicted exposure disparities were a function of the model configuration. Increasing the spatial resolution finer than approximately 1 km produced diminishing returns because the increased spatial resolution came at the expense of reduced domain size in order to maintain reasonable computational burden. Increasing domain size to capture regional trends, such as wealthier populations living in coastal areas, identified larger exposure disparities but the benefits were limited. In the current study, 4 km spatial resolution with a domain size greater than 10^4 km^2 or 1 km spatial resolution with domains size greater than 10^3 km^2 appear to be resonable CTM configurations for our desirable air pollution disparity analysis. These configurations

represent a balanced approach between statistical power, sensitivity across socio-economic groups, and computational burden when predicting current and future air pollution exposure disparities in Los Angeles. It is worth noting that the exact thresholds for achieving a target level of statistical power at a relevant level of exposure disparity is unique to each geographic region. Similar studies should be carried out in other geographic regions in order to determine the appropriate CTM domain size and spatial resolution for EJ analysis in the context of their spatial distributions for race and income.

In the final phase of research, a series of EJ assessment and health co-benefit analyses were conducted for future year 2050 at 4km spatial resolution under six future energy scenarios, across four major regions in California. Six different energy scenarios constructed using the energy-economic optimization model CA-TIMES were evaluated in future years. Criteria pollutant emissions were developed for each energy scenario using the CA-REMARQUE model using 4km spatial resolution over four major geographic areas in California: the greater San Francisco Bay Area including Sacramento (SFBA&SAC), the San Joaquin Valley (SJV), Los Angeles (LA), and San Diego (SD). The Weather Research & Forecasting (WRF) model was used to predict future meteorology fields by downscaling two different climate scenario (RCP4.5 and RCP8.5) generated by two different GCMs (the Community Climate System Model and the Canadian Earth Systems Model). Simulations were performed over 32 weeks randomly selected during the 10-year window from the year 2046 to 2055 to build up a long-term average in the presence of ENSO variability. An environmental justice (EJ) analysis shows that adoption of low-carbon energy sources in the year 2050 reduces the race/ethnicity disparity in air pollution exposure in California by as much as 20% for $PM_{2.5}$ mass and by as much as 40% for $PM_{0.1}$ mass. The trends associated with low-carbon energy adoption were relatively stable across the ensemble of locations and scenarios. Deeper reductions in the carbon intensity of energy sources progressively reduced exposure to $PM_{2.5}$ mass and $PM_{0.1}$ mass for all California residents. The greater adoption of low-carbon fuels also reduced the racial disparity in the PM exposure. The three energy scenarios that achieved an ~80% reduction in GHG emissions relative to 1990 levels simultaneously produced the greatest reduction in PM exposure for all California residents and the greatest reduction in the

racial disparity of that exposure. These findings suggest that the adoption of low-carbon energy can improve public health and reduce racial disparities through an improvement in air quality.

Chapter 6. Future Research Needs

The pattern of exposure disparities identified in this study reflects the geographical distribution of each race/ethnicity group relative to the urban cores of each study city. Black & African American residents in California are more likely to live in urban cores or near major transportation corridors / industrial facilities where air pollution emissions are higher. However, White residents are more likely living in suburban areas that are further away from concentrated emissions sources. Additional emissions controls at the regional or local level will be needed to address these location-based disparities. Future demographic changes associated with population aging and population migration could either reduce or increase the need for additional emissions controls depending on how those changes affect the clustering of race/ethnicity groups towards urban cores.

Residential heating & food cooking, tire & brake wear emissions and electricity generation were found to be three most potential source categories that can be further reduce $PM_{2.5}$/$PM_{0.1}$ exposure disparities. Future studies should consider the cost-effectiveness of each additional measure to create an optimized strategy to reduce $PM_{2.5}$/$PM_{0.1}$ exposure disparities in California.

References

American Lung Association, 2019. State of the Air 2019 [WWW Document]. URL https://www.stateoftheair.org/assets/sota-2019-full.pdf (accessed 12.26.20).

Anderson, C.M., Kissel, K.A., Field, C.B., Mach, K.J., 2018a. Climate Change Mitigation, Air Pollution, and Environmental Justice in California. Environ Sci Technol 52, 10829–10838. https://doi.org/10.1021/acs.est.8b00908

Anderson, C.M., Kissel, K.A., Field, C.B., Mach, K.J., 2018b. Climate Change Mitigation, Air Pollution, and Environmental Justice in California. Environ Sci Technol 52, 10829–10838. https://doi.org/10.1021/acs.est.8b00908

Anderson, J.O., Thundiyil, J.G., Stolbach, A., 2012. Clearing the Air: A Review of the Effects of Particulate Matter Air Pollution on Human Health. Journal of Medical Toxicology 8, 166–175. https://doi.org/10.1007/S13181-011-0203-1/TABLES/5

Baden, B.M., Noonan, D.S., Turaga, R.M.R., 2007. Scales of justice: Is there a geographic bias in environmental equity analysis? Journal of Environmental Planning and Management 50, 163–185. https://doi.org/10.1080/09640560601156433

Banzhaf, S., Ma, L., Timmins, C., 2019. Environmental Justice: The Economics of Race, Place, and Pollution. Journal of Economic Perspectives 33, 185–208. https://doi.org/10.1257/jep.33.1.185

Bieser, J., Aulinger, A., Matthias, V., Quante, M., Builtjes, P., 2011. Geoscientific Model Development SMOKE for Europe-adaptation, modification and evaluation of a comprehensive emission model for Europe. Geosci. Model Dev 4, 47–68. https://doi.org/10.5194/gmd-4-47-2011

Bond, T.C., Bhardwaj, E., Dong, R., Jogani, R., Jung, S., Roden, C., Streets, D.G., Trautmann, N.M., 2007. Historical emissions of black and organic carbon aerosol from energy-related combustion, 1850–2000. Global Biogeochem Cycles 21. https://doi.org/10.1029/2006GB002840

Boylan, J.W., Russell, A.G., 2006. PM and light extinction model performance metrics, goals, and criteria for three-dimensional air quality models. Atmos Environ 40, 4946–4959. https://doi.org/10.1016/j.atmosenv.2005.09.087

Bravo, M.A., Anthopolos, R., Bell, M.L., Miranda, M.L., 2016. Racial isolation and exposure to airborne particulate matter and ozone in understudied US populations: Environmental justice applications of downscaled numerical model output. Environ Int 92–93, 247–255. https://doi.org/10.1016/j.envint.2016.04.008

Brondfield, M.N., Hutyra, L.R., Gately, C.K., Raciti, S.M., Peterson, S.A., 2012. Modeling and validation of on-road CO2 emissions inventories at the urban regional scale. Environmental Pollution 170, 113–123. https://doi.org/10.1016/j.envpol.2012.06.003

Brook, R.D., Rajagopalan, S., Pope, C.A., Brook, J.R., Bhatnagar, A., Diez-Roux, A. v., Holguin, F., Hong, Y., Luepker, R. v., Mittleman, M.A., Peters, A., Siscovick, D., Smith, S.C., Whitsel, L., Kaufman, J.D., 2010. Particulate matter air pollution and cardiovascular disease: An update to the scientific statement from the american heart association. Circulation 121, 2331–2378. https://doi.org/10.1161/CIR.0B013E3181DBECE1

Brulle, R.J., Pellow, D.N., 2006. ENVIRONMENTAL JUSTICE: Human Health and Environmental Inequalities. Annu Rev Public Health 27, 103–124. https://doi.org/10.1146/annurev.publhealth.27.021405.102124

Bun, R., Hamal, K., Gusti, · M, Bun, · A, 2010. Spatial GHG inventory at the regional level: accounting for uncertainty. Clim Change 103, 227–244. https://doi.org/10.1007/s10584-010-9907-5

Butt, E.W., Rap, A., Schmidt, A., Scott, C.E., Pringle, K.J., Reddington, C.L., Richards, N.A.D., Woodhouse, M.T., Ramirez-Villegas, J., Yang, H., Vakkari, V., Stone, E.A., Rupakheti, M., S. Praveen, P., G. van Zyl, P., P. Beukes, J., Josipovic, M., Mitchell, E.J.S., Sallu, S.M., Forster, P.M., Spracklen, D. V., 2016. The impact of residential combustion emissions on atmospheric aerosol, human health, and climate. Atmos Chem Phys 16, 873–905. https://doi.org/10.5194/acp-16-873-2016

Cai, R., Zhao, C., Nie, X., 2019. Alumina-Based Coating with Dimples as Enabling Sustainable Technology To Reduce Wear and Emission of the Brake System. ACS Sustain Chem Eng 8, 893–899. https://doi.org/10.1021/ACSSUSCHEMENG.9B05302

CALCOG, 2019. CALGOG main webpage [WWW Document]. URL https://www.calcog.org/index.php?submenu=TypeofRegions&src=gendocs&ref=TypeofRegions&category=RegionsLead

California Air Resource Board, 2020. OFFROAD2017 (v1.0.1) Web Database [WWW Document]. URL https://www.arb.ca.gov/orion/?_ga=2.241139715.1886892688.1581021011-2036378939.1578081391 (accessed 2.6.20).

California Air Resource Board, 2017. Assembly Bill No. 617 Nonvehicular air pollution: Criteria Air Pollutions and Toxic Air Contaminants. [WWW Document]. URL https://leginfo.legislature.ca.gov/faces/billTextClient.xhtml?bill_id=201720180AB617 (accessed 7.26.21).

California Air Resource Board, 2010. 2010 OFFROAD emission inventory document - Construction and Mining Sector.

California Air Resource Board, 2006. Assembly Bill No. 32: Air Pollution: Greenhouse gases: California Global Warming Solutions Act of 2006. [WWW Document]. URL https://leginfo.legislature.ca.gov/faces/billTextClient.xhtml?bill_id=200520060AB32 (accessed 7.26.21).

California Air Resource Board, n.d. California Air Resource Board SIP 2016 Emissions Projection Data [WWW Document]. URL https://www.arb.ca.gov/app/emsinv/2017/emssumcat_query.php?F_YR=2012&F_DIV=-4&F_SEASON=A&SP=SIP105ADJ&F_AREA=CA#AREAWIDE (accessed 12.7.20).

California Air Resources Board, 2019. CEPAM2019v1.03 - Standard Emission Tool [WWW Document]. URL https://ww2.arb.ca.gov/applications/cepam2019v103-standard-emission-tool (accessed 7.22.22).

Caltrans, 2015. 2015 State of the Pavement Report.

Cambridge Systematics Inc., 2014a. California Statewide Travel Demand Model Version 2.0 - Model Overview final report.

Cambridge Systematics Inc., 2014b. California Statewide Travel Demand Model, Version 2.0 - Population, Employment, and School Enrollment final report.

Cappa, C.D., Jathar, S.H., Kleeman, M.J., Docherty, K.S., Jimenez, J.L., Seinfeld, J.H., Wexler, A.S., 2016. Simulating secondary organic aerosol in a regional air quality model using the statistical oxidation model - Part 2: Assessing the influence of vapor wall losses. Atmos Chem Phys 16, 3041–3059. https://doi.org/10.5194/ACP-16-3041-2016

Chakraborty, J., Maantay, J.A., Brender, J.D., 2011. Disproportionate proximity to environmental health hazards: Methods, models, and measurement. Am J Public Health 101, S27–S36. https://doi.org/10.2105/AJPH.2010.300109

Chen, G., Li, J., Ying, Q., Sherman, S., Perkins, N., Sundaram, R., Mendola, P., 2014. Evaluation of observation-fused regional air quality model results for population air pollution exposure estimation. Science of the Total Environment 485–486, 563–574. https://doi.org/10.1016/j.scitotenv.2014.03.107

Clark, L.P., Millet, D.B., Marshall, J.D., 2017. Changes in Transportation-Related Air Pollution Exposures by Race-Ethnicity and Socioeconomic Status: Outdoor Nitrogen Dioxide in the United States in 2000 and 2010. Environ Health Perspect 125. https://doi.org/10.1289/EHP959

CMAS, 2019. Spatial Allocator User's Manual [WWW Document]. URL https://github.com/CMASCenter/Spatial-Allocator/blob/master/docs/User_Manual/README.md (accessed 8.9.19).

CMAS, 2016. SMOKE v4.0 User's Manual.

Cohan, D.S., Hu, Y., Russell, A.G., 2006. Dependence of ozone sensitivity analysis on grid resolution. Atmos Environ 40, 126–135. https://doi.org/10.1016/j.atmosenv.2005.09.031

Colmer, J., Hardman, I., Shimshack, J., Voorheis, J., 2020. Disparities in PM2.5 air pollution in the United States. Science (1979) 369, 575–578. https://doi.org/10.1126/SCIENCE.AAZ9353

Cushing, L., Faust, J., August, L.M., Cendak, R., Wieland, W., Alexeeff, G., 2015. Racial/ethnic disparities in cumulative environmental health impacts in California: Evidence from a statewide environmental justice screening tool (CalEnviroScreen 1.1). Am J Public Health 105, 2341–2348. https://doi.org/10.2105/AJPH.2015.302643

Cushing, L., Faust, J., Meehan August, L., Cendak, R., Wieland, W., Alexeeff, G., n.d. Racial/Ethnic Disparities in Cumulative Environmental Health Impacts in California: Evidence From a Statewide Environmental Justice Screening Tool (CalEnviroScreen 1.1). https://doi.org/10.2105/AJPH.2015.302643

Dai, J., Rocke, D.M., 2000. A GIS-based approach to spatial allocation of area source solvent emissions. Environmental Modelling & Software 15, 293–302. https://doi.org/10.1016/S1364-8152(00)00004-9

Dalmau, M.E., Augsburg, K., Wenzel, F., Ivanov, V., 2020. Tire Particle Emissions: Demand on Reliable Characterization. Tire Sci Technol 48, 107–122. https://doi.org/10.2346/TIRE.19.170181

De La Cruz-Viesca, M., Chen, Z., Ong, P.M., Hamilton, D., Darity, W.A., 2016. The Color of Wealth in Los Angeles and the Insight Center for Community Economic Development.

Di, Q., Kloog, I., Koutrakis, P., Lyapustin, A., Wang, Y., Schwartz, J., 2016. Assessing PM2.5 Exposures with High Spatiotemporal Resolution across the Continental United States. Environ Sci Technol 50, 4712–4721. https://doi.org/10.1021/ACS.EST.5B06121/SUPPL_FILE/ES5B06121_SI_001.PDF

Dimanchev, E.G., Paltsev, S., Yuan, M., Rothenberg, D., Tessum, C.W., Marshall, J.D., Selin, N.E., 2019. Health co-benefits of sub-national renewable energy policy in the US. Environmental Research Letters 14, 085012. https://doi.org/10.1088/1748-9326/AB31D9

Dockery, D.W., Pope, C.A., Xu, X., Spengler, J.D., Ware, J.H., Fay, M.E., Ferris, B.G., Speizer, F.E., 1993. An Association between Air Pollution and Mortality in Six U.S. Cities. New England Journal of Medicine 329, 1753–1759. https://doi.org/10.1056/NEJM199312093292401

Donkelaar, A. Van, Martin, R., … C.L.-E. science &, 2019, undefined, 2019. Regional estimates of chemical composition of fine particulate matter using a combined geoscience-statistical method with information from satellites, models, and. ACS Publications 53, 2595–2611. https://doi.org/10.1021/acs.est.8b06392

Driscoll, C.T., Buonocore, J.J., Levy, J.I., Lambert, K.F., Burtraw, D., Reid, S.B., Fakhraei, H., Schwartz, J., 2015. US power plant carbon standards and clean air and health co-benefits. Nature Climate Change 2015 5:6 5, 535–540. https://doi.org/10.1038/nclimate2598

Eastham, S.D., Long, M.S., Keller, C.A., Lundgren, E., Yantosca, R.M., Zhuang, J., Li, C., Lee, C.J., Yannetti, M., Auer, B.M., Clune, T.L., Kouatchou, J., Putman, W.M., Thompson, M.A., Trayanov, A.L., Molod, A.M., Martin, R. V, Jacob, D.J., 2018. GEOS-Chem High Performance (GCHP v11-02c): a next-generation implementation of the GEOS-Chem chemical transport model for massively parallel applications. Geosci. Model Dev 11, 2941–2953. https://doi.org/10.5194/gmd-11-2941-2018

Evans, J.S., Wolff, S.K., Phonboon, K., Levy, J.I., Smith, K.R., 2002. Exposure efficiency: an idea whose time has come? Chemosphere 49, 1075–1091. https://doi.org/10.1016/S0045-6535(02)00242-4

Fameli, K.M., Assimakopoulos, V.D., 2015. Development of a road transport emission inventory for Greece and the Greater Athens Area: Effects of important parameters. Science of the Total Environment 505, 770–786. https://doi.org/10.1016/j.scitotenv.2014.10.015

Fenech, S., Doherty, R.M., Heaviside, C., Vardoulakis, S., Macintyre, H.L., O'Connor, F.M., 2018. The influence of model spatial resolution on simulated ozone and fine particulate matter for Europe: Implications for health impact assessments. Atmos Chem Phys 18, 5765–5784. https://doi.org/10.5194/acp-18-5765-2018

Fonseca, G., Rodrigues, C., Oliveira, Nathan Peixoto, Rodrigues, G.F.C., Oliveira, N P, Filho, W.L., De, J.B.S., Guerra, A., 2020. Impacts of Green Tire Technology: Case Study of Environmental and Customer Perspectives. Climate Change Management 271–285. https://doi.org/10.1007/978-3-030-57235-8_21

Fountoukis, C., Nenes, A., 2007. Atmospheric Chemistry and Physics ISORROPIA II: a computationally efficient thermodynamic equilibrium model for K +-Ca 2+-Mg 2+-NH + 4-Na +-SO 2− 4-NO − 3-Cl −-H 2 O aerosols. Atmos. Chem. Phys 7, 4639–4659.

Fu, M., Kelly, J.A., Clinch, J.P., 2017. Estimating annual average daily traffic and transport emissions for a national road network: A bottom-up methodology for both nationally-aggregated and spatially-disaggregated results. J Transp Geogr 58, 186–195. https://doi.org/10.1016/j.jtrangeo.2016.12.002

Gauderman, W.J., Avol, E., Gilliland, F., Vora, H., Thomas, D., Berhane, K., McConnell, R., Kuenzli, N., Lurmann, F., Rappaport, E., Margolis, H., Bates, D., Peters, J., 2004. The Effect of Air Pollution on Lung Development from 10 to 18 Years of Age. New England Journal of Medicine 351, 1057–1067. https://doi.org/10.1056/NEJMOA040610

Gent, P., Donner, L., Lawrence, D., Gent, P.R., Danabasoglu, G., Donner, L.J., Holland, M.M., Hunke, E.C., Jayne, S.R., Lawrence, D.M., Neale, R.B., Rasch, P.J., Vertenstein, M., Worley, P.H., Yang, Z.-L., Zhang ##, M., 2011. The Community Climate System Model Version 4 OCEANFILMS View project Dust Emission Modeling View project The Community Climate System Model Version 4. Article in Journal of Climate. https://doi.org/10.1175/2011JCLI4083.1

Gkatzoflias, D., Mellios, G., Samaras, Z., 2013. Development of a web GIS application for emissions inventory spatial allocation based on open source software tools. Comput Geosci 52, 21–33. https://doi.org/10.1016/J.CAGEO.2012.10.011

González, C.M., Ynoue, R.Y., Vara-Vela, A., Rojas, N.Y., Aristizábal, B.H., 2018. High-resolution air quality modeling in a medium-sized city in the tropical Andes: Assessment of local and global emissions in understanding ozone and PM 10 dynamics. Atmos Pollut Res 9, 934–948. https://doi.org/10.1016/j.apr.2018.03.003

Gov Arnold Schwarzenegger, C., 2005. Executive Order S-3-05.

Gramstat, S., 2018. Technological Measures for Brake Wear Emission Reduction: Possible Improvement in Compositions and Technological Remediation: Cost Efficiency. Non-Exhaust Emissions 205–227. https://doi.org/10.1016/B978-0-12-811770-5.00010-8

Gunier, R.B., Hertz, A., Von Behren, J., Reynolds, P., 2003. Traffic density in California: Socioeconomic and ethnic differences among potentially exposed children. J Expo Anal Environ Epidemiol 13, 240–246. https://doi.org/10.1038/sj.jea.7500276

Harper, S., Ruder, E., Roman, H.A., Geggel, A., Nweke, O., Payne-Sturges, D., Levy, J.I., 2013a. Using Inequality Measures to Incorporate Environmental Justice into Regulatory Analyses. Int J Environ Res Public Health 10, 4039. https://doi.org/10.3390/IJERPH10094039

Harper, S., Ruder, E., Roman, H.A., Geggel, A., Nweke, O., Payne-Sturges, D., Levy, J.I., 2013b. Using inequality measures to incorporate environmental justice into regulatory analyses. Int J Environ Res Public Health. https://doi.org/10.3390/ijerph10094039

Heo, J., Dulger, M., Olson, M.R., McGinnis, J.E., Shelton, B.R., Matsunaga, A., Sioutas, C., Schauer, J.J., 2013. Source apportionments of PM2.5 organic carbon using molecular marker Positive Matrix Factorization and comparison of results from different receptor models. Atmos Environ 73, 51–61. https://doi.org/10.1016/J.ATMOSENV.2013.03.004

Hernandez, C., Skyllakou, K., Rivera, P.G., Dinkelacker, B., Marshall, J., Pope, A., Robinson, A., Pandis, S., Adams, P., 2021. Bias corrections for speciated and source-resolved PM2.5 chemical transport model simulations using a geographically weighted regression. https://doi.org/10.26434/CHEMRXIV-2021-H71P5

Herrera, J.C., Work, D.B., Herring, R., Ban, X. (Jeff), Jacobson, Q., Bayen, A.M., 2010. Evaluation of traffic data obtained via GPS-enabled mobile phones: The Mobile Century field experiment. Transp Res Part C Emerg Technol 18, 568–583. https://doi.org/10.1016/j.trc.2009.10.006

Hogrefe, C., Rao, S.T., 2001. Demonstrating attainment of the air quality standards: Integration of observations and model predictions into the probabilistic framework. J Air Waste Manage Assoc 51, 1060–1072. https://doi.org/10.1080/10473289.2001.10464332

Houston, D., Li, W., Wu, J., 2014. Disparities in exposure to automobile and truck traffic and vehicle emissions near the Los Angeles-long beach port complex. Am J Public Health 104, 156–164. https://doi.org/10.2105/AJPH.2012.301120

Hu, J., Jathar, S., Zhang, H., Ying, Q., Chen, S.-H., Cappa, C.D., Kleeman, M.J., 2017. Long-term particulate matter modeling for health effect studies in California – Part 2: Concentrations and sources of ultrafine organic aerosols. Atmos Chem Phys 17, 5379–5391. https://doi.org/10.5194/acp-17-5379-2017

Hu, J., Zhang, H., Chen, S.-H., Wiedinmyer, C., Vandenberghe, F., Ying, Q., Kleeman, M.J., 2014. Predicting primary PM2.5 and PM0.1 trace composition for epidemiological studies in California. Environ Sci Technol 48, 4971–4979. https://doi.org/10.1021/es404809j

Hu, J., Zhang, H., Ying, Q., Chen, S.-H., Vandenberghe, F., Kleeman, M.J., 2015. Long-term particulate matter modeling for health effect studies in California – Part 1: Model performance on temporal and spatial variations. Atmos Chem Phys 15, 3445–3461. https://doi.org/10.5194/acp-15-3445-2015

Huang, R., Zhai, X., Ivey, C.E., Friberg, M.D., Hu, X., Liu, Y., Mulholland, J.A., Russell, A.G., 2018. Using Air Quality Model-Data Fusion Methods for Developing Air Pollutant Exposure Fields and Comparison with Satellite AOD-Derived Fields: Application over North Carolina, USA, in: Mensink, C., Kallos, G. (Eds.), Air Pollution Modeling and Its Application XXV. Springer International Publishing, Cham, pp. 207–212.

Izquierdo, R., García Dos Santos, S., Borge, R., Paz, D. de la, Sarigiannis, D., Gotti, A., Boldo, E., 2020. Health impact assessment by the implementation of Madrid City air-quality plan in 2020. Environ Res 183, 109021. https://doi.org/10.1016/j.envres.2019.109021

Jacobson, M.Z., 2010. A Solution to the Problem of Nonequilibrium Acid/Base Gas-Particle Transfer at Long Time Step. http://dx.doi.org/10.1080/027868290904546 39, 92–103. https://doi.org/10.1080/027868290904546

Jiang, X., Yoo, E. hye, 2018. The importance of spatial resolutions of Community Multiscale Air Quality (CMAQ) models on health impact assessment. Science of the Total Environment. https://doi.org/10.1016/j.scitotenv.2018.01.228

Joe, D.K., Zhang, H., DeNero, S.P., Lee, H.H., Chen, S.H., McDonald, B.C., Harley, R.A., Kleeman, M.J., 2014. Implementation of a high-resolution Source-Oriented WRF/Chem model at the Port of Oakland. Atmos Environ. https://doi.org/10.1016/j.atmosenv.2013.09.055

Karner, A.A., Eisinger, D.S., Niemeier, D.A., 2010. Near-Roadway Air Quality: Synthesizing the Findings from Real-World Data. Environ Sci Technol 44, 5334–5344. https://doi.org/10.1021/es100008x

Kelly, J.T., Jang, C.J., Timin, B., Gantt, B., Reff, A., Zhu, Y., Long, S., Hanna, A., 2019. A system for developing and projecting PM2.5 spatial fields to correspond to just meeting national

ambient air quality standards. Atmos Environ X 2. https://doi.org/10.1016/j.aeaoa.2019.100019

Kleeman, M.J., Cass, G.R., 2001a. A 3D Eulerian Source-Oriented Model for an Externally Mixed Aerosol. Environ Sci Technol 35, 4834–4848. https://doi.org/10.1021/es010886m

Kleeman, M.J., Cass, G.R., 2001b. A 3D Eulerian source-oriented model for an externally mixed aerosol. Environ Sci Technol 35, 4834–4848. https://doi.org/10.1021/es010886m

Kleeman, M.J., Zapata, C., Stilley, J., Hixson, M., 2013. PM2.5 co-benefits of climate change legislation part 2: California governor's executive order S-3-05 applied to the transportation sector. Clim Change 117, 399–414. https://doi.org/10.1007/s10584-012-0546-x

Kloog, I., Chudnovsky, A.A., Just, A.C., Nordio, F., Koutrakis, P., Coull, B.A., Lyapustin, A., Wang, Y., Schwartz, J., 2014. A new hybrid spatio-temporal model for estimating daily multi-year PM2.5 concentrations across northeastern USA using high resolution aerosol optical depth data. Atmos Environ 95, 581–590. https://doi.org/10.1016/J.ATMOSENV.2014.07.014

Krewski, D., Jerrett, M., Burnett, R.T., Ma, R., Hughes, E., Shi, Y., Turner, M.C., Newbold, B., Ramsay, T., Ross, Z., Shin, H., Tempalski, B., 2009. Extended Follow-Up and Spatial Analysis of the American Cancer Society Study Linking Particulate Air Pollution and Mortality.

Kuenen, J.J.P., Visschedijk, A.J.H., Jozwicka, M., Gon, D.H.A.C. van der, 2014. TNO-MACC_II emission inventory; a multi-year (2003–2009) consistent high-resolution European emission inventory for air quality modelling. Atmos Chem Phys 14, 10963–10976. https://doi.org/10.5194/acp-14-10963-2014

Kuik, F., Lauer, A., Churkina, G., Denier Van Der Gon, H.A.C., Fenner, D., Mar, K.A., Butler, T.M., 2016. Air quality modelling in the Berlin-Brandenburg region using WRF-Chem v3.7.1: sensitivity to resolution of model grid and input data. Geosci. Model Dev 9, 4339–4363. https://doi.org/10.5194/gmd-9-4339-2016

Laden, F., Schwartz, J., Speizer, F.E., Dockery, D.W., 2006. Reduction in fine particulate air pollution and mortality: Extended follow-up of the Harvard Six Cities study. Am J Respir Crit Care Med 173, 667–672. https://doi.org/10.1164/RCCM.200503-443OC

Laurent, O., Hu, J., Li, L., Cockburn, M., Escobedo, L., Kleeman, M.J., Wu, J., 2014. Sources and contents of air pollution affecting term low birth weight in Los Angeles County, California, 2001–2008. Environ Res 134, 488–495. https://doi.org/10.1016/j.envres.2014.05.003

Laurent, O., Wu, J., Li, L., Chung, J., Bartell, S., 2013. Investigating the association between birth weight and complementary air pollution metrics: a cohort study. Environmental Health 12, 1–15. https://doi.org/10.1186/1476-069x-12-18

Lei, Y., Zhang, Q., He, K.B., Streets, D.G., 2011. Primary anthropogenic aerosol emission trends for China, 1990-2005. Atmos Chem Phys 11, 931–954. https://doi.org/10.5194/ACP-11-931-2011

Lelieveld, J., Evans, J.S., Fnais, M., Giannadaki, D., Pozzer, A., 2015a. The contribution of outdoor air pollution sources to premature mortality on a global scale. Nature 525, 367–371. https://doi.org/10.1038/nature15371

Lelieveld, J., Evans, J.S., Fnais, M., Giannadaki, D., Pozzer, A., 2015b. The contribution of outdoor air pollution sources to premature mortality on a global scale. Nature 525, 367–371. https://doi.org/10.1038/nature15371

Lepeule, J., Laden, F., Dockery, D., Schwartz, J., 2012. Chronic Exposure to Fine Particles and Mortality: An Extended Follow-up of the Harvard Six Cities Study from 1974 to 2009. Environ Health Perspect 120, 965. https://doi.org/10.1289/EHP.1104660

Levy, J.I., Woo, M.K., Penn, S.L., Omary, M., Tambouret, Y., Kim, C.S., Arunachalam, S., 2016. Carbon reductions and health co-benefits from US residential energy efficiency measures. Environmental Research Letters 11, 034017. https://doi.org/10.1088/1748-9326/11/3/034017

Li, Y., Henze, D.K., Jack, D., Kinney, P.L., 2016. The influence of air quality model resolution on health impact assessment for fine particulate matter and its components. Air Qual Atmos Health 9, 51–68. https://doi.org/10.1007/s11869-015-0321-z

Li, Y., Rodier, C., Lea, J.D., Harvey, J., Kleeman, M.J., 2020. Improving spatial surrogates for area source emissions inventories in California. Atmos Environ 117665. https://doi.org/10.1016/j.atmosenv.2020.117665

Li, Yin, Yang, C., Li, Yiting, Kumar, A., Kleeman, M.J., 2022. Future emissions of particles and gases that cause regional air pollution in California under different greenhouse gas mitigation strategies. Atmos Environ 273, 118960. https://doi.org/10.1016/J.ATMOSENV.2022.118960

Li, Yiting, Kumar, A., Li, Yin, Kleeman, M.J., 2022. Adoption of low-carbon fuels reduces race/ethnicity disparities in air pollution exposure in California. Science of The Total Environment 155230. https://doi.org/10.1016/J.SCITOTENV.2022.155230

Liu, J., Clark, L.P., Bechle, M.J., Hajat, A., Kim, S.Y., Robinson, A.L., Sheppard, L., Szpiro, A.A., Marshall, J.D., 2021. Disparities in Air Pollution Exposure in the United States by Race/Ethnicity and Income, 1990-2010. Environ Health Perspect 129, undefined-undefined. https://doi.org/10.1289/EHP8584

Macpherson, A.J., Simon, H., Langdon, R., Misenheimer, D., 2017. A mixed integer programming model for National Ambient Air Quality Standards (NAAQS) attainment strategy analysis. Environmental Modelling and Software 91, 13–27. https://doi.org/10.1016/j.envsoft.2017.01.008

Mahmud, A., Hixson, M., Kleeman, M.J., 2012. Atmospheric Chemistry and Physics Quantifying population exposure to airborne particulate matter during extreme events in California due to climate change. Atmos. Chem. Phys 12, 7453–7463. https://doi.org/10.5194/acp-12-7453-2012

Markakis, K., Valari, M., Perrussel, O., Sanchez, O., Honore, C., 2015. Climate forced air-quality modeling at urban scale Climate forced air-quality modeling at urban scale: sensitivity to model resolution, emissions and meteorology Climate forced air-quality modeling at urban scale Climate forced air-quality modeling at urban scale. Atmos. Chem. Phys. Discuss 15, 4767–4821. https://doi.org/10.5194/acpd-15-4767-2015

Markandya, A., Sampedro, J., Smith, S.J., Van Dingenen, R., Pizarro-Irizar, C., Arto, I., González-Eguino, M., 2018. Health co-benefits from air pollution and mitigation costs of the Paris Agreement: a modelling study. Lancet Planet Health 2, e126–e133. https://doi.org/10.1016/S2542-5196(18)30029-9

Marshall, J.D., Riley, W.J., McKone, T.E., Nazaroff, W.W., 2003. Intake fraction of primary pollutants: motor vehicle emissions in the South Coast Air Basin. Atmos Environ 37, 3455–3468. https://doi.org/10.1016/S1352-2310(03)00269-3

Marshall, J.D., Swor, K.R., Nguyen, N.P., 2014. Prioritizing environmental justice and equality: Diesel emissions in Southern California. Environ Sci Technol 48, 4063–4068. https://doi.org/10.1021/es405167f

Marshall, J.D., Teoh, S.K., W. Nazaroff, W., 2005. Intake fraction of nonreactive vehicle emissions in US urban areas. Atmos Environ 39, 1363–1371. https://doi.org/10.1016/J.ATMOSENV.2004.11.008

McCollum, D., Yang, C., Yeh, S., Ogden, J., 2012. Deep greenhouse gas reduction scenarios for California – Strategic implications from the CA-TIMES energy-economic systems model. Energy Strategy Reviews 1, 19–32. https://doi.org/10.1016/j.esr.2011.12.003

McDonald, B.C., Gouw, J.A. de, Gilman, J.B., Jathar, S.H., Akherati, A., Cappa, C.D., Jimenez, J.L., Lee-Taylor, J., Hayes, P.L., McKeen, S.A., Cui, Y., Kim, S.-W., Gentner, D.R., Isaacman-VanWertz, G., Goldstein, A.H., Harley, R.A., Frost, G.J., Roberts, J.M., Ryerson, T.B., Trainer, M., 2018. Volatile chemical products emerging as largest petrochemical source of urban organic emissions. American Association for the Advancement of Science 359. https://doi.org/10.1126/science.aaq0524

McDonald, B.C., McBride, Z.C., Martin, E.W., Harley, R.A., 2014. High-resolution mapping of motor vehicle carbon dioxide emissions. Journal of Geophysical Research: Atmospheres 119, 5283–5298. https://doi.org/10.1002/2013jd021219

Millstein, D.E., Harley, R.A., 2009. Revised estimates of construction activity and emissions: Effects on ozone and elemental carbon concentrations in southern California. Atmos Environ 43, 6328–6335. https://doi.org/10.1016/j.atmosenv.2009.09.028

Miranda, M.L., Edwards, S.E., Keating, M.H., Paul, C.J., 2011. Making the Environmental Justice Grade: The Relative Burden of Air Pollution Exposure in the United States. Int J Environ Res Public Health 8, 1755–1771. https://doi.org/10.3390/ijerph8061755

NACR, 2012. User's Guide for the Advanced Research WRF (ARW) Modeling System Version 3.4itle [WWW Document]. URL https://www2.mmm.ucar.edu/wrf/users/docs/user_guide_V3/user_guide_V3.4/contents.html

Nardone, A., Chiang, J., Corburn, J., 2020. Historic Redlining and Urban Health Today in U.S. Cities. Environmental Justice 13, 109–119. https://doi.org/10.1089/ENV.2020.0011/ASSET/IMAGES/LARGE/ENV.2020.0011_FIGURE3.JPEG

Organization, W.H., 2021. WHO global air quality guidelines: particulate matter (PM2.5 and PM10), ozone, nitrogen dioxide, sulfur dioxide and carbon monoxide. World Health Organization.

Ostro, B., Hu, J., Goldberg, D., Reynolds, P., Hertz, A., Bernstein, L., Kleeman, M.J., 2015. Associations of Mortality with Long-Term Exposures to Fine and Ultrafine Particles, Species and Sources: Results from the California Teachers Study Cohort. Environ Health Perspect 123, 549–556. https://doi.org/10.1289/ehp.1408565

Ouyang, W., Gao, B., Cheng, H., Hao, Z., Wu, N., 2018. Exposure inequality assessment for PM2.5 and the potential association with environmental health in Beijing. Science of the Total Environment 635, 769–778. https://doi.org/10.1016/j.scitotenv.2018.04.190

Pan, S., Choi, Y., Roy, A., Jeon, W., 2017. Allocating emissions to 4 km and 1 km horizontal spatial resolutions and its impact on simulated NOx and O3 in Houston, TX. Atmos Environ 164, 398–415. https://doi.org/10.1016/j.atmosenv.2017.06.026

Panko, J., Kreider, M., Unice, K., 2018. Review of Tire Wear Emissions: A Review of Tire Emission Measurement Studies: Identification of Gaps and Future Needs. Non-Exhaust Emissions 147–160. https://doi.org/10.1016/B978-0-12-811770-5.00007-8

Paolella, D.A., Tessum, C.W., Adams, P.J., Apte, J.S., Chambliss, S., Hill, J., Muller, N.Z., Marshall, J.D., 2018. Effect of Model Spatial Resolution on Estimates of Fine Particulate Matter Exposure and Exposure Disparities in the United States. Environ Sci Technol Lett 5, 436–441. https://doi.org/10.1021/acs.estlett.8b00279

Perlin, S.A., Setzer, R.W., Creason, J., Sexton, K., 2002. Distribution of Industrial Air Emissions by Income and Race in The United States: An Approach Using the Toxic Release Inventory. Environ Sci Technol 29, 69–80. https://doi.org/10.1021/ES00001A008

Pope, C.A., Burnett, R.T., Thun, M.J., Calle, E.E., Krewski, D., Ito, K., Thurston, G.D., 2002. Lung Cancer, Cardiopulmonary Mortality, and Long-term Exposure to Fine Particulate Air Pollution. JAMA 287, 1132–1141. https://doi.org/10.1001/JAMA.287.9.1132

Pope, C.A., Thun, M.J., Namboodiri, M.M., Dockery, D.W., Evans, J.S., Speizer, F.E., Heath, C.W., 1995. Particulate Air Pollution as a Predictor of Mortality in a Prospective Study of U.S. Adults. Am J Respir Crit Care Med 151, 669–674. https://doi.org/10.1164/AJRCCM/151.3_PT_1.669

Ramanathan, V., Carmichael, G., 2008. Global and regional climate changes due to black carbon. Nature Geoscience 2008 1:4 1, 221–227. https://doi.org/10.1038/ngeo156

Ramaswami, A., Tong, K., Fang, A., Lal, R.M., Nagpure, A.S., Li, Y., Yu, H., Jiang, D., Russell, A.G., Shi, L., Chertow, M., Wang, Y., Wang, S., 2017. Urban cross-sector actions for carbon mitigation with local health co-benefits in China. Nature Climate Change 2017 7:10 7, 736–742. https://doi.org/10.1038/nclimate3373

Rowangould, G.M., 2013. A census of the US near-roadway population: Public health and environmental justice considerations. Transp Res D Transp Environ 25, 59–67. https://doi.org/10.1016/J.TRD.2013.08.003

Sampedro, J., Smith, S.J., Arto, I., González-Eguino, M., Markandya, A., Mulvaney, K.M., Pizarro-Irizar, C., Van Dingenen, R., 2020. Health co-benefits and mitigation costs as per the Paris Agreement under different technological pathways for energy supply. Environ Int 136, 105513. https://doi.org/10.1016/J.ENVINT.2020.105513

Sandanayake, M., Zhang, G., Setunge, S., Li, C.Q., Fang, J., 2016. Models and method for estimation and comparison of direct emissions in building construction in Australia and a case study. Energy Build. https://doi.org/10.1016/j.enbuild.2016.05.007

Saylor, R.D., Chameides, W.L., Chang, M.E., 1999. Demonstrating attainment in Atlanta using urban airshed model simulations: impact of boundary conditions and alternative forms of the NAAQS, Atmospheric Environment.

Schaap, M., Cuvelier, C., Hendriks, C., Bessagnet, B., Baldasano, J.M., Colette, A., Thunis, P., Karam, D., Fagerli, H., Graff, A., Kranenburg, R., Nyiri, A., Pay, M.T., Rouïl, L., Schulz, M., Simpson, D., Stern, R., Terrenoire, E., Wind, P., 2015. Performance of European chemistry transport models as function of horizontal resolution. Atmos Environ 112, 90–105. https://doi.org/10.1016/j.atmosenv.2015.04.003

Schfwarzenegger, V.Gov.A., 2005. Executive Order S-3-05 [WWW Document]. URL http://static1.squarespace.com/static/549885d4e4b0ba0bff5dc695/t/54d7f1e0e4b0f0798cee3010/1423438304744/California+Executive+Order+S-3-05+(June+2005).pdf (accessed 7.26.21).

Seinfeld, J.H., Pandis, S.N., 2016. Atmospheric chemistry and physics: from air pollution to climate change.

Shah, R.U., Robinson, E.S., Gu, P., Apte, J.S., Marshall, J.D., Robinson, A.L., Presto, A.A., 2020. Socio-economic disparities in exposure to urban restaurant emissions are larger than for traffic. Environmental Research Letters. https://doi.org/10.1088/1748-9326/abbc92

Sheppard, E., Leitner, H., Mcmaster, R.B., Tian, H., 1999. GIS-based measures of environmental equity: Exploring their sensitivity and significance. J Expo Sci Environ Epidemiol 9, 18–28. https://doi.org/10.1038/sj.jea.7500023

Stieb, D.M., Chen, L., Hystad, P., Beckerman, B.S., Jerrett, M., Tjepkema, M., Crouse, D.L., Omariba, W.D., Peters, P.A., Donkelaar, A. van, Martin, R. V, Burnett, R.T., Liu, S., Smith-Doiron, M., Dugandzic, R.M., 2016. A national study of the association between traffic-related air pollution and adverse pregnancy outcomes in Canada, 1999–2008. Environ Res 148, 513–526. https://doi.org/10.1016/j.envres.2016.04.025

Strak, M., Weinmayr, G., Rodopoulou, S., Chen, J., De Hoogh, K., Andersen, Z.J., Atkinson, R., Bauwelinck, M., Bekkevold, T., Bellander, T., Boutron-Ruault, M.C., Brandt, J., Cesaroni, G., Concin, H., Fecht, D., Forastiere, F., Gulliver, J., Hertel, O., Hoffmann, B., Hvidtfeldt, U.A., Janssen, N.A.H., Jöckel, K.H., Jørgensen, J.T., Ketzel, M., Klompmaker, J.O., Lager, A., Leander, K., Liu, S., Ljungman, P., Magnusson, P.K.E., Mehta, A.J., Nagel, G., Oftedal, B., Pershagen, G., Peters, A., Raaschou-Nielsen, O., Renzi, M., Rizzuto, D., Van Der Schouw, Y.T., Schramm, S., Severi, G., Sigsgaard, T., Sørensen, M., Stafoggia, M., Tjønneland, A., Monique Verschuren, W., Vienneau, D., Wolf, K., Katsouyanni, K., Brunekreef, B., Hoek, G., Samoli, E., 2021. Long term exposure to low level air pollution and mortality in eight European cohorts within the ELAPSE project: pooled analysis. The BMJ 374. https://doi.org/10.1136/BMJ.N1904

Su, J.G., Jerrett, M., Morello-Frosch, R., Jesdale, B.M., Kyle, A.D., 2012. Inequalities in cumulative environmental burdens among three urbanized counties in California. Environ Int 40, 79–87. https://doi.org/10.1016/j.envint.2011.11.003

Swart, N.C., Cole, J.N.S., Kharin, V. V., Lazare, M., Scinocca, J.F., Gillett, N.P., Anstey, J., Arora, V., Christian, J.R., Hanna, S., Jiao, Y., Lee, W.G., Majaess, F., Saenko, O.A., Seiler, C., Seinen, C., Shao, A., Sigmond, M., Solheim, L., Von Salzen, K., Yang, D., Winter, B., 2019. The Canadian Earth System Model version 5 (CanESM5.0.3). Geosci Model Dev 12, 4823–4873. https://doi.org/10.5194/GMD-12-4823-2019

Tagaris, E., Liao, K.J., Delucia, A.J., Deck, L., Amar, P., Russell, A.G., 2009. Potential impact of climate change on air pollution-related human health effects. Environ Sci Technol 43, 4979–

4988. https://doi.org/10.1021/ES803650W/ASSET/IMAGES/LARGE/ES-2008-03650W_0002.JPEG

Tan, J., Zhang, Y., Ma, W., Yu, Q., Wang, J., Chen, L., 2015. Impact of spatial resolution on air quality simulation: A case study in a highly industrialized area in Shanghai, China. Atmos Pollut Res 6, 322–333. https://doi.org/10.5094/apr.2015.036

Tessum, C.W., Apte, J.S., Goodkind, A.L., Muller, N.Z., Mullins, K.A., Paolella, D.A., Polasky, S., Springer, N.P., Thakrar, S.K., Marshall, J.D., Hill, J.D., 2019. Inequity in consumption of goods and services adds to racial-ethnic disparities in air pollution exposure. Proc Natl Acad Sci U S A. https://doi.org/10.1073/pnas.1818859116

Tessum, C.W., Paolella, D.A., Chambliss, S.E., Apte, J.S., Hill, J.D., Marshall, J.D., 2021. PM2.5 polluters disproportionately and systemically affect people of color in the United States. Sci Adv 7, 4491–4519. https://doi.org/10.1126/sciadv.abf4491

Thakrar, S.K., Balasubramanian, S., Adams, P.J., Azevedo, M.L., Muller, N.Z., Pandis, S.N., Polasky, S., Arden, C., Robinson, A.L., Apte, J.S., Tessum, C.W., Marshall, J.D., Hill, J.D., 2020. Reducing Mortality from Air Pollution in the United States by Targeting Specific Emission Sources. Cite This: Environ. Sci. Technol. Lett 7, 639–645. https://doi.org/10.1021/acs.estlett.0c00424

Thind, M.P.S., Tessum, C.W., Azevedo, I.L., Marshall, J.D., 2019. Fine Particulate Air Pollution from Electricity Generation in the US: Health Impacts by Race, Income, and Geography. Environ Sci Technol 53, 14010–14019. https://doi.org/10.1021/ACS.EST.9B02527

Thompson, T.M., Saari, R.K., Selin, N.E., 2014. Air quality resolution for health impact assessment: influence of regional characteristics. Atmos Chem Phys 14, 969–978. https://doi.org/10.5194/acp-14-969-2014

Thompson, T.M., Selin, N.E., 2012. Atmospheric Chemistry and Physics Influence of air quality model resolution on uncertainty associated with health impacts. Atmos. Chem. Phys 12, 9753–9762. https://doi.org/10.5194/acp-12-9753-2012

Trombetti, M., Thunis, P., Bessagnet, B., Clappier, A., Couvidat, F., Guevara, M., Kuenen, J., López-Aparicio, S., 2018. Spatial inter-comparison of Top-down emission inventories in European urban areas. Atmos Environ 173, 142–156. https://doi.org/10.1016/J.ATMOSENV.2017.10.032

United State Census Bureau, 2020. American Community Survey (ACS) data [WWW Document]. URL https://www2.census.gov/geo/tiger/TIGER_DP/ (accessed 12.14.20).

United State Census Bureau, 2019. OnTheMap: Data Overview (LODES Version 7).

US EPA, 2021. Technical Support Document (TSD) for the Final Revised Cross-State Air Pollution Rule Update for the 2008 Ozone Season NAAQS [WWW Document]. URL https://www.epa.gov/sites/default/files/2021-03/documents/estimating_pm2.5-_and_ozone-attributable_health_benefits_tsd_march_2021.pdf

US EPA, 2017. Emissions Inventory Guidance for Implementation of Ozone and Particulate Matter National Ambient Air Quality Standards (NAAQS) and Regional Haze Regulations.

US EPA, 1999. The Particle Pollution Report Current Understanding of Air Quality and Emissions through 2003 PM 2.5 Concentrations are Declining.

Valari, M., Menut, L., 2008. Does an Increase in Air Quality Models' Resolution Bring Surface Ozone Concentrations Closer to Reality? J Atmos Ocean Technol 25, 1955–1968. https://doi.org/10.1175/2008jtecha1123.1

Van Donkelaar, A., Martin, R. V., Brauer, M., Hsu, N.C., Kahn, R.A., Levy, R.C., Lyapustin, A., Sayer, A.M., Winker, D.M., 2016. Global Estimates of Fine Particulate Matter using a Combined Geophysical-Statistical Method with Information from Satellites, Models, and Monitors. Environ Sci Technol 50, 3762–3772. https://doi.org/10.1021/ACS.EST.5B05833

Van Donkelaar, A., Martin, R. V, Spurr, R.J.D., Burnett, R.T., 2015. High-Resolution Satellite-Derived PM2.5 from Optimal Estimation and Geographically Weighted Regression over North America. Environ Sci Technol 49, 10482–10491. https://doi.org/10.1021/acs.est.5b02076

Walker, G., 2009. Beyond distribution and proximity: Exploring the multiple spatialities of environmental justice, in: Antipode. John Wiley & Sons, Ltd, pp. 614–636. https://doi.org/10.1111/j.1467-8330.2009.00691.x

Wang, M., Sampson, P.D., Hu, J., Kleeman, M., Keller, J.P., Olives, C., Szpiro, A.A., Vedal, S., Kaufman, J.D., 2016. Combining Land-Use Regression and Chemical Transport Modeling in a Spatiotemporal Geostatistical Model for Ozone and PM2.5. Environ Sci Technol 50, 5111–5118. https://doi.org/10.1021/acs.est.5b06001

Wang, T., Jiang, Z., Zhao, B., Gu, Y., Liou, K.N., Kalandiyur, N., Zhang, D., Zhu, Y., 2020. Health co-benefits of achieving sustainable net-zero greenhouse gas emissions in California. Nat Sustain 3, 597–605. https://doi.org/10.1038/s41893-020-0520-y

West, J.J., Fiore, A.M., Horowitz, L.W., Mauzerall, D.L., 2017. Global health benefits of mitigating ozone pollution with methane emission controls. Proc Natl Acad Sci U S A 103, 3988–3993. https://doi.org/10.1073/pnas.0600201103

Woody, M.C., Baker, K.R., Hayes, P.L., Jimenez, J.L., Koo, B., Pye, H.O.T., 2016. Understanding sources of organic aerosol during CalNex-2010 using the CMAQ-VBS. Atmos. Chem. Phys 16, 4081–4100. https://doi.org/10.5194/acp-16-4081-2016

World Health Organization, 2021. Fact sheets: Ambient (outdoor) air pollution [WWW Document]. URL https://www.who.int/news-room/fact-sheets/detail/ambient-(outdoor)-air-quality-and-health (accessed 4.25.22).

Yang, C., Yeh, S., Zakerinia, S., Ramea, K., McCollum, D., 2015. Achieving California's 80% greenhouse gas reduction target in 2050: Technology, policy and scenario analysis using CA-TIMES energy economic systems model. Energy Policy 77.

Ying, Q., Fraser, M.P., Griffin, R.J., Chen, J., Kleeman, M.J., 2007. Verification of a source-oriented externally mixed air quality model during a severe photochemical smog episode. Atmos Environ 41.

Ying, Q., Lu, J., Allen, P., Livingstone, P., Kaduwela, A., Kleeman, M., 2008. Modeling air quality during the California Regional PM10/PM2.5 Air Quality Study (CRPAQS) using the UCD/CIT source-oriented air quality model – Part I. Base case model results. Atmos Environ 42, 8954–8966. https://doi.org/10.1016/J.ATMOSENV.2008.05.064

Yu, X., Venecek, M., Kumar, A., Hu, J., Tanrikulu, S., Soon, S.T., Tran, C., Fairley, D., Kleeman, M.J., 2019. Regional sources of airborne ultrafine particle number and mass concentrations in California. Atmos Chem Phys 19, 14677–14702. https://doi.org/10.5194/ACP-19-14677-2019

Zapata, C., Muller, N., Kleeman, M.J., 2013. PM2.5 co-benefits of climate change legislation part 1: California's AB 32. Clim Change 117, 377–397. https://doi.org/10.1007/s10584-012-0545-y

Zapata, C.B., Yang, C., Yeh, S., Ogden, J., Kleeman, M.J., 2018a. Low-carbon energy generates public health savings in California. Atmos Chem Phys 18, 4817–4830. https://doi.org/10.5194/acp-18-4817-2018

Zapata, C.B., Yang, C., Yeh, S., Ogden, J., Kleeman, M.J., 2018b. Estimating criteria pollutant emissions using the California Regional Multisector Air Quality Emissions (CA-REMARQUE) model v1.0. Geosci Model Dev 11, 1293–1320. https://doi.org/10.5194/gmd-11-1293-2018

Zapata, C.B., Yang, C., Yeh, S., Ogden, J., Kleeman, M.J., 2017. Low Carbon Energy Generates Public Health Savings in California. ACP.

Zasina, D., Zawadzki, J., 2017. Spatial surrogate for domestic combustion's air emissions: A case study from Silesian Metropolis, Poland. J Air Waste Manage Assoc 67, 1012–1019. https://doi.org/10.1080/10962247.2017.1316327

Zenou, Y., Boccard, N., 2000. Racial Discrimination and Redlining in Cities. J Urban Econ 48, 260–285. https://doi.org/10.1006/JUEC.1999.2166

Zhang, H., Denero, S.P., Joe, D.K., Lee, H.H., Chen, S.H., Michalakes, J., Kleeman, M.J., 2014. Development of a source oriented version of the WRF/Chem model and its application to the California regional PM10/PM2.5 air quality study. Atmos Chem Phys 14, 485–503. https://doi.org/10.5194/acp-14-485-2014

Zhang, L., Jacob, D.J., Downey, N. V, Wood, D.A., Blewitt, D., Carouge, C.C., van Donkelaar, A., Jones, D.B.A., Murray, L.T., Wang, Y., 2011. Improved estimate of the policy-relevant background ozone in the United States using the GEOS-Chem global model with 1/2° × 2/3° horizontal resolution over North America. Atmos Environ 45, 6769–6776. https://doi.org/10.1016/j.atmosenv.2011.07.054

Zhang, Y., Bowden, J.H., Adelman, Z., Naik, V., Horowitz, L.W., Smith, S.J., West, J.J., 2016. Co-benefits of global and regional greenhouse gas mitigation for US air quality in 2050. Atmos Chem Phys 16, 9533–9548. https://doi.org/10.5194/acp-16-9533-2016

Zhang, Y., Smith, S.J., Bowden, J.H., Adelman, Z., West, J.J., 2017. Co-benefits of global, domestic, and sectoral greenhouse gas mitigation for US air quality and human health in 2050. Environmental Research Letters 12. https://doi.org/10.1088/1748-9326/aa8f76

Zhao, B., Wang, P., Ma, J.Z., Zhu, S., Pozzer, A., Li, W., 2012. A high-resolution emission inventory of primary pollutants for the Huabei region, China. Atmos Chem Phys 12, 481–501. https://doi.org/10.5194/acp-12-481-2012

Zhao, B., Wang, T., Jiang, Z., Gu, Y., Liou, K.N., Kalandiyur, N., Gao, Y., Zhu, Y., 2019. Air Quality and Health Cobenefits of Different Deep Decarbonization Pathways in California. Environ Sci Technol 53, 7163–7171. https://doi.org/10.1021/acs.est.9b02385

Zhao, J., Gladson, L., Cromar, K., 2018. A novel environmental justice indicator for managing local air pollution. Int J Environ Res Public Health 15. https://doi.org/10.3390/ijerph15061260

Zheng, B., Zhang, Q., Tong, D., Chen, C., Hong, C., Li, M., Geng, G., Lei, Y., Huo, H., He, K., 2017. Resolution dependence of uncertainties in gridded emission inventories: A case study in Hebei, China. Atmos Chem Phys 17, 921–933. https://doi.org/10.5194/acp-17-921-2017

Zhou, Y., Zhao, Y., Mao, P., Zhang, Q., Zhang, J., Qiu, L., Yang, Y., 2017. Development of a high-resolution emission inventory and its evaluation and application through air quality modeling for Jiangsu Province, China. Atmos Chem Phys 17, 211–233. https://doi.org/10.5194/acp-17-211-2017

Appendix 1

S1.1 Introduction

Table S 1-1. Full list of California Air Resources Board (CARB) spatial surrogates

Surrogate Number	Surrogate Name	Surrogate Number	Surrogate Name
100	Airports	431	OILWELL
110	All_PavedRds	432	OIL_SEEP
120	AutobodyShops	440	Population
140	Comm_Airports	450	Pop_ComEmp_Hos
150	Drycleaners	460	Ports
160	DryLakeBeds	470	POTWs
170	Elev5000ft	480	PrimaryRoads
180	Employ_Roads	485	TRU
190	Forestland	490	Raillines
200	GasStations	491	LINEHAUL
211	GASWELL	500	RailYards
212	GAS_SEEP	510	Rds_HE
214	GAS_DISTRIBUTION	512	PEST_NO_ME_BR
220	GolfCourses	514	PEST_ME_BR
230	HE_Sqft	520	RefinieriesTankFarms
240	Hospitals	530	ResGasHeating
250	Housing	540	Residential_Chg
260	Housing_Autobody	550	ResNonResChg_IndEmp
270	Housing_Com_Emp	560	Restaurants
280	Housing_Restaurants	561	CHARBROILING
300	Industrial_Emp	570	ResWoodHeating
310	InlandShippingLanes	571	ResOilHeat
320	Irr_Cropland	572	ResLPGHeat
321	NON_PASTURE_AG	580	Res_NonRes_Chg
323	HARVEST	585	CONSTRUCTION_EQUIP
330	Lakes_Coastline	590	SandandGravelMines
332	FERRIES	610	SecondaryPavedRds
333	FISHING_COMM	620	Service_Com_Emp
334	TUG_TOW	630	Ser_ComEmp_Sch_GolfC_Cem
335	LAKES_RIVERS_RECBOAT	640	Shiplanes
336	OCEAN_LAKES_RECBOAT	641	CREW_SUPPLY
338	OCEAN_RECBOAT	650	SingleHousingUnits
339	DREDGE	660	UnpavedRds

341	LANDFILLS	672	Devplnd_HiDensity
343	COMPOST	674	Devplnd_LoDensity
350	LiveStock	680	Wineries
351	CAFO	690	LANDPREP
352	SILAGE	720	FARMRD_VMT
353	CATTLE_FEEDLOTS	730	INDUSTRIAL
354	CATTLE_RANGE	731	PRINT
355	POULTRY	732	WOOD
356	HORSE_RANCHES	733	AEROSPACE
360	Metrolink_Lines	734	CANCOIL
380	MiltaryBases	735	FABRIC
382	MILITARY_AIRCRAFT	736	MARINE
383	MILITARY_SHIPS	737	METALFURN
384	MILITARY_TACTICAL	738	METALPARTS
390	NonIrr_Pastureland	739	OTHERCOAT
391	PASTURE	740	PAPER
400	NonRes_Chg	741	PLASTIC
412	Fugitive_Dust	742	SEMICONDUCT
		743	WOODFURN

S1.2 Input Datasets

Table S 1-2. Available MPOs/COGs and CSTDM data source

County	Name	Counties Covered	Website
FRESNO	Fresno Council of Governments	Fresno	www.fresnocog.org
KERN	Kern Council of Governments	Kern	www.kerncog.org
KINGS	Kings County Association of Governments	Kings	www.kingscog.org
MADERA	Madera County Transportation Commission	Madera	http://www.ca-ilg.org/MPO-profile/madera-county-transportation-commission
SSM*	San Joaquin Council of Governments, Stanislaus Council of Governments, Merced County Association of Governments	San Joaquin, Stanislaus, Merced	www.sjcog.org www.stancog.org www.mcagov.org
MTC	Metropolitan Transportation Commission	Alameda, Contra Costa, Marin, Napa, San Francisco, San Mateo, Santa Clara, Solano, Sonoma	www.mtc.ca.gov
SACOG	Sacramento Area Council of Governments	El Dorado, Placer, Sacramento, Sutter, Yolo, Yuba	www.sacog.org
SCAG	Southern California Association of Governments	Imperial, Los Angeles, Orange, Riverside, San Bernardino, Ventura	www.scag.ca.gov
SLOCOG	San Luis Obispo Council of Governments	San Luis Obispo	www.slocog.org
SBCAG	Santa Barbara County Association of Governments	Santa Barbara	www.sbcag.org
SANDAG	San Diego Association of Governments	San Diego	www.sandag.org
others	California Department of Transportation / California Statewide Travel Demand Model	All remaining counties not listed above	http://www.dot.ca.gov/hq/tpp/offices/omsp/statewide_modeling/cstdm.html

** SSM: Counties of San Joaquin, Stanislaus, Merced*

S1.2.1 Improvement of spatial surrogates for industrial-related activities

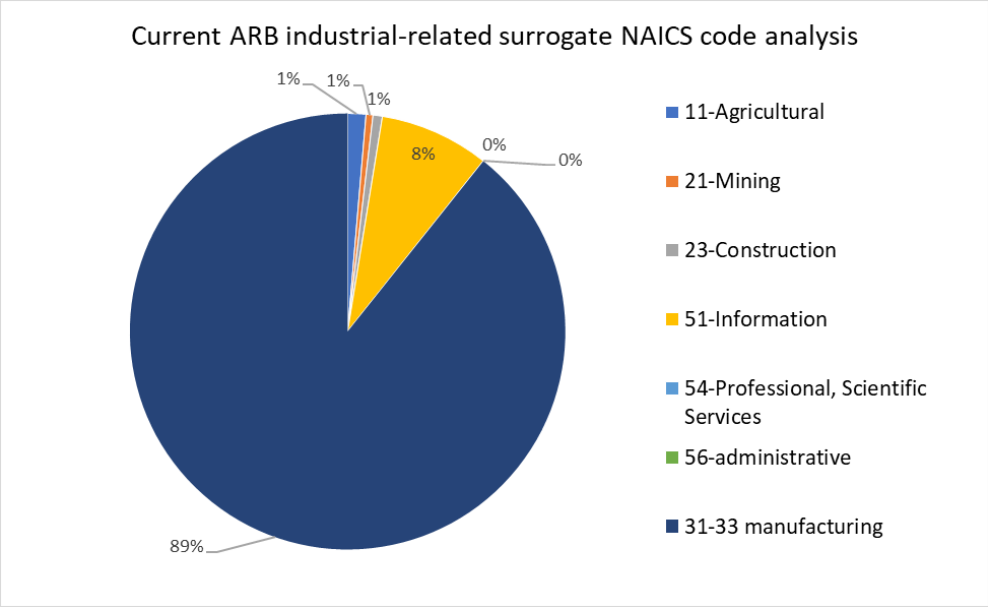

Figure S 1-1. NAICS codes composition analysis for current CARB industrial-related surrogate.

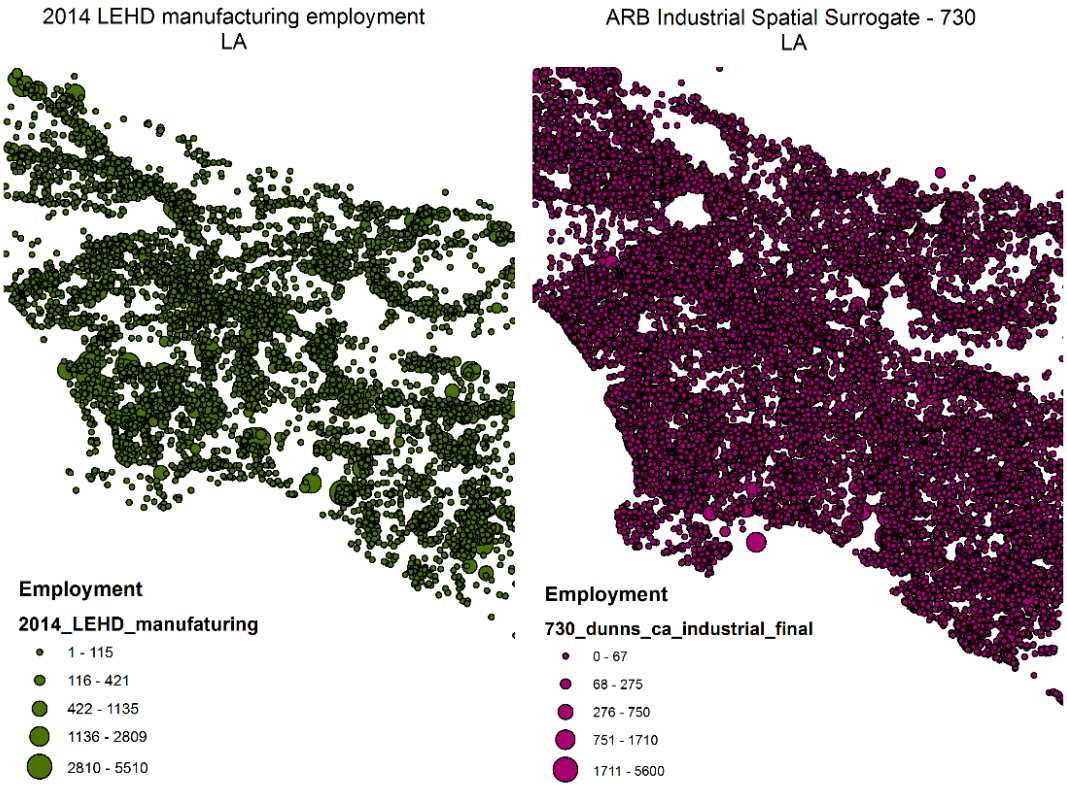

Figure S 1-2. Comparison of 2014 LEHD manufacturing employment and ARB industrial-related spatial surrogate 730 for Los Angeles area.

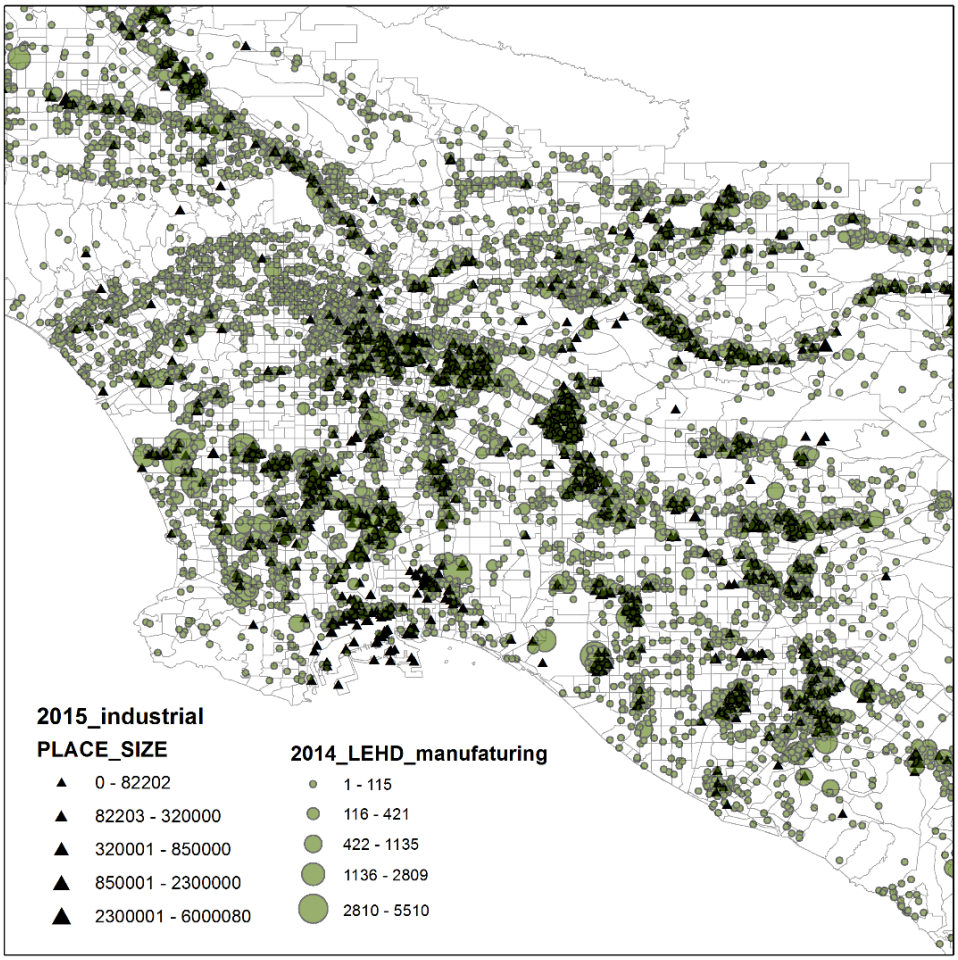

Figure S 1-3. Comparison between 2015 STORM industrial activity permit data and 2014 LEHD manufacturing employment data at Los Angeles area.

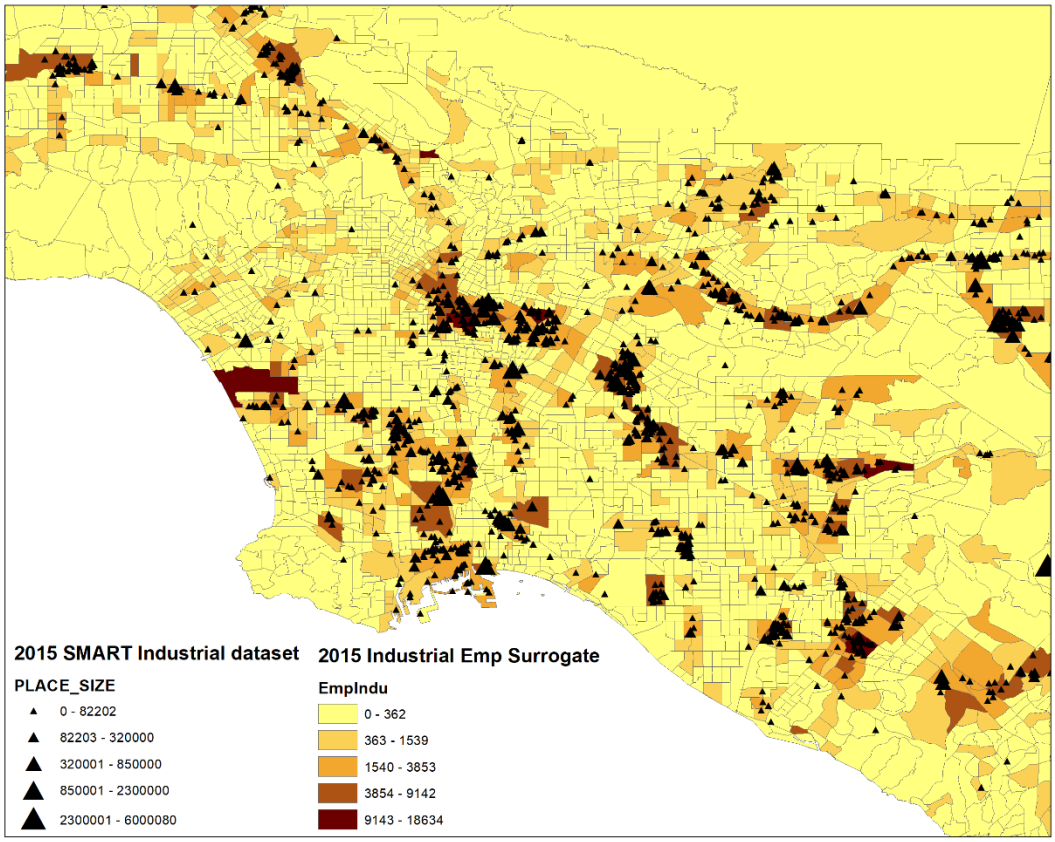

Figure S 1-4. Comparison between 2015 STORM industrial activity permit data and 2015 industrial employment surrogate created in Section 1.2.1 at Los Angeles area.

S1.2.2 Future off-road construction equipment surrogate

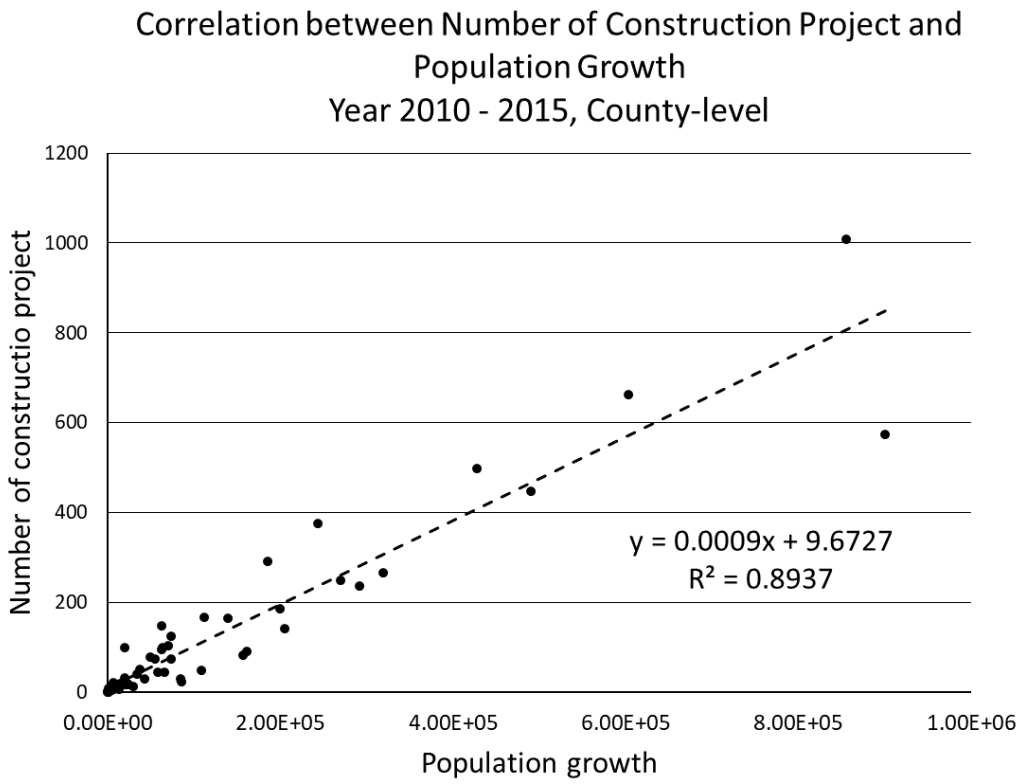

Figure S 1-5. Correlation between county-level number of construction project and population growth for year 2010 to 2015.

S1.2.3 Future on-road construction equipment surrogate

Figure S 1-6 summarizes the procedure to create future on-road construction surrogates as a flow chart. The red dashed box contains the steps needed to generate possible construction events at each future year. The green dashed box shows how to generate surrogate at the target year in shapefile format.

The datasets used by the statistical forecast model were provided by the University of California Pavement Research Center (UCPRC). Treatments are divided into 13 work codes, and further separated into 30 treatments. Each work code can be linked to several treatment as shown in Table S 1-3.

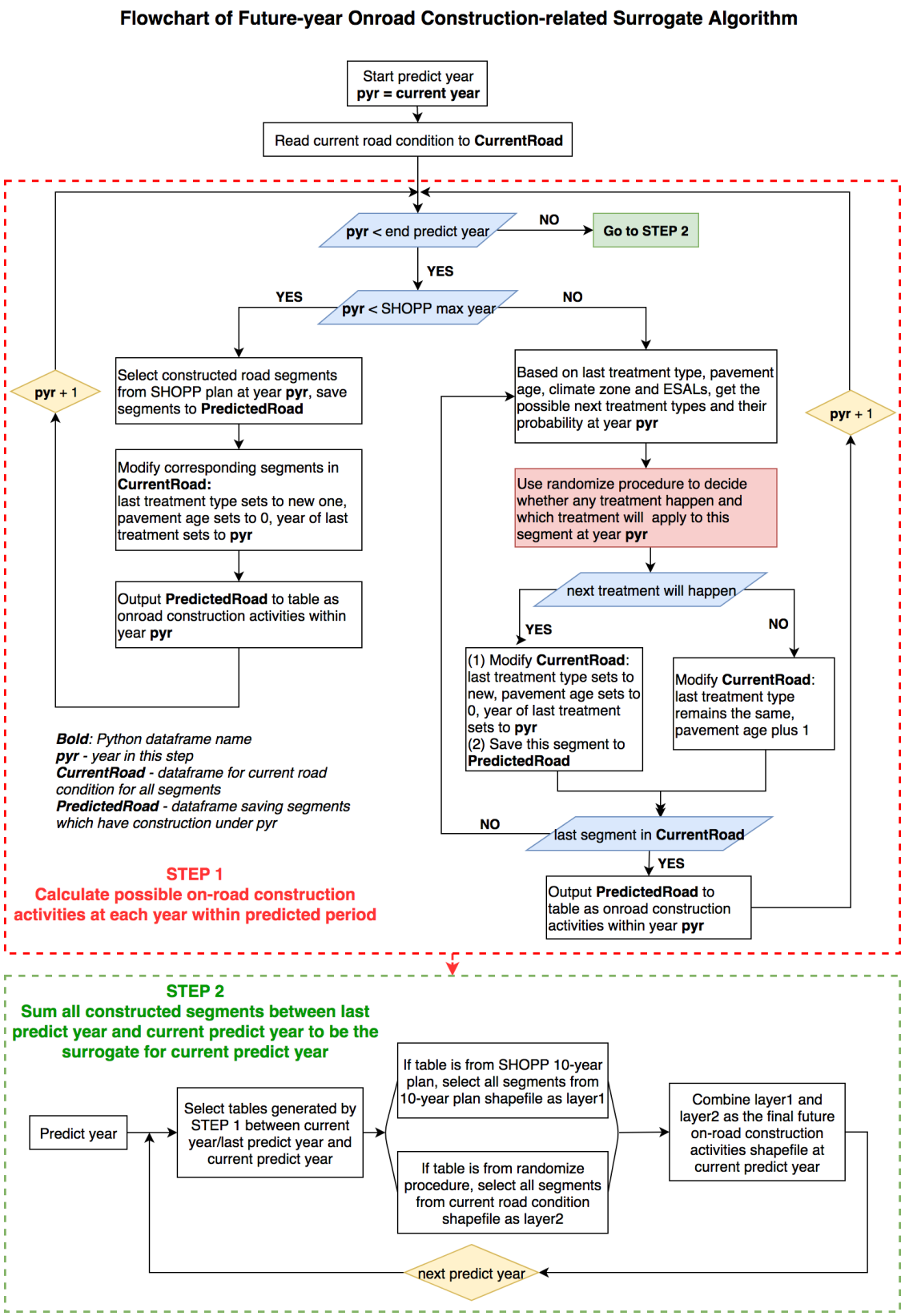

Figure S 1-6. Flowchart of future-year on-road construction-related surrogate algorithm

Table S 1-3 Cross reference table for treatments and work codes

Treatment	Work Code
New CRCP Lane	Lane replacement
CRCP Lane Replacement	Lane replacement
New PCC Lane	Lane replacement
PCC Lane Replacement	Lane replacement
PCC Overlay	Lane replacement
Repair PCC Slabs	Lane replacement
Dowel Bar Retrofit	Grind/Replace slabs
Groove PCC Pavement	Grind
Grinding	Grind
Grind/Replace Slabs	Grind/Replace slabs
Slab Replacement with Pre-Cast	Slab replacement
Slab Replacement	Slab replacement
Slab Replacement with Asphalt	Slab replacement
HMA Overlay on PCC	Lane replacement
Crack Seat and Overlay	CSOL
Full Depth Reclamation	Full Depth Reclamation
Hot In-Place Recycling	Cold In-Place
Cold In-Place Recycling	Cold In-Place
New HMA Lane	Lane replacement
HMA Lane Replacement	Lane replacement
HMA Thick Overlay	Thick Overlay
HMA Medium Overlay	Medium Overlay
HMA Thin Overlay	Thin Overlay
Mill and Fill	Thin Overlay
Microsurfacing	Seal Coat
Chip Seal	Seal Coat
Slurry Seal	Seal Coat
Digouts	Digouts
Fog Seal	Seal Coat
Unknown	Unknown
Unknown	Seal Cracks

The main features of each dataset used for the on-road construction statistical forecast model are as follows:

SHOPP 10-year plan: Master Work Plan xlsx. This spreadsheet tabulates each planned construction event from 2012 to 2022. Similar to Caltrans construction project records, SHOPP records are based on highway number, start/end postmile value, and start/end date for each constructed road segment. SHOPP records also describe the last treatment type which is needed to estimate the timing and type of subsequent treatments.

Current road segment condition: Network Master Data.xlsx. In this spreadsheet, each California highway is divided into coarse segments described by start/end post mile value, last treatment type, treatment age, climate zone, and ESAL level. Road segments in the Inland Valley, Central Coast, Desert, and South Coast are in the mild climate zone. Other road segments are in the severe climate region. ESAL has three level, level-A ESAL is larger than 300,000, level-C ESAL is smaller than 60,000, and level-B is between A and C. Level-A ESAL indicates heavy traffic loads to the road segment, which means reduced time between treatments. Treatment types in this table are summarized as work codes (Table S 1-3). Network Master Data also comes with a shapefile version, which was used in Step 2 shown in Figure S 1-6.

Probability of transitioning table: tpm.xlsx. This spreadsheet lists the probability that a construction project is needed to apply the next road treatment based on age, ESAL level and climate region. This table uses 30 treatment types instead of work code (Table S 1-3). Figure S 1-7 shows an example based on data within tpm.xlsx and clarifies how the 13 work codes relate to the 30 possible treatments. Figure S 1-7 assumes the road segment is ESAL level A, the climate zone is mild, and the last work code was grind. Under work code grind, there are two corresponding treatments – groove PCC pavement or grinding. If the last treatment was groove PCC pavement, the possible next treatment types and probabilities at each age year are shown in the upper figure. NA means no treatment will apply at this year. If the last treatment was grinding, the possible next treatment types and probabilities are shown in the bottom figure. The Monte

Carlo simulation assumes equal probabilities for all treatments under the same work code. The sum of treatment probabilities (including no treatment) is 1.0 in each year. Figure S 1-7 shows that the probability of treatment in a given year increases with age since last treatment.

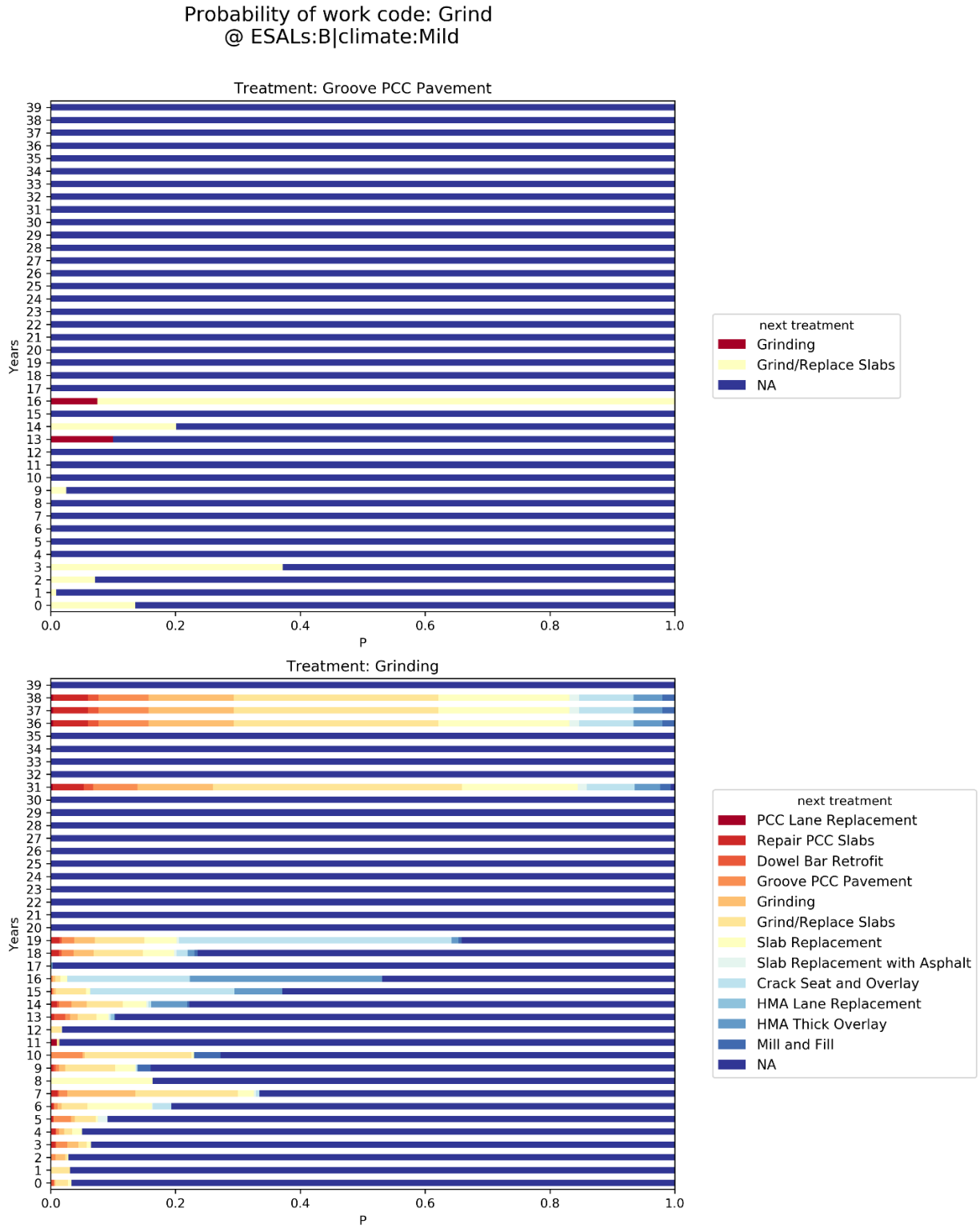

Figure S 1-7. Stacked probability of transitioning for treatment Grind at Level-B ESAL and mild climate zone. x-axis P is probability, y-axis Year is years since the last treatment – Grind happened. NA means no transitions.

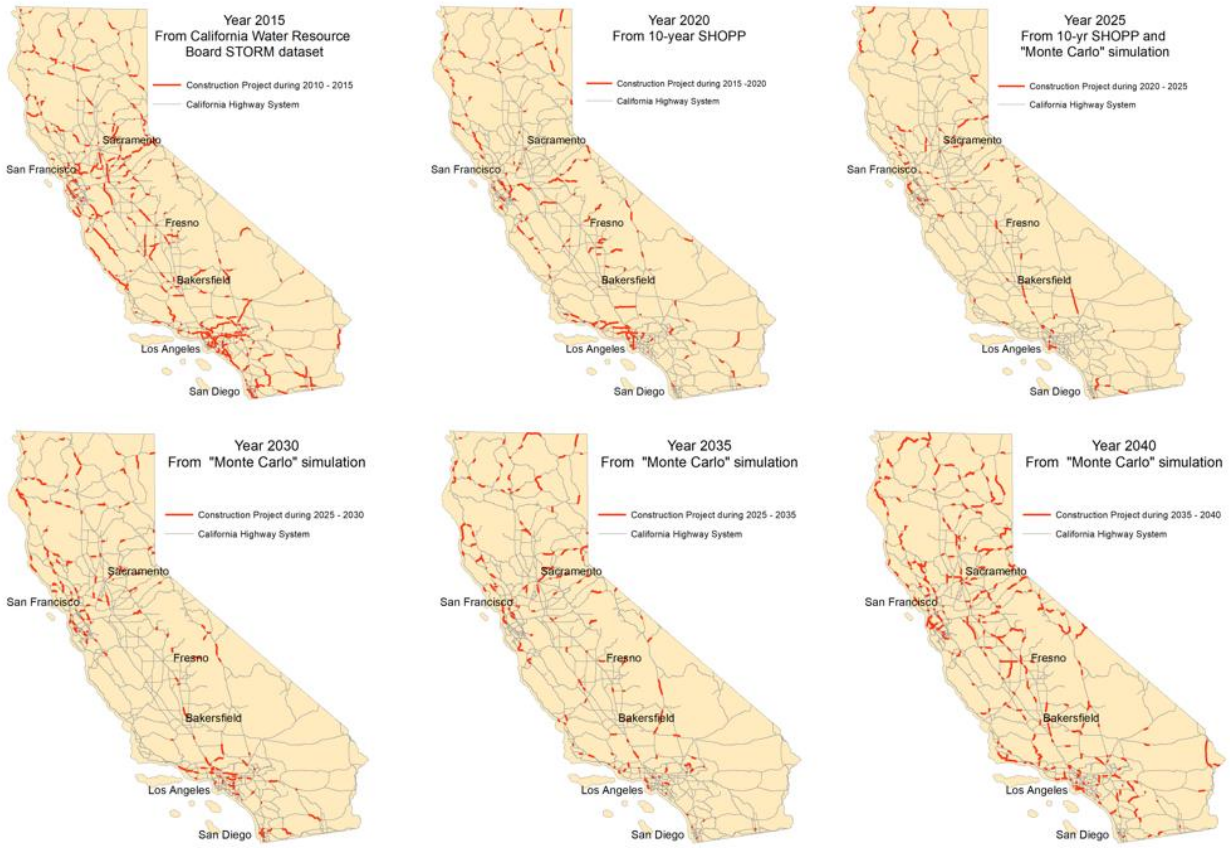

Figure S 1-8. 2015 on-road construction surrogate (from realistic dataset), and future year on-road construction surrogates (2020 -2040, in 5-yr interval). Red line sections indicate construction projects, gray lines indicate California highway system.

S1.3 Improvement of spatial surrogates from socio-economic data

Table S 1-4. Available years of Socioeconomic Datasets

MPO/COG/CSTDM	Available Years
FRESNO	2014, 2017, 2020, 2023, 2025, 2032, 2035, 2040
KERN	2014, 2017, 2020, 2023, 2025, 2032, 2035, 2040
KINGS	2014, 2017, 2018, 2020, 2023, 2025, 2032, 2035, 2040
SSM*	2014, 2017, 2020, 2023, 2025, 2032, 2035, 2040
MTC	2010, 2015, 2020, 2030, 2040
SACOG	2008, 2020, 2035
SCAG	2012, 2016, 2017, 2018, 2019, 2020, 2021, 2022, 2023, 2025, 2026, 2031
SLOCOG	2010, 2020, 2035
SBCAG	2010, 2020, 2035, 2040
SANDAG	2012, 2020, 2025, 2030, 2035, 2040, 2050
CSTDM	2010, 2015, 2020, 2035, 2040

** SSM: Counties of San Joaquin, Stanislaus, Merced*

S1.3.1 Surrogates of total population, total housing, single family and total employment

Table S 1-5 shows how total population was derived for different counties in California. The "Source" column in Table S 1-5 indicates the data source, the "Population Variables" column indicates the names of the variables used to construct total population, and the "Description" column describes how the variables were manipulated to create total population. "Existing" means directly translating the original variable; "Sum" means total population is the sum of variables listed in the "Population Variables" column. For example, FRESNO total population was calculated as the sum of population by age: POP0005, POP0514, POP1517, POP1824, POP2554, POP5564, POP6574, POP75. In contrast, MPO data for MTC has a variable named TOTPOP which can be directly converted to total population in the final product.

Table S 1-5. Strategy of improving total population spatial surrogate

County	Source	Population Variables	Description
FRESNO	MPOs	POP0005 POP0514 POP1517 POP1824 POP2554 POP5564 POP6574 POP75	Sum
KERN	MPOs	POP0005 POP0514 POP1517 POP1824 POP2554 POP5564 POP6574 POP75	Sum
KINGS	MPOs	POP0005 POP0514 POP1517 POP1824 POP2554 POP5564 POP6574 POP75	Sum
MADERA	MPOs	POP0005 POP0514 POP1517 POP1824 POP2554 POP5564 POP6574 POP75	Sum
SSM*	MPOs	POP0005 POP0514 POP1517 POP1824 POP2554 POP5564 POP6574 POP75	Sum
MTC	MPOs	TOTPOP	Existing
SACOG	MPOs	POP	Existing
SCAG	MPOs	POP	Existing
SLOCOG	MPOs	POP0019 POP2024 POP2544 POP4564 POP6500	Sum
SBCAG	MPOs	POPULATION	Existing
SANDAG	MPOs	hhp, gq_civ, gq_mil	Sum
others	CSTDM	Pop	Existing

** SSM: Counties of San Joaquin, Stanislaus, Merced*

Methods used to create single family spatial surrogates are shown in Table S 1-6. Counties in central California divide single family by age;. MTC and SCAG have existing single family housing. SLOCOG divides single family housing into detached (RUG1), attached (RUG2), and multi-family (RUG3). CSTDM and SACOG do not provide data on single family housing thus the fraction of single-family housing to total housing in these regions was estimated based on information from other MPOs/COGs. From the frequency distribution of (total households/single family households) where data is available for the year 2010, we found single family accounts for approximately 1/3 of total households. Based on these results, we calculated the number of single-family households as (total households/2.7) for CSTDM and SACOG.

Table S 1-6. Strategy of single-family households spatial surrogate

County	Source	Single Family	Description
FRESNO	MPOs	RU1_AGE1524RU1_AGE2564 RU1_AGE6574 RU1_AGE75	Sum
KERN	MPOs	RU1_AGE1524 RU1_AGE2564 RU1_AGE6574 RU1_AGE75	Sum
KINGS	MPOs	RU1_AGE1524 RU1_AGE2564 RU1_AGE6574 RU1_AGE75	Sum
MADERA	MPOs	RU1_AGE1524 RU1_AGE2564 RU1_AGE6574 RU1_AGE75	Sum
SSM*	MPOs	RU1_AGE1524 RU1_AGE2564 RU1_AGE6574 RU1_AGE75	Sum
MTC	MPOs	SFDU	Existing
SACOG		HouseHold / 2.7	Calculate
SCAG	MPOs	SFDU	Existing
SLOCOG	MPOs	RUG1 RUG2	Sum
SBCAG	MPOs	SINGLE_FAM	Existing
SANDAG	MPOs	hs_sf	Existing
others	CSTDM	Household / 2.7	Calculate

** SSM: Counties of San Joaquin, Stanislaus, Merced*

All MPOs/COGs and CSTDM have total employment and total household information that was directly used in the final spatial surrogate field. Table S 1-7 shows an example of how the total household spatial surrogate was developed in California.

Table S 1-7 Strategy used to create total household spatial surrogate

County	Source	Households Variables	Description
FRESNO	MPOs	TOTHH	Existing
KERN	MPOs	TOTHH	Existing
KINGS	MPOs	TOTHH	Existing
MADERA	MPOs	TOTHH	Existing
SSM*	MPOs	TOTHH	Existing
MTC	MPOs	TOTHH	Existing
SACOG	MPOs	HouseHold	Existing
SCAG	MPOs	HH	Existing
SLOCOG	MPOs	TOTHH	Existing
SBCAG	MPOs	HOUSEHOLDS	Existing
SANDAG	MPOs	hh	Existing
others	CSTDM	hh	Existing

** SSM: Counties of San Joaquin, Stanislaus, Merced*

*Table S 1-8. Accuracy analysis for total population and total households**

		2010		2015		If did interpolation
		POP	HH	POP	HH	
FRESNO	Total	940143.8287	317441.2761	1006201.626	340159.0301	Yes
	Census	932642	321955	974861	327780	2014
	Error	-0.80%	1.40%	-3.21%	-3.78%	2017
KERN	Total	787196.3049	253429.6716	878341.7144	285375	Yes
	Census	839627	**264461.31**[a]	882176	259700	2014
	Error	6.24%	4.17%	0.43%	***-9.89%***	2017
KINGS	Total	134607.3333	41014.66667	143410.6667	43736.66667	Yes
	Census	152982	40796.31	150965	**42561.45**	2014
	Error	***12.01%***	-0.54%	5.00%	-2.76%	2017
MTC	Total	7162615	2612482	7414396	2726202	No
	Census	7150739	2608023	7654869	2662572	
	Error	-0.17%	-0.17%	3.14%	-2.39%	
SACOG	Total	2265861.167	843891.8333	2392904.083	905428.9167	Yes
	Census	2134977	**785968.11**[a]	2260697	**823683.25**	2008
	Error	-6.13%	***-7.37%***	-5.85%	***-9.92%***	2020
SANDAG	Total	3091352.75	1090418.5	3253035.5	1131180.375	Yes
	Census	3224432	1068797	3299521	1094157	2015
	Error	4.13%	-2.02%	1.41%	-3.38%	2020
SCAG	Total	18045521.5	5759141.5	18755419.25	6081292	Yes
	Census	18051853	**5888842.77**[a]	18859954	5901400	2012
	Error	0.04%	2.20%	0.55%	-3.05%	2016
SLOCOG	Total	252958.0002	99755	259906.8185	102551.5	Yes
	Census	269599	103576	281401	**112396.08**[a]	2010
	Error	6.17%	3.69%	7.64%	8.76%	2020
SSM	Total	1354918	450019.6667	1474607.667	489779.6667	Yes
	Census	1455557	496956	1532949	505813	2014
	Error	6.91%	9.44%	3.81%	3.17%	2017
CSTDM LA county	Total	9516684	3308834	10022257	3552490	No
	Census	9818605	3262069	10137915	3,263,069	
	Error	3.07%	-1.43%	1.14%	-8.87%	
CSTDM Santa Clara county	Total	1682993	595954	1867548	661093	No
	Census	1781642	604204	1918044	621,463	
	Error	5.54%	1.37%	2.63%	-6.38%	

[a]Estimated from total households multiplied by an average occupancy rate of 0.93.

* error of each MPO/COG/CSTDM region for total population (POP) and total households (HH) calculated as (Census – Total)/Census

S1.3.2 Surrogates of industrial employment, service & commercial employment, agricultural employment

Table S 1-9, Table S 1-10 and Table S 1-11 show the optimal strategy to map MPOs/COGs and CSTDM employment data to the definitions in Table 1-2 without invoking LEHD information. The third column in each Table lists the MPOs/COGs fields that are combined using the operator listed in the fourth column to create intermediate variables (EAgri, EInd, or ESerCom) that contain employment within the NAICS codes listed in the fifth column. The operator "EXISTING" indicates a single native MPOs/COGs and CSTDM variable contributes to the intermediate variable, while the operator "SUM" indicates that multiple native MPOs/COGs and CSTDM variables contribute to the intermediate variable.

The basic uniform strategy shows that more than half of the employment data map to blended NAICS categories rather than the individual NAICS categories. For example, MTC, SCAG and SLOCOG combined Mining Sector (21) employment and Agriculture Sector (11) employment in a single native field. CSTDM and SACOG combined Agriculture Sector (11) employment with various Industry Category employment types. SACOG omitted employment in the Information Sector (51) and the Administrative Sector (56).

The intermediate variables defined in Table S 1-9, Table S 1-10, and Table S 1-11 provide a basis for interpolating the MPOs/COGs and CSTDM data for the years needed. Python function UniCategory.py creates these intermediate variables and assigns a value of 0.0001 to any missing values (for example, SACOG and CSTDM agriculture category).

Table S 1-9. Agricultural employment basic uniform strategy

County	Source	Agriculture Variables (EAgri)	Description	NAICS (11)
FRESNO	MPOs	EMPOTH	Existing	11
KERN	MPOs	AGRICULTUR	Existing	11
KINGS	MPOs	AGRICULTUR	Existing	11
MADERA	MPOs	AGRICULTUR	Existing	11
SSM*	MPOs	Ag_Other	Existing	11, **21**, **81****
MTC	MPOs	AGREMPN	Existing	11, **21****
SACOG	MPOs	(calculate#)	Estimate	
SCAG	MPOs	Ag_emp	Existing	11, **21**
SLOCOG	MPOs	AG_MINING	Existing	11, **21**
SBCAG	MPOs	AGRICULTUR	Existing	11
SANDAG	MPOs	emp_ag	Existing	11, **21**
others	CSTDM	(calculate#)	Estimate	

* SSM: Counties of San Joaquin, Stanislaus, Merced

** bold numbers mean this NAICS sector shouldn't be in this category

means this category will be calculated by Python programs

Table S 1-10. Industrial employment basic uniform strategy

County	Source	Industry Variables (EInd)	Description	NAICS (21, 22, 23, 31-33, 42, 48-49)
FRESNO	MPOs	EMPIND	Existing	21, 22, 31-33, 42, 48-49
KERN	MPOs	MINING, UTILITIES, CONSTRUCTN, MANUFACTUR, WHOLESALE, WAREHOUSE	Sum	21, 22, 23, 31-33, 42, 48-49
KINGS	MPOs	MINING, UTILITIES, CONSTRUCTN, MANUFACTUR, WHOLESALE, WAREHOUSE	Sum	21, 22, 23, 31-33, 42, 48-49
MADERA	MPOs	MINING, UTILITIES, CONSTRUCTN, MANUFACTUR, WHOLESALE, WAREHOUSE	Sum	21, 22, 23, 31-33, 42, 48-49
SSM*	MPOs	Industrial	Sum	22, 23, 31-33, 42, 48-49
MTC	MPOs	MWTEMPN	Existing	22, 31-33, 42, 48-49
SACOG	MPOs	EMPIND	Existing	**11****, 21, 22, 23, 31-33, 42, [49]***
SCAG	MPOs	Const_emp, Manu_emp, Whole_emp, Trans_emp	Sum	22, 23, 31-33, 42, 48-49
SLOCOG	MPOs	LIGHT_IND	Existing	22, 23, 31-33, 42, 48-49
SBCAG	MPOs	INDUSTRIAL	Existing	21, 22, 23, 31-33, 42, 48-49
SANDAG	MPOs	emp_const_, emp_const1, emp_utilit, emp_util_1, emp_cons_1, emp_cons_2, emp_mfg_pr, emp_mfg_of, emp_whsle_, emp_trans	Sum	22, 23, 31-33, 42, 48-49
others	CSTDM	Prim_Sec, Tran_U, Whole,	Sum	**11**, 22, 23, 31-33, 42, 48-49

* SSM: Counties of San Joaquin, Stanislaus, Merced

** bold numbers mean this NAICS sector shouldn't be in this category

*** bracket means this NAICS is missing in this MPO

Table S 1-11. Service & commercial employment basic uniform strategy

County	Source	Service & Commercial Variables (ESerCom)	Description	NAICS (44-45, 51-56, 61, 62, 71, 72, 81, 92)
FRESNO	MPOs	EMPRET, EMPOFC, EMPEDU, EMPMED, EMPSVC, EMOFOO, EMPGOV	Sum	**23**, 44-45, 51-56, 61, 62, 71, 72, 81, 92
KERN	MPOs	RETAIL, INFORMATIN, FINAN_INSR, REALESTATE, SVC_PROF, SVC_MNGMNT, SVC_ADMIN, EDUCATION, HEALTH, ENT_REC, ACCOMODTNS, FOOD, SVC_OTHER, PUBLIC	Sum	44-45, 51-56, 61, 62, 71, 72, 81, 92
KINGS	MPOs	RETAIL, INFORMATN, FINAN_INSR, REALESTATE, SVC_PROF, SVE_MNGMNT, SVC_ADMIN, EDUCATION, HEALTH, ENT_RECM, ACCOMODTNS, FOOD, SVC_OTHER, PUBLIC	Sum	44-45, 51-56, 61, 62, 71, 72, 81, 92
MADERA	MPOs	RETAIL, INFORMATN, FINAN_INSR, REALESTATE, SVC_PROF, SVE_MNGMNT, SVC_ADMIN, EDUCATION, HEALTH, ENT_RECM, ACCOMODTNS, FOOD, SVC_OTHER, PUBLIC	Sum	44-45, 51-56, 61, 62, 71, 72, 81, 92
SSM*	MPOs	Retail, Office, Public_Civ, Education, Hotel_Hosp, Health	Sum	44-45, 51-56, 61, 62, 71, 72, 92
MTC	MPOs	RETEMPN, FPSEMPN, HEREMPN, OTHEMPN	Sum	**23**, 44-45, 51-56, 61, 62, 71, 72, 81, 92
SACOG	MPOs	EMPEDU, EMPFOOD, EMPGOV, EMPOFC, EMPOTH, EMPRET, EMPSVC, EMPMED	Sum	44-45, **48**, [51]**, 52-55, [56], 61, 62, 71, 72, 81, 92
SCAG	MPOs	Ret_emp, Infor_emp, FIRE_emp, Prof_emp, Educ_emp, ArtEnt_emp, OthSer_emp, PubAdm_emp	Sum	44-45, 51-56, 61, 62, 71, 72, 81, 92
SLOCOG	MPOs	RETAIL, OFFICE, GOVERNMENT, EDUCHEALTH, LEIS_HOSP, OTHERSVCS	Sum	44-45, 51-56, 61, 62, 71, 72, 81, 92
SBCAG	MPOs	COMMERCIAL, OFFICE_EMP, SERVICE_EM	Sum	44-45, 51-56, 61, 62, 71, 72, 81, 92
SANDAG	MPOs	emp_retail, emp_prof_b, emp_prof_1, emp_pvt_ed, emp_pvt__1, emp_health, emp_person, emp_amusem, emp_hotel, emp_restau, emp_pers_1, emp_religi, emp_pvt_hh, emp_state_, emp_fed_no, emp_fed_mi, emp_state1, emp_stat_1, emp_public	Sum	44-45, 51-56, 61, 62, 71, 72, 81, 92
others	CSTDM	Retail, Office, EduMed, LeisHops, OthServ	Sum	44-45, 51-56, 61, 62, 71, 72, 81, 92

* SSM: Counties of San Joaquin, Stanislaus, Merced

** bracket means this NAICS is missing in this county

When MPOs/COGs and CSTDM data did not align with standard output years, interpolation to those standard output years was performed using the Python for intermediate variables (EAgri, EInd, or ESerCom) and any native MPO/CSTDM variables that were used with the LEHD modification procedure described in following paragraphs. Table S 1-12 lists the native categories which required interpolation, and which intermediate variable they contribute to. Using Fresno as an example, the category EMPOFC requires interpolation. Following interpolation, Construction (23) was separated from the Service & Commercial employment total and added to Industry employment total to satisfy the standard NAICS category definitions.

Table S 1-12. Other categories which required interpolation by year

	Categories which need to be interpolated		
County	**Agriculture (EAgri)**	**Industry (EInd)**	**Service & commercial (ESerCom)**
FRESNO		EMPOFC (23)	
SSM*	Ag_Other (21, 81)		
MTC	AGREMPN (21)	OTHEMPN (23)	
SACOG	EMPIND (11)		EMPSVC (48), EMPOFC
SCAG	Ag_emp (21)		
SLOCOG	AG_MINING (21)		
SANDAG	emp_ag (21)		
CSTDM	Prim_Sec (11)		

* SSM: Counties of San Joaquin, Stanislaus, Merced

Table S 1-13 summarizes a variable comparison table for step of unifying category and step of interpolating by years. For example, variable TPOP (total population) in unifying category corresponds to TotPop in step of interpolating by years.

Table S 1-13. Lookup table for variable names between step of unifying category and step of interpolating by years

Type	Variable Name in UniCategory.py	Variable Name in InterpoYear.py
Common	TPOP	TotPop
	THH	TotHousing
	SF	SingleF
	MF	MultiF
	TEmp	TotalEmp
	EAgri	EmpAgri
	EInd	EmpIndu
	ESerCom	EmpSerCom
FRESNO	EMPOFC	fre_ofc
SSM*	Ag_Other	ssm_agri
MTC	AGREMPN	mtc_agri
	OTHEMPN	mtc_oth
SACOG	EMPIND	sac_ind
	EMPOFC	sac_ofc
	EMPSVC	sac_svc
SCAG	Ag_emp	sca_agri
SLOCOG	Ag_Mining	slo_agmin
SANDAG	emp_ag	san_agri
CSTDM	Prim_sec	cst_prim

* SSM: Counties of San Joaquin, Stanislaus, Merced

LEHD has very detailed employment information corresponding to individual NAICS code categories. It is possible to examine the employment in the LEHD sectors corresponding to each lumped intermediate variable summarized in Table S 1-9 through Table S 1-11. The ratio of each individual LEHD sector to the LEHD lumped category total provides a profile that can be multiplied into the MPO/CSTDM lumped intermediate variable to estimate employment by individual NAICS code. This procedure yields employment fields for each NAICS code but it inherently assumes that the LEHD employment profile stays constant for all years.

Table S 1-14 shows which MPOs/COGs or CSTDM regions required disaggregation using LEHD data and what operations were carried out to estimate employment for each NAICS categories. Using FRESNO as an example, construction sector (23) is in the MPO variable EMPOFC along with various

unrelated service and commercial employment categories (51, 52, 53, 54, 55, 56). The fraction of construction employment in EMPOFC f(23) is estimated as LEHD construction sector (23) divided by LEHD sectors (23+51+52+53+54+55+56).

Table S 1-14. Calculation expression for obtaining fraction of specific sectors by using LEHD dataset

County	Sharing	Expression (Number is NAICS code)
FRESNO	f(23)	23 / (23 + 51 + 52 + 53 + 54 + 55 + 56))
SSM*	f(21)	21 / (11 + 21 + 81)
	f(81)	81 / (11 + 21 + 81)
MTC	f(21)	21 / (11 + 21)
	f(23)	23 / (23 + 51 + 92)
SACOG	f(11)	11 / (11 + 21 + 22 + 23 + 31-33 + 42)
	f(48-49)	48-49 / (48-49 + 71 + 81)
SLOCOG	f(21)	21 / (11 + 21)
SANDAG	F(21)	21 / (11 + 21)
CSTDM	f(11)	11 / (11 + 21 + 23 + 31-33)

* SSM: Counties of San Joaquin, Stanislaus, Merced

Table S 1-15. lists all expressions that separate misplaced sectors from native MPOs/COGs and CSTDM variables and place them in other categories to be consistent with the NAICS variables listed in Table 1-2. Using FRESNO as an example, estimated Construction employment (23) is separated from the Service and Commercial Employment total and added to the Industry employment total.

A special case occurs for the SACOG EMPSVC variable that includes contributions from NAICS category 48. The standard NAICS definitions group categories 48-49 and LEHD data follow this convention. Thus, LEHD data can only estimate the combined total of NAICS 48-49 from the variable EMPSVC in the SACOG. In the current study the combined ratio of NAICS 48-49 was used to estimate the fraction of EMPSVC attributed to NAICS 48 in the SACOG.

Table S 1-15. Calculation expression for modifying MPOs/COGs and CSTDM categories by using LEHD OnTheMap dataset

County	Variables	Expression
FRESNO	EmpIndu	EmpIndu + fre_ofc * f(23)
	EmpSerCom	EmpSerCom - fre_ofc * f(23)
SSM**	EmpAgri	EmpAgri – ssm_agri * (f(21) + f(81))
	EmpIndu	EmpIndu + ssm_agri * f(21)
	EmpSerCom	EmpSerCom + ssm_agri * f(81)
MTC	EmpAgri	EmpAgri – mtc_agri * f(21)
	EmpIndu	EmpIndu + mtc_agri * f(21) + mtc_oth * f(23)
	EmpSerCom	EmpSerCom - mtc_oth * f(23)
SACOG	EmpAgri	EmpAgri + sac_ind * f(11)
	EmpIndu	EmpIndu – sac_ind * f(11) + sac_svc * f(48-49)
	EmpSerCom	EmpSerCom - sac_svc * f(48-49)
SLOCOG	EmpAgri	EmpAgri – slo_agmin * f(21)
	EmpIndu	EmpIndu + slo_agmin * f(21)
SANDAG	EmpAgri	EmpAgri – san_agri * f(21)
	EmpIndu	EmpIndu + san_agri * f(21)
CSTDM	EmpAgri	EmpAgri + cst_prim * f(11)
	EmpIndu	EmpIndu - cst_prim * f(11)

** SSM: Counties of San Joaquin, Stanislaus, Merced

Missing Service & Commercial employment data in the SACOG was estimated using LEHD data and growth rate derived from the SACOG data. A specific program was written to address this missing SACOG data problem for Information employment (51) and Administrative and Support employment (56). A summary of the procedure is presented below:

- Base year
  (1) Calculate ratio of (51, 56) in MPO and LEHD data to make sure the sector from LEHD is consistent with MPO data. Here we choose EMPOFC category in the SACOG data as a reference of (51, 56) ratio since EMPOFC is the most similar category to (51, 61):

$$f_{MPO/LEHD} = \frac{EMPOFC\ in\ MPO}{EMPOFC\ sector\ in\ LEHD}$$

  (2) Calculate (51, 61) value in MPO:

$$ValueInMPO_{(51,56)} = f_{MPO/LEHD} \times ValueInLEHD_{(51,56)}$$

  (3) Modify corresponding MPO/CSTDM-based category:

$$EmpSerCom = EmpSerCom + VauleInMPO_{(51,56)}^{base\ year}$$

(4) Update total employment:

$$TotalEmp = TotalEmp + VauleInMPO_{(51,56)}^{base\ year}$$

- Future year

(1) Use base year data to calculate future year data. First to calculate growth rate of (51, 56):

$$Growth\ Rate_{(51,56)} = \frac{VauleInMPO_{EMPOFC}^{future\ year} - VauleInMPO_{EMPOFC}^{base\ year}}{VauleInMPO_{EMPOFC}^{base\ year}}$$

(2) Calculate future year (51, 56):

$$VauleInMPO_{(51,56)}^{future\ year} = VauleInMPO_{(51,56)}^{base\ year}\ (1 + Growth\ Rate_{(51,56)})$$

(3) Modify corresponding MPO/CSTDM-based category:

$$EmpSerCom = EmpSerCom + VauleInMPO_{(51,56)}^{future\ year}$$

(4) Update total employment:

$$TotalEmp = TotalEmp + VauleInMPO_{(51,56)}^{future\ year}$$

S1.4 Relationships between surrogates and emissions

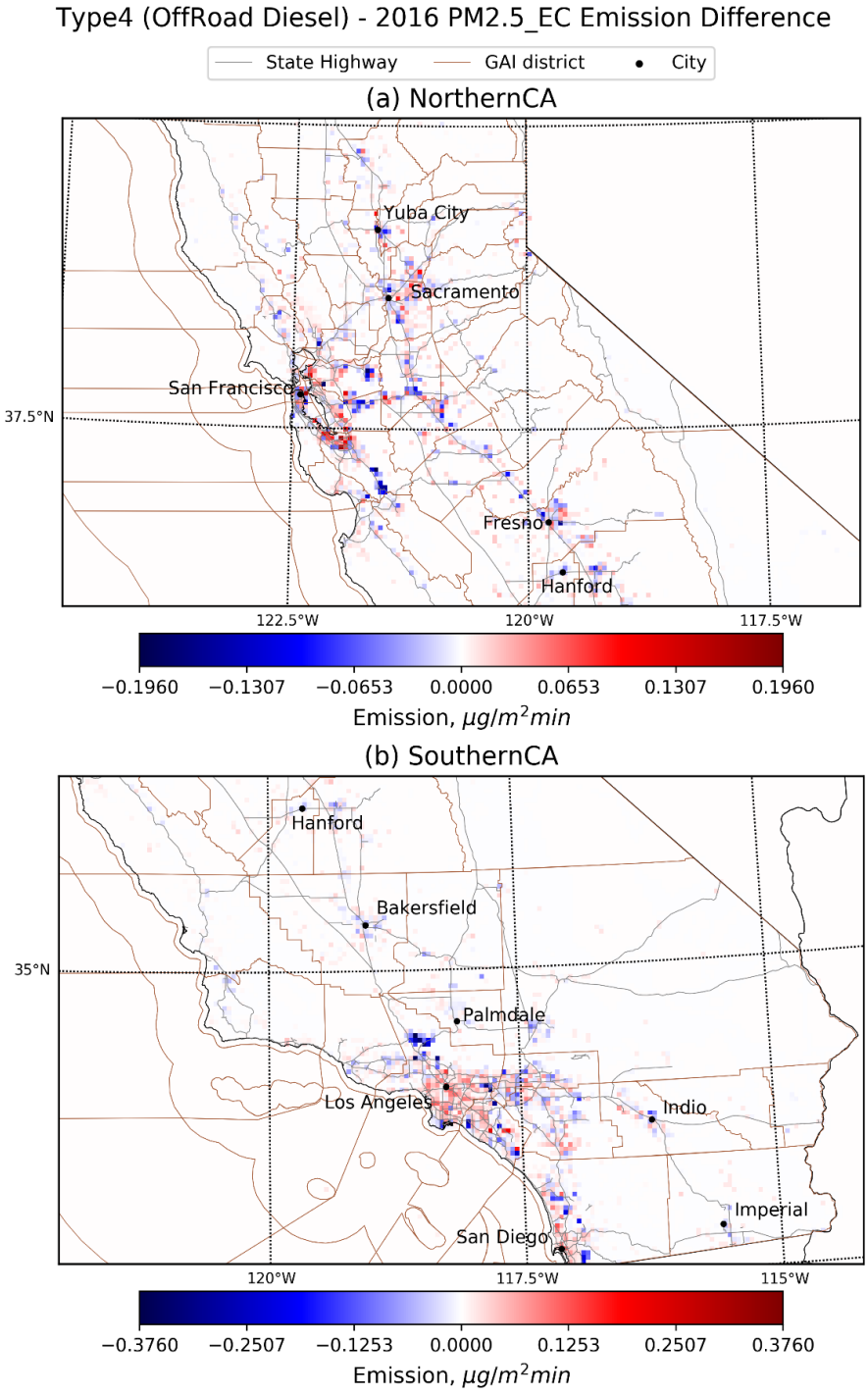

Figure S 1-9. Annual PM2.5 EC Emission difference between updated case and base case for type 4 – off-road diesel emission on 2016. Figure (a) shows northern California, figure (b) shows southern California.

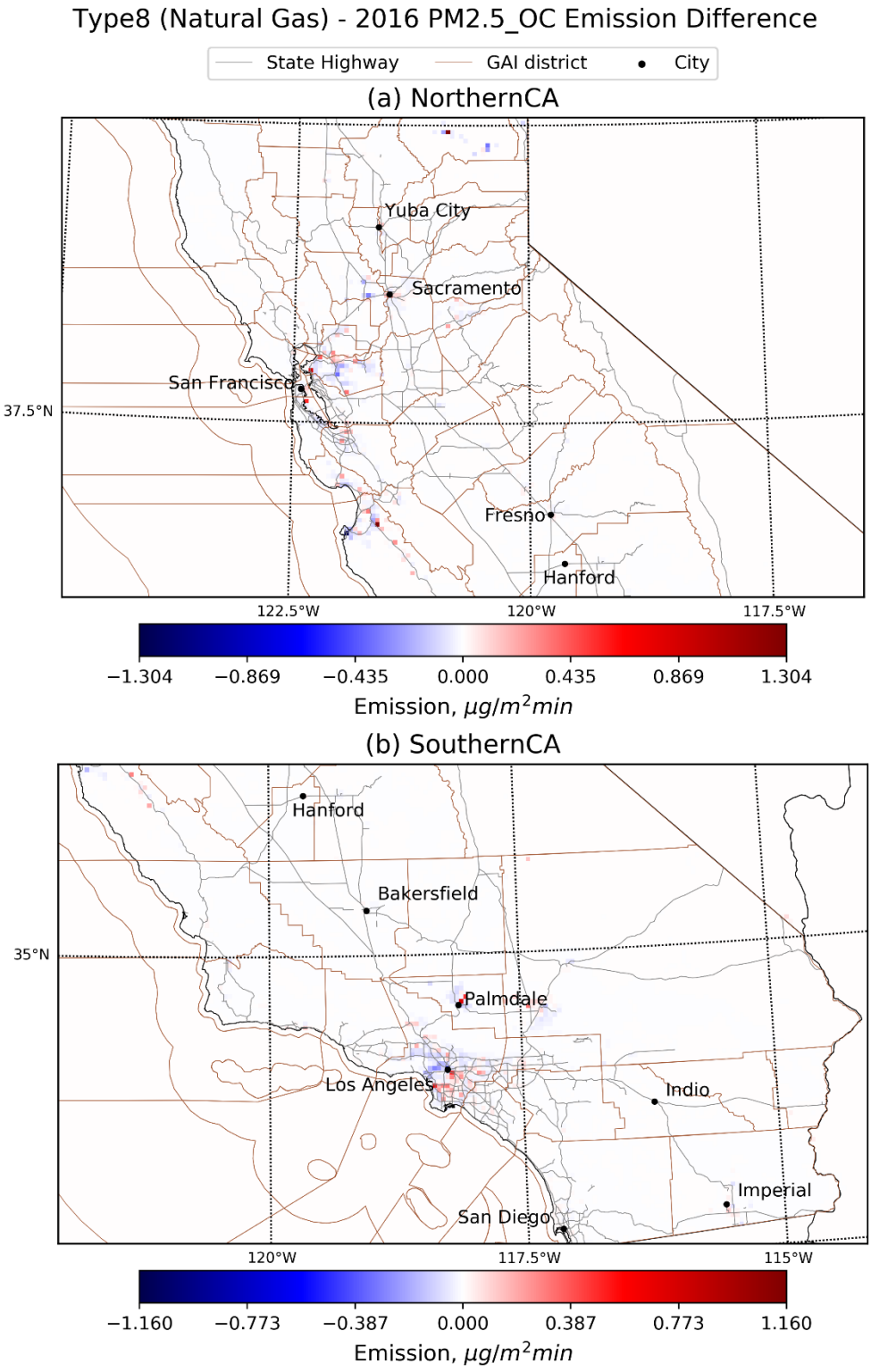

Figure S 1-10. Annual PM2.5 OC Emission difference between updated case and base case for type 8 – natural gas emission on 2016. Figure (a) shows northern California, figure (b) shows southern California.

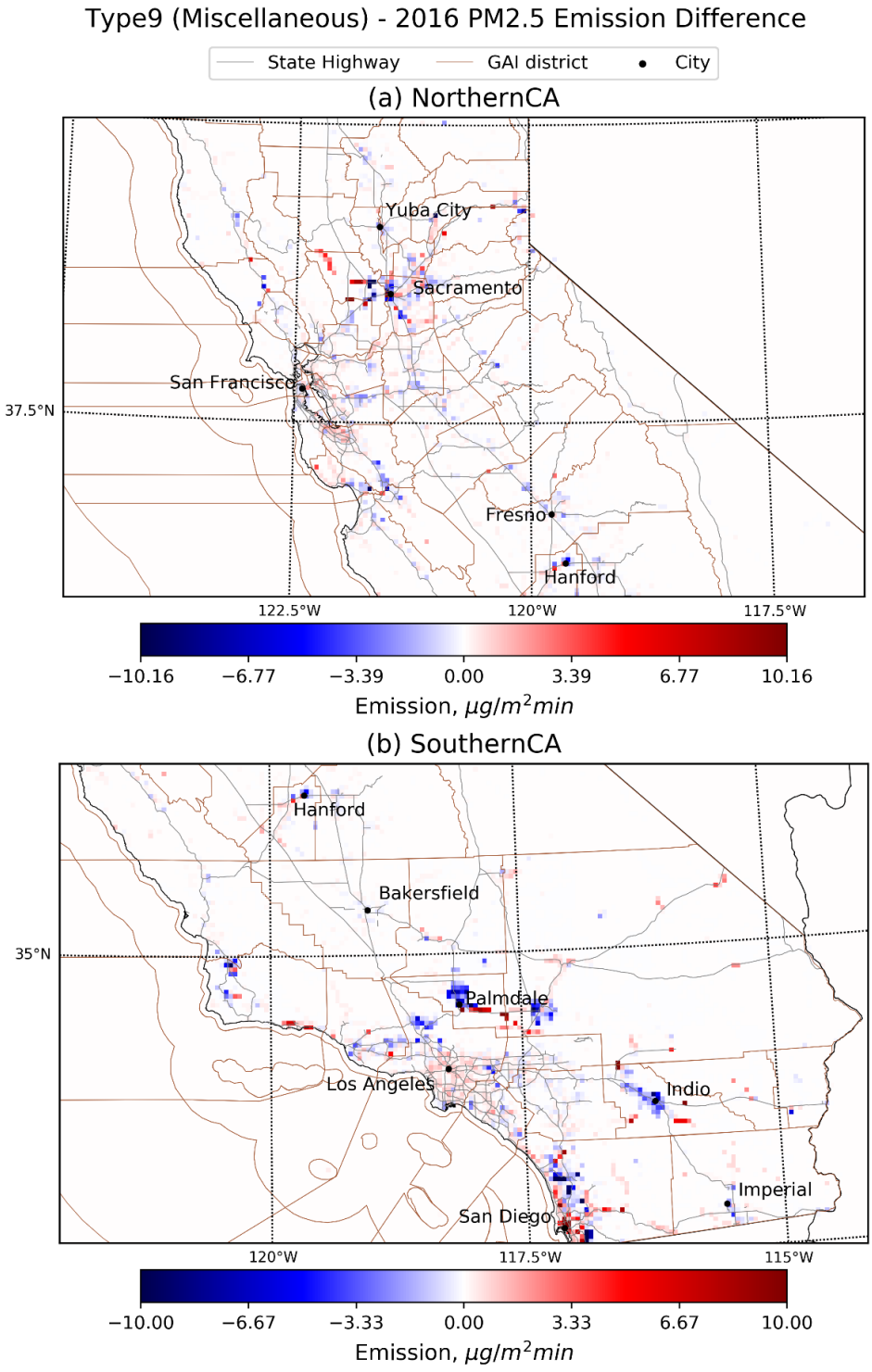

Figure S 1-11. Annual PM2.5 Emission difference between updated case and base case for type 9 – miscellaneous emission on 2016. Figure (a) shows northern California, figure (b) shows southern California.

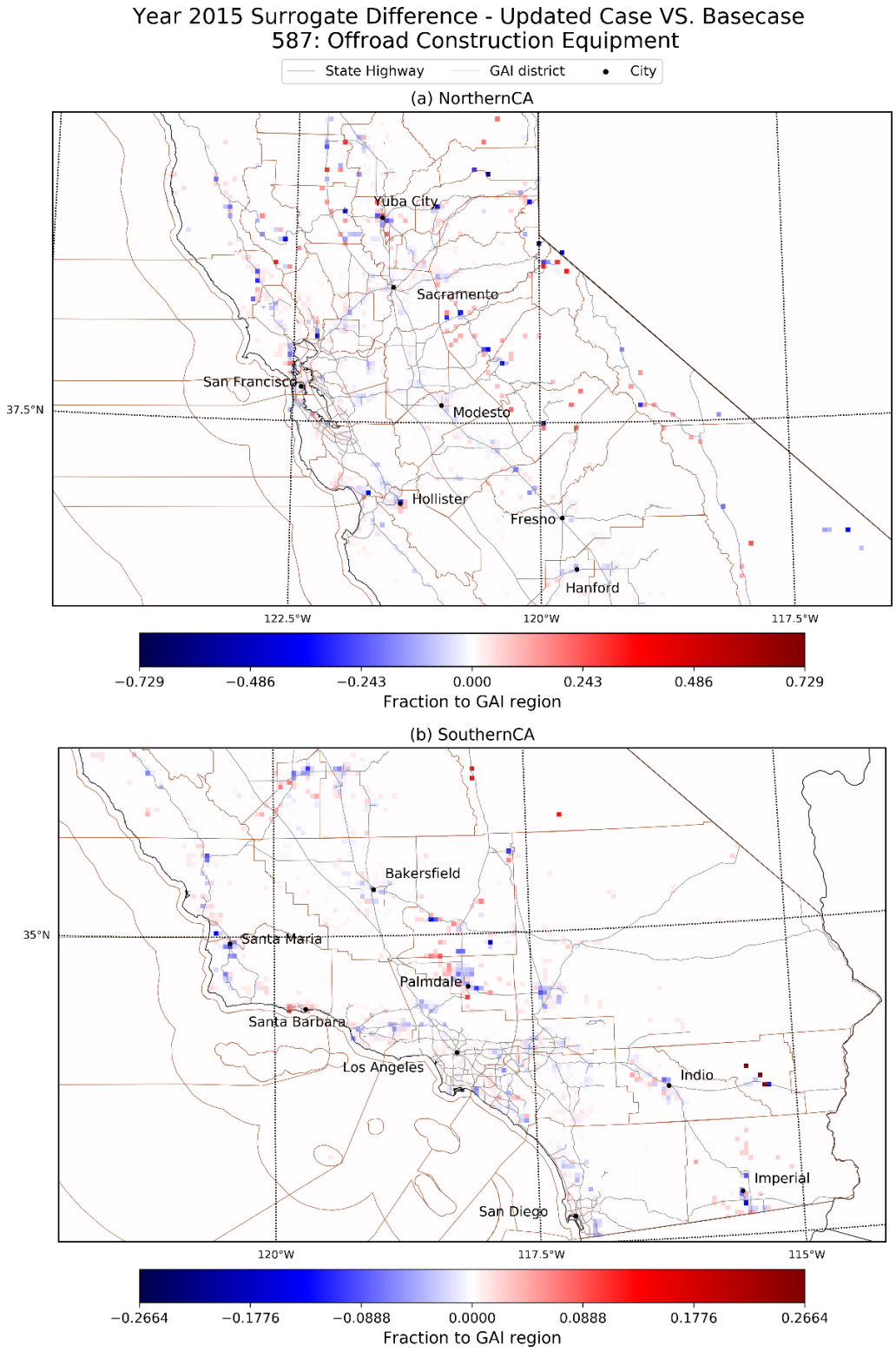

Figure S 1-12. Surrogate difference between updated case off-road construction equipment surrogate 587 and base case surrogate 585 for year 2015. (a) shows Northern California, (b) shows Southern California. Gray line is California State Highway

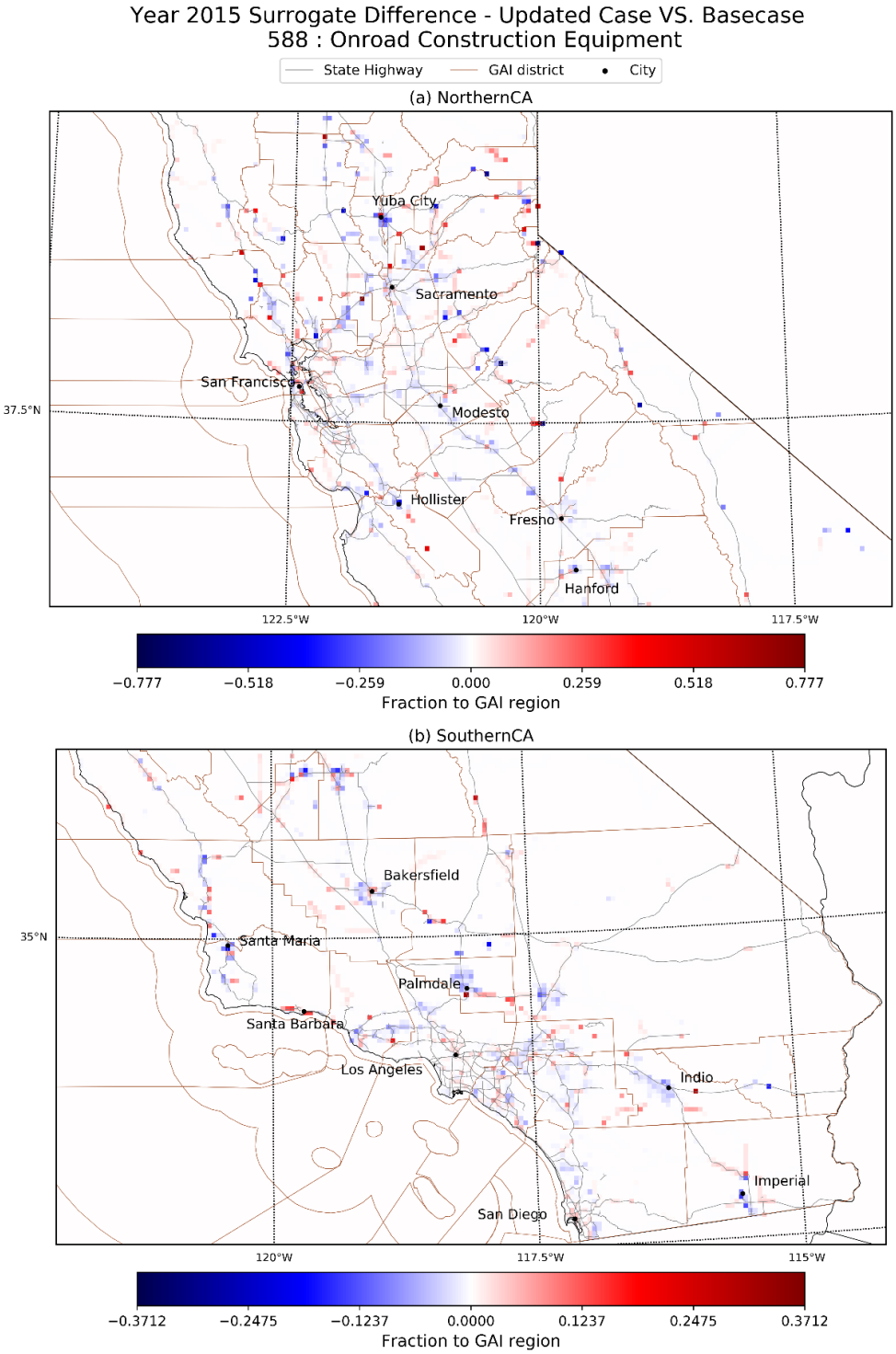

Figure S 1-13. Surrogate difference between updated case on-road construction equipment surrogate 588 and base case surrogate 585 for year 2015. (a) shows Northern California, (b) shows Southern California. Gray line is California State Highway

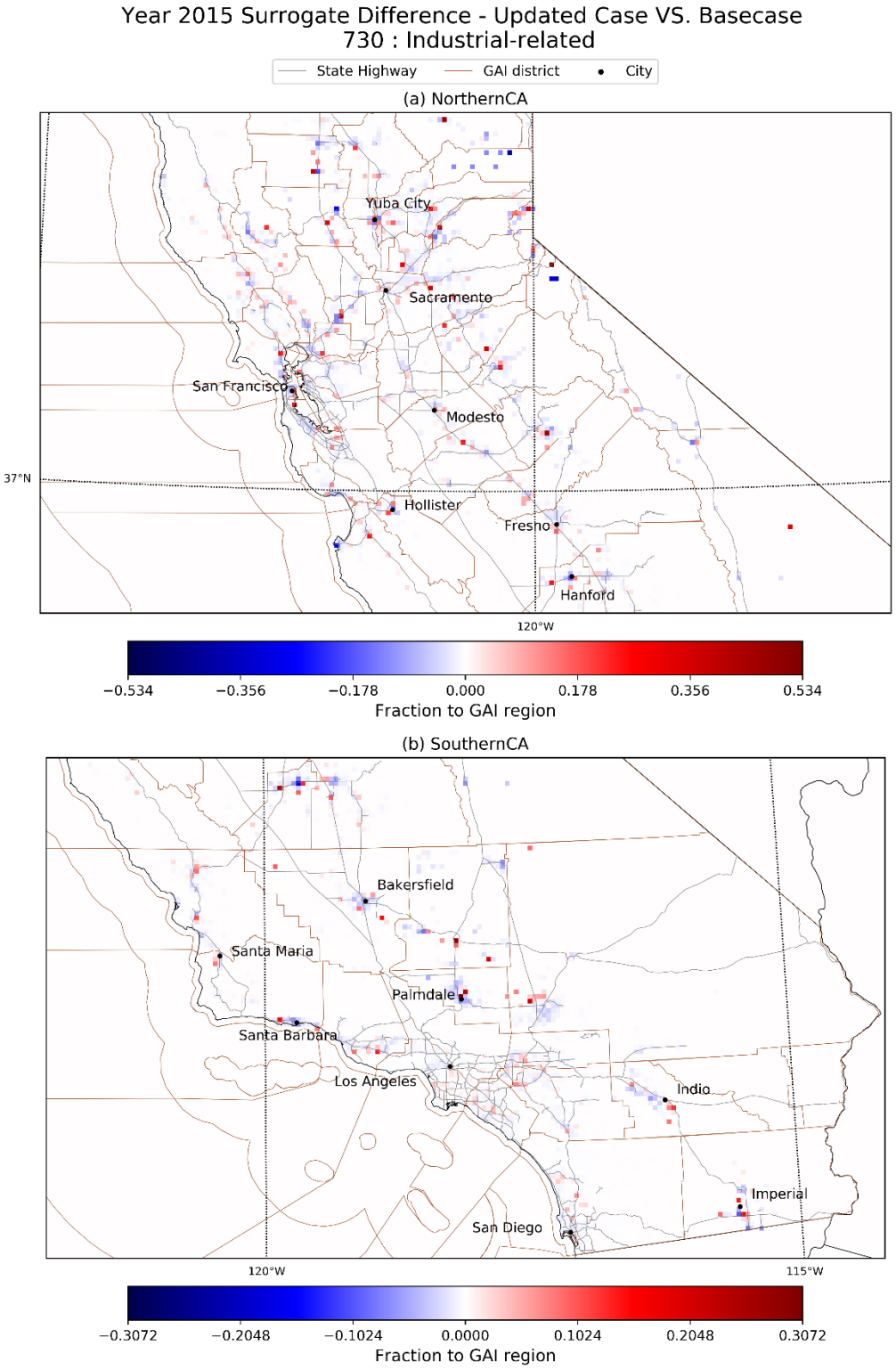

Figure S 1-14. Surrogate difference between updated case on-road construction equipment surrogate 588 and base case surrogate 585 for year 2015. (a) shows Northern California, (b) shows Southern California. Gray line is California State Highway

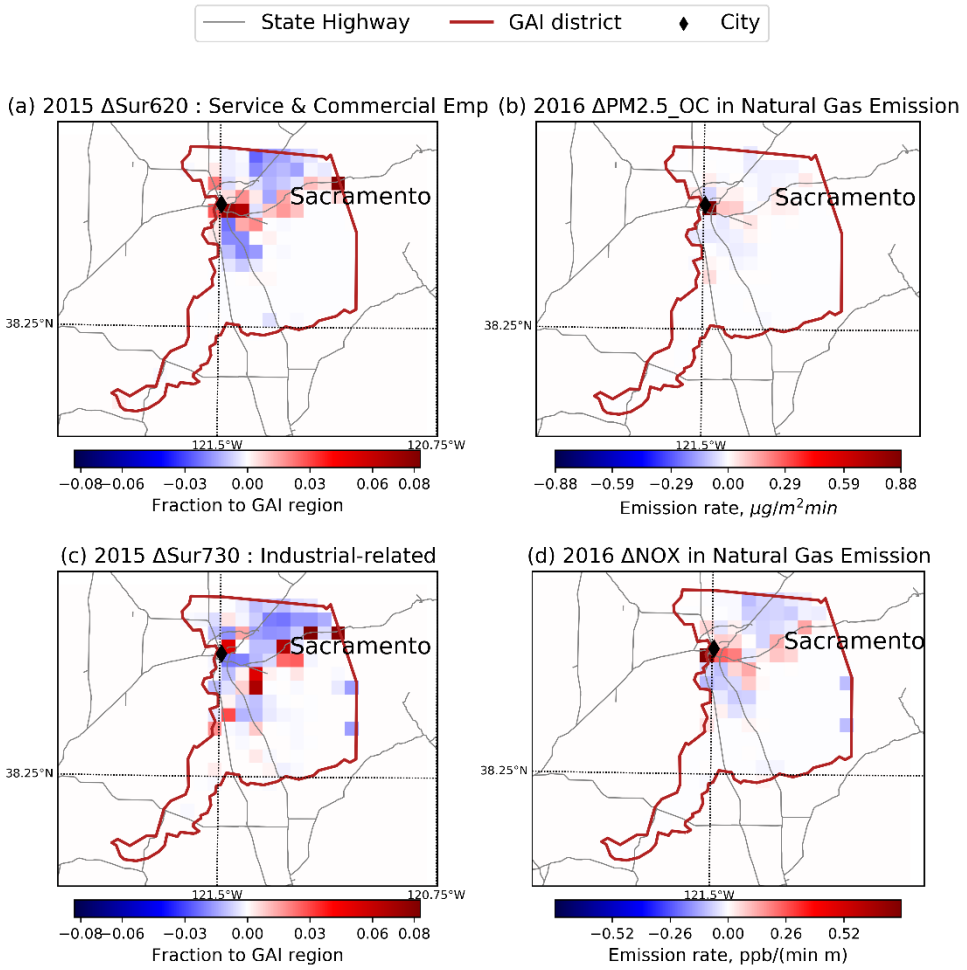

Figure S 1-15. Relationship between service & commercial employment, industrial-related surrogates and PM2.5 OC, NOx in natural gas emission. Figure (a) and (c) are surrogate difference between original and updated service & commercial/industrial-related surrogates at Sacramento county. Figure (b) (d) are PM2.5 OC and NOx difference in natural gas emission at the same corresponding area.

Appendix 2

S2.1 Methodology

Table S 2-1. Surrogates used to downscale 4km emissions to 1km/250m emissions

Emissions	Surrogate Name	Data Source
Area	Off-road construction equipment	see details in reference paper: DOI 10.1016/j.atmosenv.2020.117665
	On-road construction equipment	
	Total population	
	Service & Commercial employment	
	Single-family housing	
	Industrial-related/industrial employment	
	Forestland	California Air Resource Board (CARB)
	Residential heating gas	
	Unpaved road	
	Farm road VMT	
	Restaurant	Food service market dataset from Esri (NACIS 7225)
	Residential wood burning	Census Data
	Secondary paved road[1]	Tiger/Line shapefile, S1400 + S1630 + S1640
	Primary road[1]	Tiger/Line shapefile, S1100 + S1200
Mobile	Tire & brake wear	0.86*(gasoline mobile) + 0.14*(diesel mobile)
	Gasoline mobile	0.7*(AADT) + 0.3*(all road length)
	Diesel mobile	0.8*(Truck AADT) + 0.2*(truck road length)
Point		Directly processed by SMOKE

[1] Roads in this shapefile are divided into 13 types based on its function and dimension. Followed the CARB definition of these two surrogates, primary road surrogate includes S1100 (primary road), S1200 (secondary road); secondary paved road surrogate includes S1400 (local neighborhood road, rural road, city street), S1630 (ramp), S1640 (service drive usually along a limited access highway).

S2.1.1 Gasoline and diesel mobile surrogate data sources

Gasoline vehicle traffic count – Average Annual Daily Traffic (AADT) can be found in Federal Highway Administration HPMS website (https://www.fhwa.dot.gov/policyinformation/hpms/shapefiles.cfm, accessed August 2020).

Diesel vehicle traffic count – Truck AADT (with three or more axles) were obtained from Caltrans.

All road shapefile can be found in US Census Bureau (https://www.census.gov/geographies/mapping-files/time-series/geo/tiger-line-file.html, accessed August 2020).

Truck road network can be found in Freight Analysis Framework (Federal Highway Administration, https://ops.fhwa.dot.gov/freight/freight_analysis/faf/, accessed August 2020).

S2.1.2 Chemical transport model domain settings

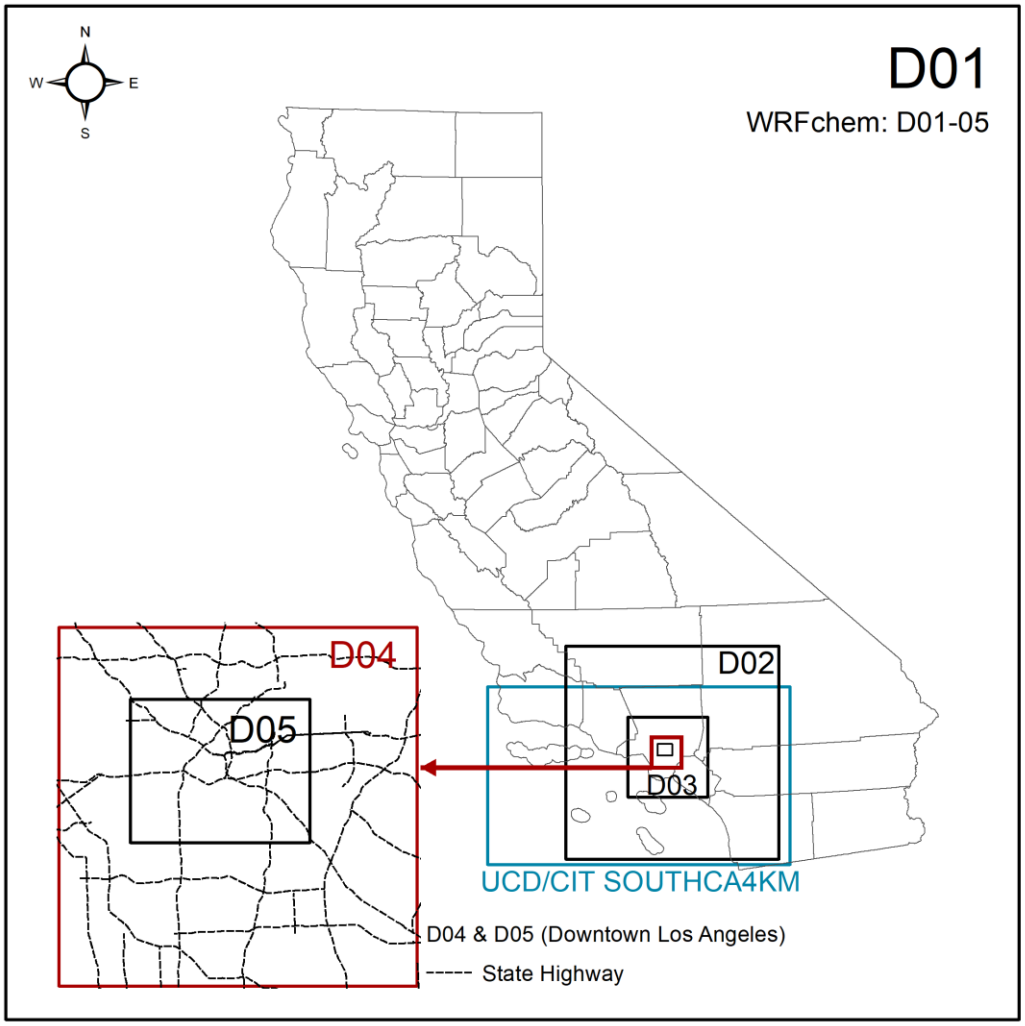

Figure S 2-1. WRF-Chem and UCD/CIT domain settings. Gird cells in each domain listed below. D01: 38 x 38; D02: 24 x 24; D03: 27 x 27; D04: 40 x 40; D05: 80 x 64; UCD/CIT statewide 24KM: 43 x 42; UCD/CIT SOUTHCA4KM: 102 x 60.

S2.1.3 Environment justice analysis

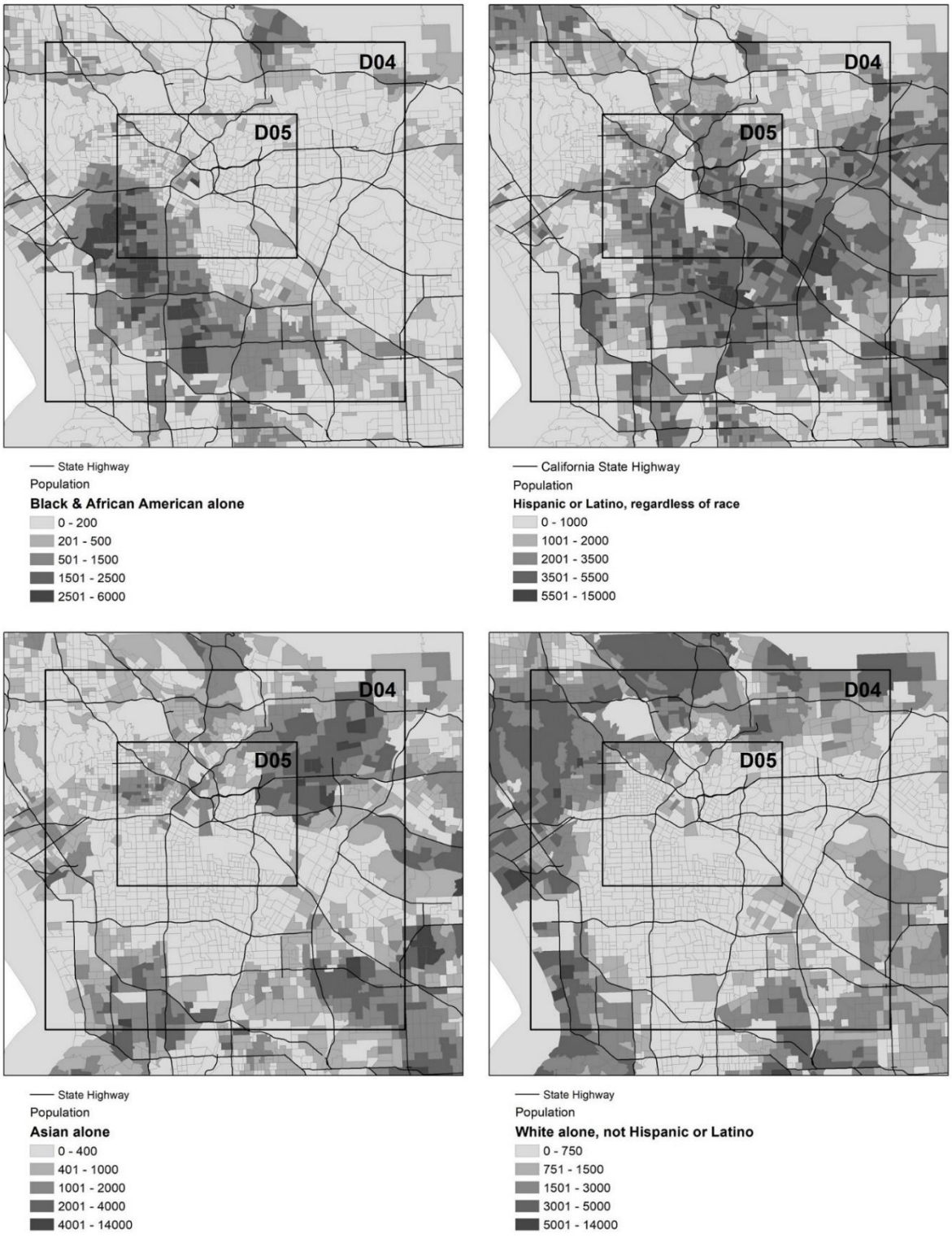

Figure S 2-216. Population distribution over WRF-chem domain 4 & 5 (Los Angeles, California, US) by race & ethnicity.

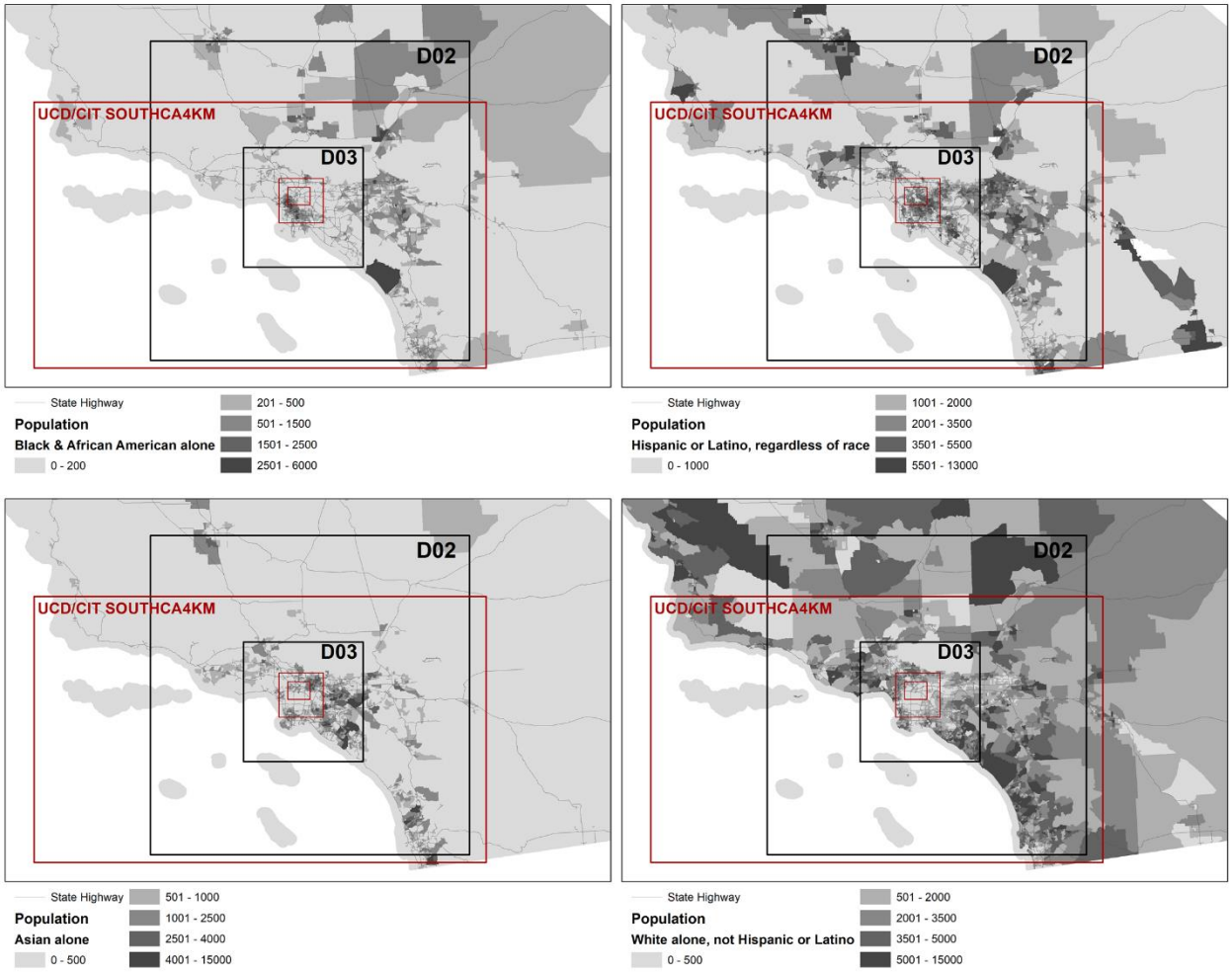

Figure S 2-3. Population distribution over WRF-chem domain 2 & 3 and UCD/CIT 4KM domain (California South Coast) by race & ethnicity.

Table S 2-2. Population by race/ethnicity summary of D01 – D05. Hispanic refers to Hispanic or Latino; White refers to White alone, not Hispanic or Latino; Asian refers to Asian alone; Black refers to Black & African American alone. Dataset is from ACS 2012-2016.

Domain	Total population	Hispanic	White	Asian	Black
D01	37,911,191	14,643,677	14,567,169	5,275,929	2,163,112
D02	20,820,288	9,119,153	7,131,465	2,672,181	1,330,157
D03	13,075,358	5,955,699	3,909,022	2,051,040	828,927
D04	5,868,760	3,060,596	1,207,408	880,960	593,772
D05	1,778,440	1,189,405	169,603	241,691	157,722

Table S 2-3. Population by ratio of income to poverty level of D01 – D05. Dataset is from ACS 2012-2016.

Ratio of income to poverty level	D04	D05
Under .50	456,831	194,678
.50 to .99	695,480	299,631
1.00 to 1.24	378,316	154,563
1.25 to 1.49	364,165	143,364
1.50 to 1.84	464,053	170,319
1.85 to 1.99	178,352	63,508
2.00 and over	3,331,564	752,377
Total Population	5,868,760	1,778,440

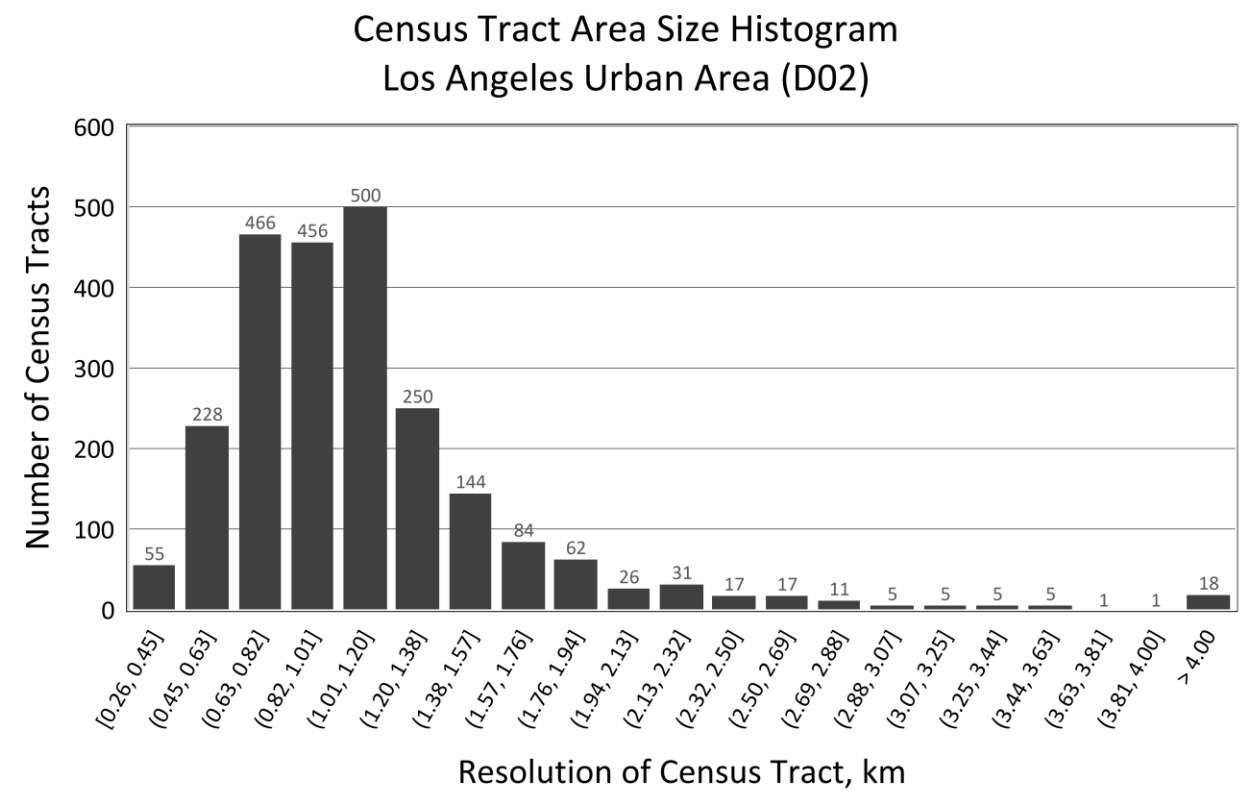

Figure S 2-4. American Community Survey (ACS) 2012-2016 data Census tract resolution histogram within domain D02, which covers the urban Los Angeles area.

S2.2 Results

S2.2.1 High resolution model results

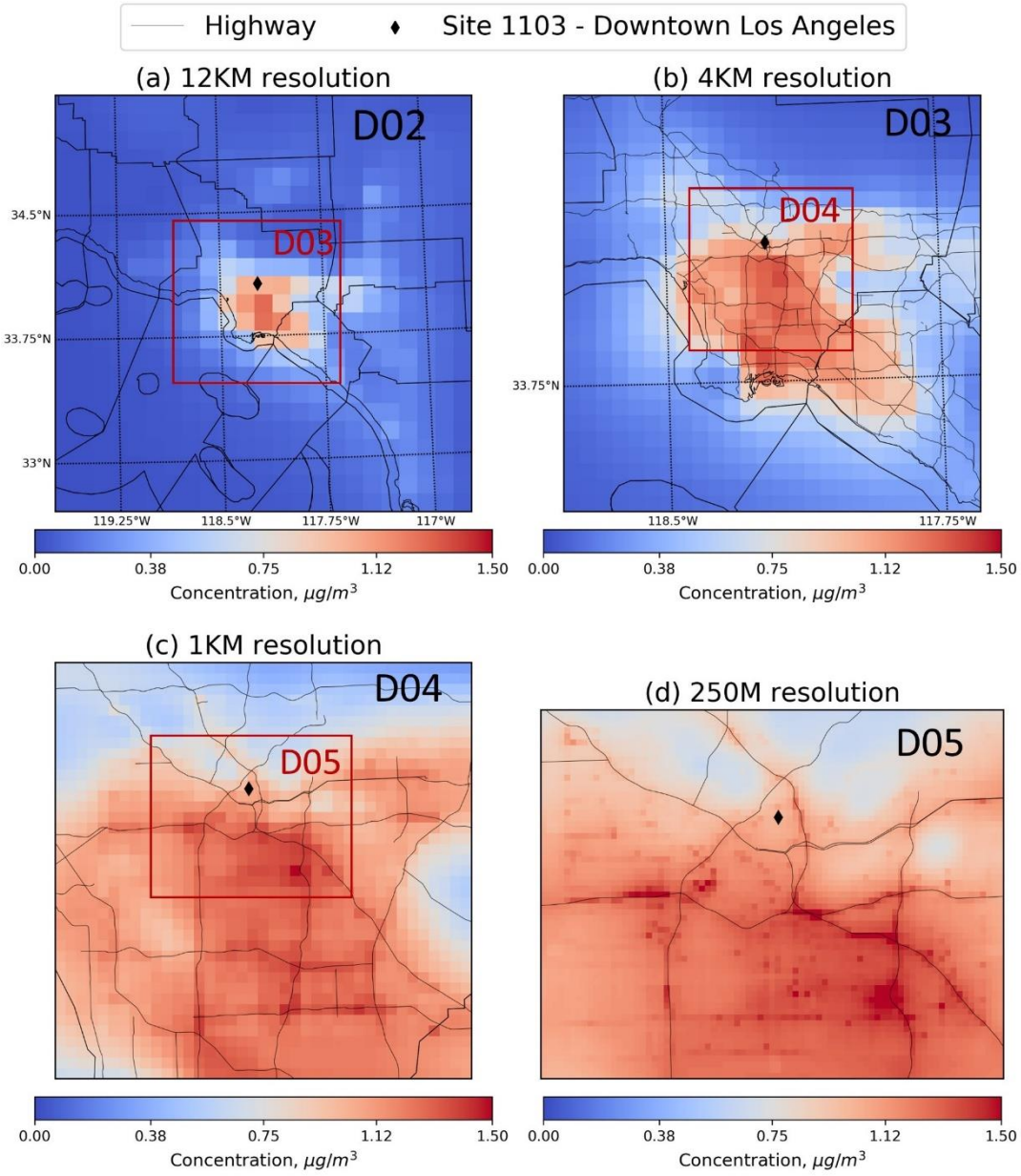

*Figure S 2-5. WRF-chem 2016 Annual average PM2.5 **EC** concentration at 12km (a), 4km (b), 1km (c), 250m (d) spatial resolution.*

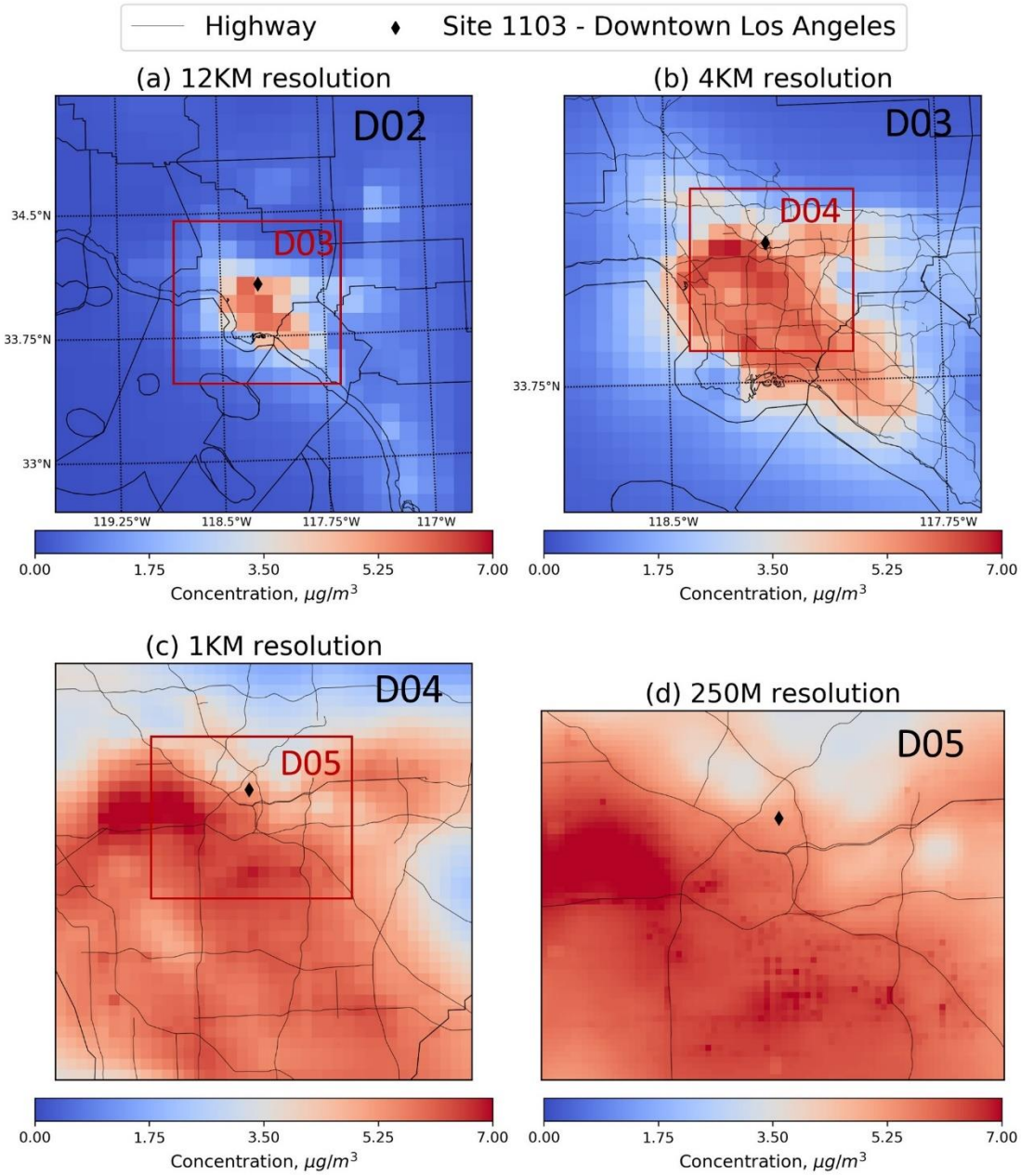

Figure S 2-617. WRF-chem 2016 Annual average PM2.5 ***OC*** *concentration at 12km (a), 4km (b), 1km (c), 250m (d) spatial resolution.*

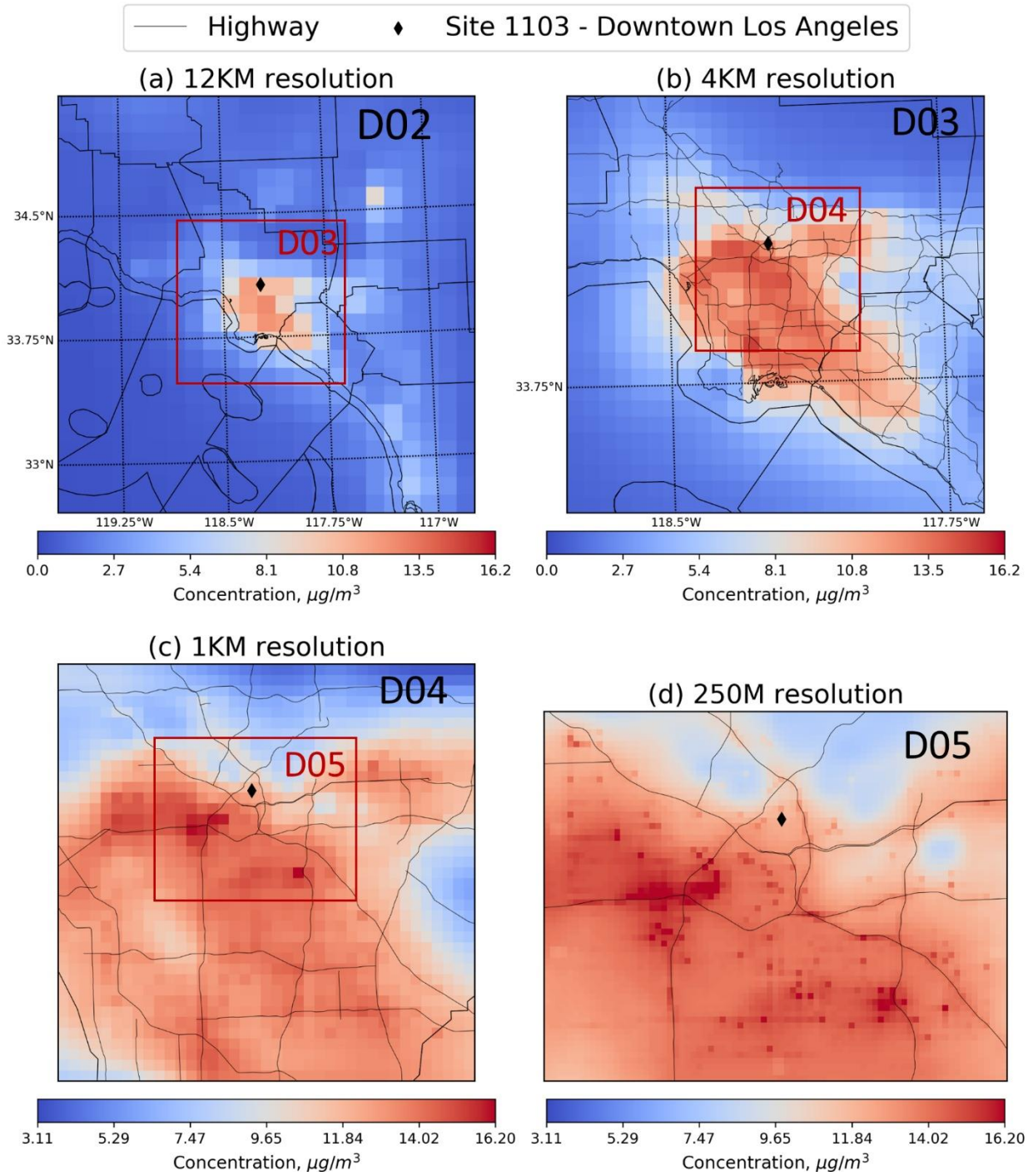

Figure S 2-7. WRF-chem 2016 Annual average PM2.5 ***Primary mass*** *concentration at 12km (a), 4km (b), 1km (c), 250m (d) spatial resolution*

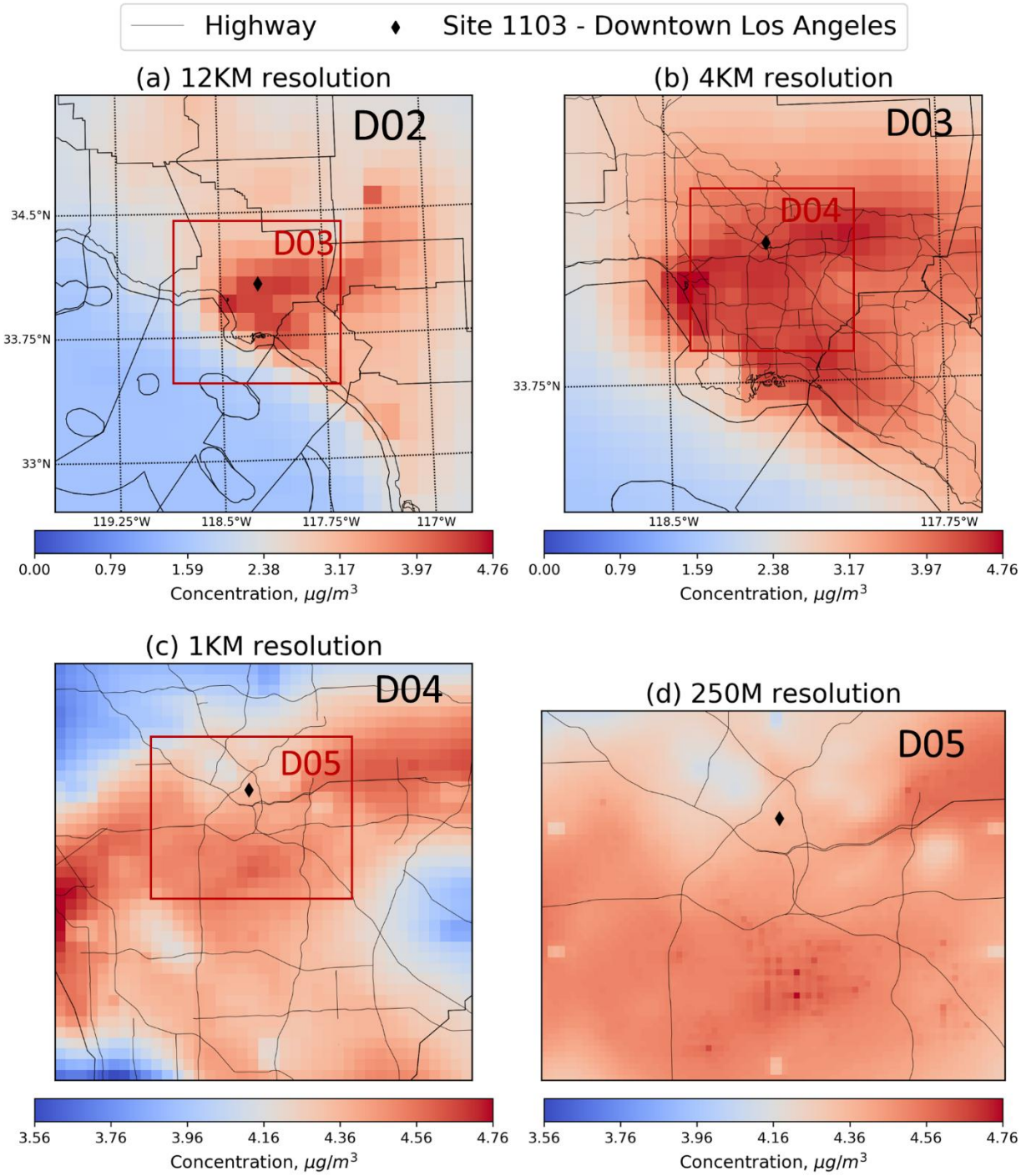

Figure S 2-8. WRF-chem 2016 Annual average PM2.5 ***Secondary mass*** *concentration at 12km (a), 4km (b), 1km (c), 250m (d) spatial resolution*

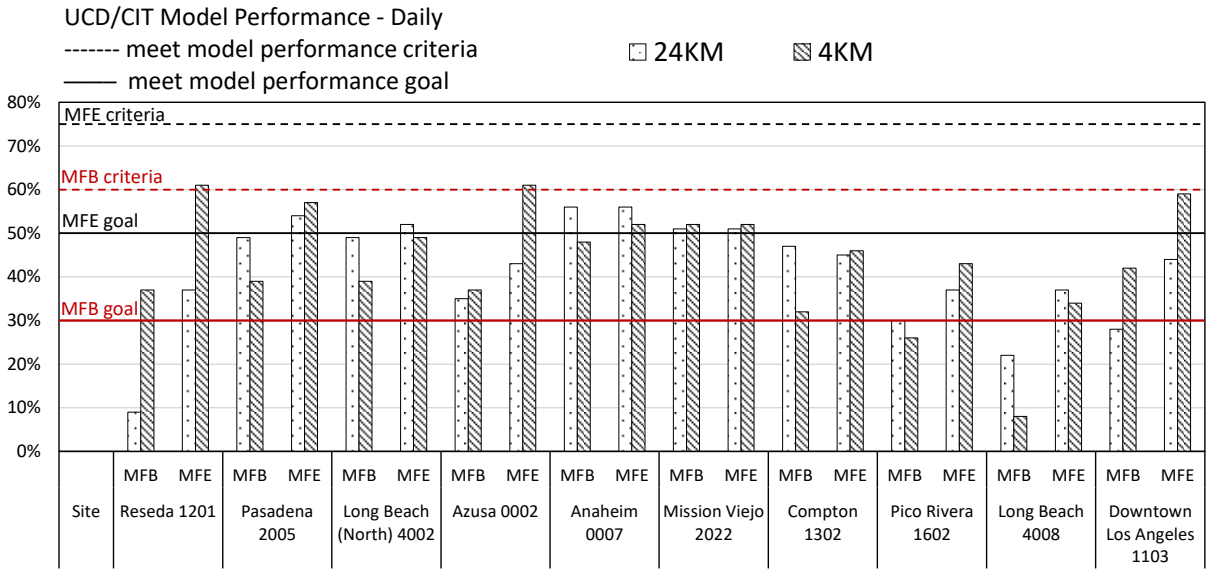

*Figure S 2-9. UCD/CIT Year 2016 daily $PM_{2.5}$ mass, EC, OC **M**ean **F**ractional **B**ias (MFB) and **M**ean **F**ractional **E**rror (MFE) for available measurement sites.*

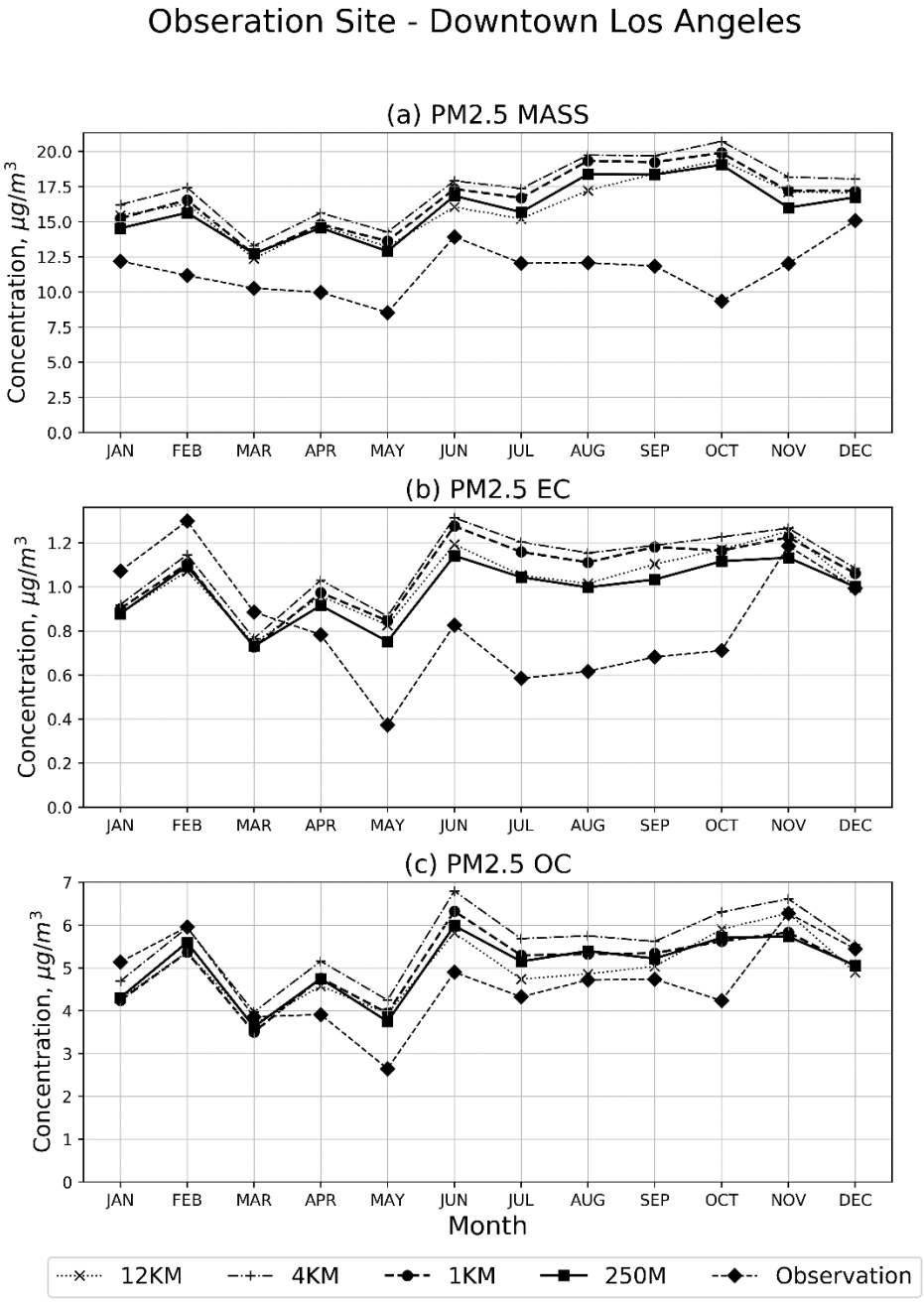

Figure S 2-10. WRF-chem Year 2016 monthly average predicted and measured PM2.5 MASS (a), EC (b), OC (c) concentrations at 12km, 4km, 1km and 250m spatial resolution

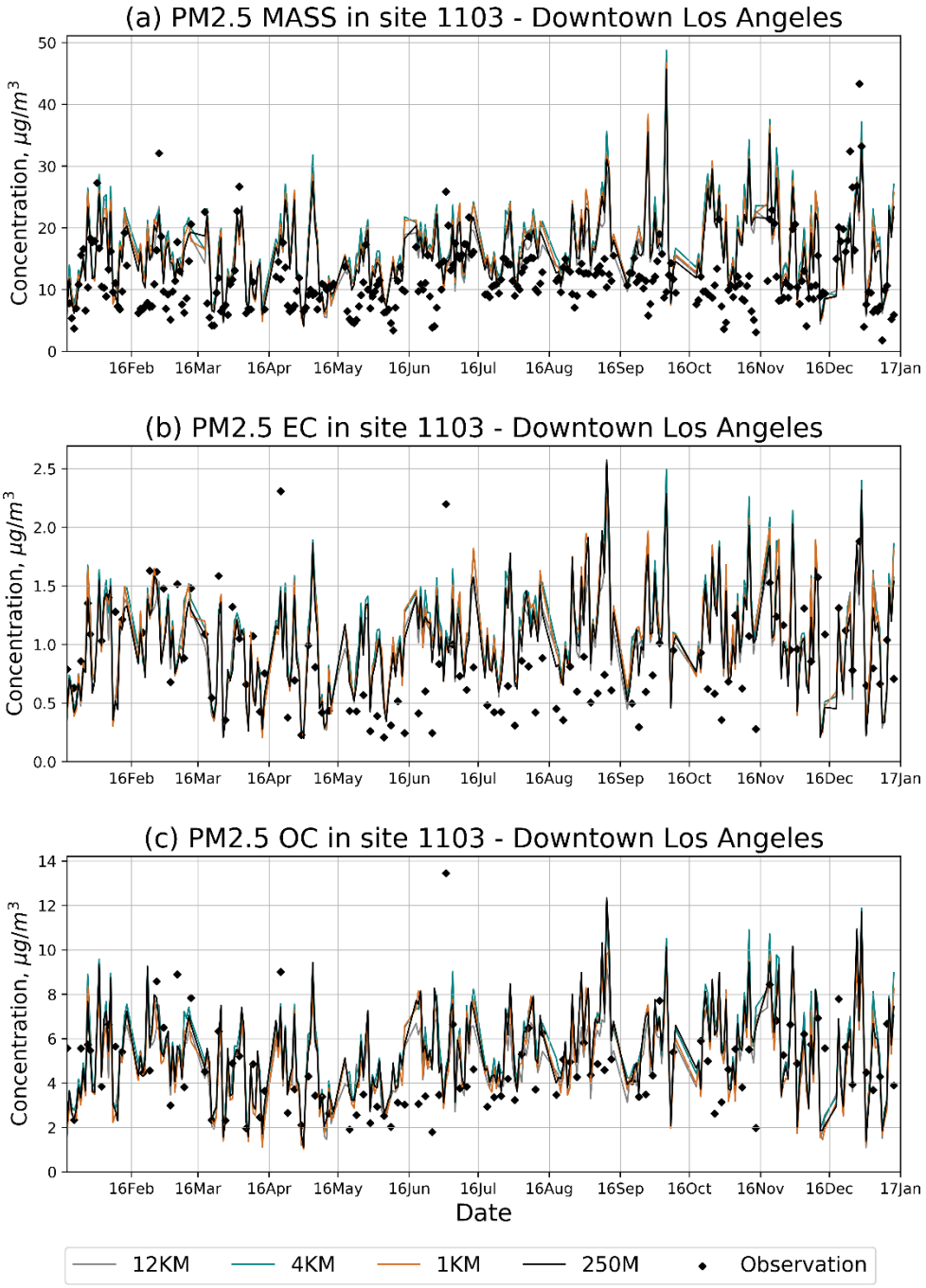

Figure S 2-11. WRF-chem Year 2016 daily predicted and measured PM2.5 MASS (a), EC (b), OC (c) concentrations at 12km, 4km, 1km and 250m spatial resolution

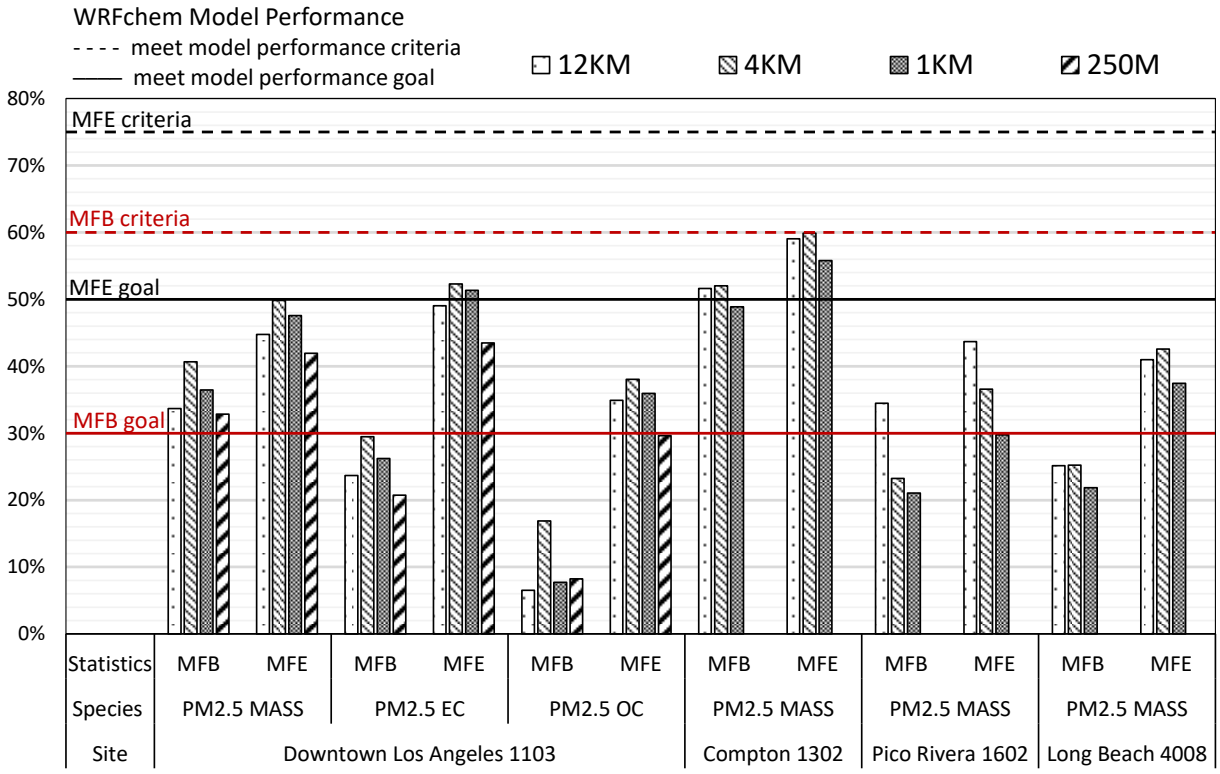

*Figure S 2-12. WRF-chem Year 2016 daily $PM_{2.5}$ mass, EC, OC **M**ean **F**ractional **B**ias (MFB) and **M**ean **F**ractional **E**rror (MFE) for available measurement sites in D04.*

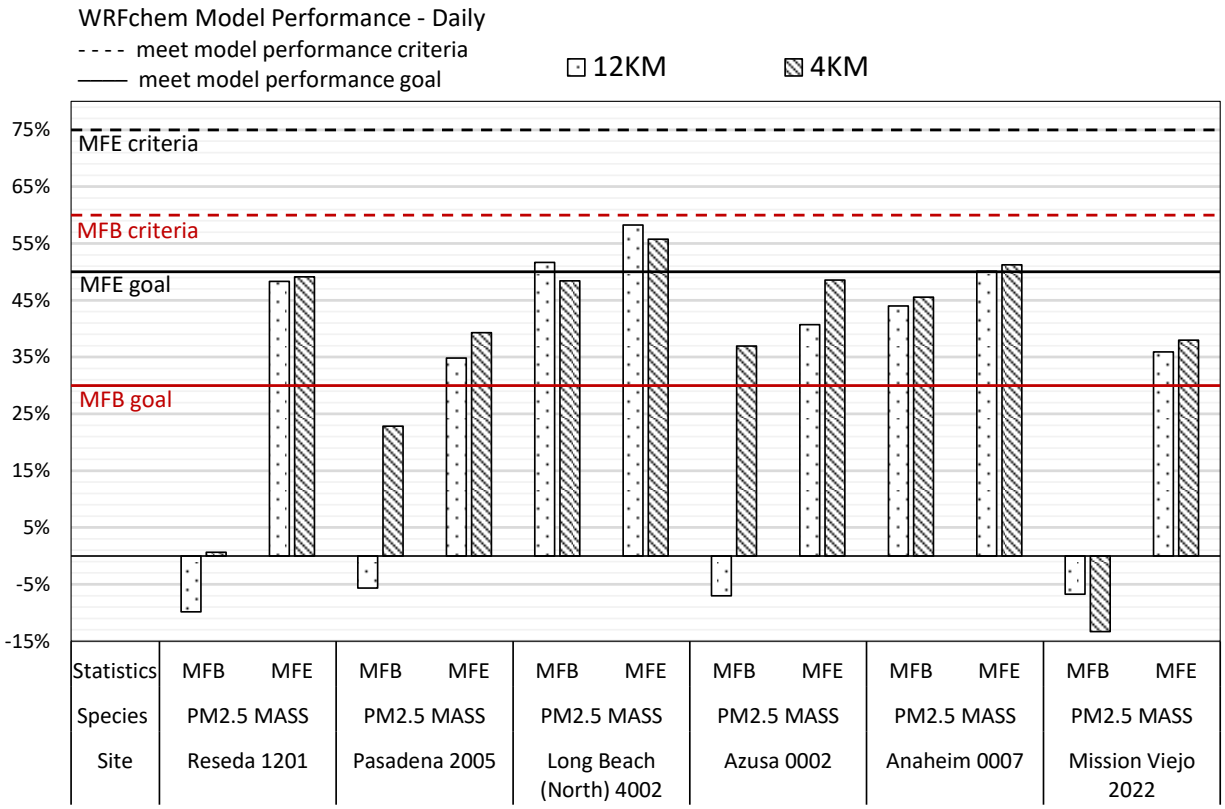

*Figure S 2-13. WRF-chem Year 2016 daily $PM_{2.5}$ mass, EC, OC **M**ean **F**ractional **B**ias (MFB) and **M**ean **F**ractional **E**rror (MFE) for available measurement sites in D03, outside of D04.*

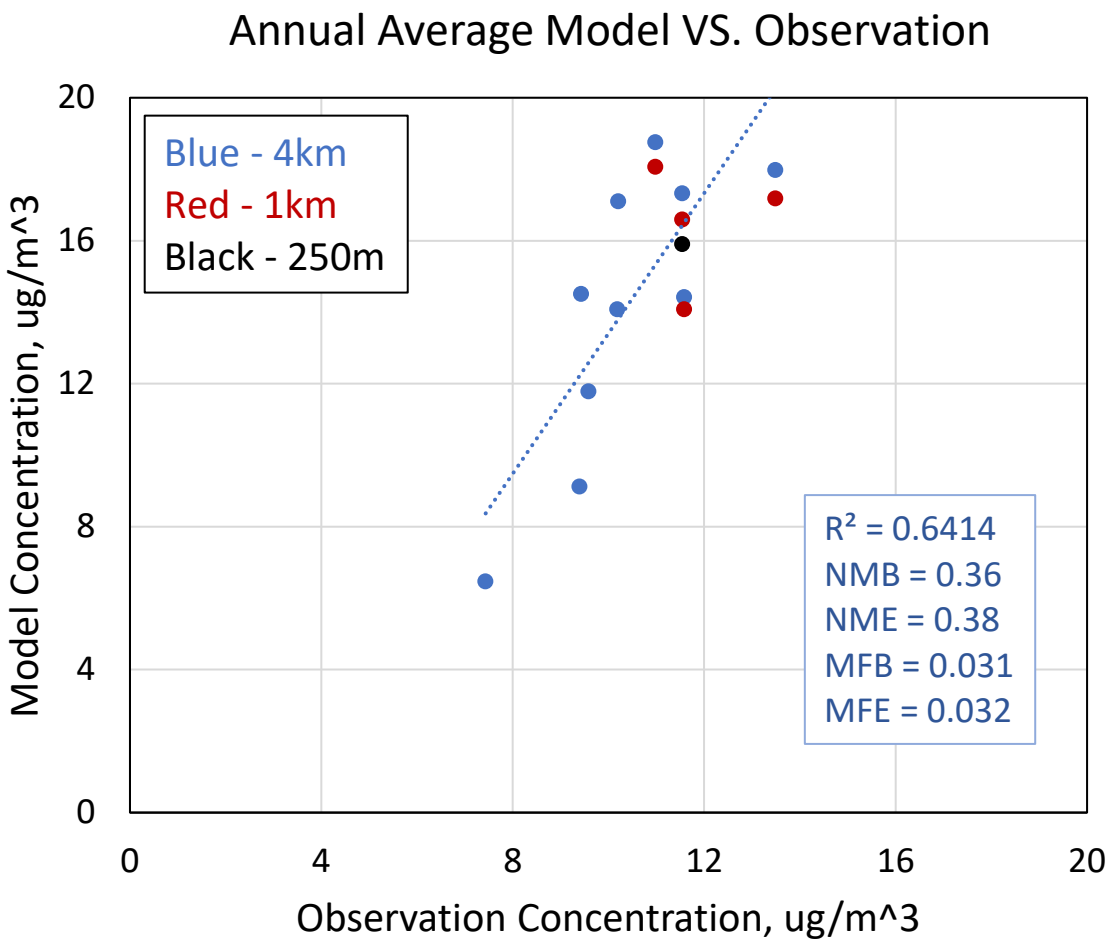

Figure S 2-14. Annual average comparison between Model predictions and Observations for all available sites in D03. Blue data point is 4km, Red data point is 1km, black data point is 250m. R^2 is 0.6114 for 4km data points, Normalized Mean Bias (NMB) is 0.36; Normalized Mean Error (NME) is 0.38; Mean Fractional Bias (MFB) is 0.031; and Mean Fractional Error (MFE) is 0.032.

S2.2.2 EJ analysis – race, species, and spatial resolution

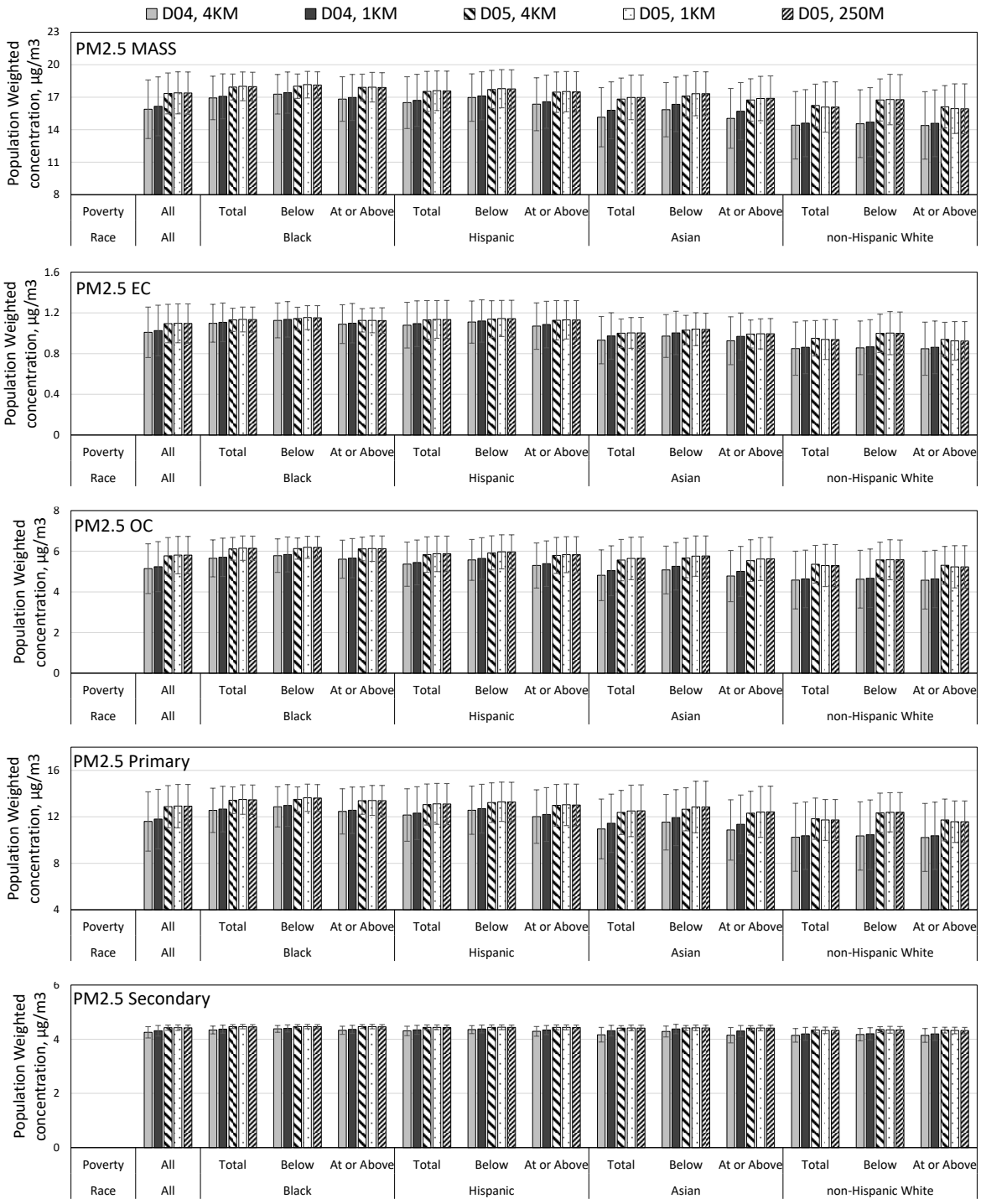

Figure S 2-15. WRF-chem Annual average PM2.5 MASS, EC, OC, primary, secondary aerosol population weighted concentration at 250m, 1km, 4km spatial resolution, domain D04, D05 by race and poverty level. Error bars are weighted standard deviation.

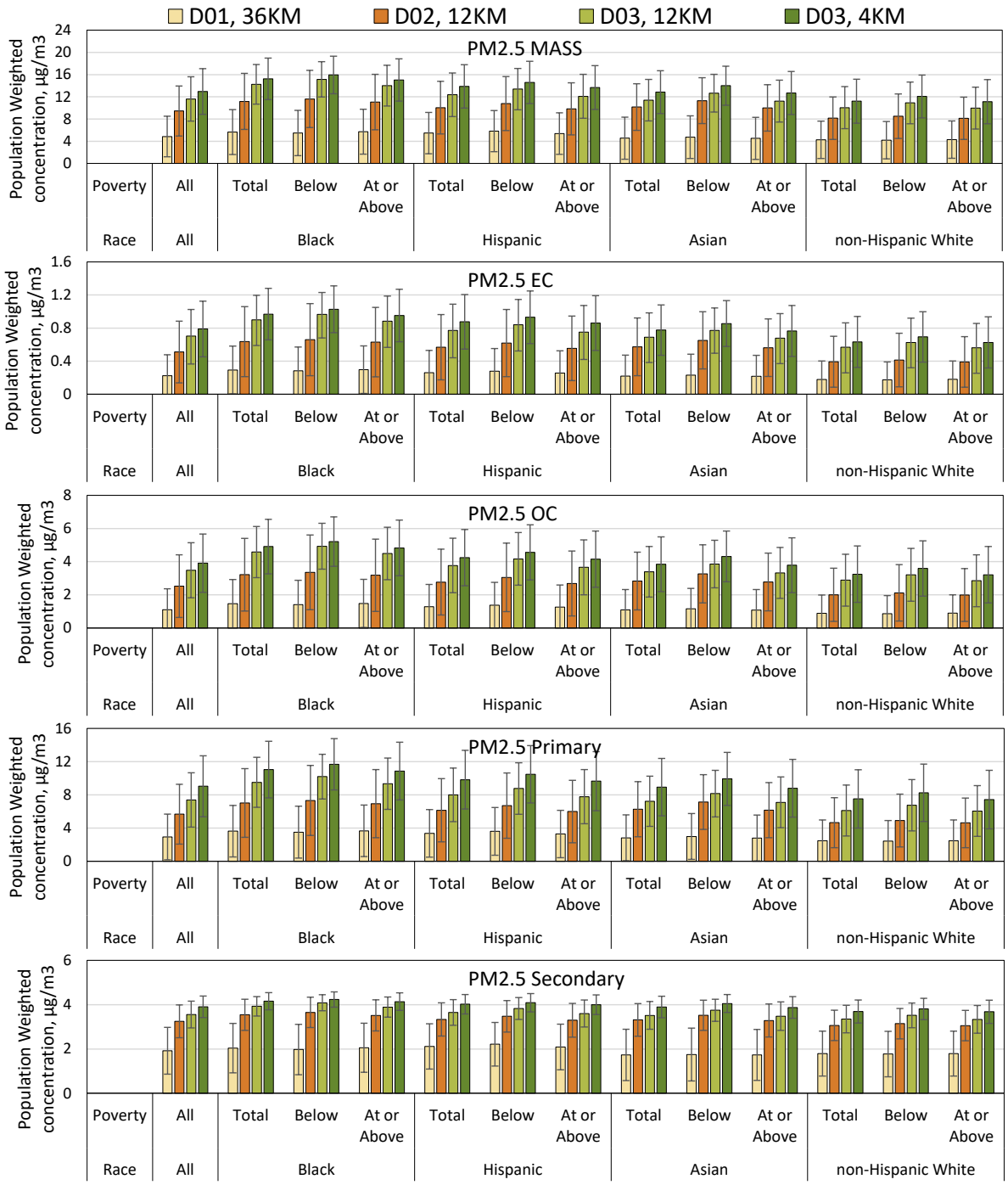

Figure S 2-16. WRF-chem Annual average PM2.5 MASS, EC, OC, primary, secondary aerosol population weighted concentration at 36km, 12km, and 4km spatial resolution, domain D01, D02, and D03 by race and poverty level. Error bars are weighted standard deviation.

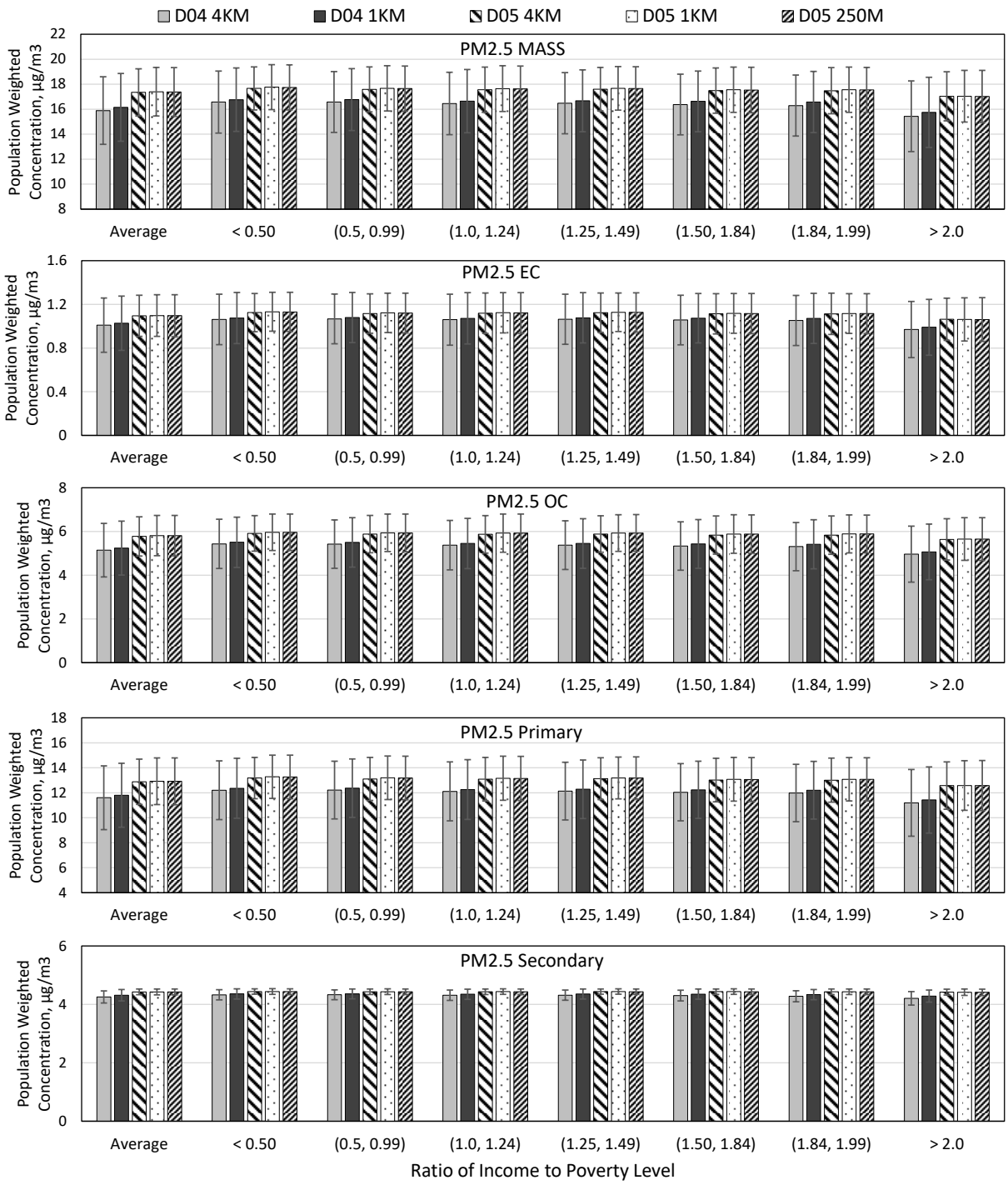

Figure S 2-17. WRF-chem Annual average PM2.5 MASS, EC, OC, primary, secondary aerosol population weighted concentration at 250m, 1km, 4km spatial resolution, domain D04, D05 by ratio of income to poverty level. Error bars are weighted standard deviation.

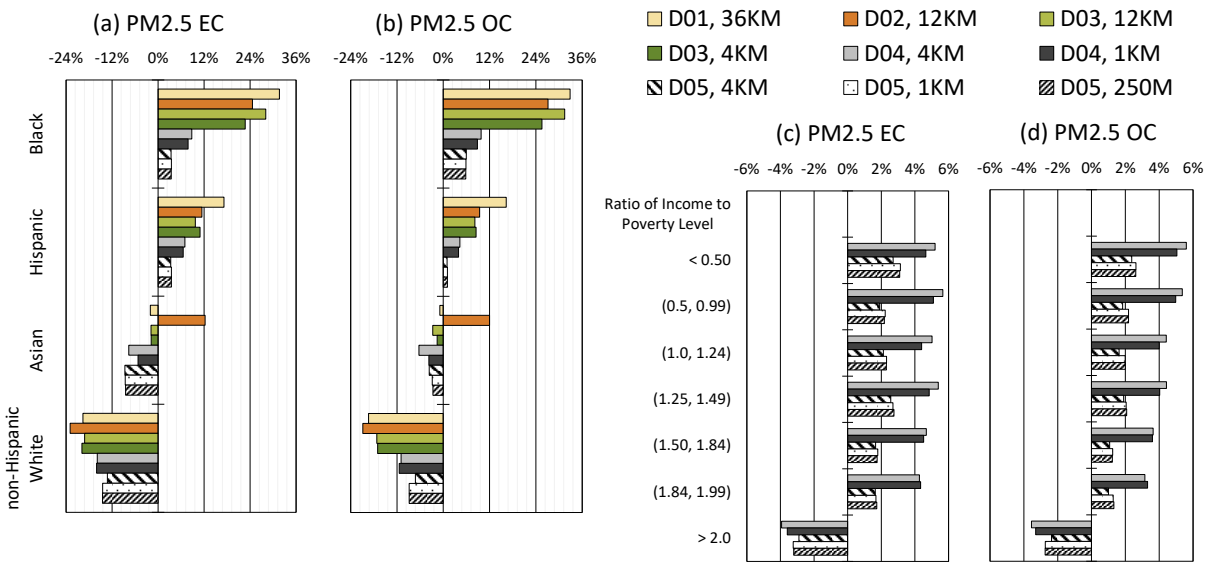

Figure S 2-18. Exposure difference relative to population average for (a,c) PM2.5 EC, (b,d) PM2.5OC as a function of domain size and resolution. Right panels analyze race/ethnicity. Left panels analyze income.

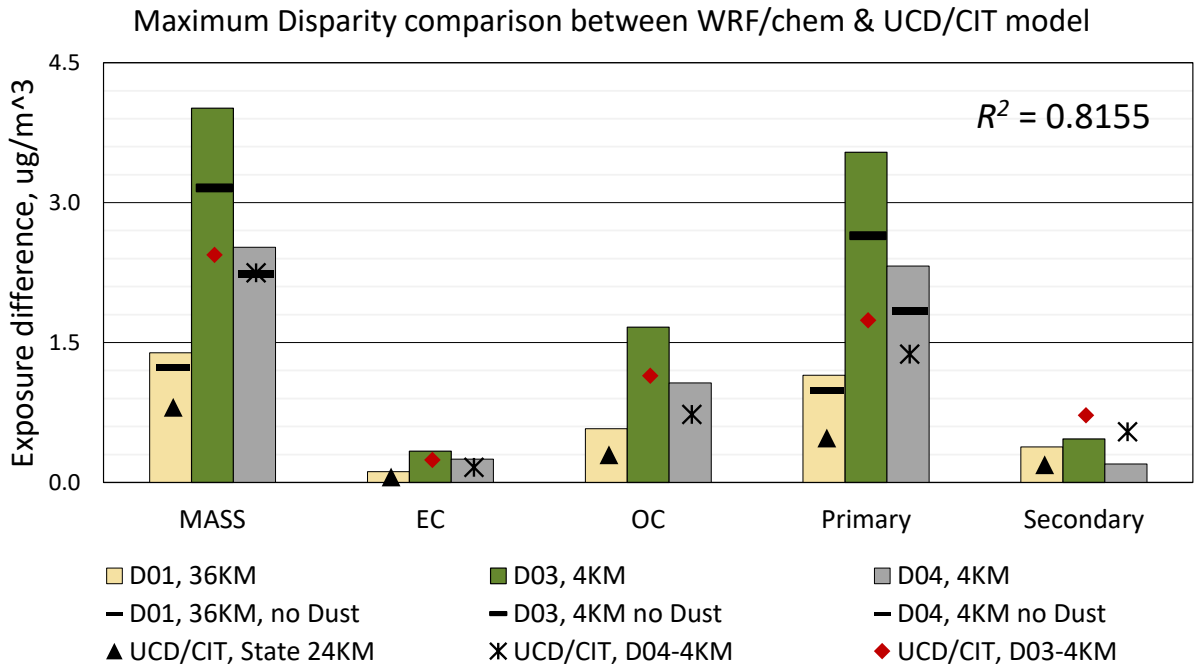

Figure S 2-19. Maximum Disparity comparison between WRF/Chem & UCD/CIT model (race only). Maximum disparities for all PM metrics occur between Black and non-Hispanic White. Bars represent WRF/Chem results. Horizontal black lines represent WRF/Chem results after the subtraction of excess dust emissions. Triangle, diamond, and asterisk symbols represent UCD/CIT results. R^2 represents correlations between WRF/Chem and UCD/CIT for all species listed here.

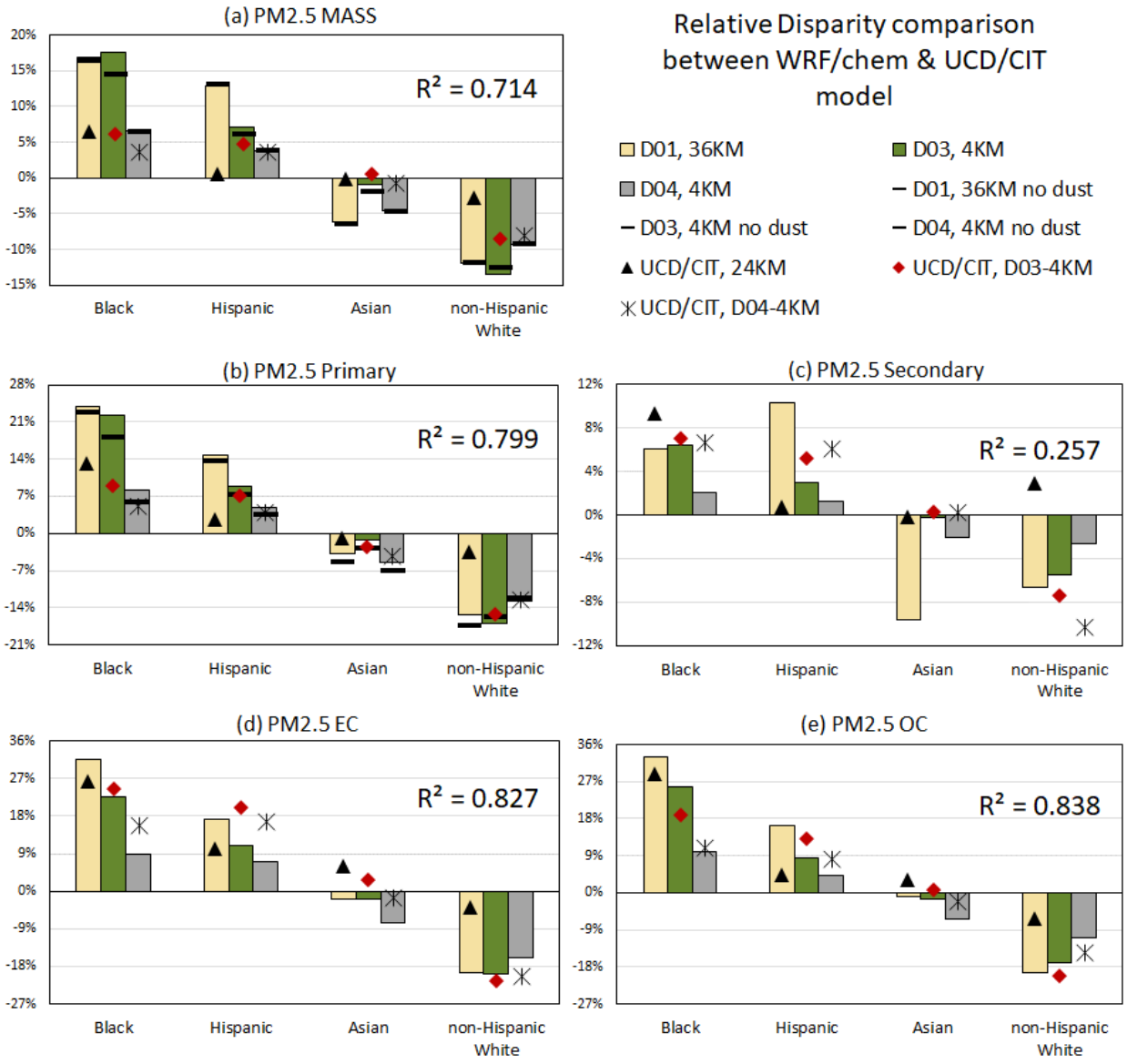

Figure S 2-20. Relative disparity comparison between WRF/Chem & UCD/CIT model (consider race only). The maximum disparities are all between Black and non-Hispanic White. Bars represent WRF/chem results. Dashes represent WRF/chem results but accounts for dust affects. Scattered dots represent UCD/CIT results. R^2 represents the correlation between WRF/Chem and UCD/CIT model.

S2.2.3 Type I hypothesis test

The statistical tests were carried out as a comparison of weighted means (x_w) between different populations. Weighted means ($\bar{x}_w$) were calculated using weighting factors (w_i = population count) in each grid cell multiplied with the concentration in that grid cell and then divided by the sum of all weighting factors.

$$\overline{x}_w = \frac{\sum_{i=1}^{N} x_i w_i}{\sum_{i=1}^{N} w_i}$$

where:

w_i – weight for the i^{th} observation, population for i^{th} grid cell in this study

$\sum_{i=1}^{N} w_i$ – total population within domain in this study

x_i –concentration for i^{th} grid cell in this study

N – the number of grid cells used in the sample

The number of sample points N in this calculations is the number of grid cells used in the model simulation. Sample weighted standard deviations were calculated with the equation:

$$s_w = \frac{\sqrt{\sum_{i=1}^{N} w_i (x_i - \bar{x}_w)^2}}{\sqrt{\frac{(N' - 1)\sum_{i=1}^{N} w_i}{N'}}}$$

where

N' - the number of non-zero weights, number of non-zero grid cell used in the sample

Given:

μ_{w1} = population weighted mean of sample 1

μ_{w2} = population weighted mean of sample 2

n_1 = sample size of sample 1

n_2 = sample size of sample 2

s_{w1} = weighted standard deviation of sample 1

s_{w1} = weighted standard deviation of sample 2

$H_0 : \mu_1 = \mu_2$

$H_1 : \mu_1 \neq \mu_2$

Two-sample hypothesis tests on the population weighted means were conducted using the test statistic

$$T = \frac{(\bar{x}_{w1} - \bar{x}_{w2}) - (\mu_{w1} - \mu_{w2})}{\sqrt{{s_{w1}}^2/n_1 + {s_{w2}}^2/n_2}}$$

that follows the T distribution with $n_1 + n_2 - 2$ degrees of freedom. Results can be expressed either as rejection / failure to reject H_0 at the specified confidence level $\alpha = 0.01$, or as a P-value that can be compared to α.

Table S 2-4. Mean value, standard deviation (std) and N number used in Type I hypothesis test shown in Table S2-9. Socioeconomic classes are considered both race and poverty level. Mean is exposure concentration within certain domain. N is sample size.

Race & Poverty level										
H0	u1-u2=0	u1	black & African American; below poverty level							
H1	u1-u2>0	u2	white only, no hispanic or Latino, at or above poverty level							
	D04, 4KM		D04, 1KM		D05, 4KM		D05, 1KM		D05, 250M	
	u1	u2	u1	u2	u1	u2	u1	u2	u1	u2
mean	17.27	14.39	17.42	14.59	18.02	16.11	18.16	15.94	18.13	15.93
std	1.83	3.11	1.91	3.08	1.12	1.96	1.23	2.29	1.21	2.30
N	100	100	1454	1581	20	20	296	320	4049	5033
H0	u1-u2=0	u1	Hispanic or Latino, below poverty level							
H1	u1-u2>0	u2	white only, no hispanic or Latino, at or above poverty level							
	D04, 4KM		D04, 1KM		D05, 4KM		D05, 1KM		D05, 250M	
	u1	u2	u1	u2	u1	u2	u1	u2	u1	u2
mean	16.97	14.39	17.12	14.59	17.71	16.11	17.78	15.94	17.76	15.93
std	2.19	3.11	2.21	3.08	1.77	1.96	1.76	2.29	1.76	2.30
N	100	100	1565	1581	20	20	320	320	5099	5033
H0	u1-u2=0	u1	Asian; below poverty level							
H1	u1-u2>0	u2	white only, no hispanic or Latino, at or above poverty level							
	D04, 4KM		D04, 1KM		D05, 4KM		D05, 1KM		D05, 250M	
	u1	u2	u1	u2	u1	u2	u1	u2	u1	u2
mean	15.85	14.39	16.35	14.59	17.10	16.11	17.32	15.94	16.09	15.93
std	2.51	3.11	2.52	3.08	1.90	1.96	2.04	2.29	2.33	2.30
N	100	100	1526	1581	20	20	303	320	5078	5033
H0	u1-u2=0	u1	black & African American; below poverty level							
H1	u1-u2>0	u2	Asian;at or above poverty level							
	D04, 4KM		D04, 1KM		D05, 4KM		D05, 1KM		D05, 250M	
	u1	u2	u1	u2	u1	u2	u1	u2	u1	u2
mean	17.27	15.04	17.42	15.71	18.02	16.74	18.16	16.88	18.13	16.89
std	1.83	2.76	1.91	2.64	1.12	1.95	1.23	2.05	1.21	2.08
N	100	100	1454	1578	20	20	296	319	4049	4739

Table S 2-5. Mean value, standard deviation (std) and N number used in Type I hypothesis test shown in Table S2-10. Socioeconomic classes are considered both race and poverty level. Mean is exposure concentration within certain domain. N is sample size.

Race & Poverty								
H0	u1-u2=0	u1	black & African American; below poverty level					
H1	u1-u2>0	u2	white only, no hispanic or Latino, at or above poverty level					
	D03, 4KM		D03, 12KM		D02, 12KM		D01, 36KM	
	u1	u2	u1	u2	u1	u2	u1	u2
mean	15.94	11.13	15.15	9.97	11.61	8.12	5.48	4.28
std	3.38	3.97	3.18	3.78	5.16	3.81	4.09	3.36
N	560	630	87	97	467	585	668	750
H0	u1-u2=0	u1	Hispanic or Latino, below poverty level					
H1	u1-u2>0	u2	white only, no hispanic or Latino, at or above poverty level					
	D03, 4KM		D03, 12KM		D02, 12KM		D01, 36KM	
	u1	u2	u1	u2	u1	u2	u1	u2
mean	14.59	11.13	13.39	9.97	10.79	8.12	5.82	4.28
std	3.81	3.97	3.73	3.78	4.87	3.81	3.71	3.36
N	598	630	89	97	534	585	742	750
H0	u1-u2=0	u1	Asian; below poverty level					
H1	u1-u2>0	u2	white only, no hispanic or Latino, at or above poverty level					
	D03, 4KM		D03, 12KM		D02, 12KM		D01, 36KM	
	u1	u2	u1	u2	u1	u2	u1	u2
mean	14.00	11.13	12.65	9.97	10.16	8.12	4.74	4.28
std	3.52	3.97	3.40	3.78	4.19	3.81	3.85	3.36
N	484	630	75	97	573	585	621	750
H0	u1-u2=0	u1	black & African American; below poverty level					
H1	u1-u2>0	u2	Asian;at or above poverty level					
	D03, 4KM		D03, 12KM		D02, 12KM		D01, 36KM	
	u1	u2	u1	u2	u1	u2	u1	u2
mean	15.94	12.69	15.15	11.23	11.61	10.01	5.48	4.53
std	3.38	3.88	3.18	3.76	5.16	4.18	4.09	3.79
N	560	612	87	97	467	568	668	714

Table S 2-6. Mean value, standard deviation (std) and N number used in Type I hypothesis test shown in Table S2-9. Socioeconomic classes are considered race only. Mean is exposure concentration within certain domain. N is sample size.

Race only										
H0	u1-u2=0	u1	black & African American							
H1	u1-u2>0	u2	white only, no hispanic or Latino							
	D04, 4KM		D04, 1KM		D05, 4KM		D05, 1KM		D05, 250M	
	u1	u2	u1	u2	u1	u2	u1	u2	u1	u2
mean	16.93	14.41	17.08	14.60	17.94	16.23	18.00	16.09	17.97	16.09
std	2.01	3.11	2.08	3.09	1.20	1.97	1.33	2.32	1.32	2.33
N	100	100	1546	1581	20	20	319	320	4808	5078
H0	u1-u2=0	u1	Hispanic or Latino							
H1	u1-u2>0	u2	white only, no hispanic or Latino							
	D04, 4KM		D04, 1KM		D05, 4KM		D05, 1KM		D05, 250M	
	u1	u2	u1	u2	u1	u2	u1	u2	u1	u2
mean	16.50	14.41	16.71	14.60	17.54	16.23	17.60	16.09	17.58	16.09
std	2.39	3.11	2.41	3.09	1.84	1.97	1.83	2.32	1.84	2.33
N	100	100	1581	1581	20	20	320	320	5120	5078
H0	u1-u2=0	u1	Asian							
H1	u1-u2>0	u2	white only, no hispanic or Latino							
	D04, 4KM		D04, 1KM		D05, 4KM		D05, 1KM		D05, 250M	
	u1	u2	u1	u2	u1	u2	u1	u2	u1	u2
mean	15.15	14.41	15.79	14.60	16.82	16.23	16.97	16.09	16.98	16.09
std	2.73	3.11	2.63	3.09	1.95	1.97	2.05	2.32	2.07	2.33
N	100	100	1580	1581	20	20	319	320	4857	5078

Table S 2-7. Mean value, standard deviation (std) and N number used in Type I hypothesis test shown in Table S2-9. Socioeconomic classes are considered race only. Mean is exposure concentration within certain domain. N is sample size.

Race only								
H0	u1-u2=0	u1	black & African American					
H1	u1-u2>0	u2	white only, no hispanic or Latino					
	D03, 4KM		D03, 12KM		D02, 12KM		D01, 36KM	
	u1	u2	u1	u2	u1	u2	u1	u2
mean	15.23	11.22	14.24	10.05	11.17	8.16	5.66	4.27
std	3.74	3.97	3.57	3.78	5.04	3.83	4.05	3.37
N	599	630	89	97	503	585	712	750
H0	u1-u2=0	u1	Hispanic or Latino					
H1	u1-u2>0	u2	white only, no hispanic or Latino					
	D03, 4KM		D03, 12KM		D02, 12KM		D01, 36KM	
	u1	u2	u1	u2	u1	u2	u1	u2
mean	13.87	11.22	12.37	10.05	10.04	8.16	5.47	4.27
std	3.92	3.97	3.92	3.78	4.74	3.83	3.73	3.37
N	628	630	97	97	591	585	757	750
H0	u1-u2=0	u1	Asian					
H1	u1-u2>0	u2	white only, no hispanic or Latino					
	D03, 4KM		D03, 12KM		D02, 12KM		D01, 36KM	
	u1	u2	u1	u2	u1	u2	u1	u2
mean	12.85	11.22	11.40	10.05	10.16	8.16	4.55	4.27
std	3.85	3.97	3.73	3.78	4.19	3.83	3.80	3.37
N	612	630	97	97	573	585	723	750

Table S 2-8. Mean value, standard deviation (std) and N number used in Type I hypothesis test shown in Table S2-9 and S2-10. Socioeconomic classes are considered poverty level only. Mean is exposure concentration within certain domain. N is sample size.

H0	u1-u2=0	u1	(race), below					
H1	u1-u2>0	u2	(race), at or above					
	no Hispanic or Latino		**Asian**		**African & Black**		**Hsipanic**	
D05, 250M								
	below	at or above	below	at or above	below	at or above	below	at or above
mean	16.77	15.93	17.32	16.89	18.13	17.90	17.76	17.50
std	2.31	2.30	2.02	2.08	1.21	1.37	1.76	1.86
N	4516	5033	4110	4739	4049	4463	5099	5116
D05, 1KM								
	below	at or above	below	at or above	below	at or above	below	at or above
mean	16.78	15.94	17.32	16.88	18.16	17.92	17.78	17.52
std	2.32	2.29	2.04	2.05	1.23	1.36	1.76	1.85
N	4516	5033	4110	4739	4049	4463	5099	5116
D05, 4KM								
	below	at or above	below	at or above	below	at or above	below	at or above
mean	16.75	16.11	17.10	16.74	18.02	17.90	17.71	17.47
std	1.94	1.96	1.90	1.95	1.12	1.23	1.77	1.87
N	4516	5033	4110	4739	4049	4463	5099	5116
D04, 1KM								
	below	at or above	below	at or above	below	at or above	below	at or above
mean	14.69	14.59	16.35	15.71	17.42	16.97	17.12	16.58
std	3.18	3.08	2.52	2.64	1.91	2.12	2.21	2.45
N	4516	5033	4110	4739	4049	4463	5099	5116
D04, 4KM								
	below	at or above	below	at or above	below	at or above	below	at or above
mean	14.55	14.39	15.85	15.04	17.27	16.83	16.97	16.35
std	3.13	3.11	2.51	2.76	1.83	2.06	2.19	2.44
N	4516	5033	4110	4739	4049	4463	5099	5116
D03, 4KM								
	below	at or above	below	at or above	below	at or above	below	at or above
mean	12.07	11.13	14.00	12.69	15.94	15.03	14.59	13.67
std	3.86	3.97	3.52	3.88	3.38	3.82	3.81	3.93
N	629	630	484	612	560	529	598	628
D03, 12KM								
	below	at or above	below	at or above	below	at or above	below	at or above
mean	10.91	9.97	12.65	11.23	15.15	14.01	13.39	12.09
std	3.76	3.78	3.40	3.76	3.18	3.66	3.73	3.97
N	97	97	75	97	87	82	89	97
D02, 12KM								
	below	at or above	below	at or above	below	at or above	below	at or above
mean	8.51	8.12	11.31	10.01	11.61	11.06	10.79	9.84
std	4.02	3.81	4.12	4.18	5.16	5.01	4.87	4.70
N	583	585	458	568	467	471	534	585
D01, 36KM								
	below	at or above	below	at or above	below	at or above	below	at or above
mean	4.19	4.28	4.74	4.53	5.48	5.72	5.82	5.38
std	3.37	3.36	3.85	3.79	4.09	4.04	3.71	3.73
N	749	750	621	714	668	687	742	750

Table S 2-9. P-value of Type I hypothesis test for selected socioeconomic classes, target for $PM_{2.5}$ mass. $H_0: u1 = u2$; $H_1: u1 > u2$; $\alpha = 1\%$. D04 – regional-level; D05 – community-level

$u1$	$u2$	D04, 4KM	D04, 1KM	D05, 4KM	D05, 1KM	D05, 250M
Race & Poverty level						
Black, low[1]	White, high[2]	0.00%	0.00%	0.04%	0.00%	0.00%
Hispanic, low	White, high	0.00%	0.00%	0.51%	0.00%	0.00%
Asian, low	White, high	0.01%	0.00%	**5.68%***	0.00%	0.04%
Black, low	Asian, high	0.00%	0.00%	0.85%	0.00%	0.00%
Race only						
Black, total[3]	White, total	0.00%	0.00%	0.12%	0.00%	0.00%
Hispanic, total	White, total	0.00%	0.00%	**1.82%**	0.00%	0.00%
Asian, total	White, total	**3.43%**	0.00%	**17.41%**	0.00%	0.00%
Poverty level only						
Black, low	Black, high	**4.93%**	0.00%	**37.95%**	**1.09%**	0.00%
Hispanic, low	Hispanic, high	**2.85%**	0.17%	**33.71%**	**3.10%**	0.00%
Asian, low	Asian, high	**1.42%**	0.00%	**28.11%**	0.39%	0.00%
White, low	White, high	**35.62%**	**17.99%**	**15.57%**	0.00%	0.00%

[1] Black who below poverty level (low income Black)

[2] Non-Hispanic White who at or above poverty level (high income White)

[3] Total Black without poverty information

* bold % means not significant when $\alpha = 1\%$

Table S 2-10. P-value of Type I hypothesis test for selected socioeconomic classes, target for $PM_{2.5}$ mass. $H_0: u1 = u2$; $H_1: u1 > u2$; $\alpha = 1\%$. D01 – statewide; D02 – South Coast; D03 – region-level

$u1$	$u2$	D01, 36KM	D02, 12KM	D03, 12KM	D03, 4KM
Race & Poverty level					
Black, low[1]	White, high[2]	0.00%	0.00%	0.00%	0.00%
Hispanic, low	White, high	0.00%	0.00%	0.00%	0.00%
Asian, low	White, high	**1.04%***	0.00%	0.00%	0.00%
Black, low	Asian, high	0.00%	0.00%	0.00%	0.00%
Race only					
Black, total[3]	White, total	0.00%	0.00%	0.00%	0.00%
Hispanic, total	White, total	0.00%	0.00%	0.00%	0.00%
Asian, total	White, total	**6.85%**	0.00%	0.66%	0.00%
Poverty level only					
Black, low	Black, high	**68.96%**	**4.75%**	**1.68%**	0.00%
Hispanic, low	Hispanic, high	**15.73%**	0.05%	**1.11%**	0.00%
Asian, low	Asian, high	**86.15%**	0.00%	0.53%	0.00%
White, low	White, high	**1%**	**4.48%**	**4.08%**	0.00%

[1] Black who below poverty level (low income Black)

[2] Non-Hispanic White who at or above poverty level (high income White)

[3] Total Black without poverty information

* bold % means not significant when $\alpha = 1\%$

Table S 2-11. Exposure disparity (units: µg/m^3) by PM2.5 species between top income category "household income > $200,000" and bottom income category "household income < $10,000". Income dataset is from ACS 2012-2016 household income.

Domain	**D03**	**D04**	**D05**
Resolution	**4KM**	**1KM**	**250M**
PM2.5 MASS	2.661	1.669	1.483
PM2.5 EC	0.217	0.155	0.151
PM2.5 OC	1.062	0.683	0.636
PM2.5 Primary	2.328	1.554	1.415
PM2.5 Secondary	0.327	0.107	0.064

S2.2.4 Exposure distribution by race/ethnicity

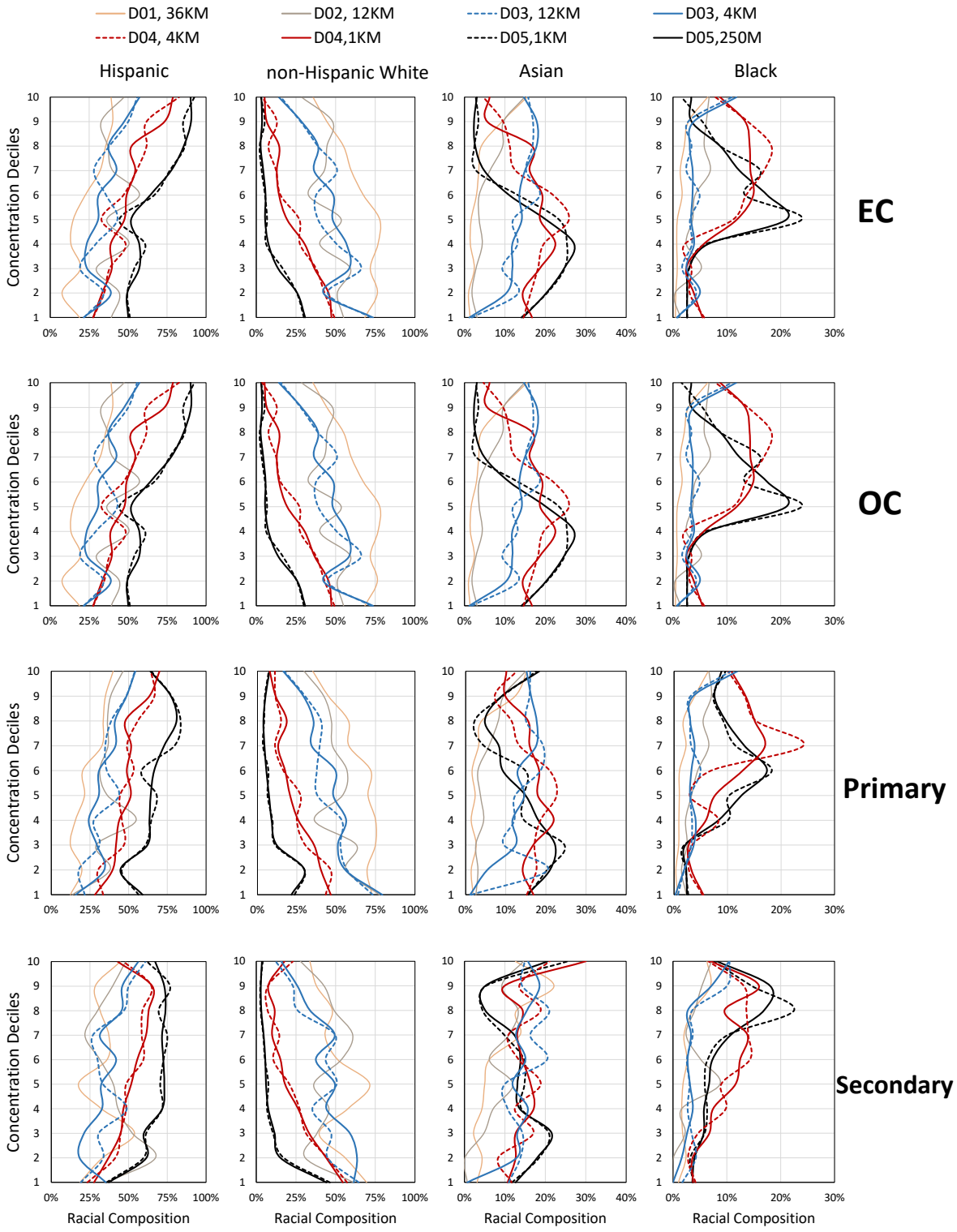

Figure S 2-21. $PM_{2.5}$ EC, OC, primary aerosol mass and secondary aerosol mass exposure distribution across racial-ethnic population. Figures focus on spatial resolution and domain scope changes on racial-ethnic population exposure distribution.

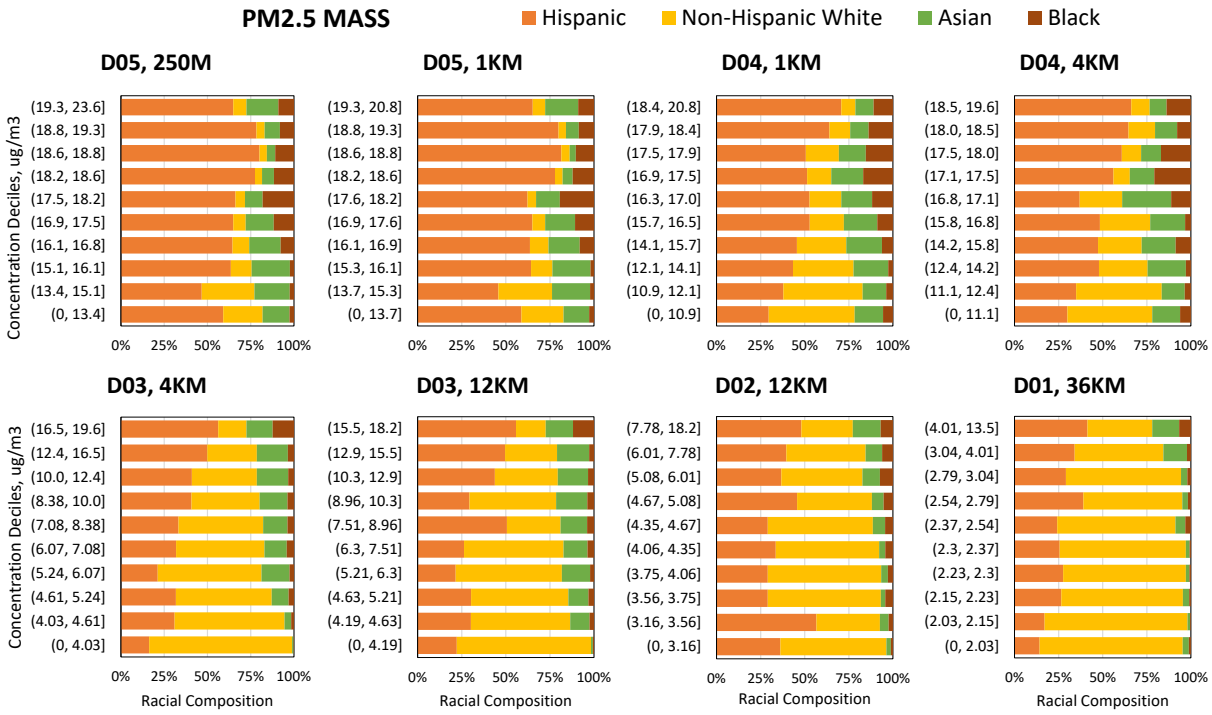

Figure S 2-22. PM2.5 mass exposure distribution across racial-ethnic population using different domain – resolution combinations. Values at each concentration decile (y axis) describe the racial composition at that concentration level (x axis). Comparisons between panels show the effects of domain size and resolution.

Appendix 3

S3.1 Socio-economic data

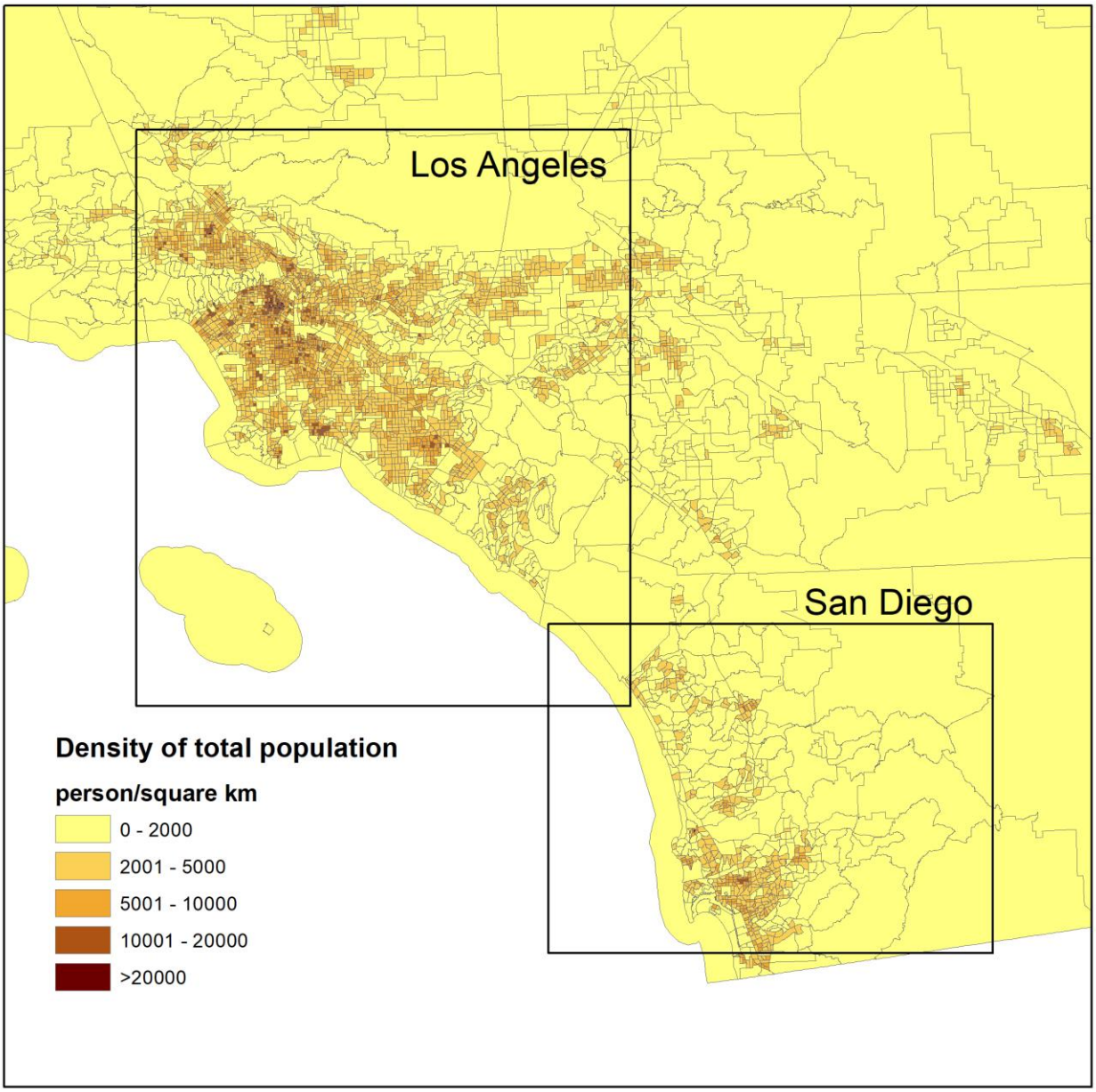

Figure S 3-1. Total population density of Southern California.

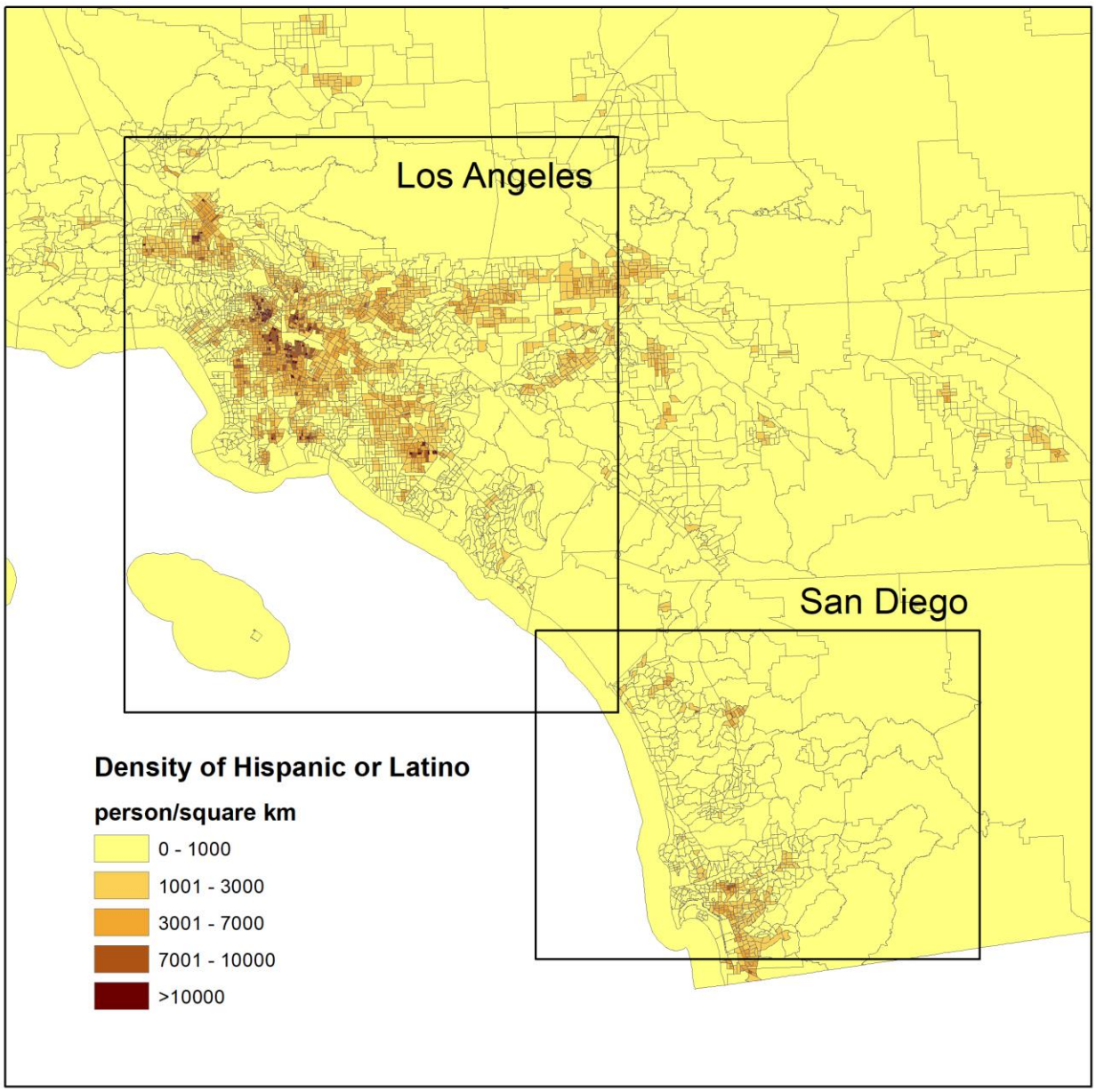

Figure S 3-2. Hispanic or Latino population density of Southern California.

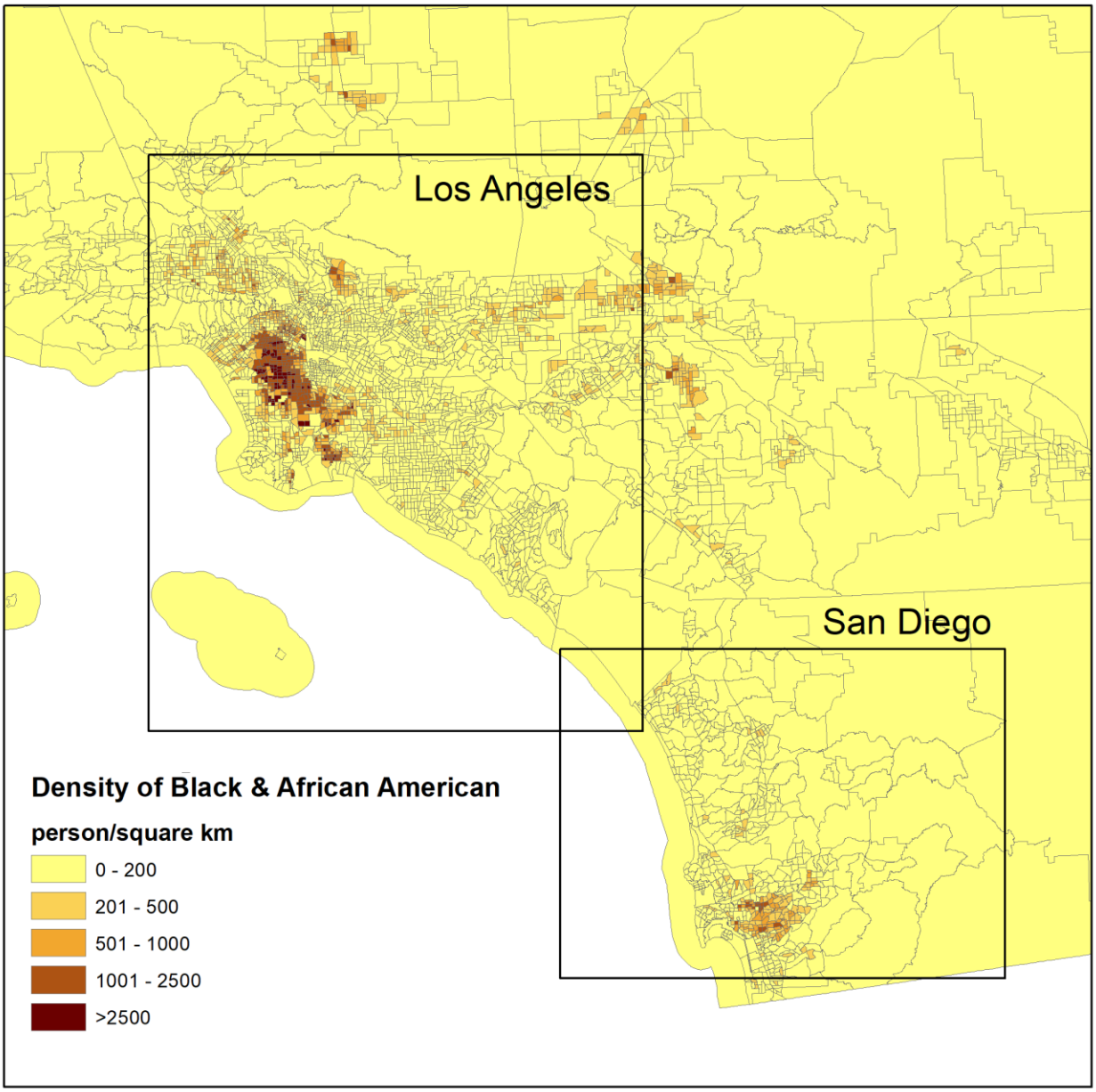

Figure S 3-3. Black & African American population density of Southern California.

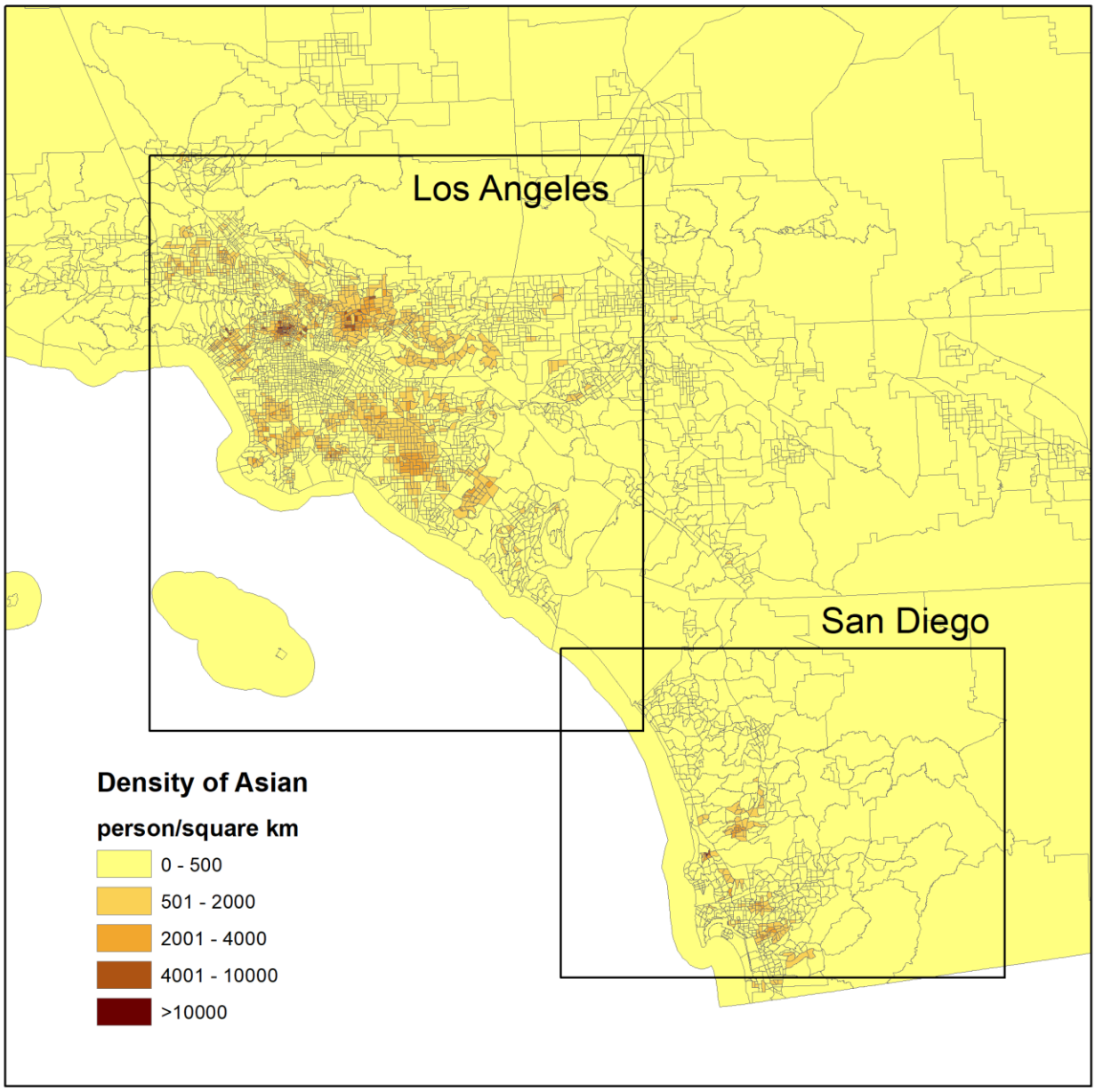

Figure S 3-4. Asian population density of Southern California.

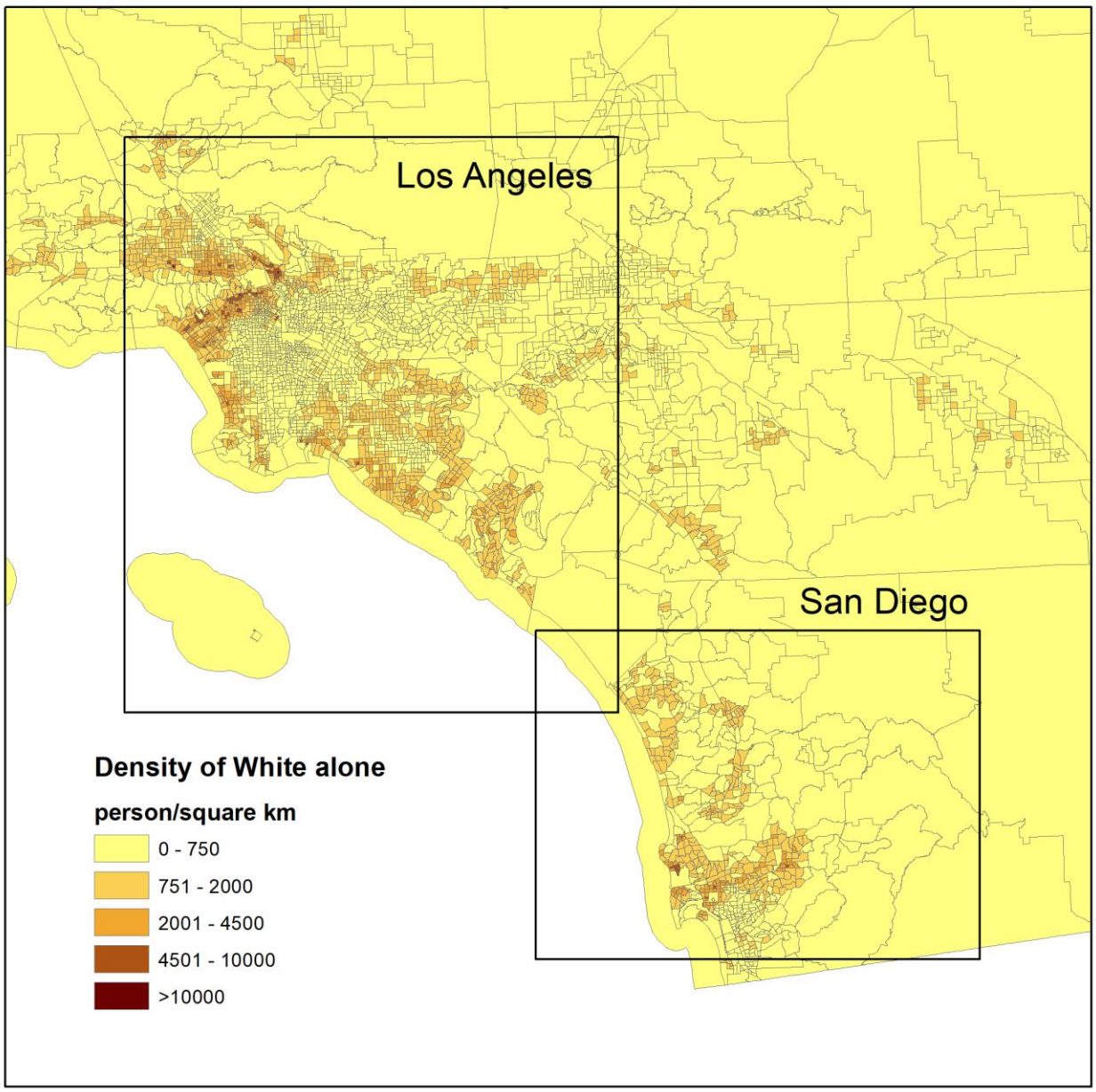

Figure S 3-5. White population density of Southern California.

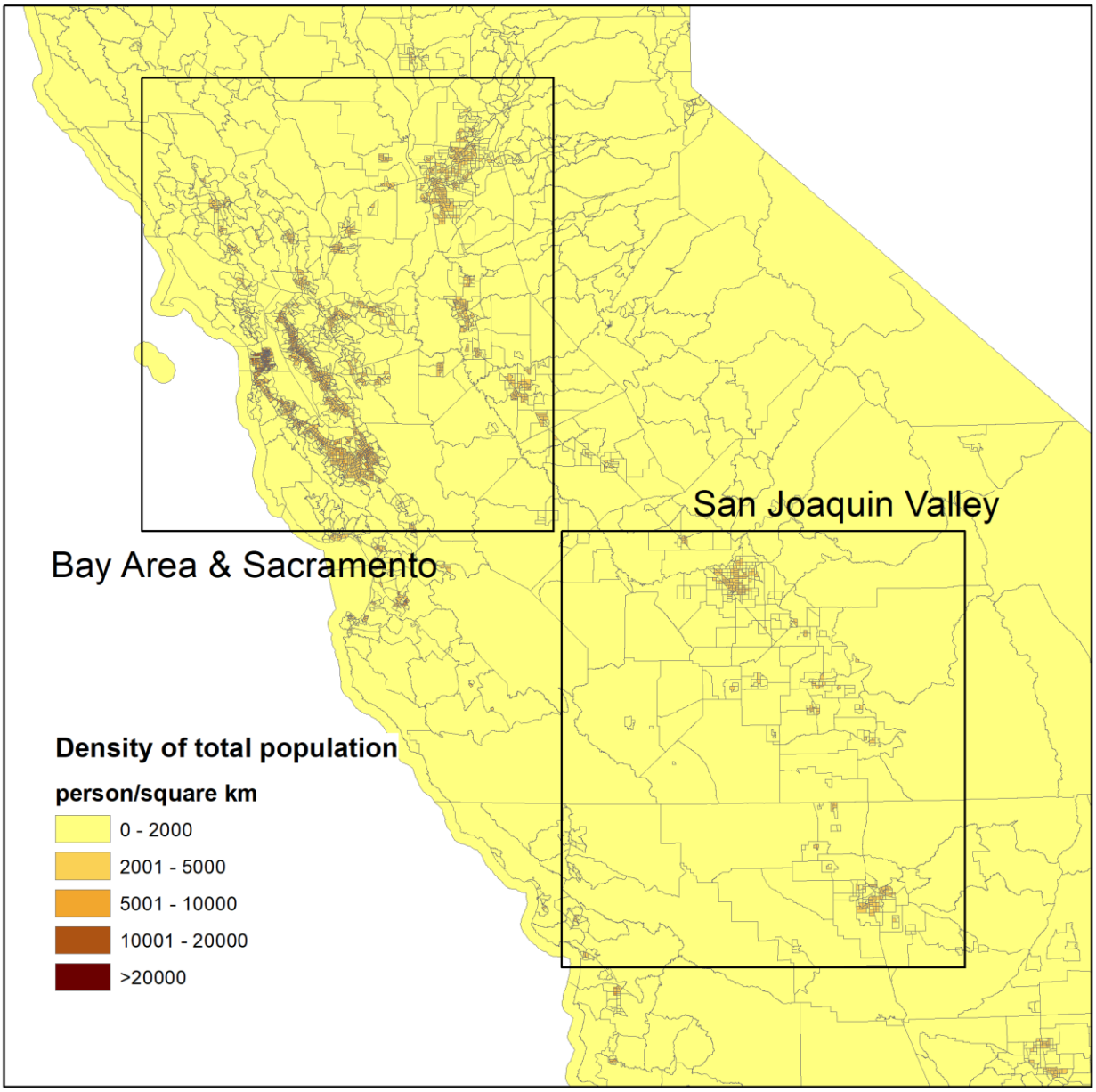

Figure S 3-6. Total population density of Northern California.

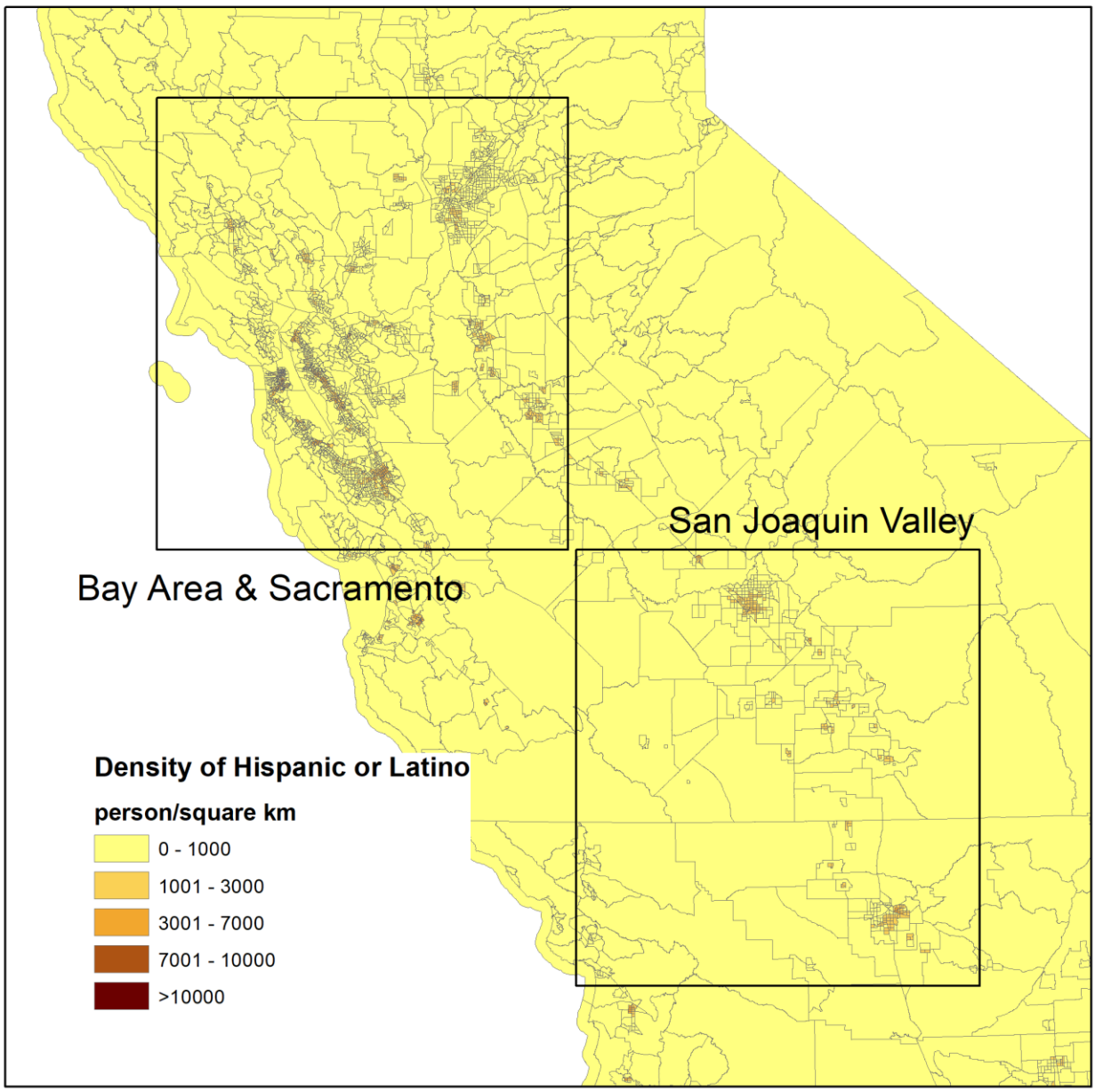

Figure S 3-7. Hispanic or Latino population density of Northern California.

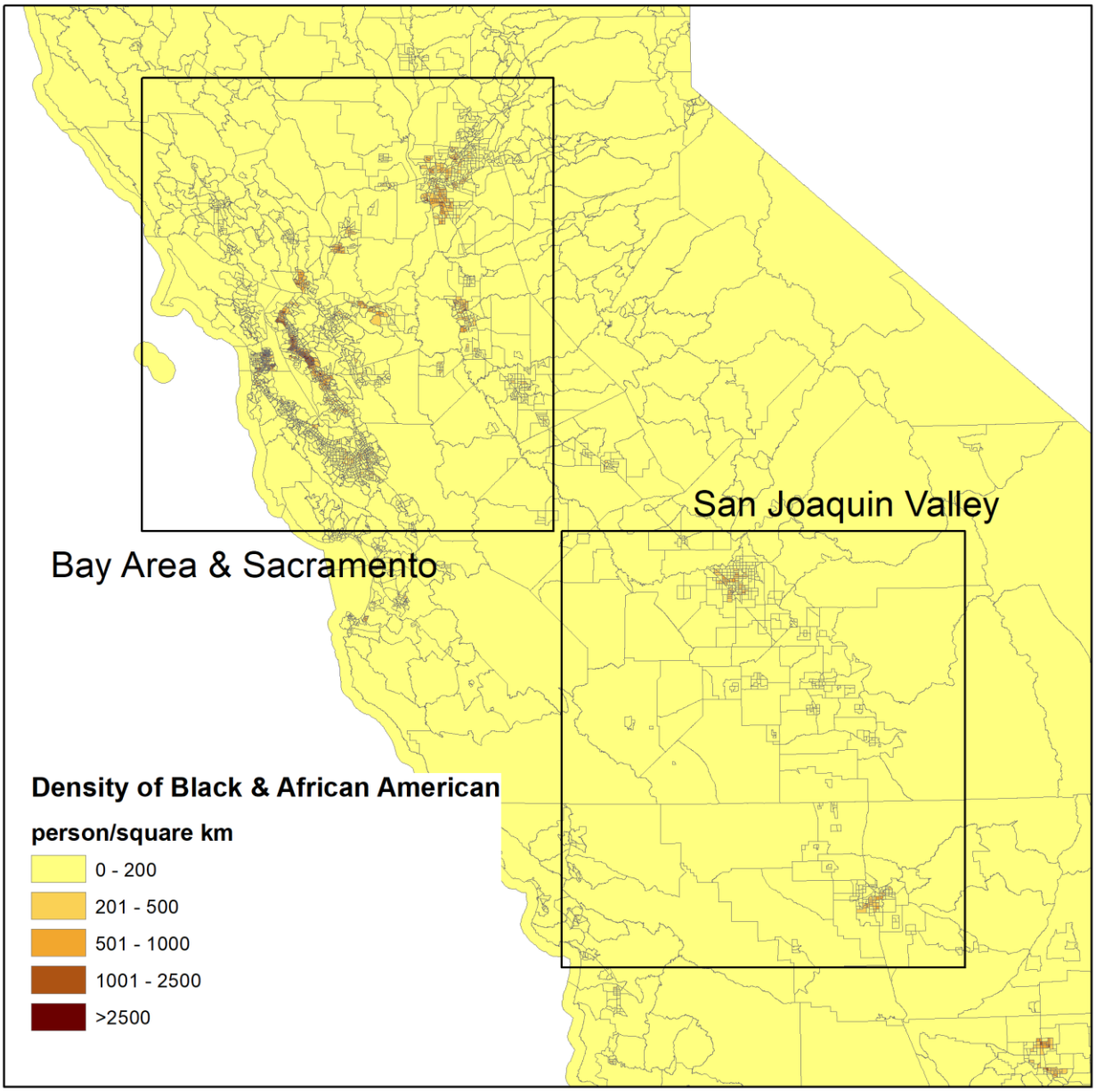

Figure S3-8. Black & African American population density of Northern California.

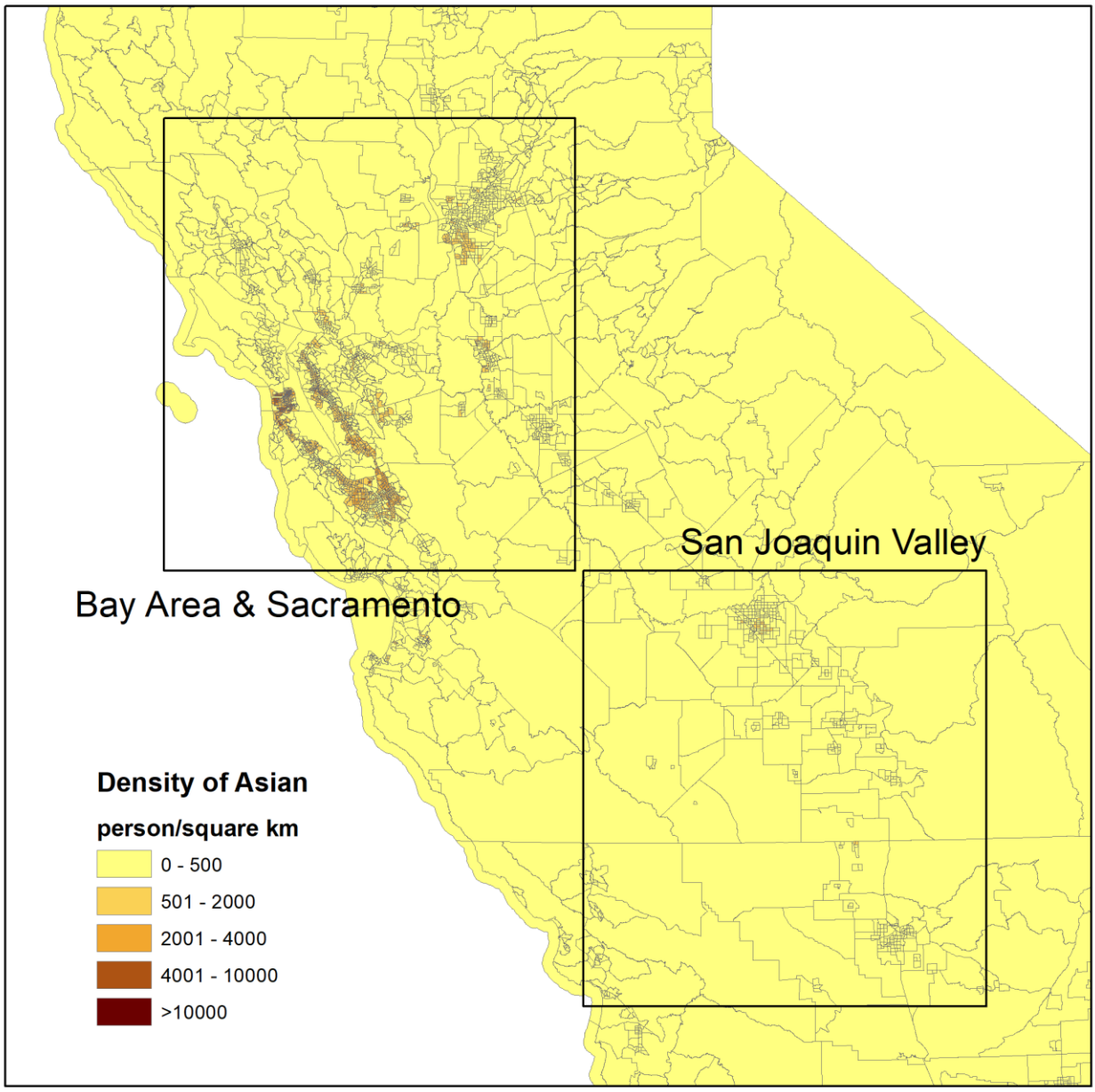

Figure S 3-9. Asian population density of Northern California.

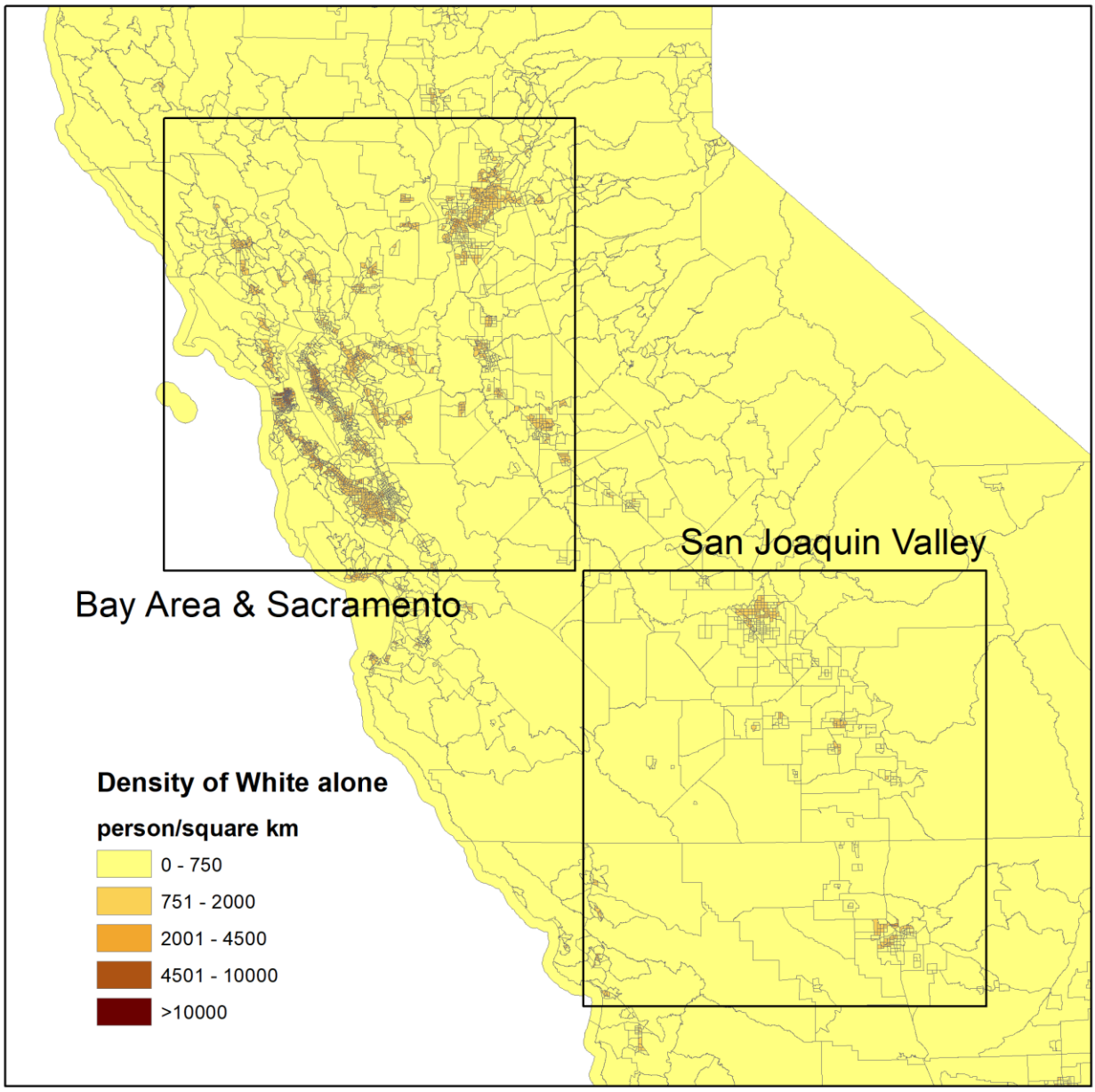

Figure S 3-10. White population density of Northern California.

S3.2 Absolute exposure

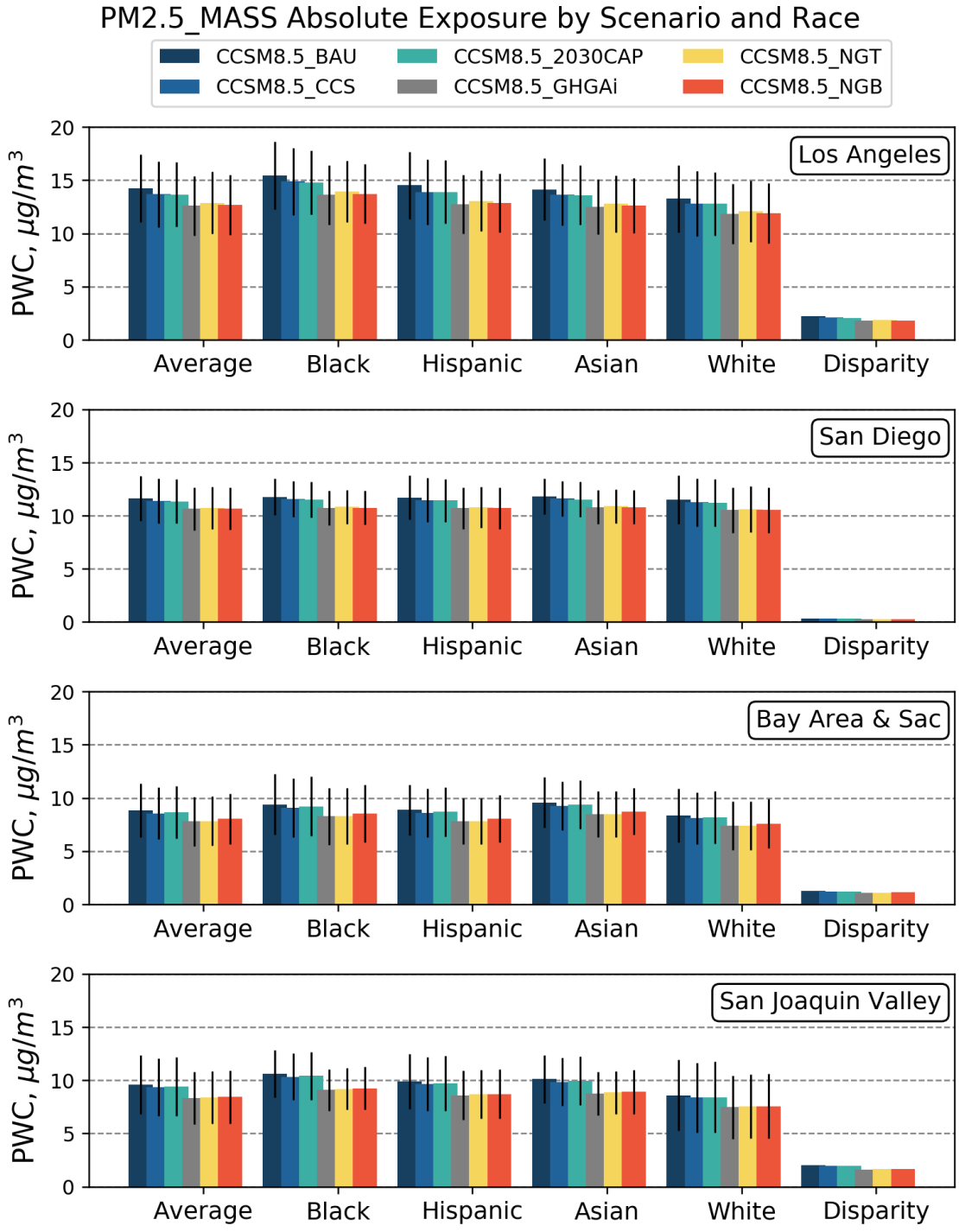

Figure S 3-11. Future year 2050 ***PM2.5*** *absolute exposure by energy scenario and race/ethnicity at 4 regions in California. Exposures under* ***CCSM8.5*** *met scenarios. Error bar represents population weighted standard deviation. The category on the far right quantifies absolute disparity between racial groups.*

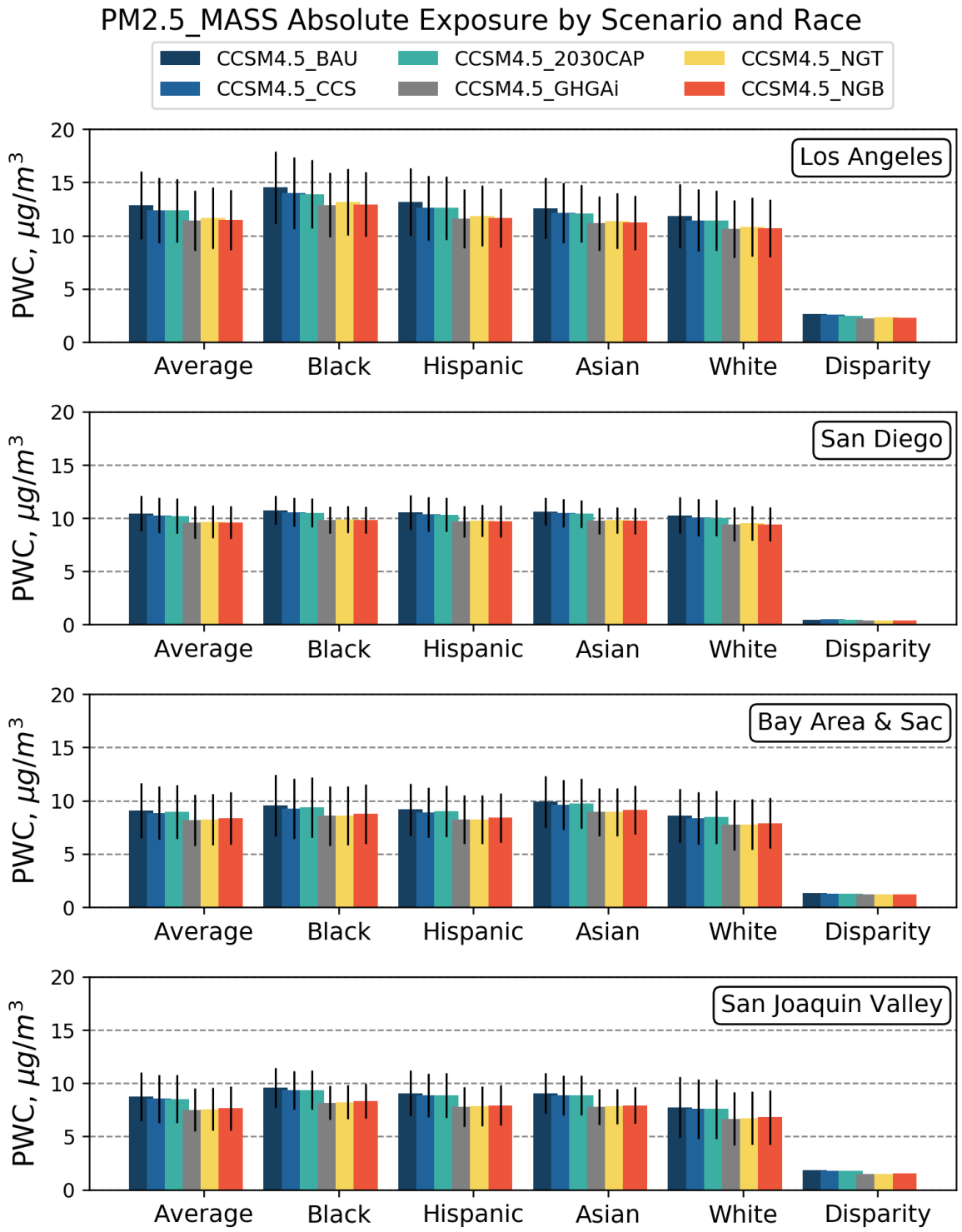

Figure S 3-12. Future year 2050 ***PM2.5*** *absolute exposure by energy scenario and race/ethnicity at 4 regions in California. Exposures under* ***CCSM4.5*** *met scenarios. Error bar represents population weighted standard deviation. The category on the far right quantifies absolute disparity between racial groups.*

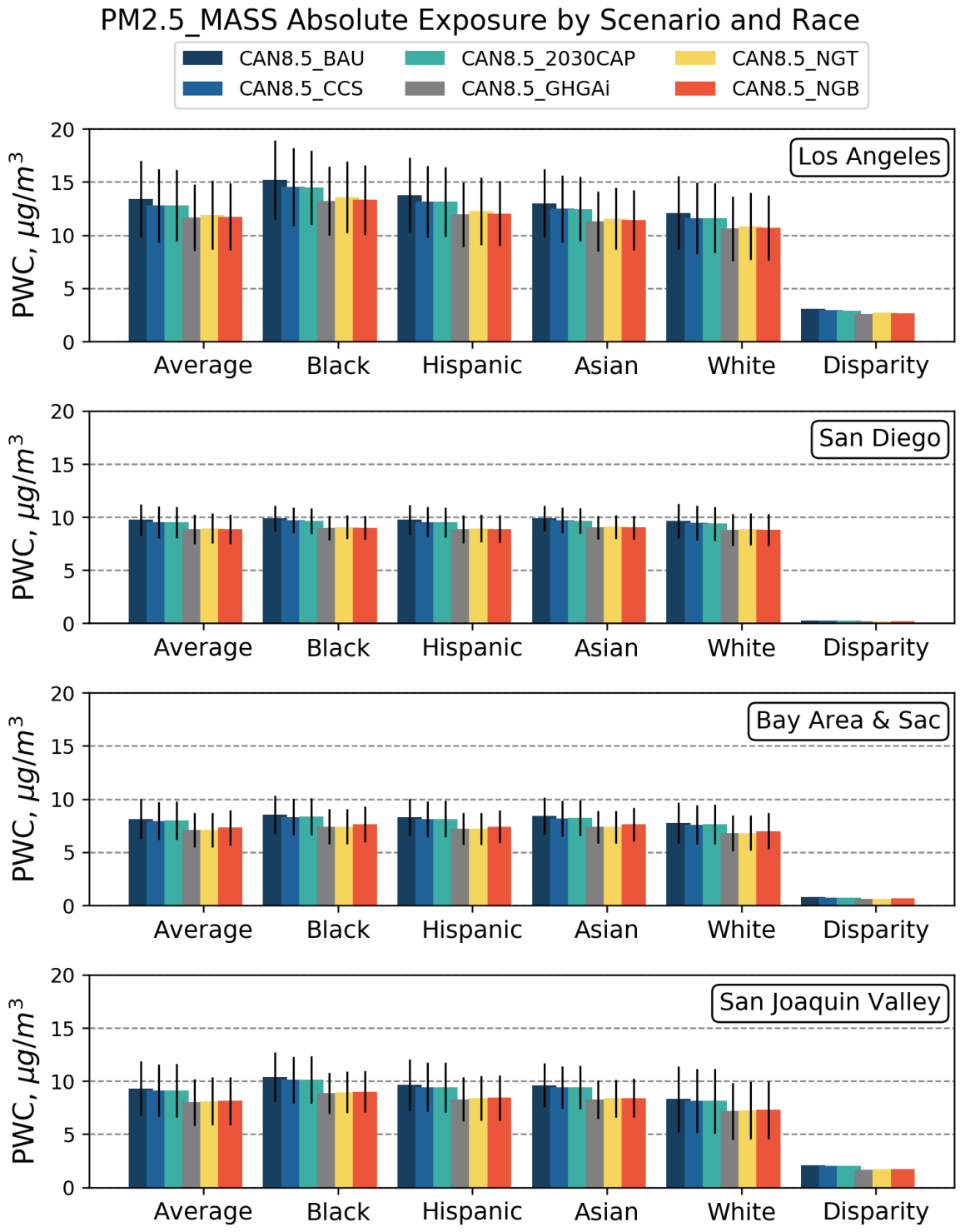

Figure S 3-13. Future year 2050 ***PM2.5*** *absolute exposure by energy scenario and race/ethnicity at 4 regions in California. Exposures under* ***CAN8.5*** *met scenarios. Error bar represents population weighted standard deviation. The category on the far right quantifies absolute disparity between racial groups.*

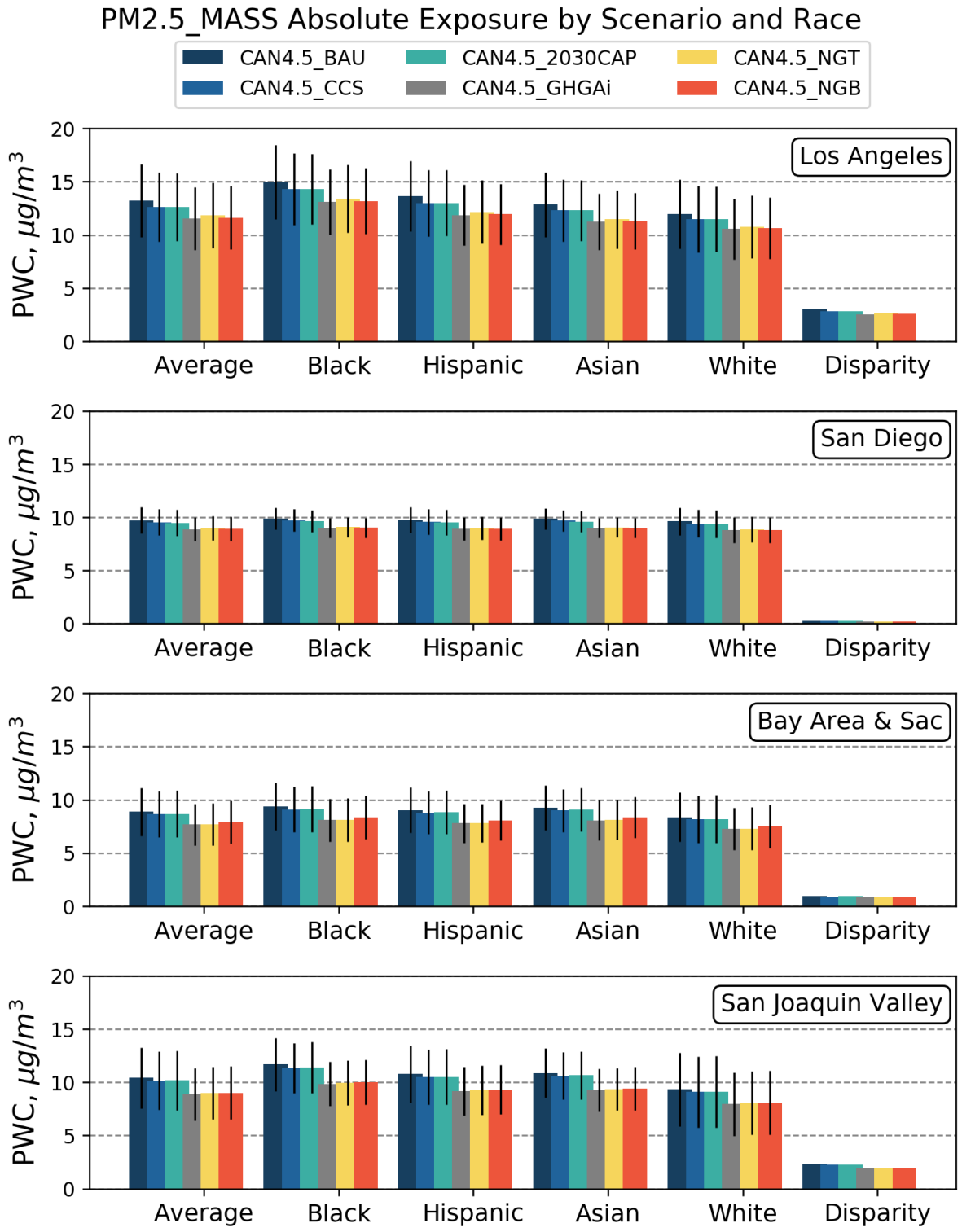

Figure S 3-14. Future year 2050 ***PM2.5*** *absolute exposure by energy scenario and race/ethnicity at 4 regions in California. Exposures under* ***CAN4.5*** *met scenarios. Error bar represents population weighted standard deviation. The category on the far right quantifies absolute disparity between racial groups.*

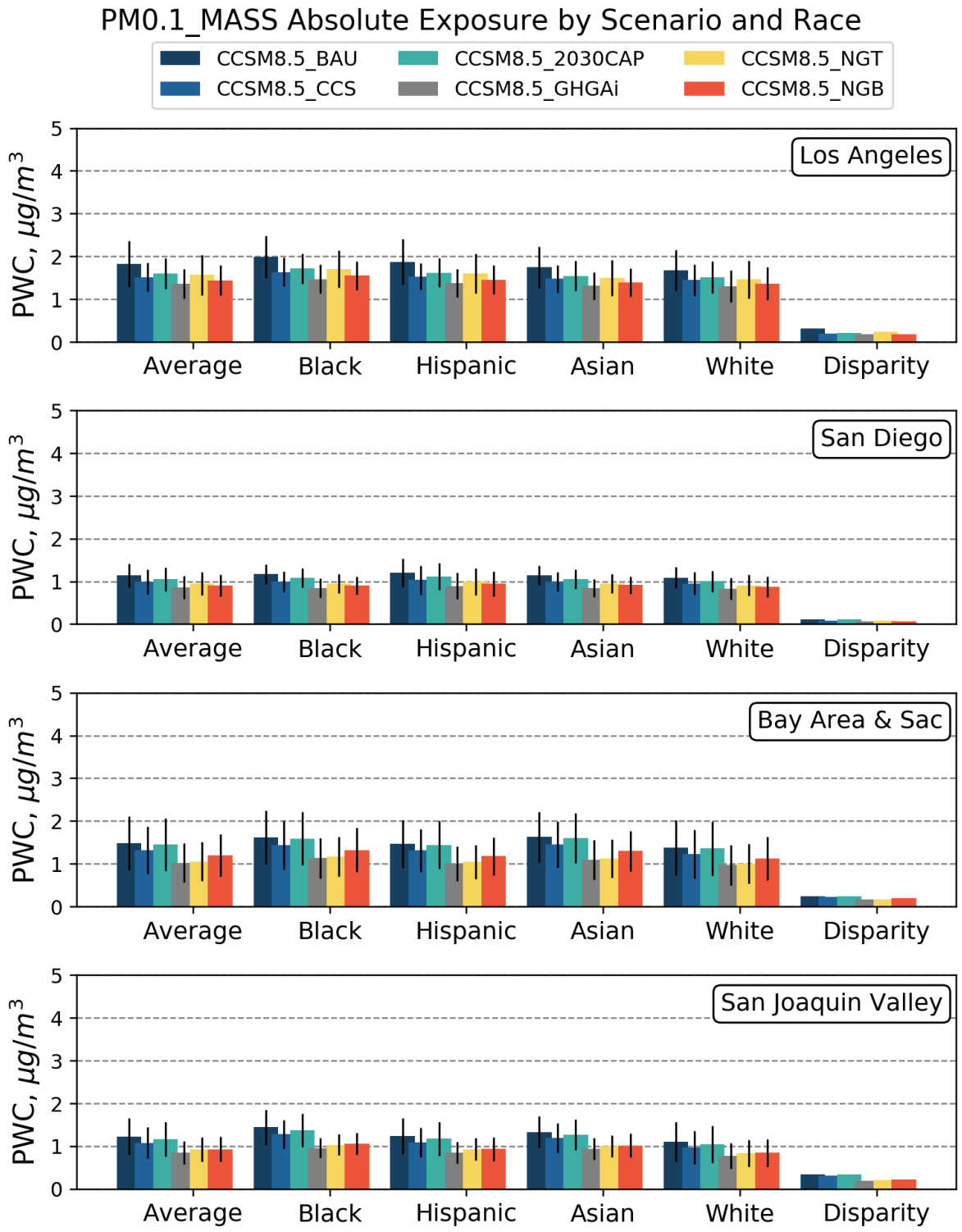

Figure S 3-15. Future year 2050 ***PM0.1*** *absolute exposure by energy scenario and race/ethnicity at 4 regions in California. Exposures under* ***CCSM8.5*** *met scenarios. Error bar represents population weighted standard deviation. The category on the far right quantifies absolute disparity between racial groups.*

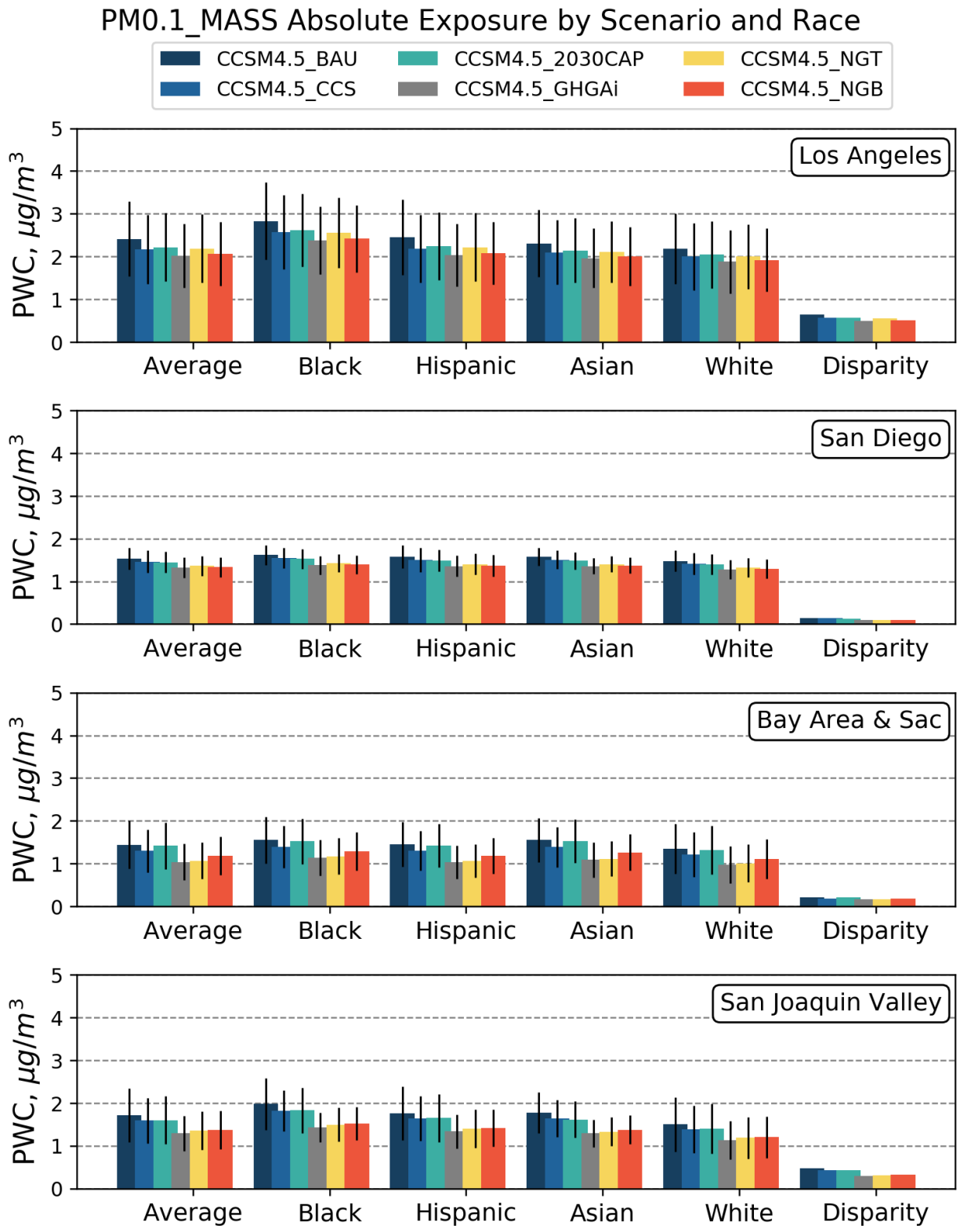

Figure S 3-16. Future year 2050 ***PM0.1*** *absolute exposure by energy scenario and race/ethnicity at 4 regions in California. Exposures under* ***CCSM4.5*** *met scenarios. Error bar represents population weighted standard deviation. The category on the far right quantifies absolute disparity between racial groups.*

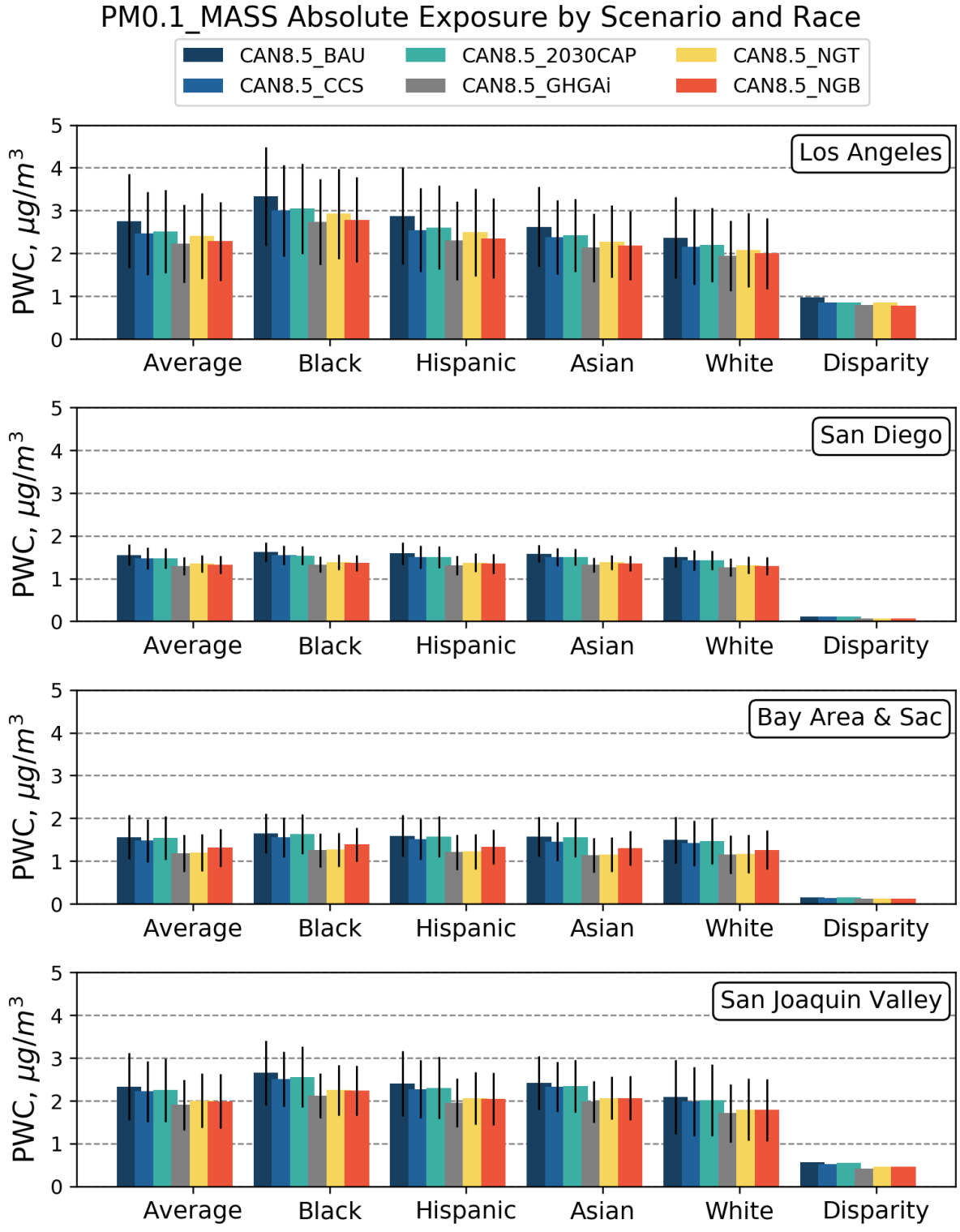

Figure S 3-17. Future year 2050 ***PM0.1*** *absolute exposure by energy scenario and race/ethnicity at 4 regions in California. Exposures under* ***CAN8.5*** *met scenarios. Error bar represents population weighted standard deviation. The category on the far right quantifies absolute disparity between racial groups.*

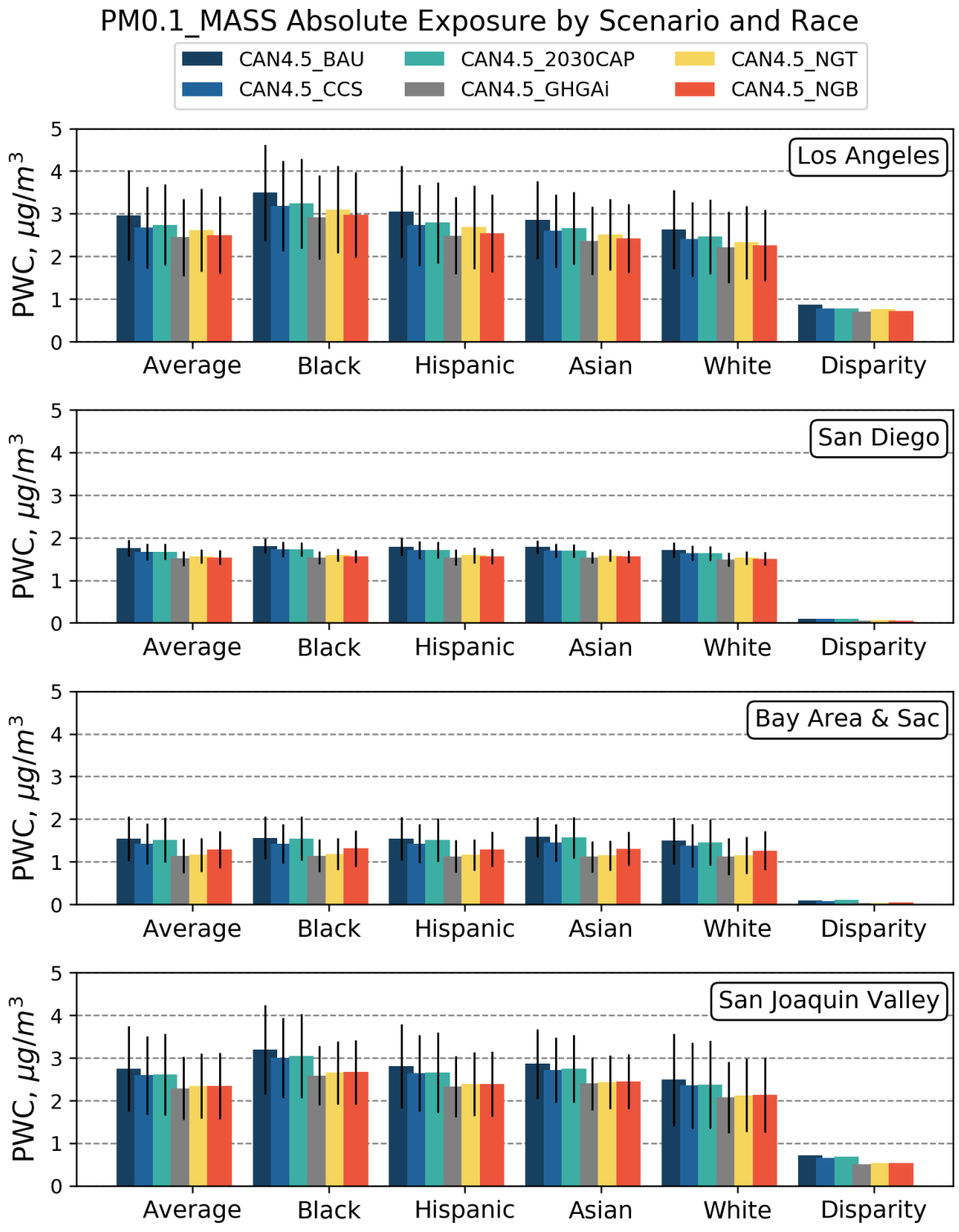

Figure S 3-18. Future year 2050 ***PM0.1*** *absolute exposure by energy scenario and race/ethnicity at 4 regions in California. Exposures under* ***CAN4.5*** *met scenarios. Error bar represents population weighted standard deviation. The category on the far right quantifies absolute disparity between racial groups.*

S3.3 Relative exposure

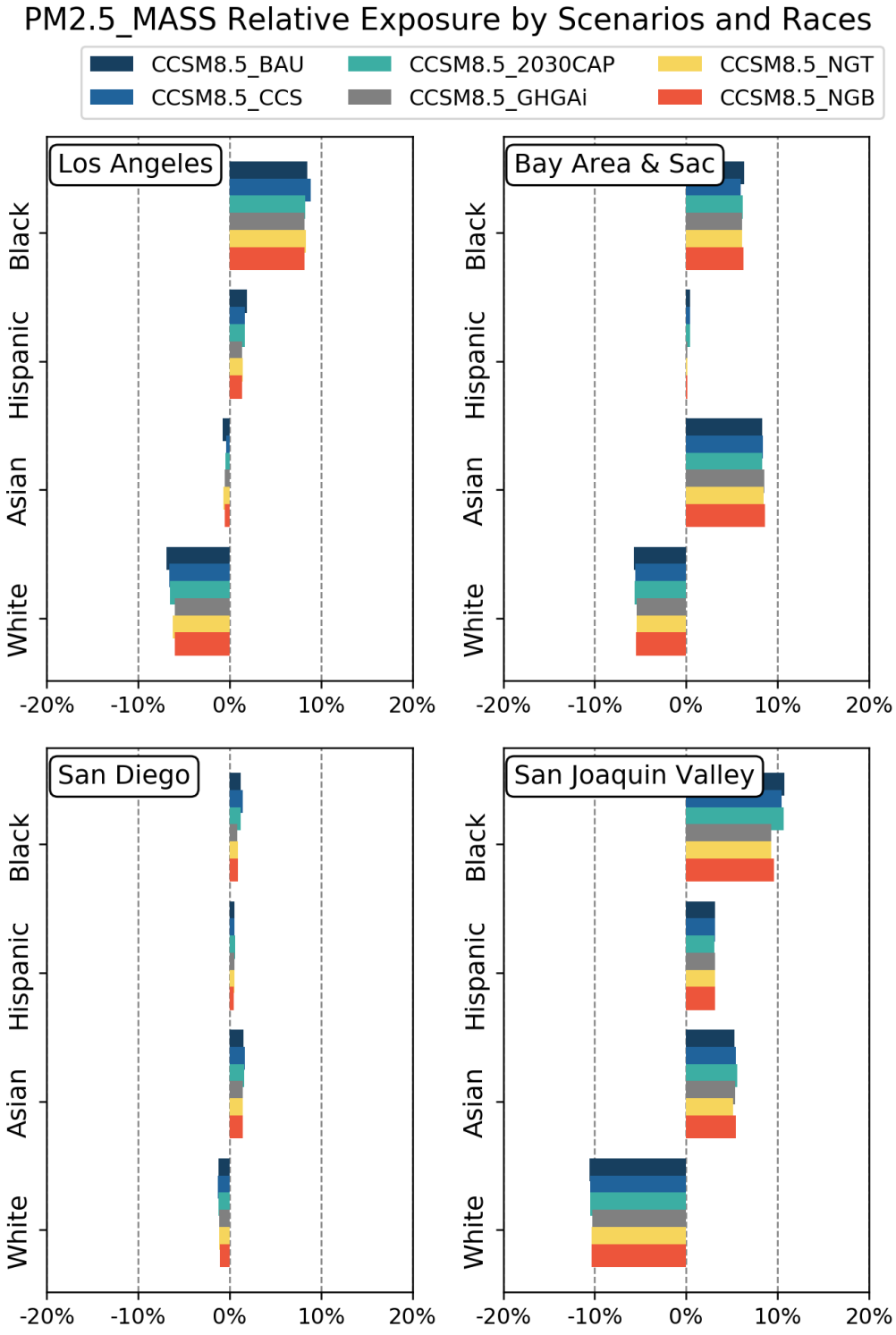

Figure S 3-19. Future year 2050 ***PM2.5*** *mass relative exposure (to total population) disparity by scenario and race/ethnicity at 4 regions in California under met scenario* ***CCSM8.5****.*

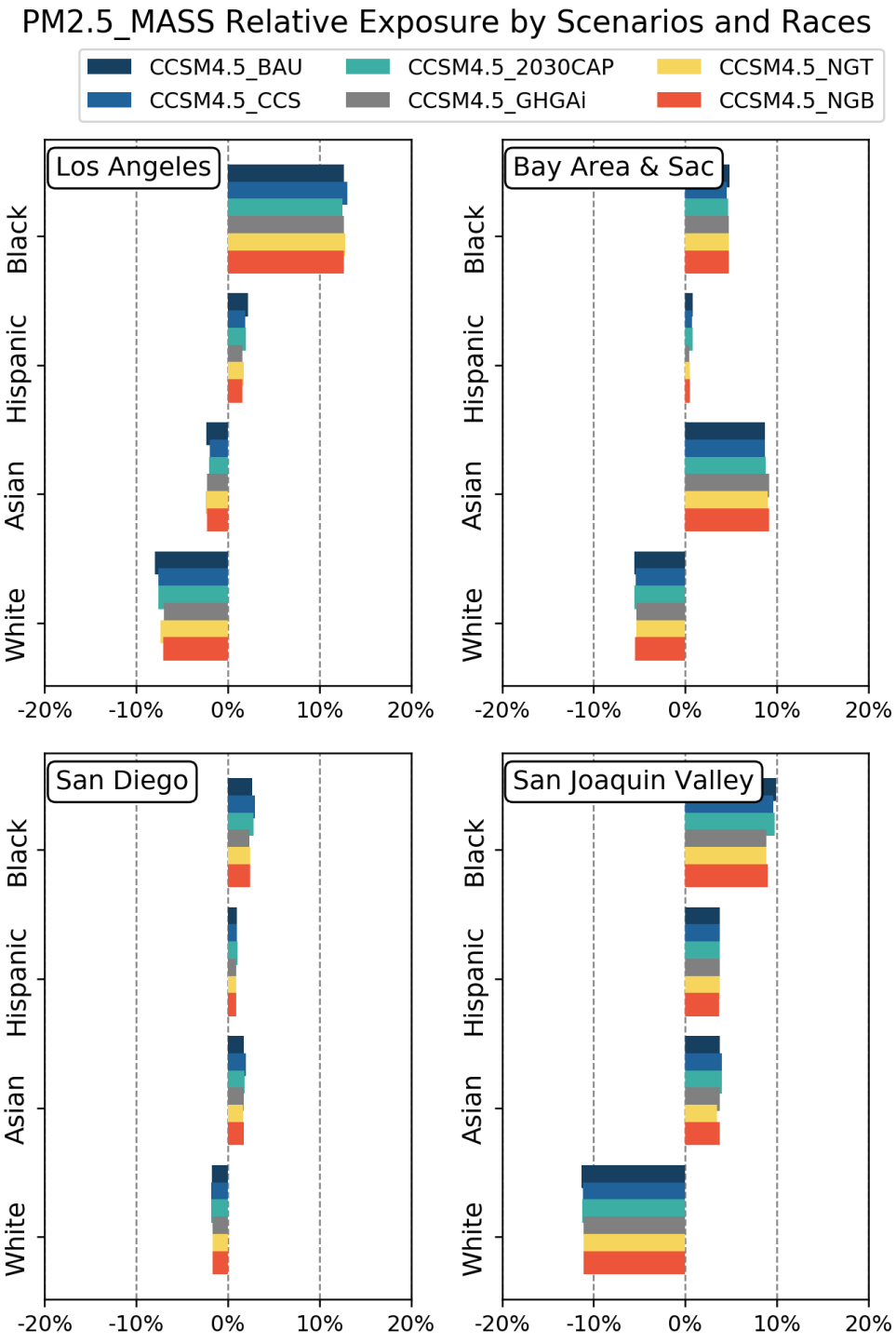

Figure S 3-20. Future year 2050 ***PM2.5*** *mass relative exposure (to total population) disparity by scenario and race/ethnicity at 4 regions in California under met scenario* ***CCSM4.5****.*

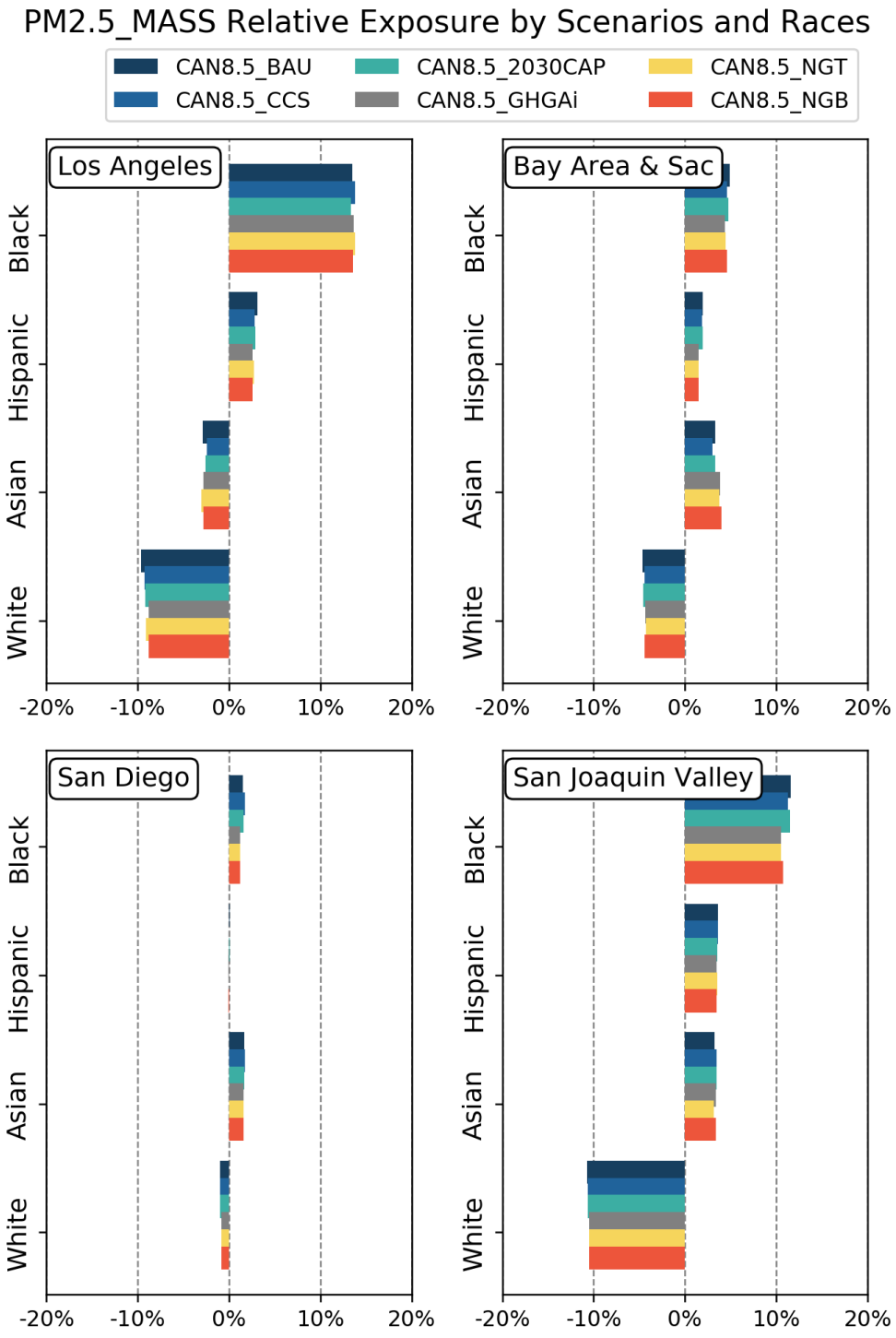

Figure S 3-21. Future year 2050 ***PM2.5*** *mass relative exposure (to total population) disparity by scenario and race/ethnicity at 4 regions in California under met scenario* ***CAN8.5****.*

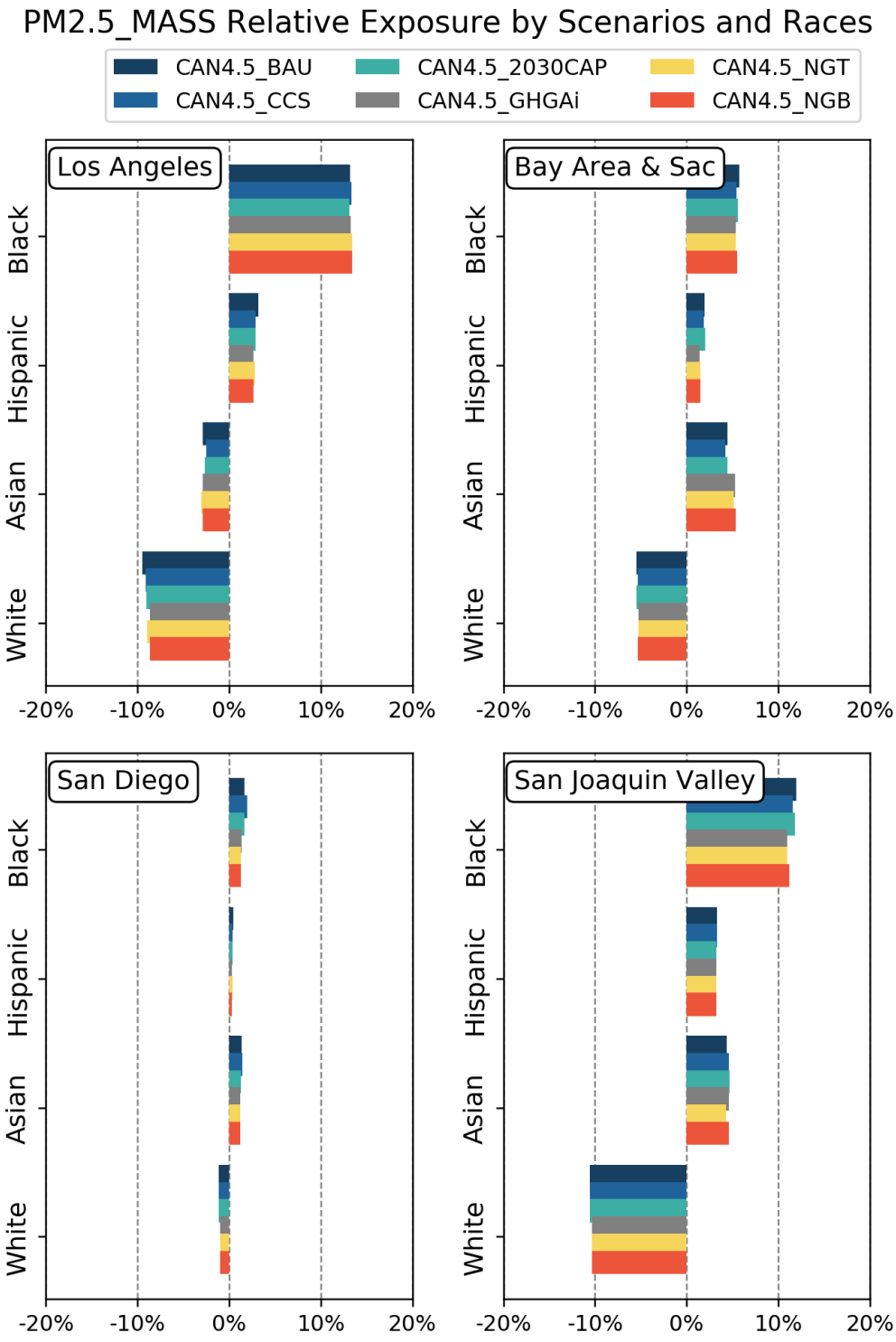

Figure S 3-22. Future year 2050 ***PM2.5*** *mass relative exposure (to total population) disparity by scenario and race/ethnicity at 4 regions in California under met scenario* ***CAN4.5****.*

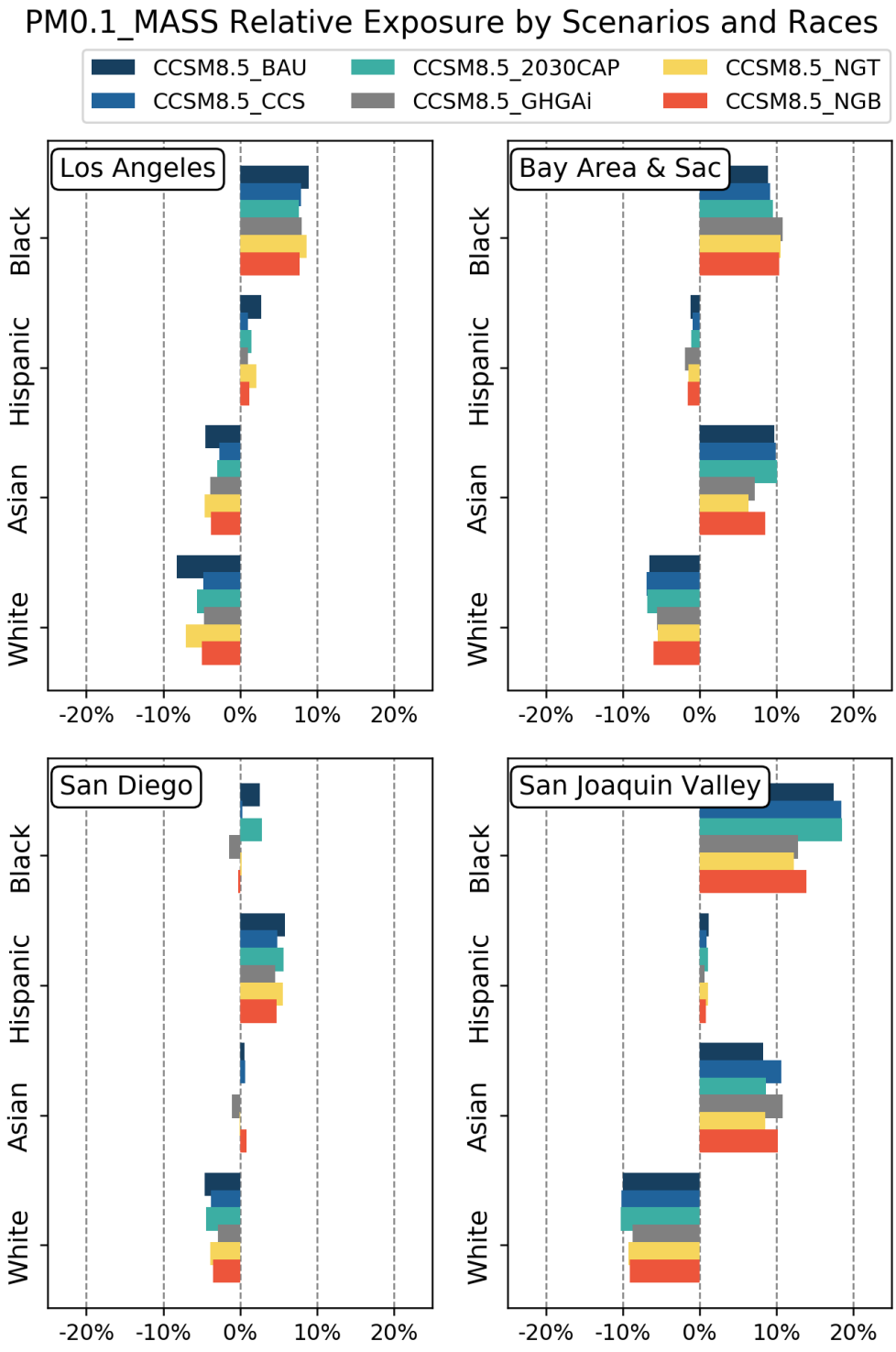

Figure S 3-23. Future year 2050 ***PM0.1*** *mass relative exposure (to total population) disparity by scenario and race/ethnicity at 4 regions in California under met scenario* ***CCSM8.5****.*

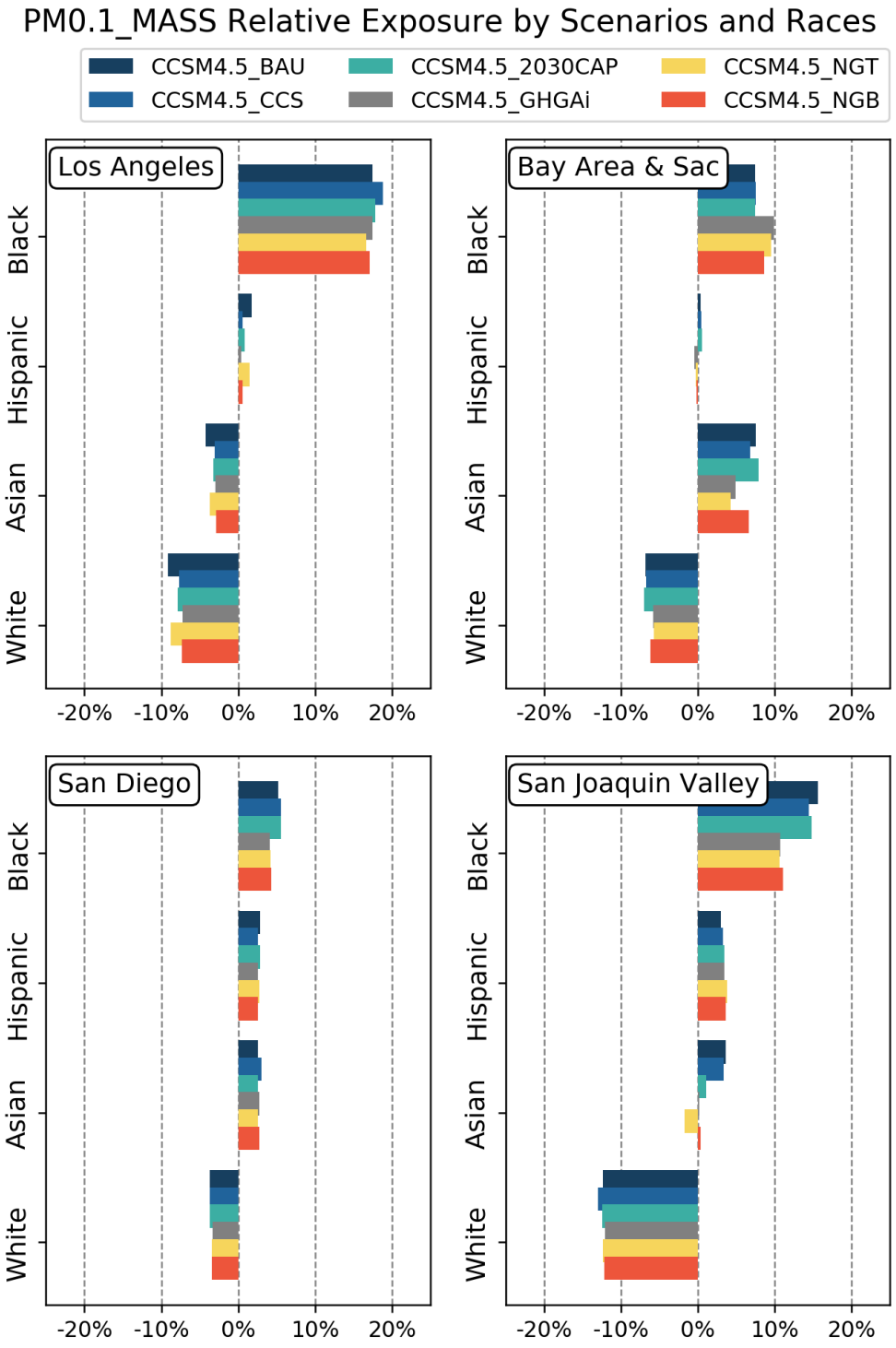

Figure S 3-24. Future year 2050 ***PM0.1*** *mass relative exposure (to total population) disparity by scenario and race/ethnicity at 4 regions in California under met scenario* ***CCSM4.5****.*

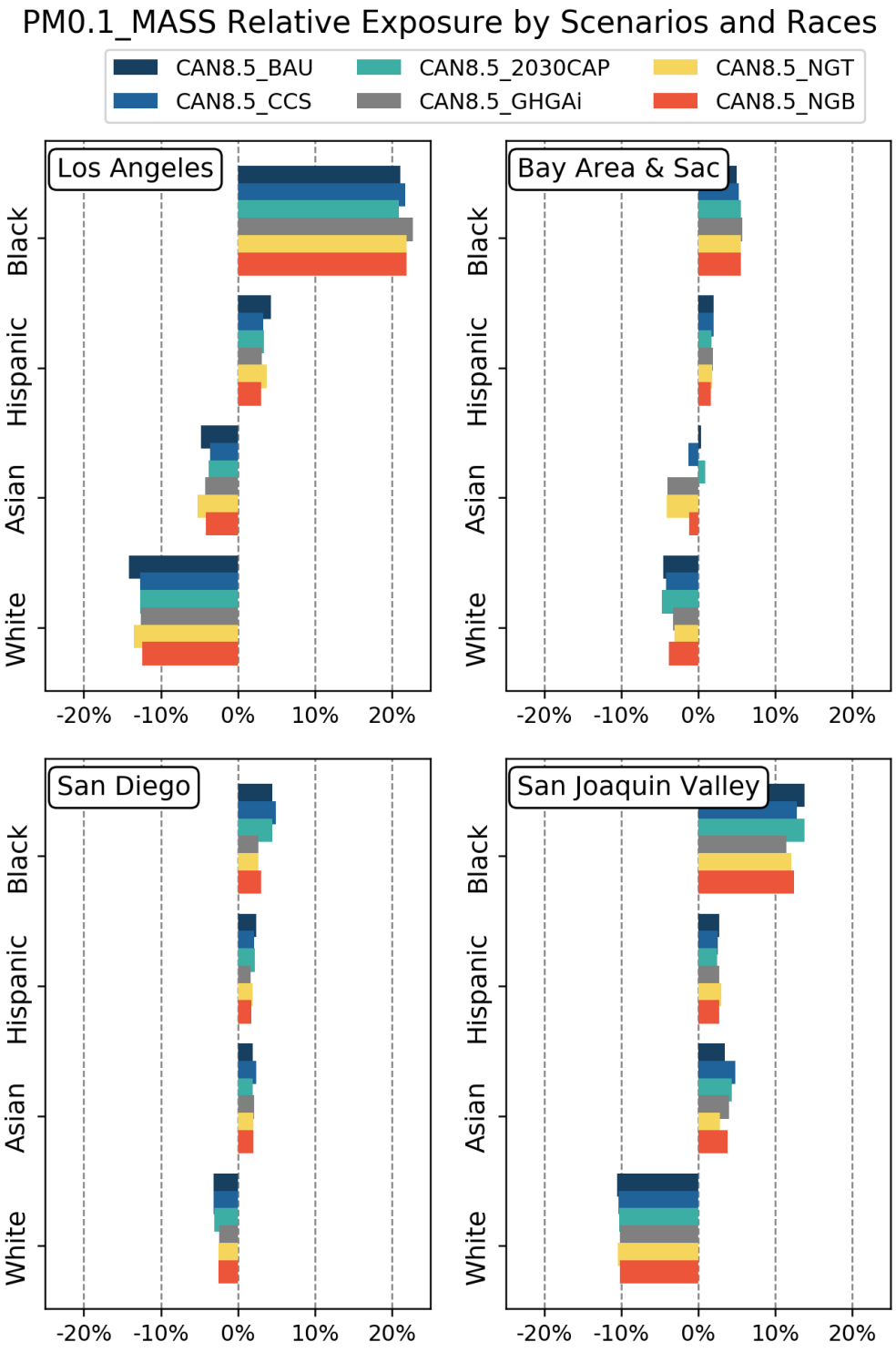

Figure S 3-25. Future year 2050 ***PM0.1*** *mass relative exposure (to total population) disparity by scenario and race/ethnicity at 4 regions in California under met scenario* ***CAN8.5****.*

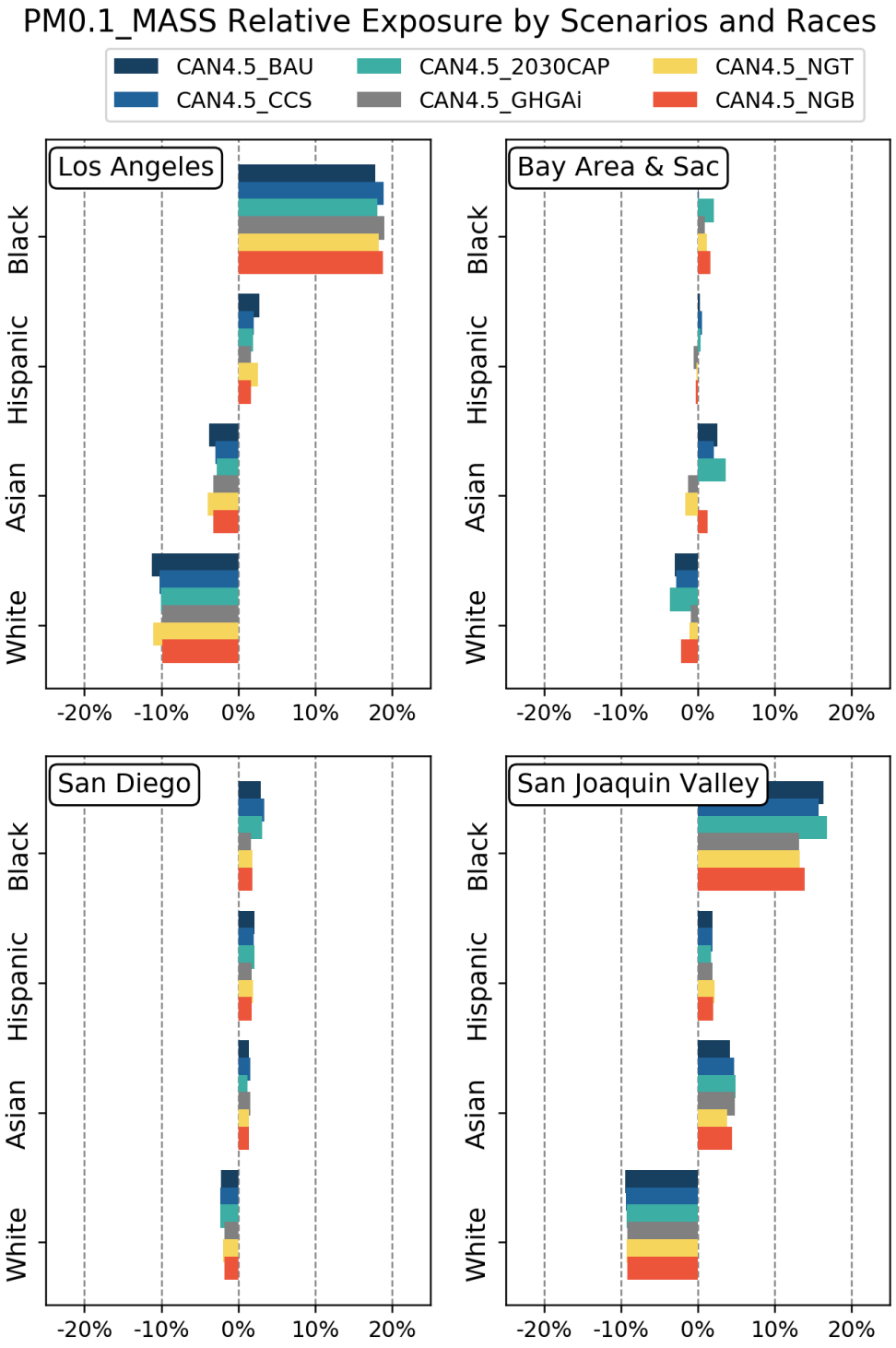

Figure S 3-26. Future year 2050 ***PM0.1*** *mass relative exposure (to total population) disparity by scenario and race/ethnicity at 4 regions in California under met scenario* ***CAN4.5****.*

S3.4 Source composition

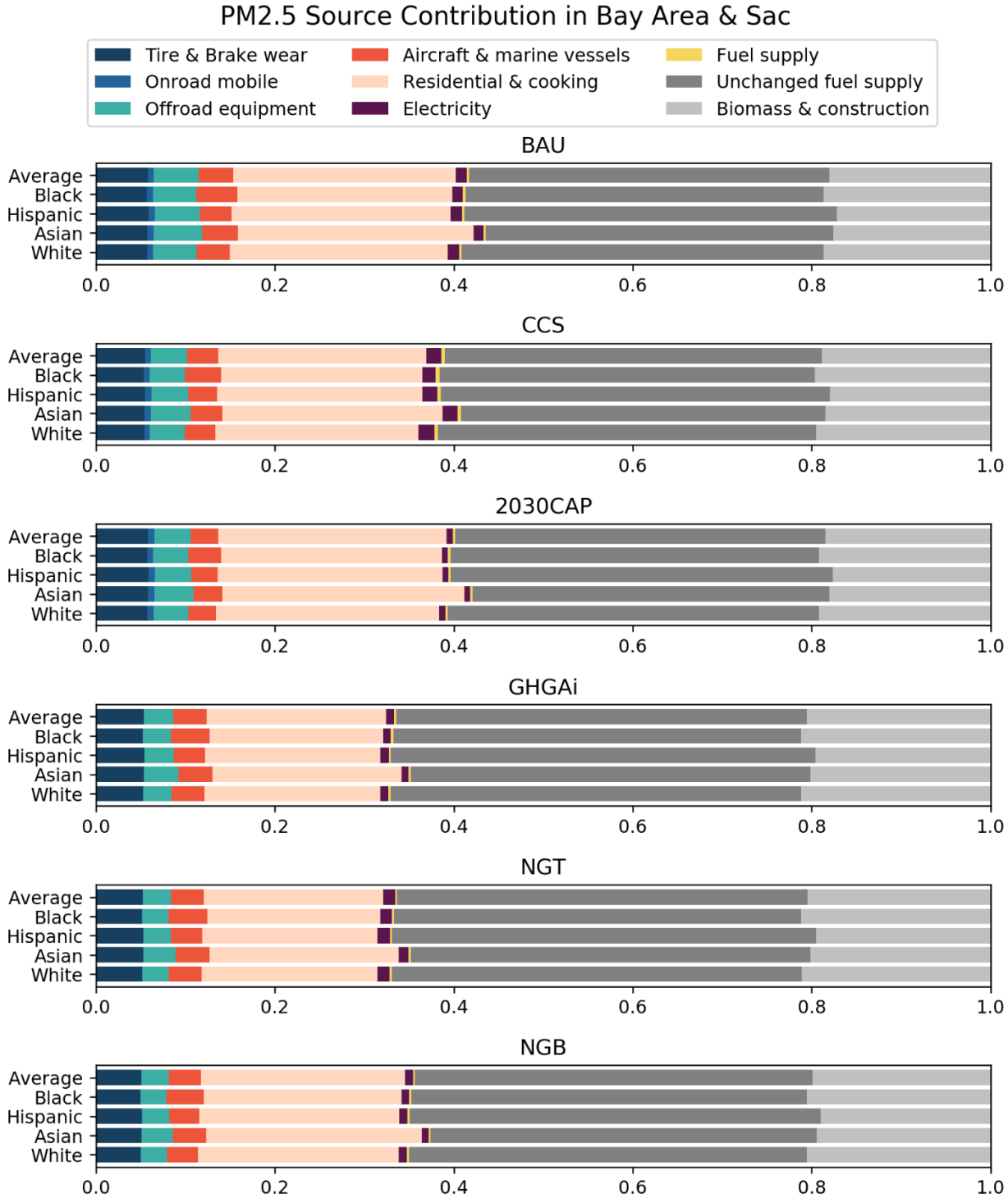

Figure S 3-27. PM2.5 source contributions in Bay Area & Sacramento by energy scenarios and race/ethnicity. Each value represents the average across four meteorological scenarios.

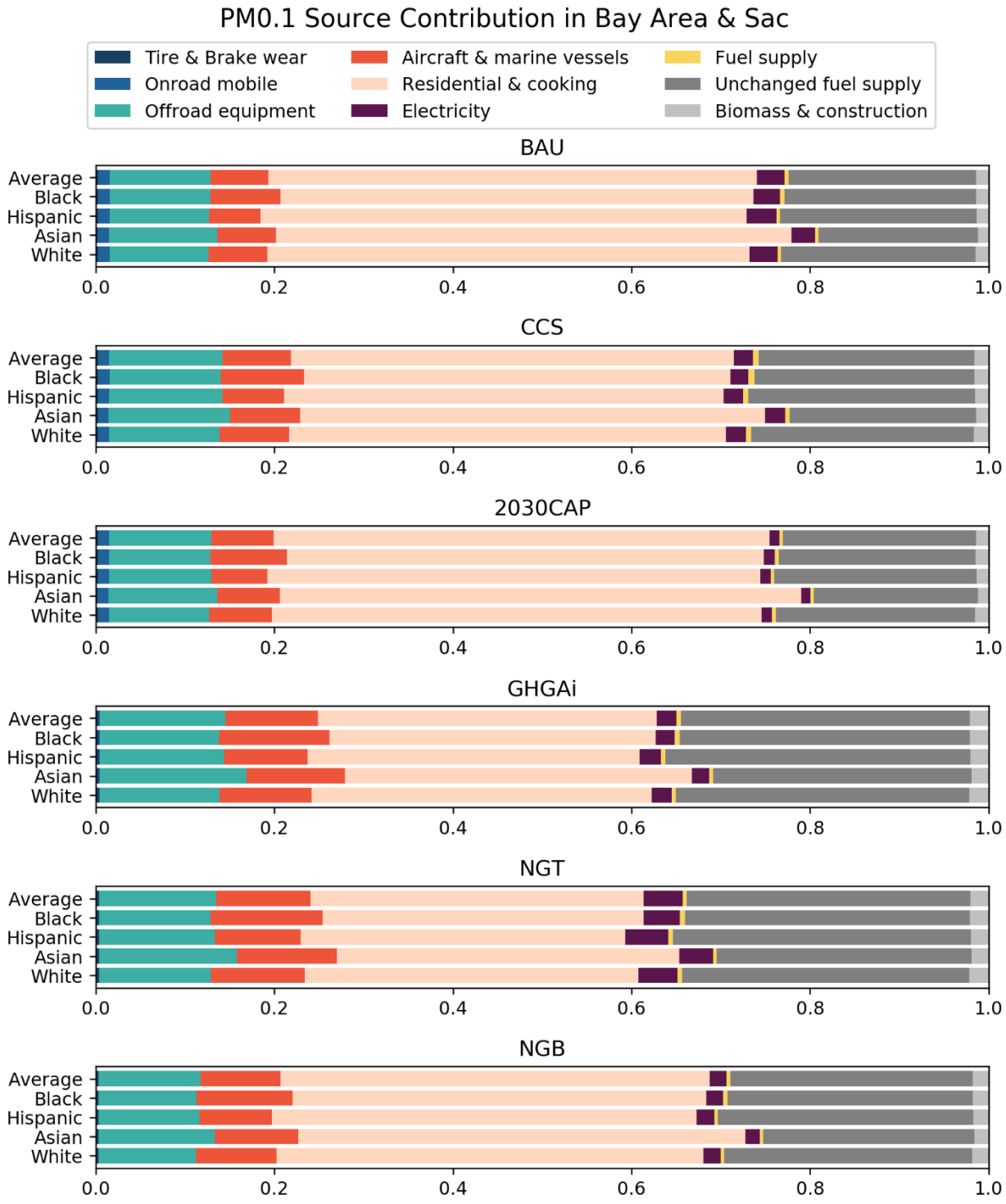

Figure S 3-28. PM0.1 source contributions in Bay Area & Sacramento by energy scenarios and race/ethnicity. Each value represents the average across four meteorological scenarios.

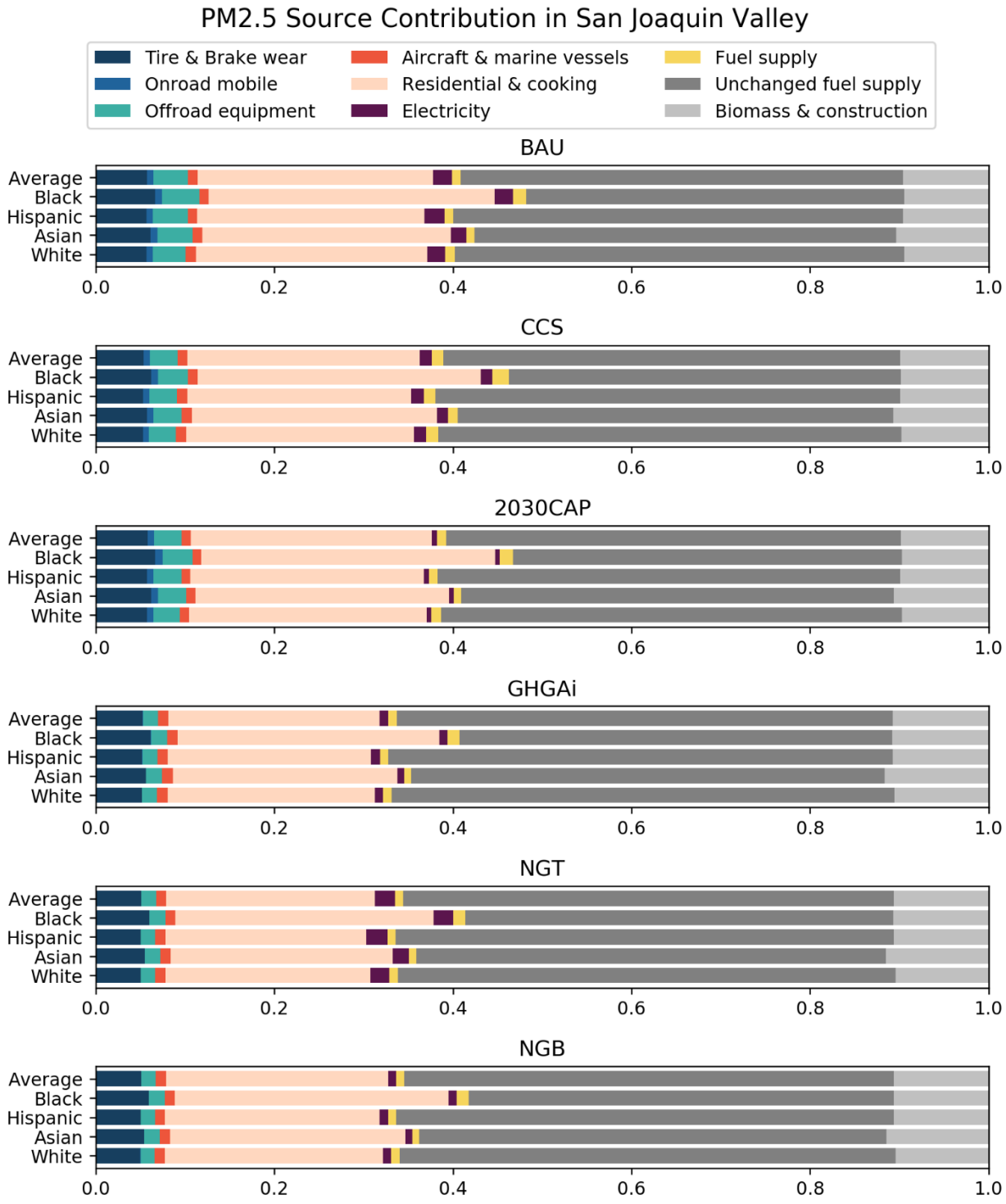

Figure S 3-29. PM2.5 source contributions in San Joaquin Valley by energy scenarios and race/ethnicity. Each value represents the average across four meteorological scenarios.

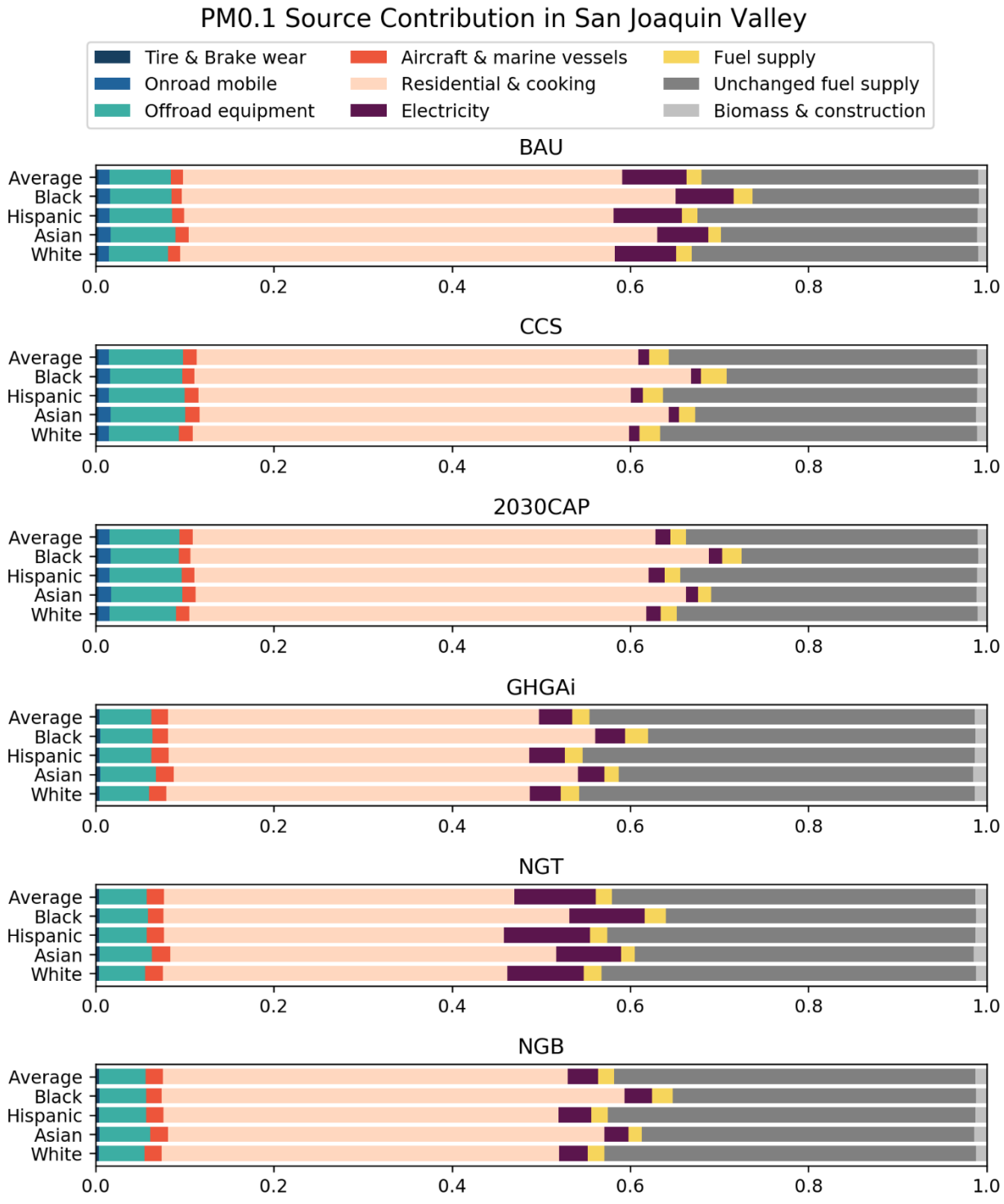

Figure S 3-30. PM0.1 source contributions in San Joaquin Valley by energy scenarios and race/ethnicity. Each value represents the average across four meteorological scenarios.

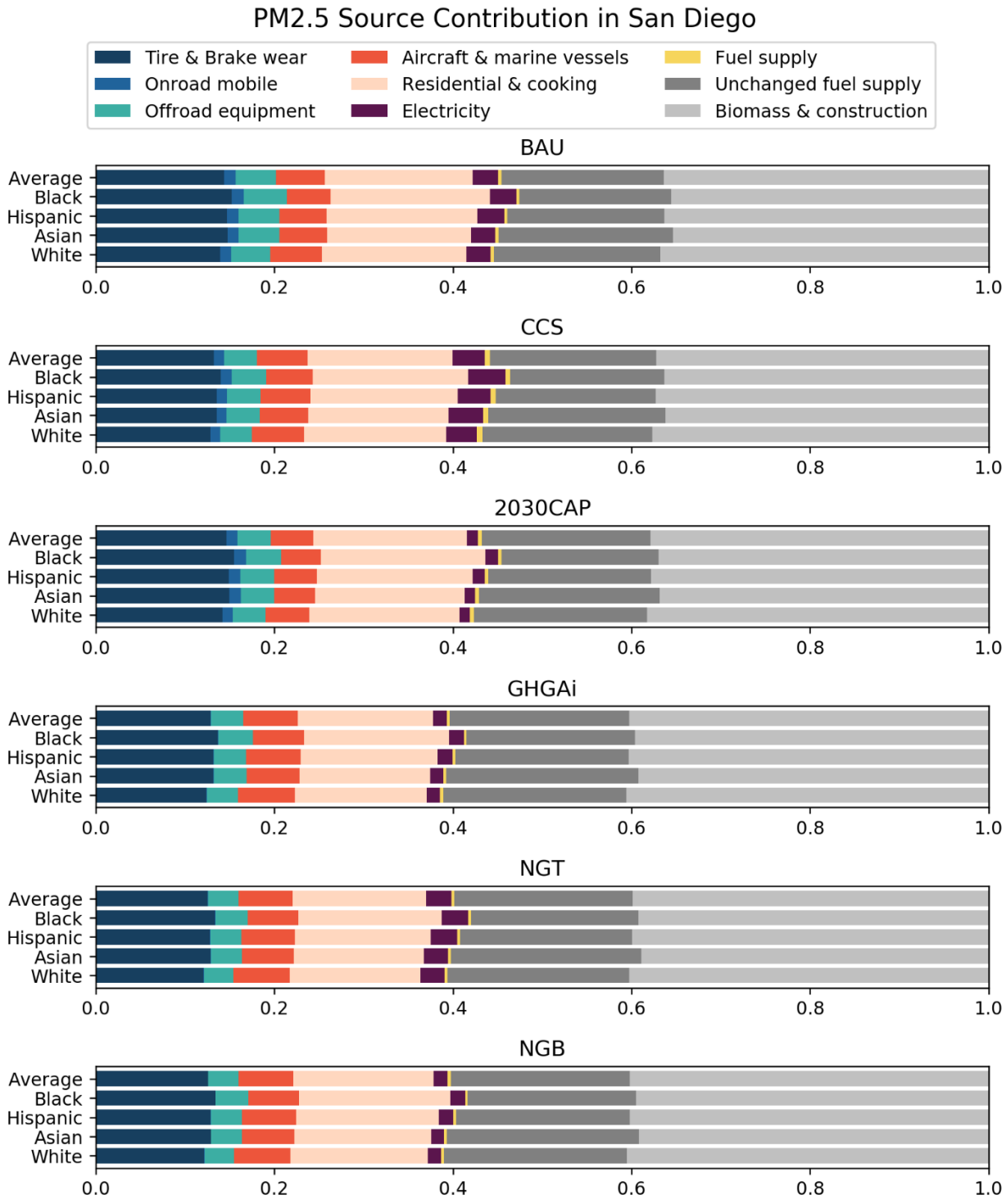

Figure S 3-31. PM2.5 source contributions in San Diego by energy scenarios and race/ethnicity. Each value represents the average across four meteorological scenarios.

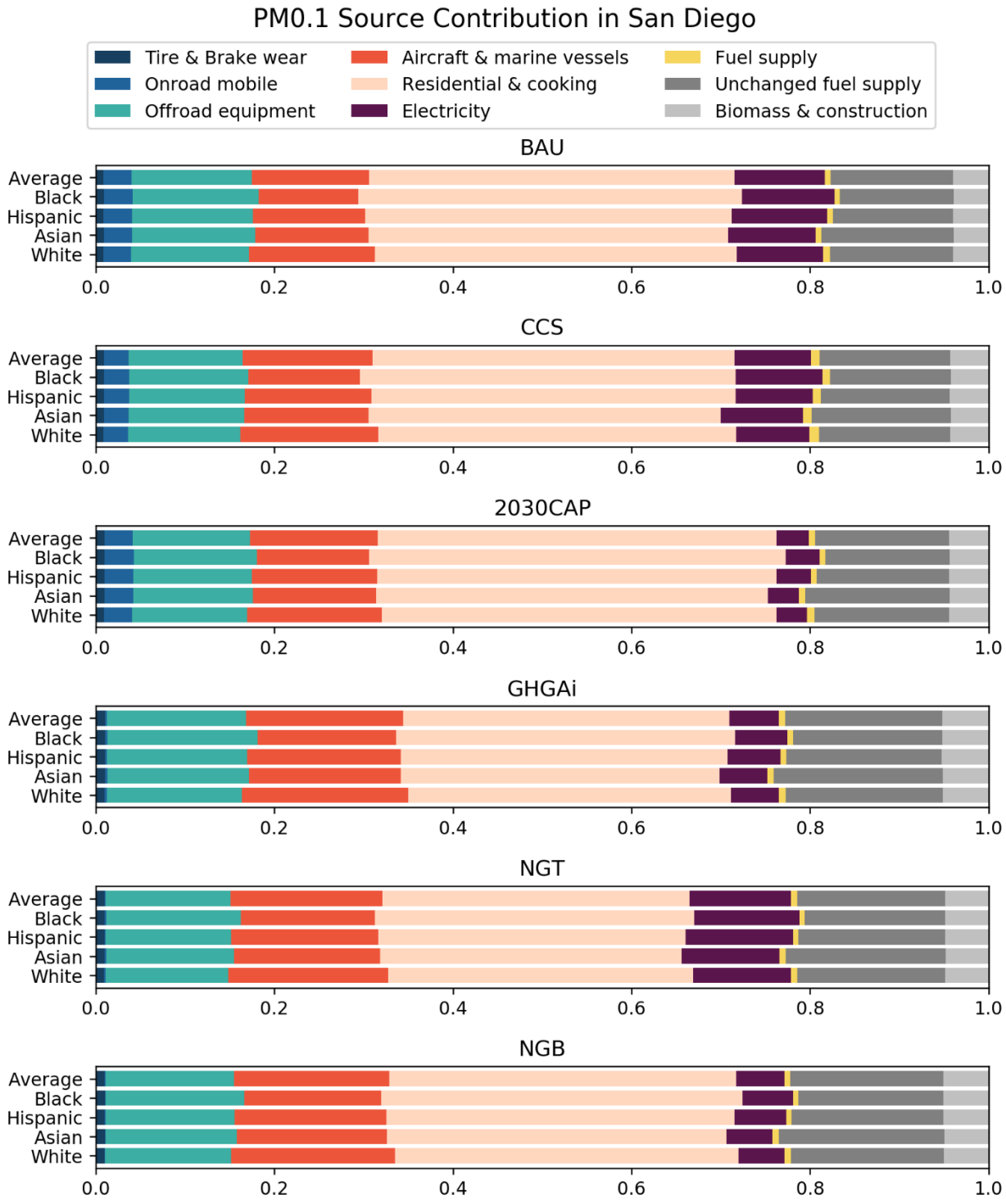

Figure S 3-32. PM0.1 source contributions in San Diego by energy scenarios and race/ethnicity. Each value represents the average across four meteorological scenarios.

S3.5 Potential for Further Improvements

S3.5.1 Improvements for Total Population Exposure

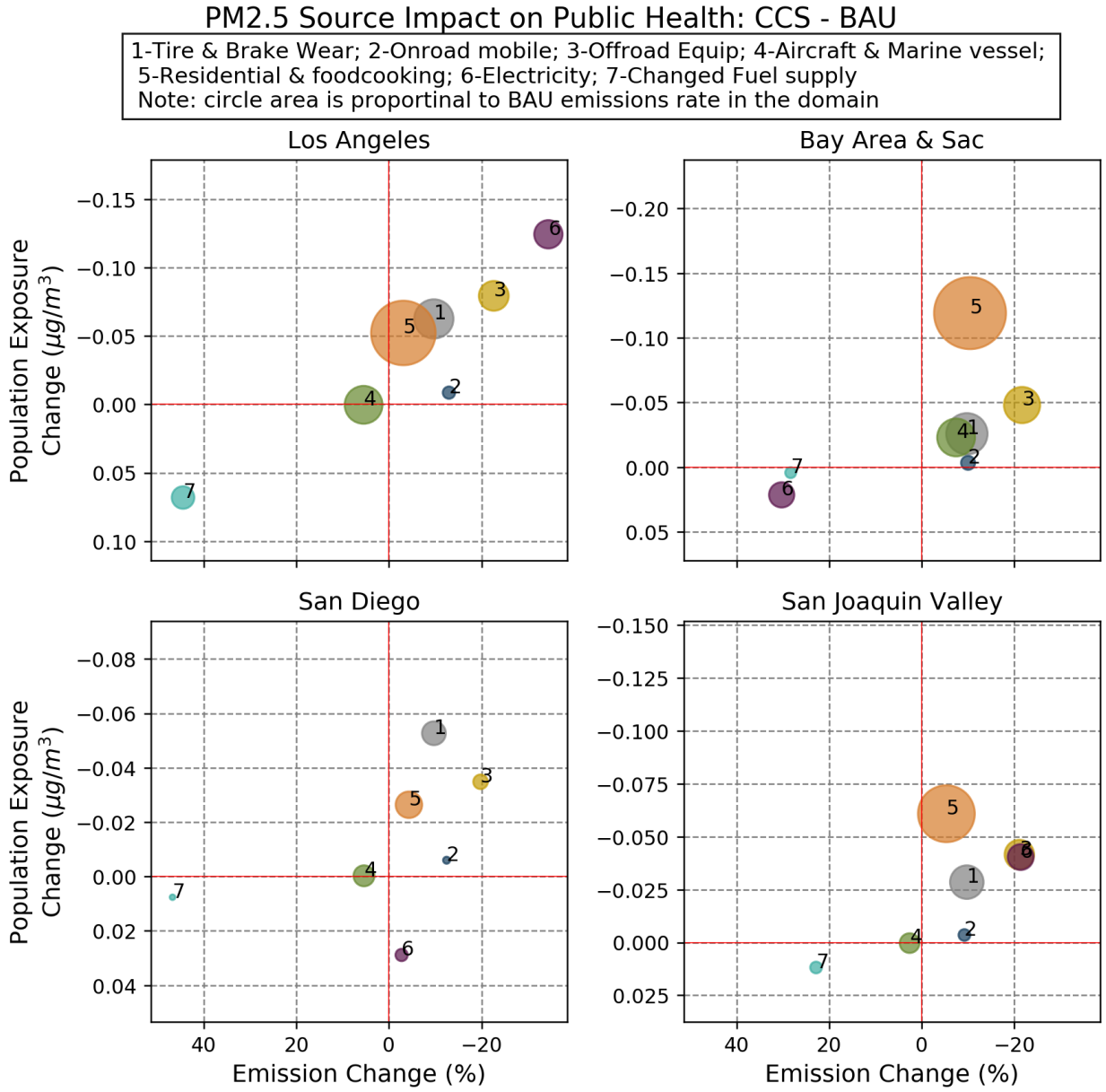

Figure S 3-33. PM2.5 source impact on public health (regardless of race) for CCS energy scenario. X-axis indicates emissions (source) changes between BAU and CCS scenario. Y-axis indicates PWC changes between BAU and CCS scenario for specific source. All results averaged across four meteorological scenarios.

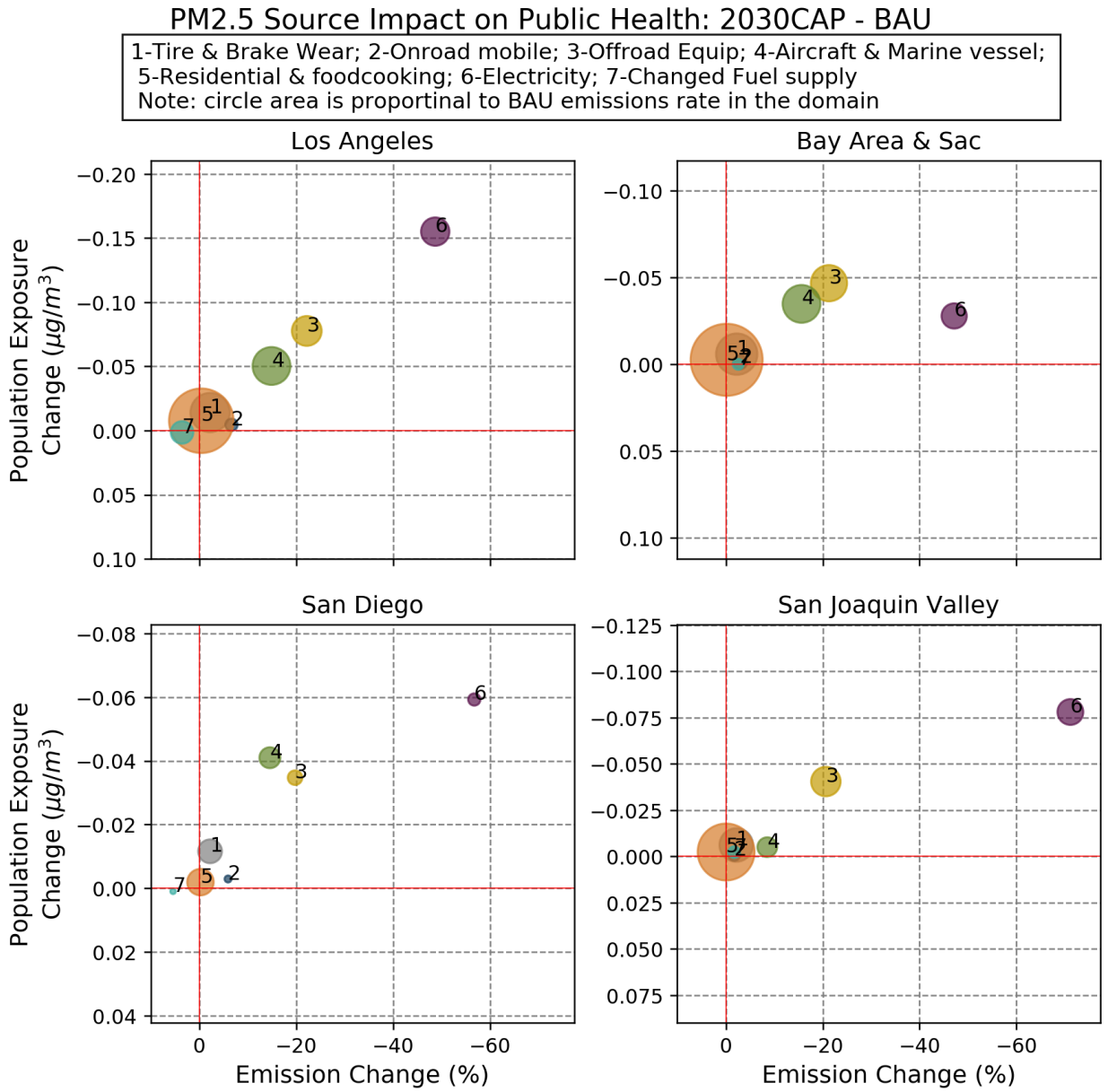

Figure S 3-34. PM2.5 source impact on public health (regardless of race) for 2030CAP energy scenario. X-axis indicates emissions (source) changes between BAU and 2030CAP scenario. Y-axis indicates PWC changes between BAU and 2030CAP scenario for specific source. All results averaged across four meteorological scenarios.

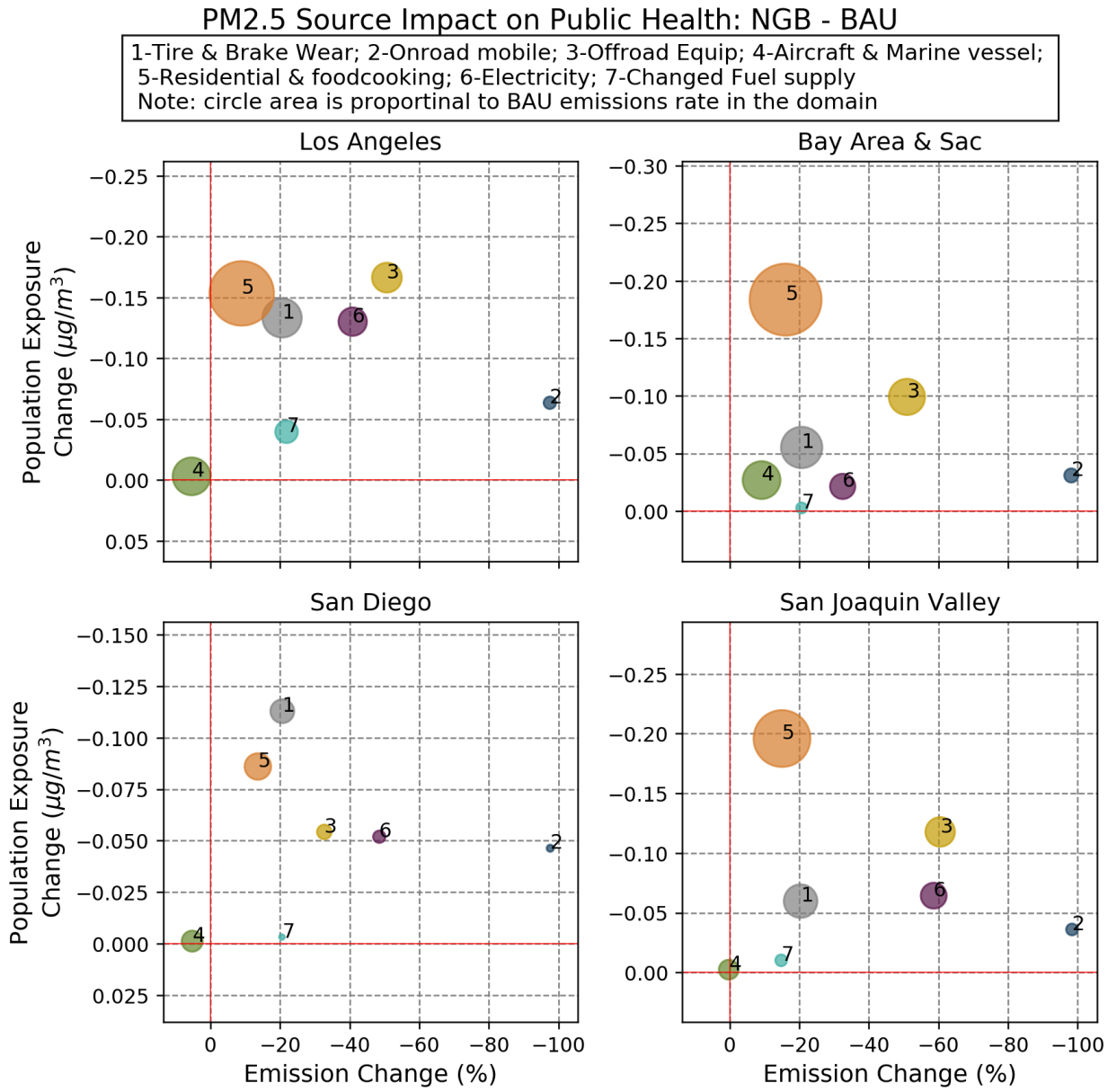

Figure S 3-35. PM2.5 source impact on public health (regardless of race) for NGB energy scenario. X-axis indicates emissions (source) changes between BAU and NGB scenario. Y-axis indicates PWC changes between BAU and NGB scenario for specific source. All results averaged across four meteorological scenarios.

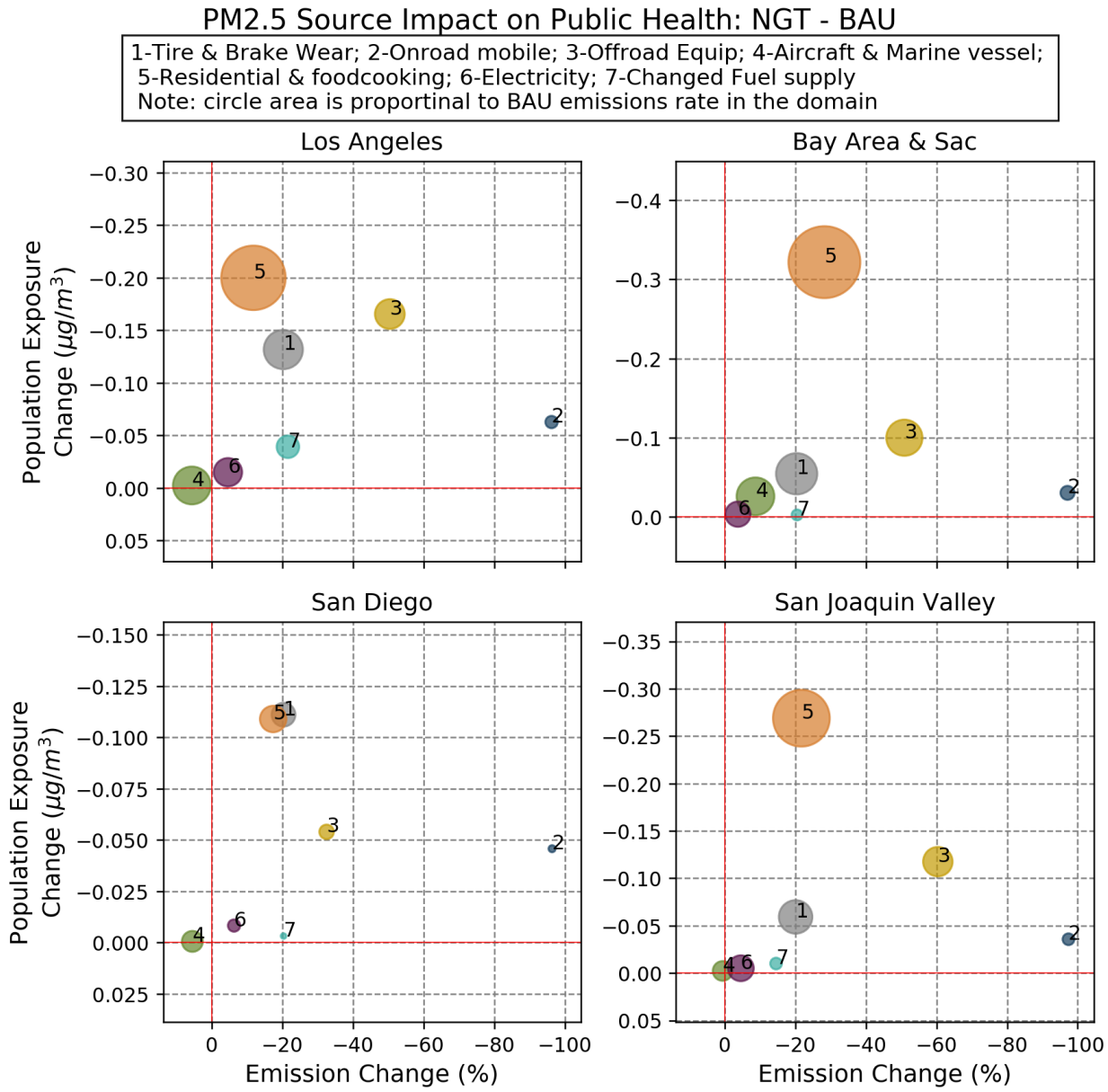

Figure S 3-36. PM2.5 source impact on public health (regardless of race) for NGT energy scenario. X-axis indicates emissions (source) changes between BAU and NGT scenario. Y-axis indicates PWC changes between BAU and NGT scenario for specific source. All results averaged across four meteorological scenarios.

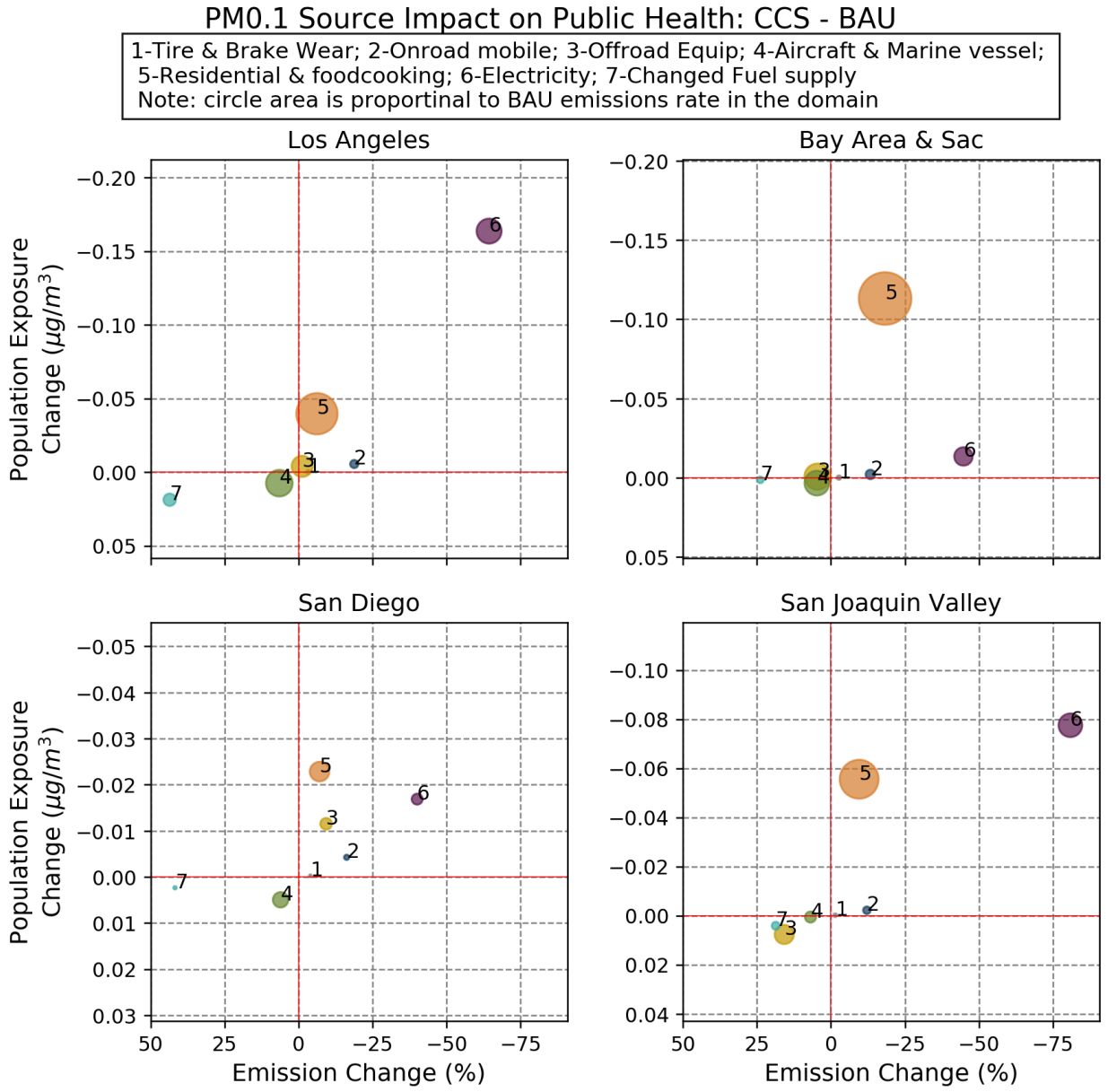

Figure S 3-37. PM0.1 source impact on public health (regardless of race) for CCS energy scenario. X-axis indicates emissions (source) changes between BAU and CCS scenario. Y-axis indicates PWC changes between BAU and CCS scenario for specific source. All results averaged across four meteorological scenarios.

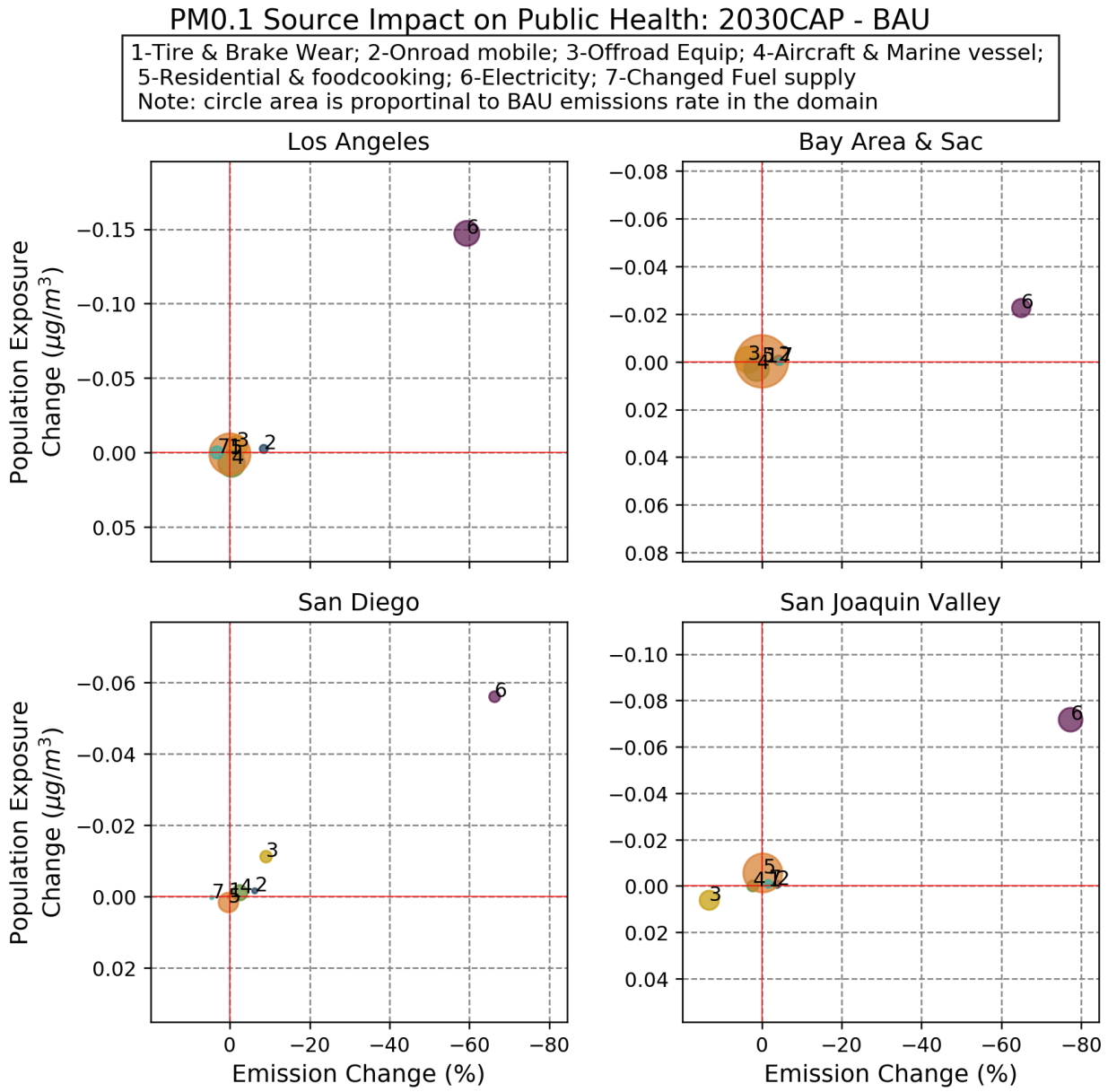

Figure S 3-38. PM0.1 source impact on public health (regardless of race) for 2030CAP energy scenario. X-axis indicates emissions (source) changes between BAU and 2030CAP scenario. Y-axis indicates PWC changes between BAU and 2030CAP scenario for specific source. All results averaged across four meteorological scenarios.

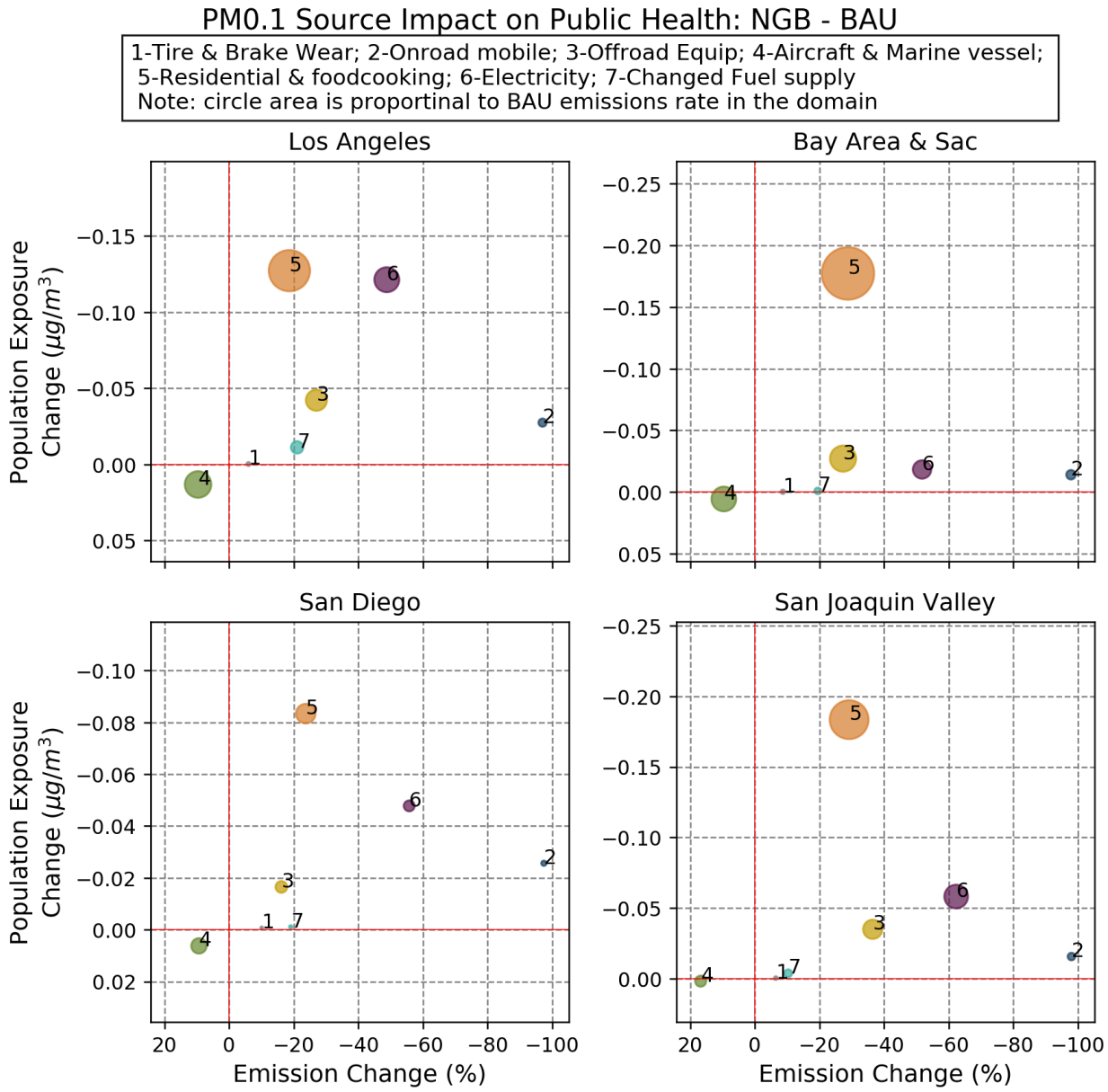

Figure S 3-39. PM0.1 source impact on public health (regardless of race) for NGB energy scenario. X-axis indicates emissions (source) changes between BAU and NGB scenario. Y-axis indicates PWC changes between BAU and NGB scenario for specific source. All results averaged across four meteorological scenarios.

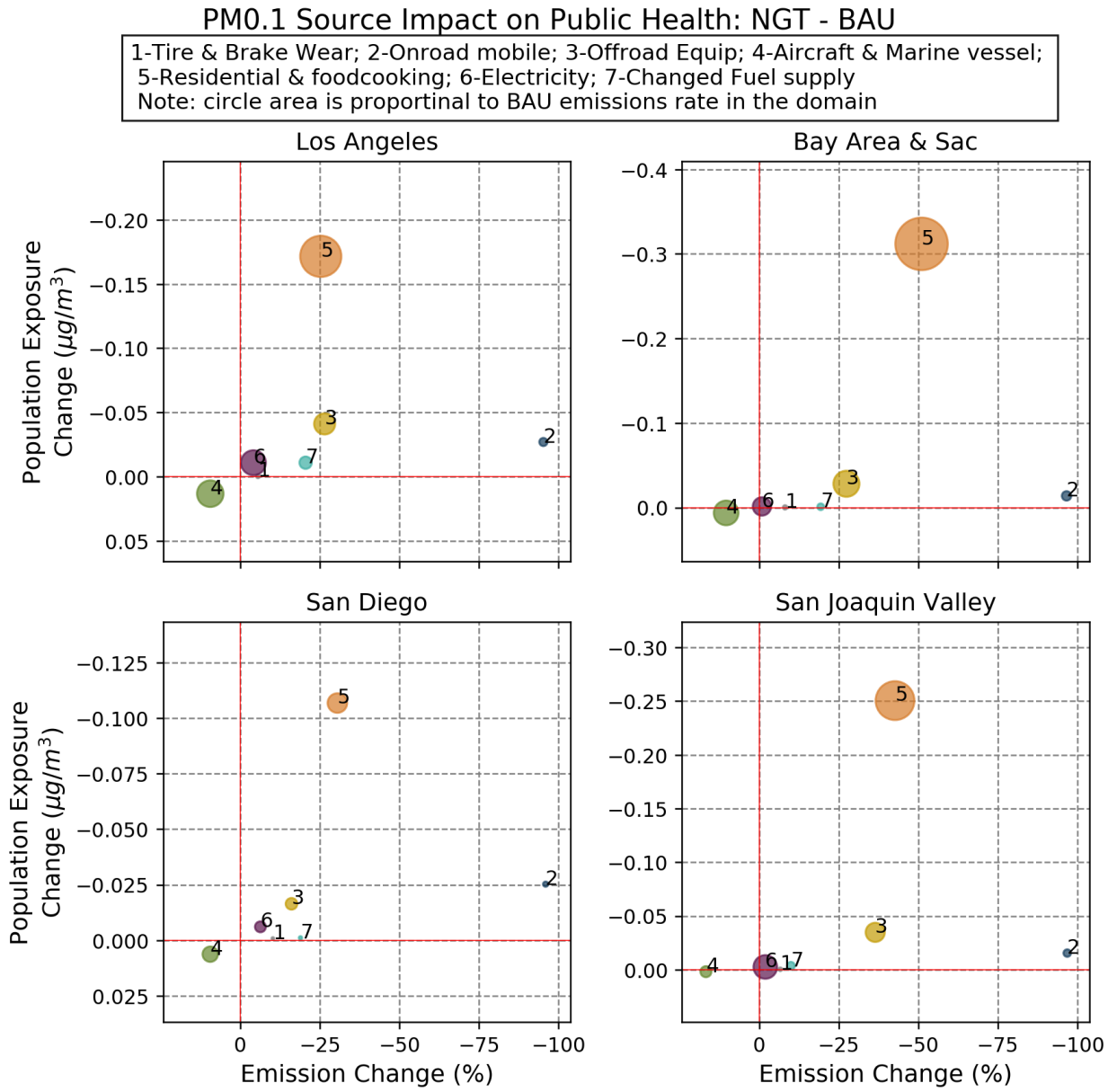

Figure S 3-40. PM0.1 source impact on public health (regardless of race) for NGT energy scenario. X-axis indicates emissions (source) changes between BAU and NGT scenario. Y-axis indicates PWC changes between BAU and NGT scenario for specific source. All results averaged across four meteorological scenarios.

S3.5.2 Improvements to Reduce Disparity across Race/Ethnicity

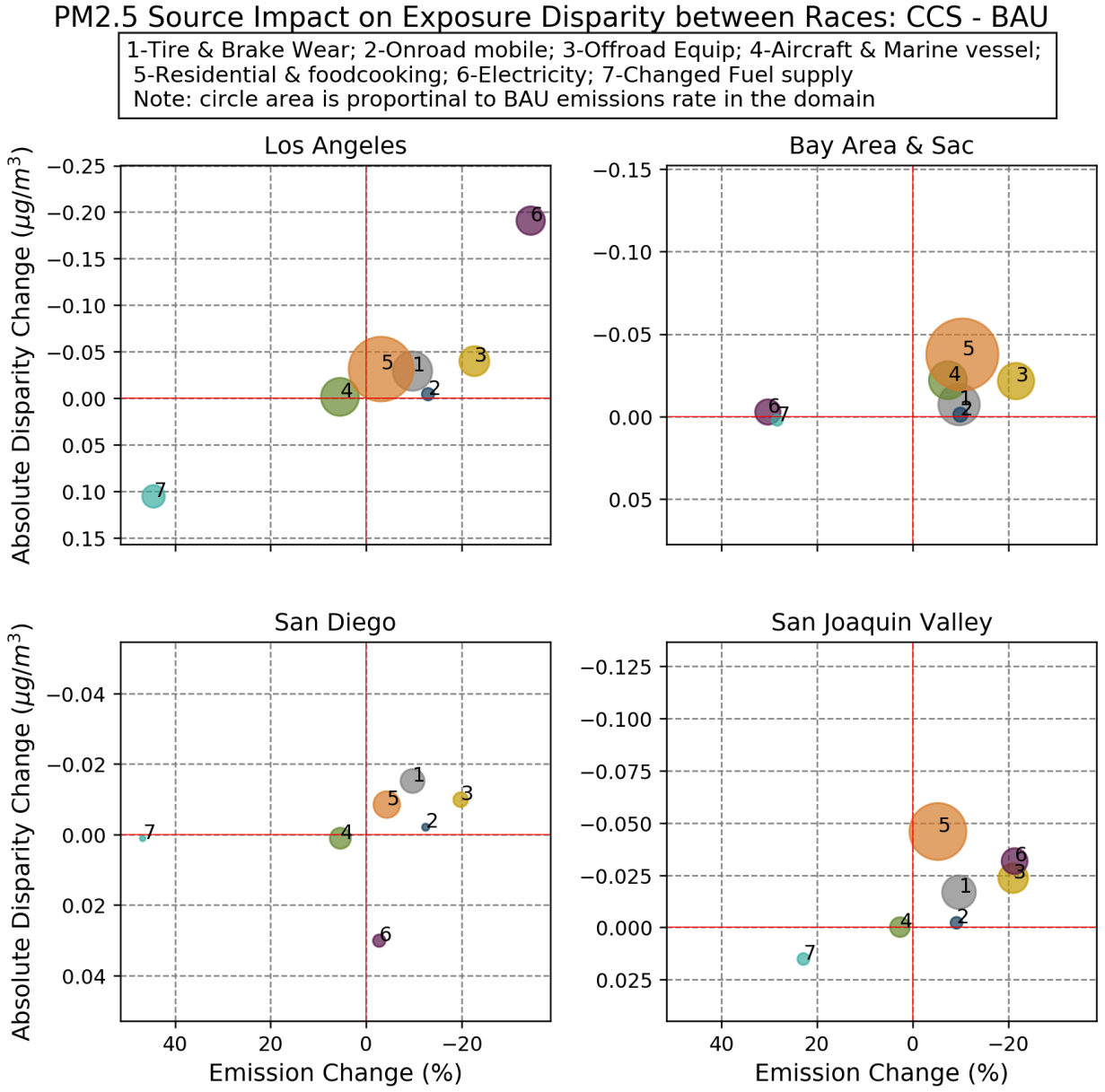

Figure S 3-41. PM2.5 source impact on exposure disparity between races for CCS energy scenario. X-axis indicates emissions (source) changes between BAU and CCS scenario. Y-axis indicates emission absolute disparity changes between BAU and CCS scenario for specific source. All results averaged across four meteorological scenarios.

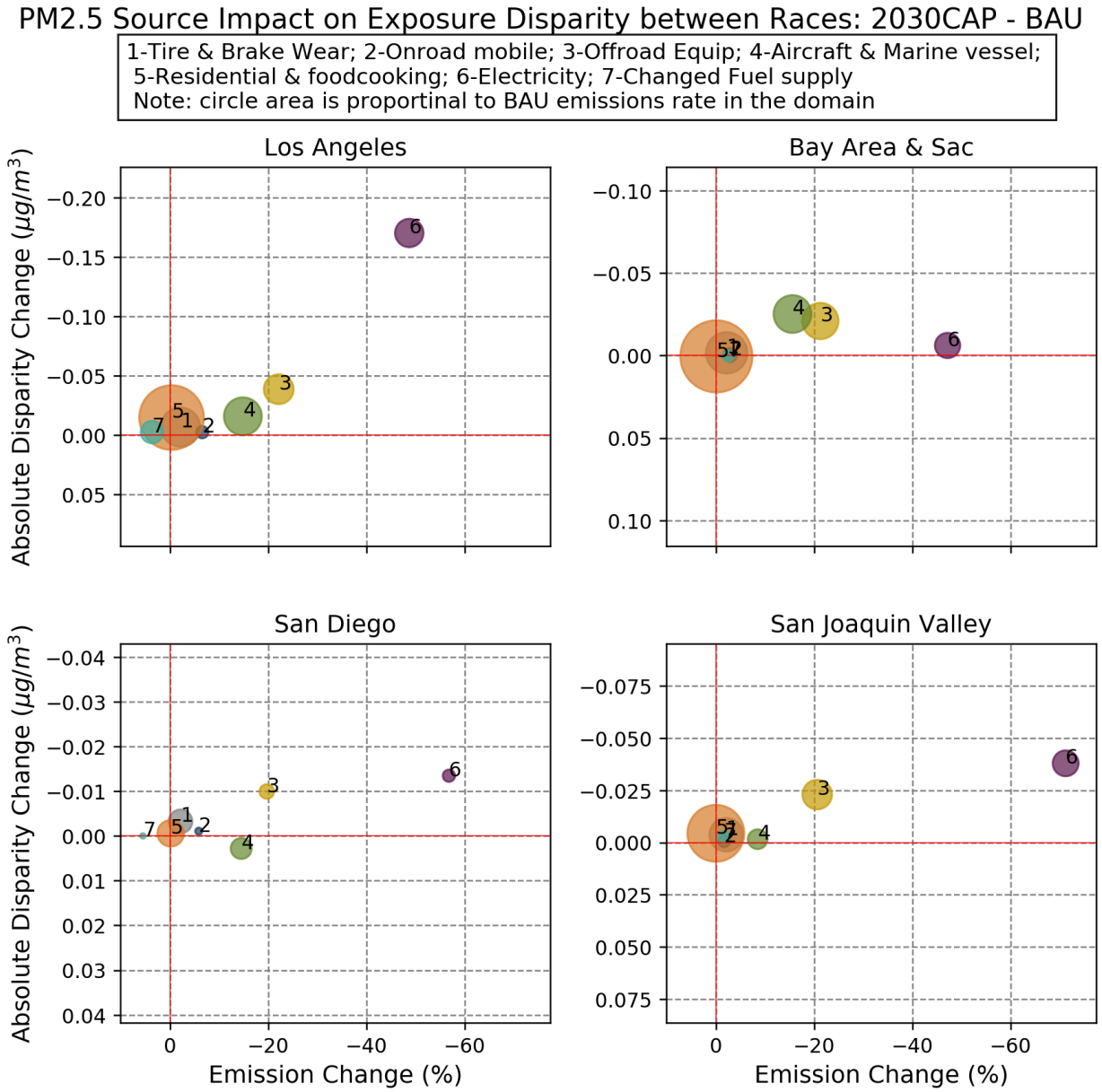

Figure S 3-42. PM2.5 source impact on exposure disparity between races for 2030CAP energy scenario. X-axis indicates emissions (source) changes between BAU and 2030CAP scenario. Y-axis indicates emission absolute disparity changes between BAU and 2030CAP scenario for specific source. All results averaged across four meteorological scenarios.

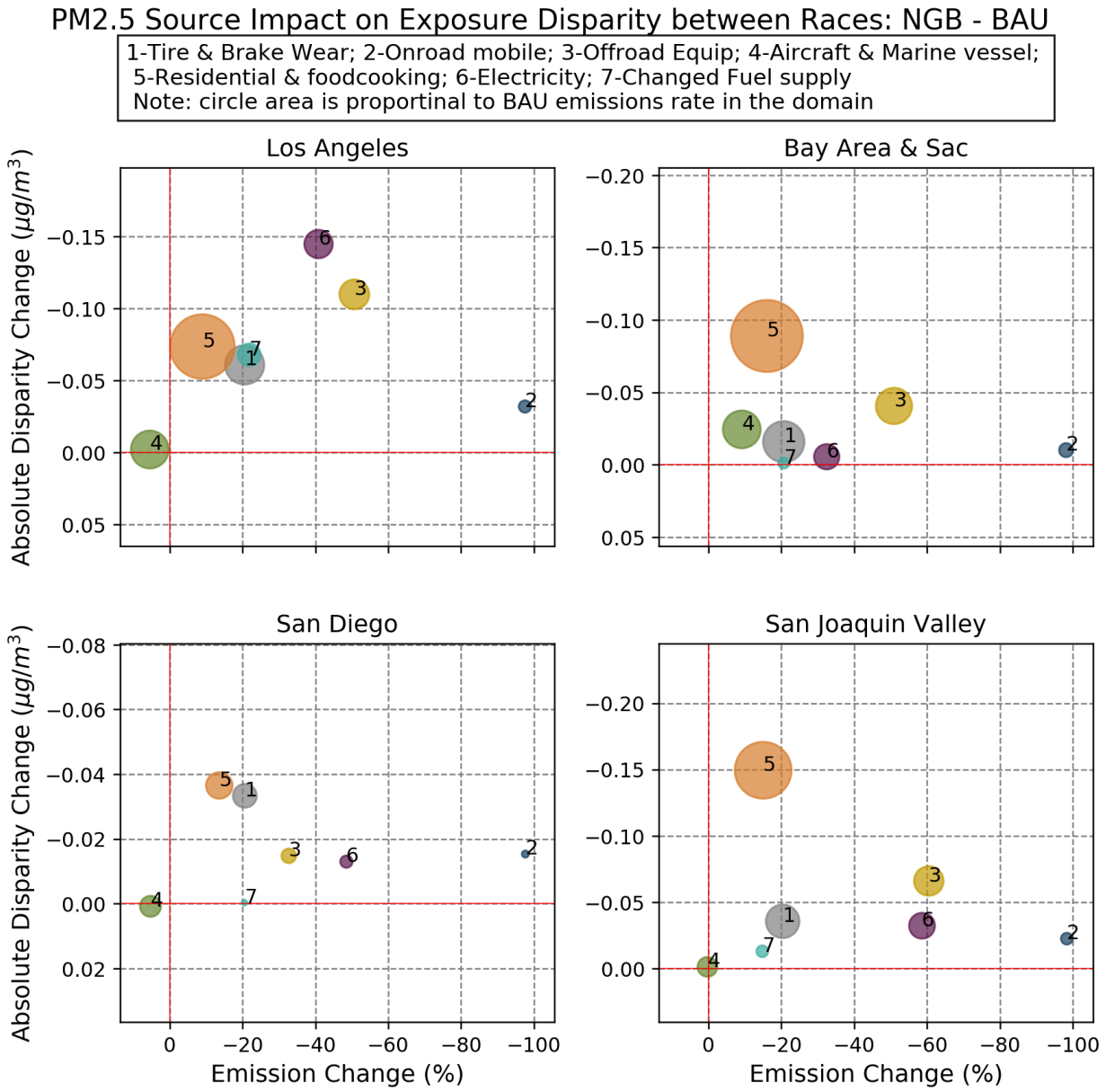

Figure S 3-43. PM2.5 source impact on exposure disparity between races for NGB energy scenario. X-axis indicates emissions (source) changes between BAU and NGB scenario. Y-axis indicates emission absolute disparity changes between BAU and NGB scenario for specific source. All results averaged across four meteorological scenarios.

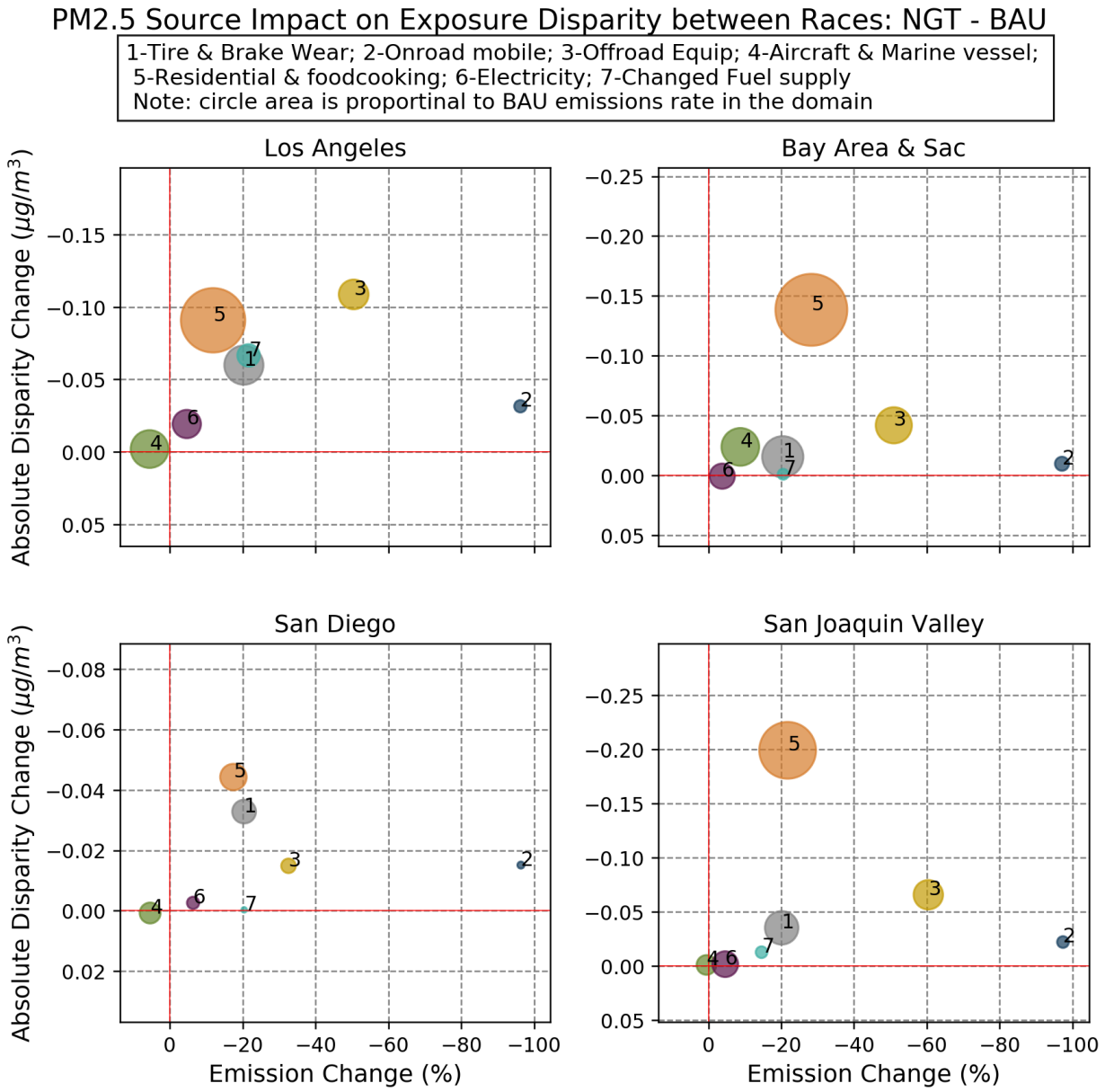

Figure S 3-44. PM2.5 source impact on exposure disparity between races for NGT energy scenario. X-axis indicates emissions (source) changes between BAU and NGT scenario. Y-axis indicates emission absolute disparity changes between BAU and NGT scenario for specific source. All results averaged across four meteorological scenarios.

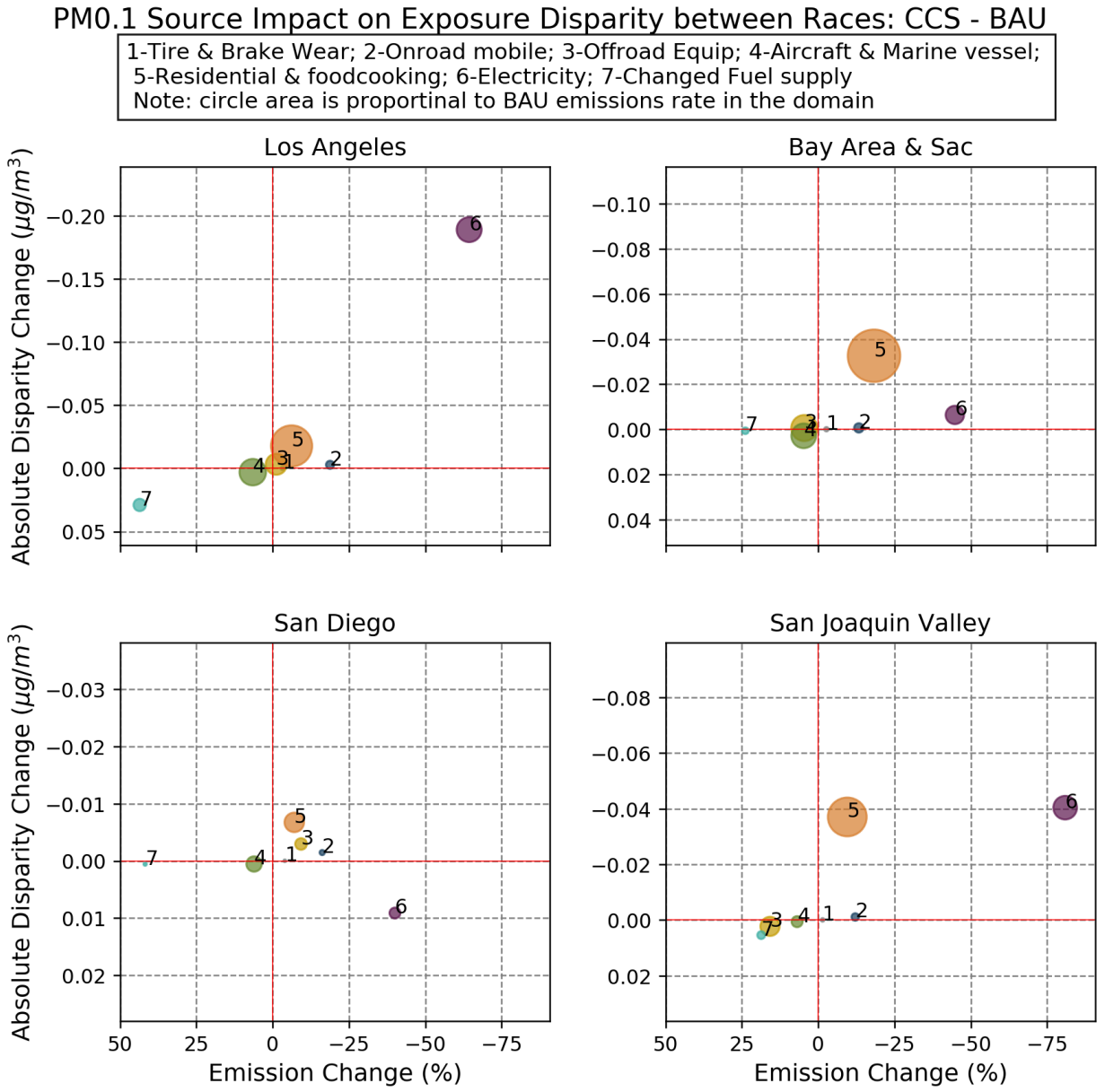

Figure S 3-45. PM0.1 source impact on exposure disparity between races for CCS energy scenario. X-axis indicates emissions (source) changes between BAU and CCS scenario. Y-axis indicates emission absolute disparity changes between BAU and CCS scenario for specific source. All results averaged across four meteorological scenarios.

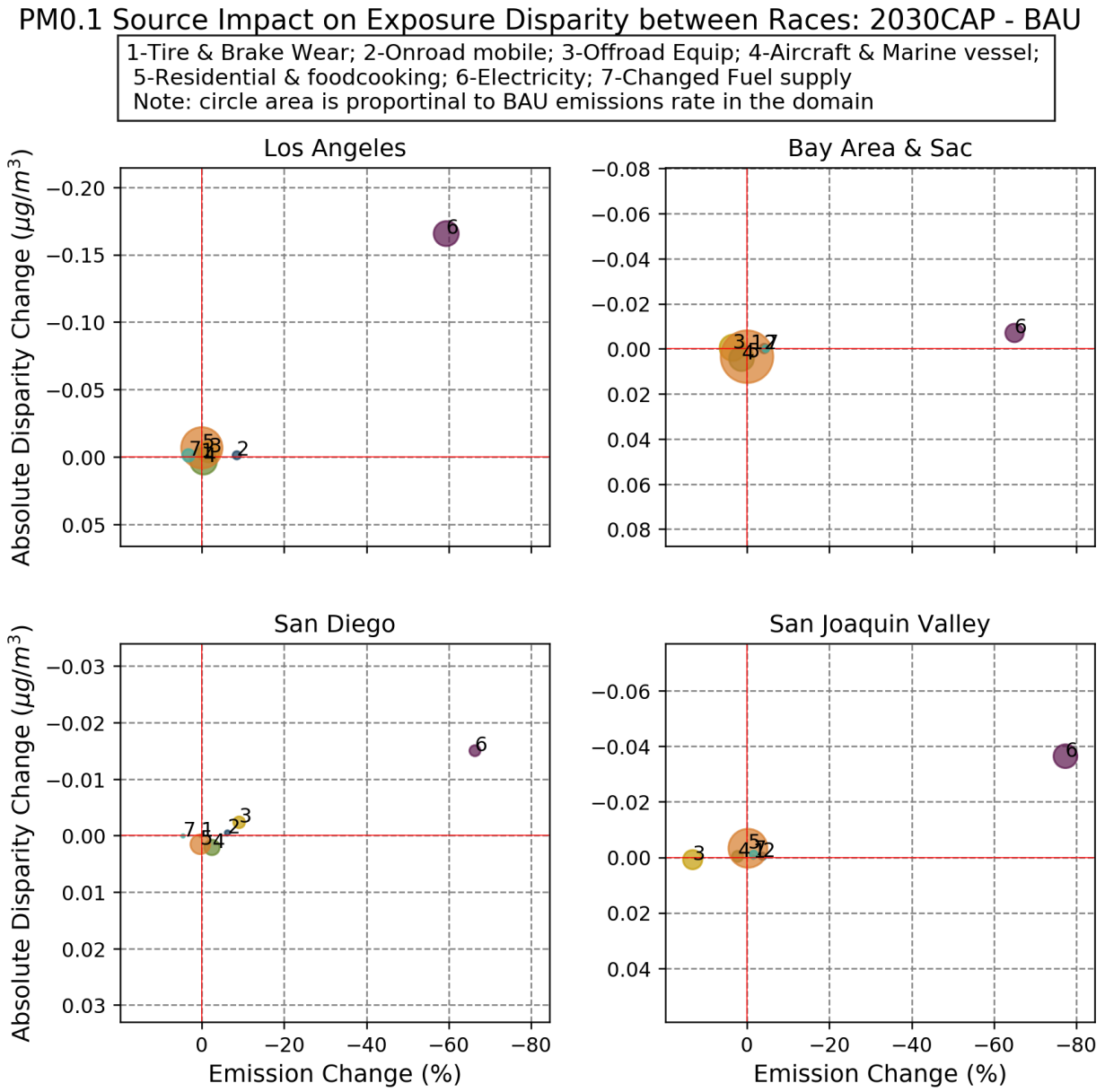

Figure S 3-46. PM0.1 source impact on exposure disparity between races for 2030CAP energy scenario. X-axis indicates emissions (source) changes between BAU and 2030CAP scenario. Y-axis indicates emission absolute disparity changes between BAU and 2030CAP scenario for specific source. All results averaged across four meteorological scenarios.

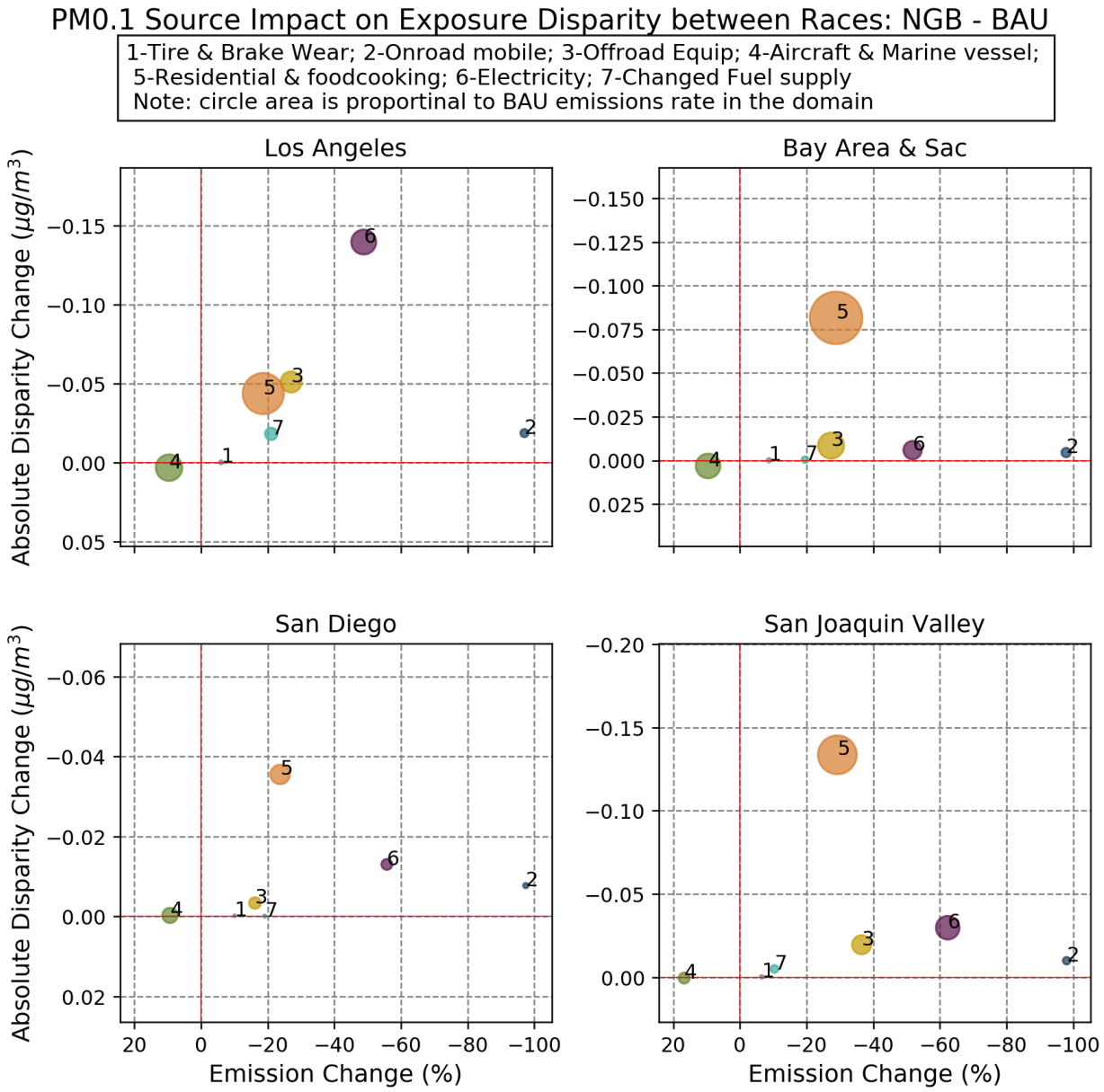

Figure S 3-47. PM0.1 source impact on exposure disparity between races for NGB energy scenario. X-axis indicates emissions (source) changes between BAU and NGB scenario. Y-axis indicates emission absolute disparity changes between BAU and NGB scenario for specific source. All results averaged across four meteorological scenarios.

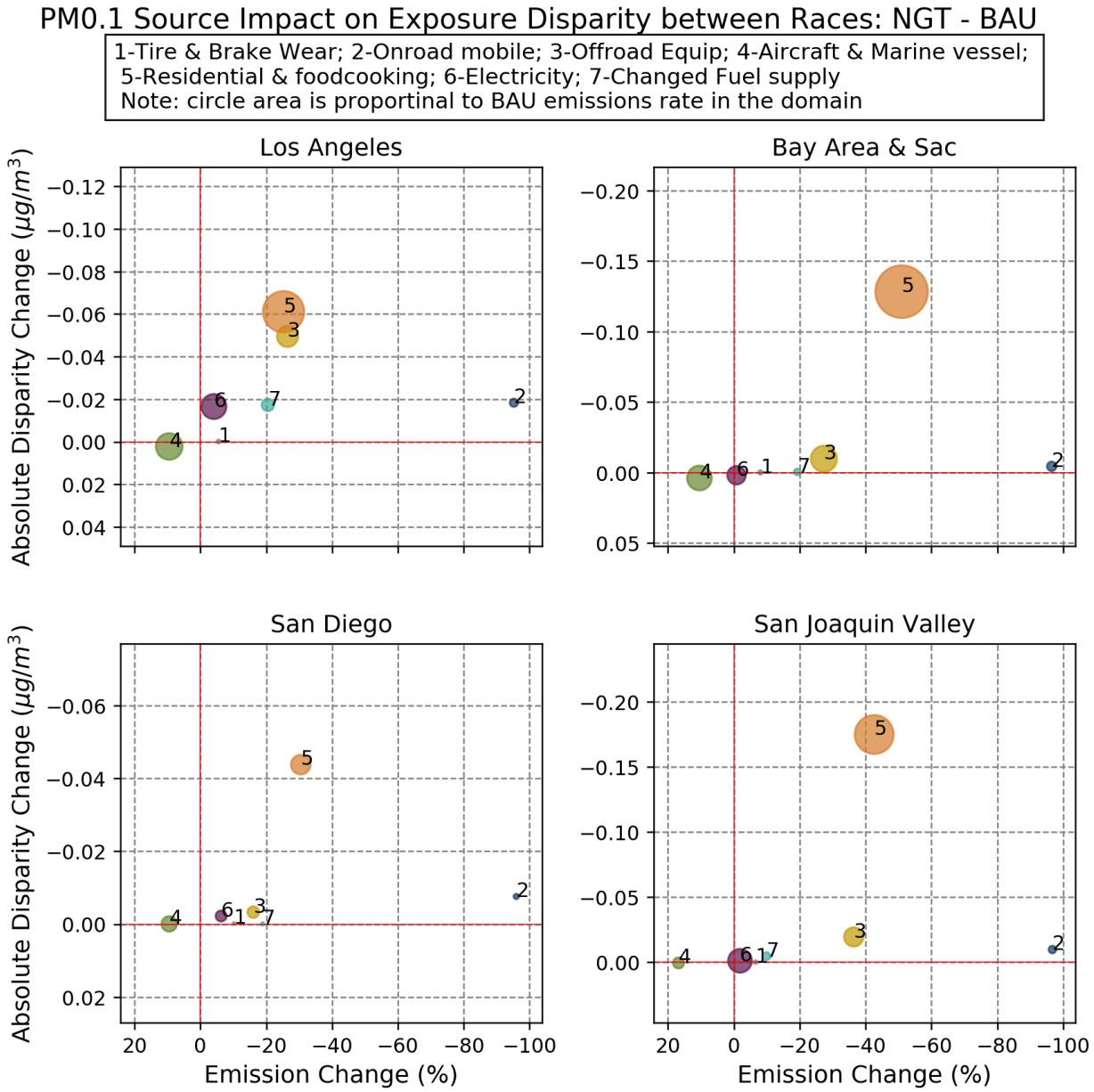

Figure S 3-48. PM0.1 source impact on exposure disparity between races for NGT energy scenario. X-axis indicates emissions (source) changes between BAU and NGT scenario. Y-axis indicates emission absolute disparity changes between BAU and NGT scenario for specific source. All results averaged across four meteorological scenarios.

S3.5.3 Balancing Benefits for Total Population and Reduced Disparity

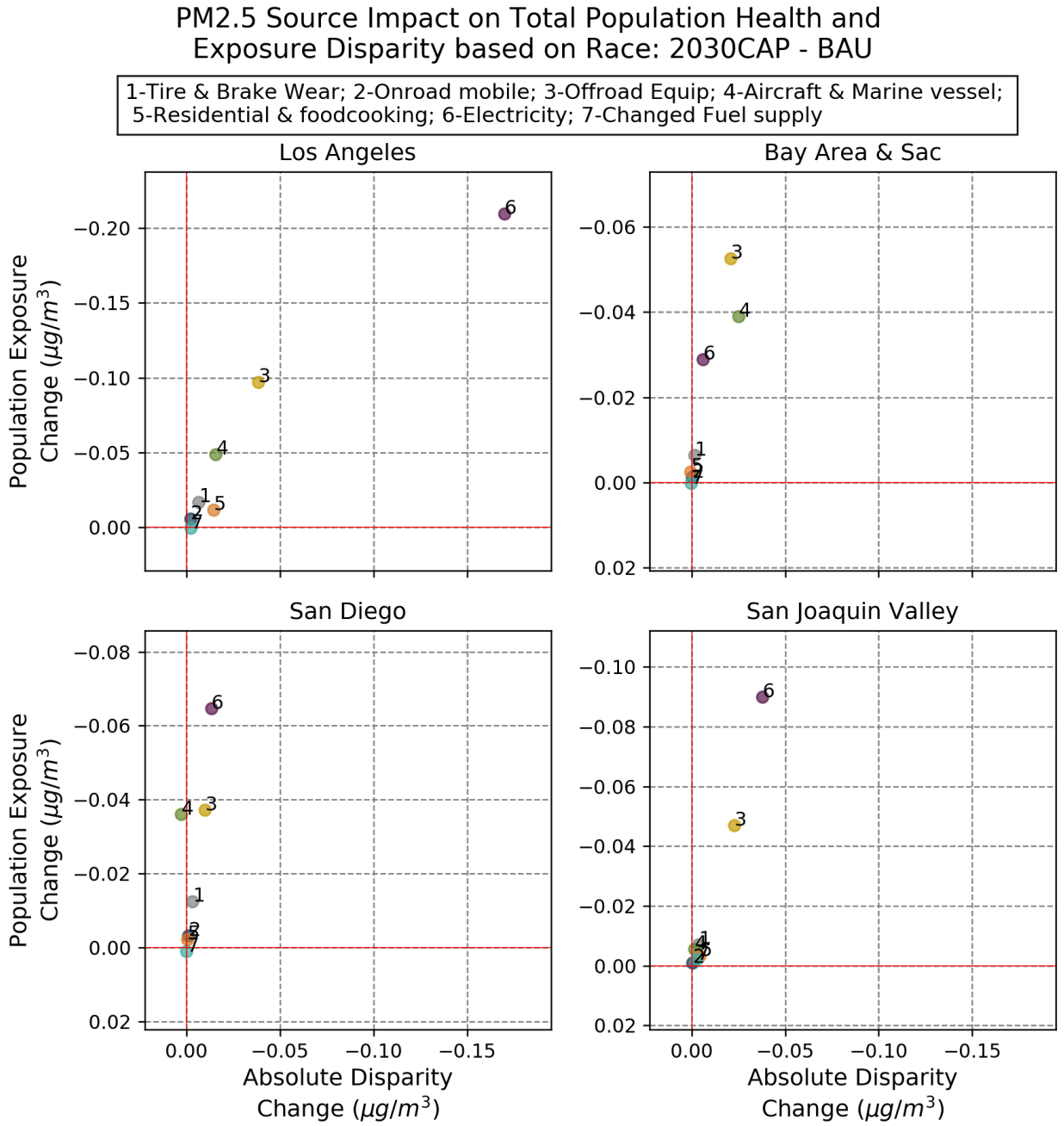

Figure S 3-49. PM2.5 source impact on total population exposure and exposure disparity based on race for 2030CAP energy scenario. X-axis indicates largest disparity changes between BAU and 2030CAP scenario for each specific source. Y-axis indicates PWC changes between BAU and 2030CAP scenario for each specific source. All results averaged across four meteorological scenarios.

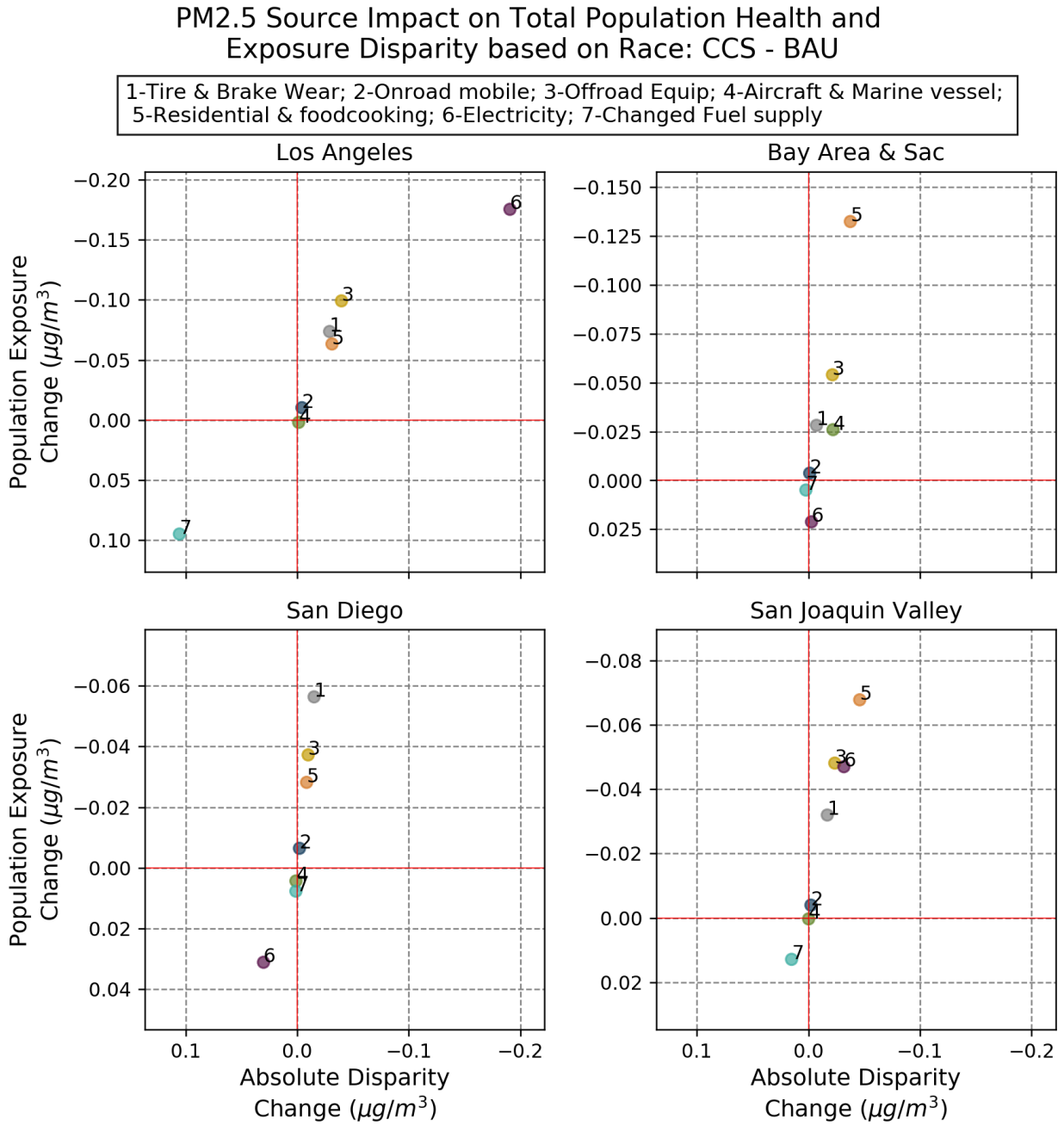

Figure S 3-50. PM2.5 source impact on total population exposure and exposure disparity based on race for CCS energy scenario. X-axis indicates largest disparity changes between BAU and CCS scenario for each specific source. Y-axis indicates PWC changes between BAU and CCS scenario for each specific source. All results averaged across four meteorological scenarios.

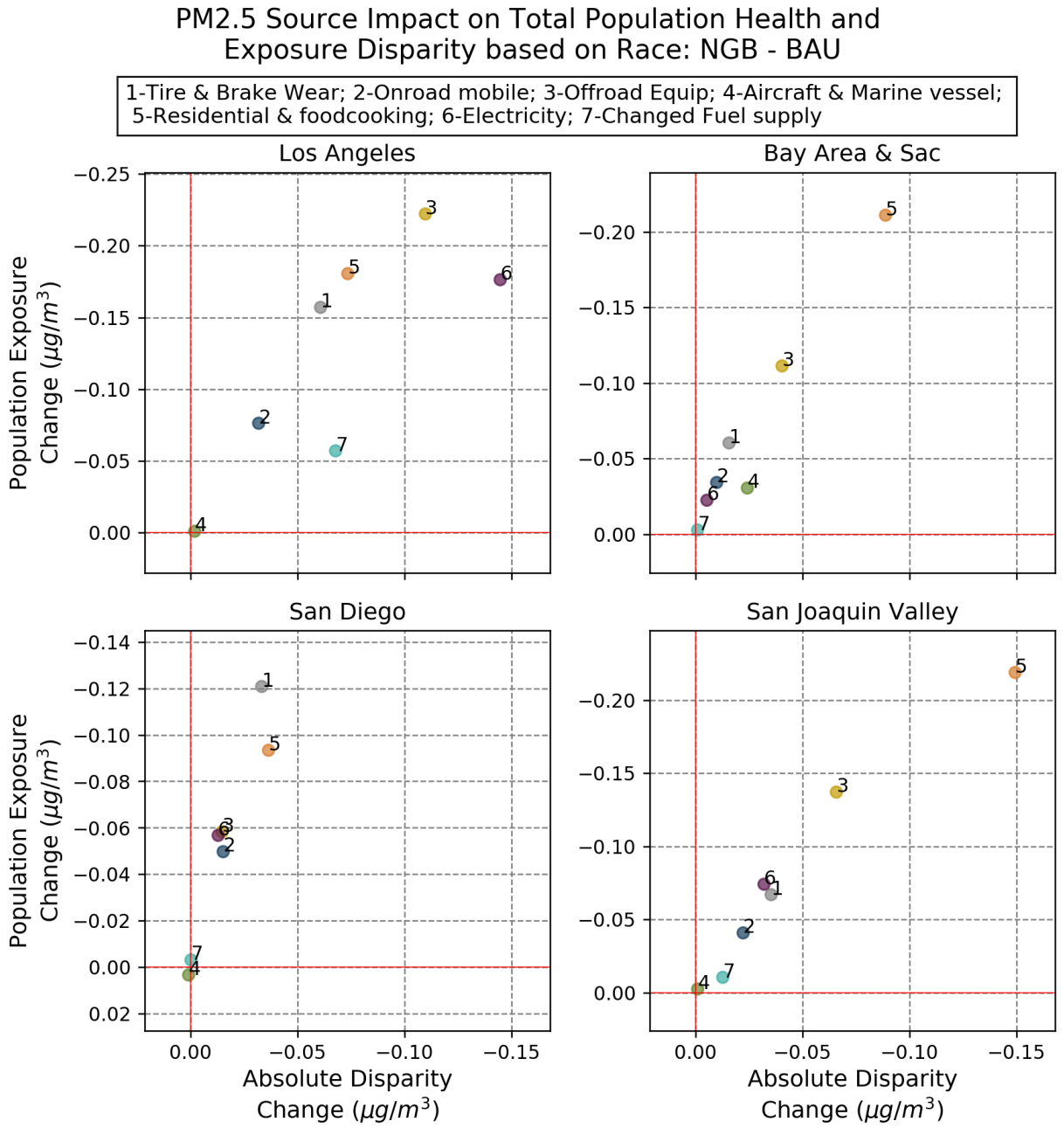

Figure S 3-51. PM2.5 source impact on total population exposure and exposure disparity based on race for NGB energy scenario. X-axis indicates largest disparity changes between BAU and NGB scenario for each specific source. Y-axis indicates PWC changes between BAU and NGB scenario for each specific source. All results averaged across four meteorological scenarios.

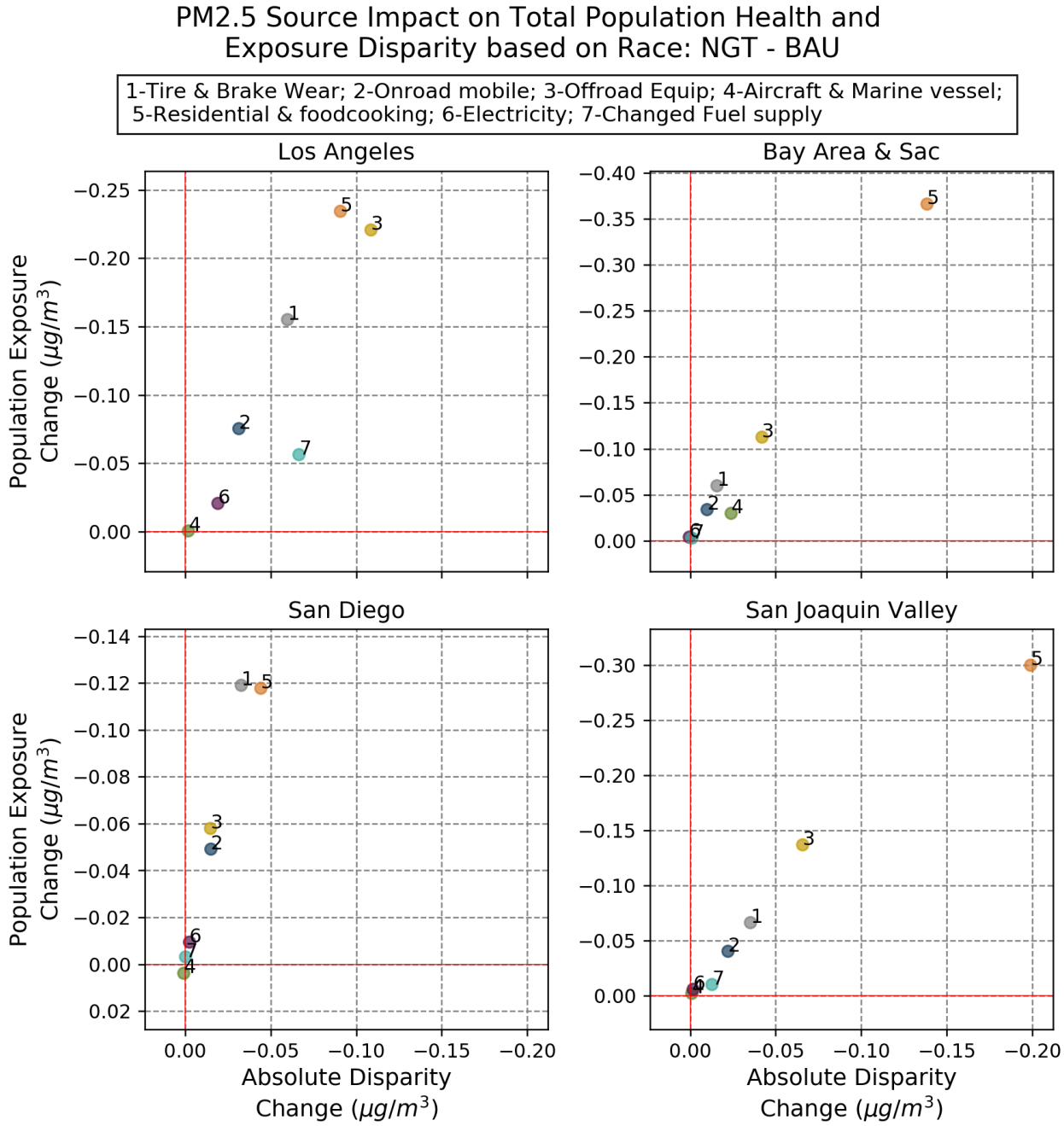

Figure S 3-52. PM2.5 source impact on total population exposure and exposure disparity based on race for NGT energy scenario. X-axis indicates largest disparity changes between BAU and NGT scenario for each specific source. Y-axis indicates PWC changes between BAU and NGT scenario for each specific source. All results averaged across four meteorological scenarios.

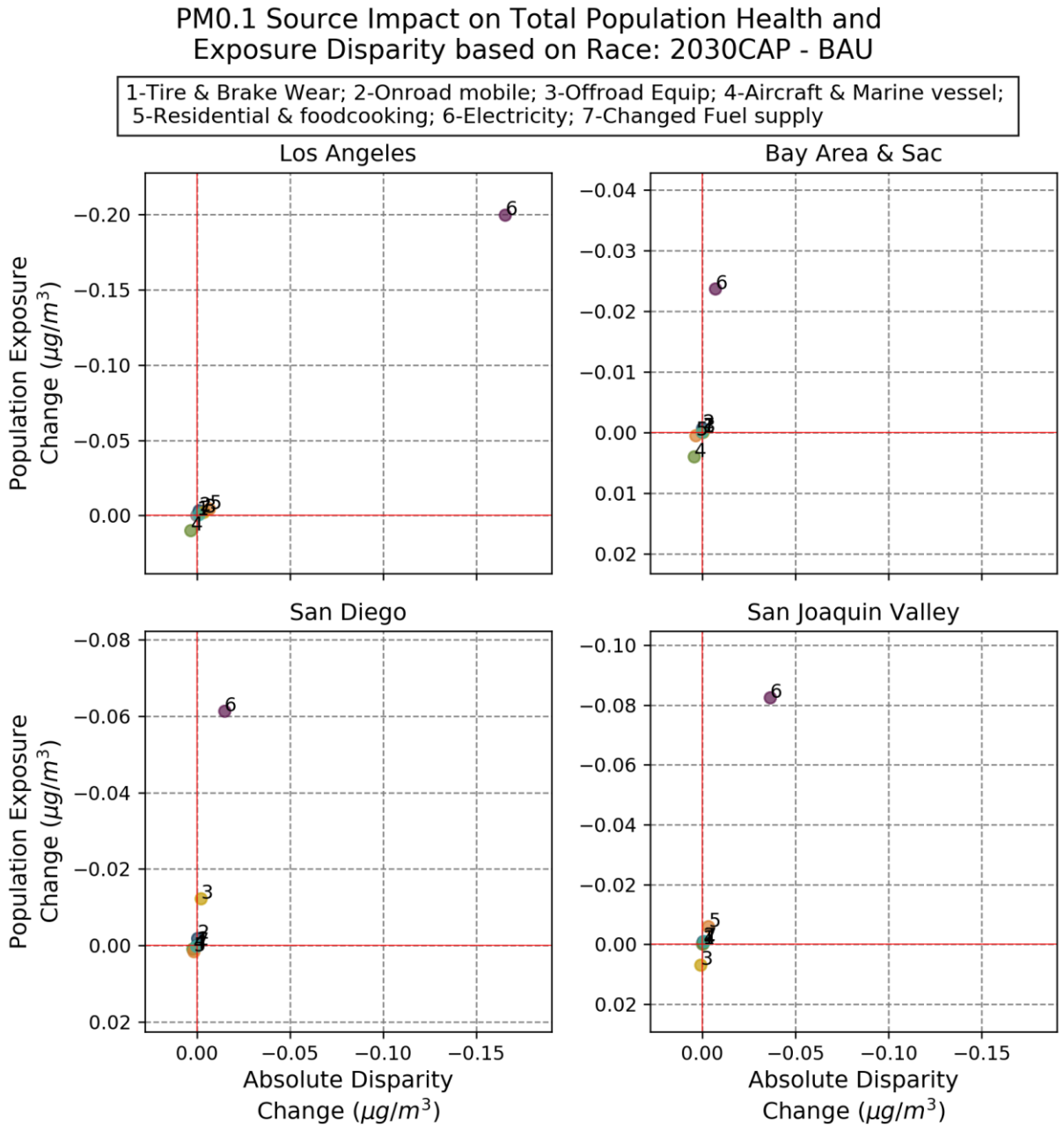

Figure S 3-53. PM0.1 source impact on total population exposure and exposure disparity based on race for 2030CAP energy scenario. X-axis indicates largest disparity changes between BAU and 2030CAP scenario for each specific source. Y-axis indicates PWC changes between BAU and 2030CAP scenario for each specific source. All results averaged across four meteorological scenarios.

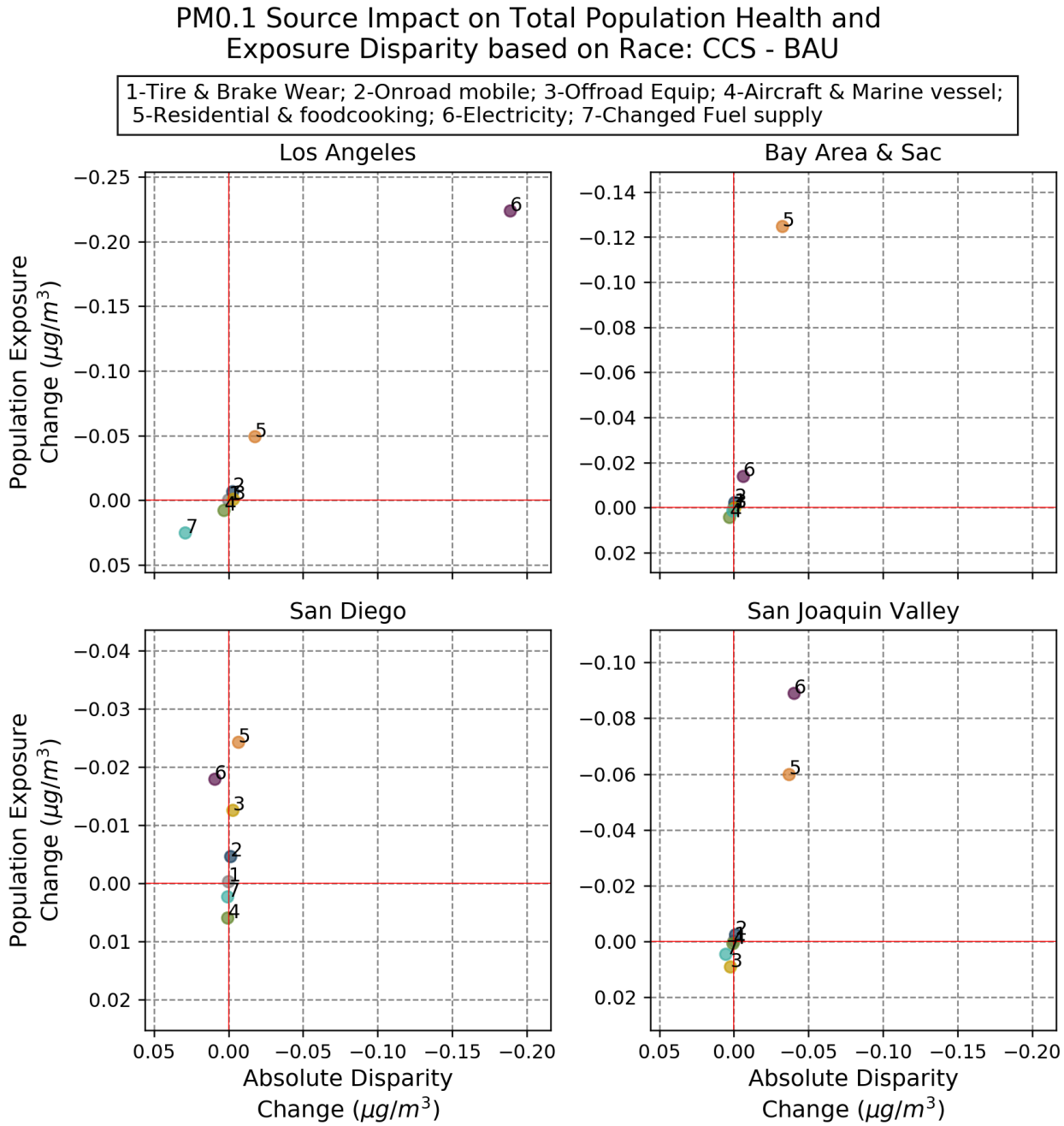

Figure S 3-54. PM0.1 source impact on total population exposure and exposure disparity based on race for CCS energy scenario. X-axis indicates largest disparity changes between BAU and CCS scenario for each specific source. Y-axis indicates PWC changes between BAU and CCS scenario for each specific source. All results averaged across four meteorological scenarios.

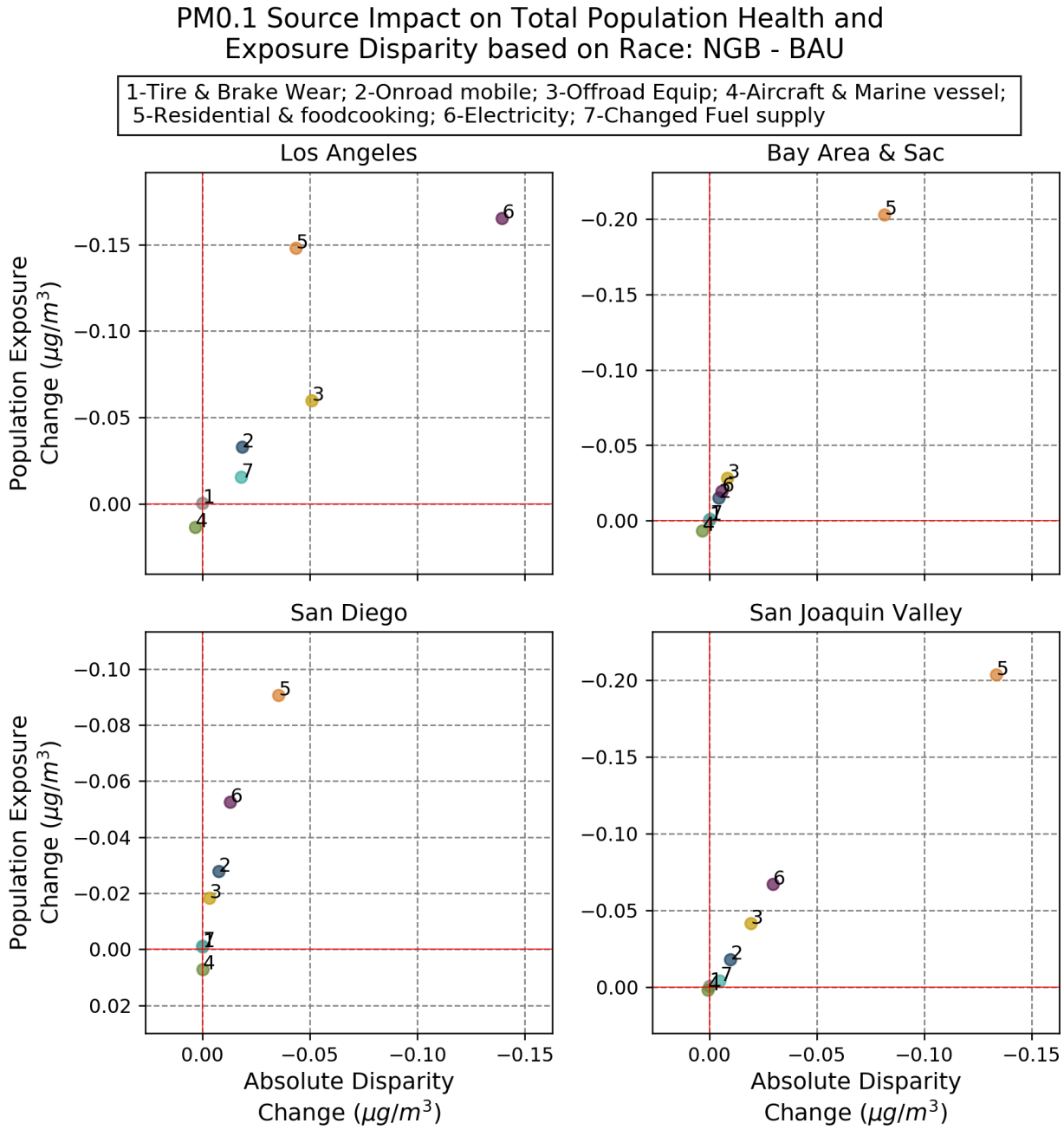

Figure S 3-55. PM0.1 source impact on total population exposure and exposure disparity based on race for NGB energy scenario. X-axis indicates largest disparity changes between BAU and NGB scenario for each specific source. Y-axis indicates PWC changes between BAU and NGB scenario for each specific source. All results averaged across four meteorological scenarios.

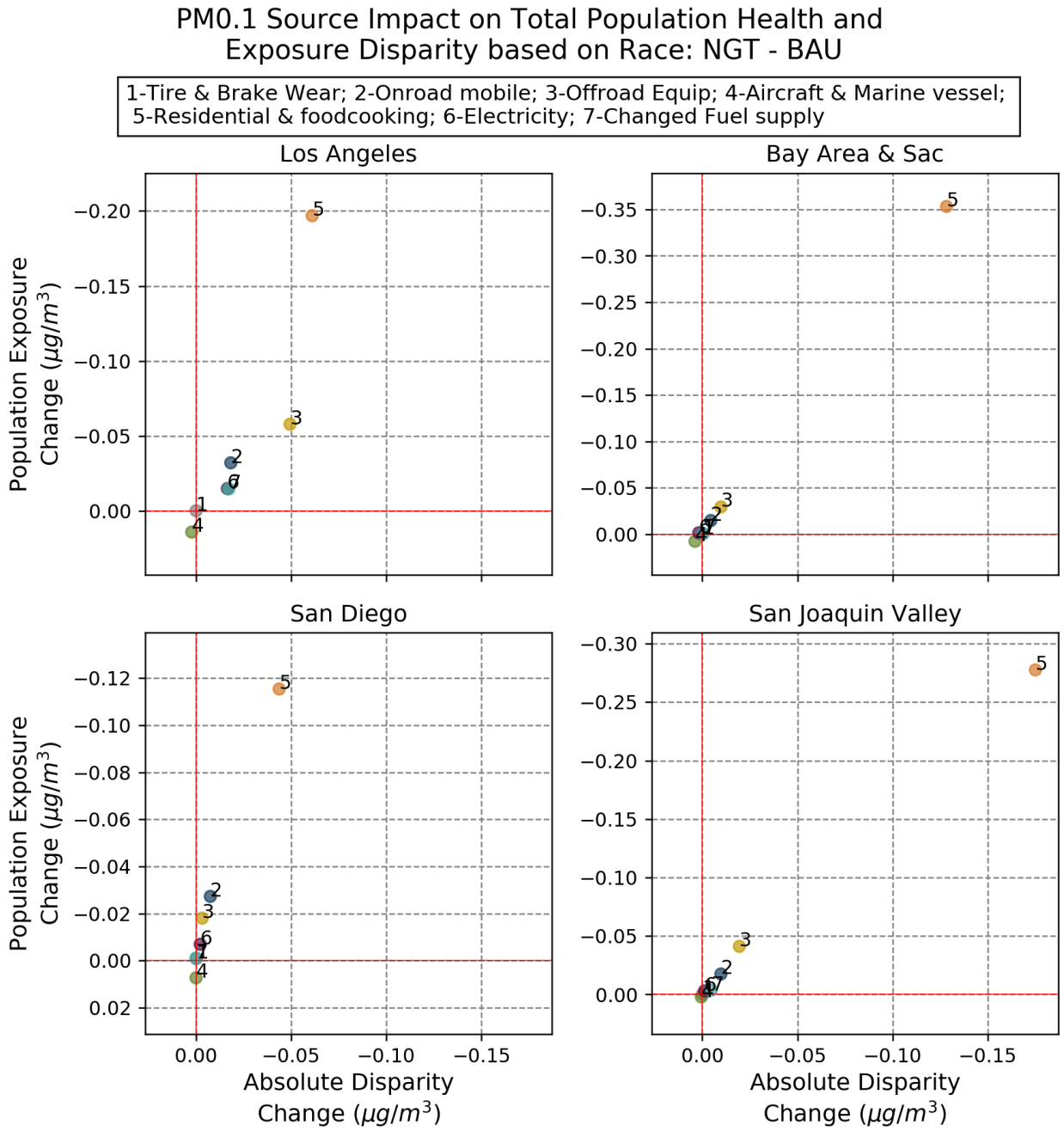

Figure S 3-56. PM0.1 source impact on total population exposure and exposure disparity based on race for NGT energy scenario. X-axis indicates largest disparity changes between BAU and NGT scenario for each specific source. Y-axis indicates PWC changes between BAU and NGT scenario for each specific source. All results averaged across four meteorological scenarios.